Flood-Entrained Debris Impacts on Structures - A Structural-Hydraulic Numerical Analysis

by

Patrick Joynt

Thesis submitted to the University of Ottawa
In partial fulfillment of the requirements for the
M.A.Sc. degree in Civil Engineering

Academic advisors: Prof. Ioan Nistor and Prof. Dan Palermo



uOttawa

Civil Engineering
Faculty of Engineering
University of Ottawa

© Patrick Joynt, Ottawa, Canada, 2021

Abstract

Tsunamis are extreme hydrodynamic events that have devastating economic, social, and environmental impacts on coastal communities. Recent devastation caused by extreme hydrodynamic events, such as the 2010 Tsunami in Chile, 2011 Tohoku Tsunami in Japan, and the 2018 Indonesian Tsunami, have increased awareness about the effectiveness of design codes used to estimate loads generated during such extreme events. The American Society of Civil Engineers (ASCE) released Chapter 6 of ASCE 7-16, which was the world's first standard that addressed tsunami resilient design prescriptions in mandatory language. Chapter 6 of ASCE 7-16 classifies tsunami loads into three categories: (1) Hydrostatic loads; (2) Hydrodynamic loads; and (3) Debris impact loads. Previous literature has mainly focused on classifying the hydraulic loading conditions and up until recently there has been limited research that addressed debris impact loads generated from objects entrained within the tsunami flow. Hence, the focus of this thesis will be on debris impact loads generated from extreme hydrodynamic events.

There are two main objectives of this thesis: (1) To investigate how Chapter 6 of ASCE 7-16 defines debris impact loads and how the assumptions made about debris impact loads in ASCE 7-16 influence structural response parameters; and (2) investigate the validity and practicality of numerically simulating dam-break wave generated debris impact events.

The first objective of this thesis is achieved by investigating how Chapter 6 of ASCE 7-16 defines debris impact loads and comparing these loads to alternative methods for estimating debris impact loads. Furthermore, these debris impact loads are applied to a numerical model of a physical structure and the response of the model is compared to response of the physical structure. It was shown that when debris impact loads are generated by following the guidelines outlined in Chapter 6 of ASCE 7-16 the resulting force response of the structural model overestimated both the magnitude and frequency of the experimental force response. Additionally, how the debris impact force history shape influences the response of the structural model was also investigated to understand the significance of the assumptions made about debris impact loads in Chapter 6 of ASCE 7-16, which assumes a rectangular impact shape. It was shown that the most conservative force response was generated when the debris impact force history shape was assumed to be a rectangular pulse. Finally, a study of how the structural response changed as the stiffness of the numerical model increased was also completed. From this study, it was shown that within the elastic range of a column, the forces developed in the column increased and the deformations decreased as the structural stiffness increased.

The second objective of this thesis is achieved by numerically simulating a dam-break wave generated debris impact event and comparing the numerical model to an experimental program of dam-break wave generated debris impact events. The numerical model was shown to be capable of estimating the water surface elevations, hydrodynamic forces, debris impact loads, and debris transport when compared to experimental data. Furthermore, it was also shown that the numerical model is capable of simulating multi-debris transport and impact events, while not requiring an unreasonably large amount of computational time and cores.

Acknowledgements

First and foremost, I would like to acknowledge my academic supervisors, Dr. Ioan Nistor and Dr. Dan Palermo, without their dedication to academia, technical expertise, and guidance, I would not have been able to have such an excellent experience in my graduate studies. They have both supported me immensely throughout my studies and have allowed me to grow both as a researcher and as a professional, I am very grateful to have had the opportunity to be mentored by both of them. I would also like to thank Dr. Nistor for presenting to undergraduate students the benefits of pursuing a graduate degree, which after a couple of meetings with him, ultimately led me to pursue my M.A.Sc.

Additionally, I want to thank Dr. Jacob Stolle for sharing his experimental data that proved to be instrumental in the development of this thesis. Furthermore, his guidance and willingness to teach have assisted me in numerous ways that have allowed me to grow my knowledge in the field of Coastal Engineering. Additionally, I would like to thank Dr. H. Ronald Riggs for his invaluable input and guidance throughout the advancement of my thesis, while also allowing me the opportunity to participate in the international experienced program.

I would also like to thank all of the professors and staff of the Faculty of Civil Engineering at the University of Ottawa for all of their guidance throughout both my undergrad and graduate studies. Furthermore, my gratitude is extended to all of the graduate students of the water resources department, who have supported and encouraged me throughout my studies.

I would also like to acknowledge the Ontario Graduate Scholarship and the International Experience Scholarship for their financial support throughout my graduate studies. Additionally, I would like to acknowledge the support provided by my supervisors through their research funds.

Furthermore, I would like to acknowledge that this research was enabled in part by support provided by Compute Ontario and Compute Canada.

Finally, I would like to thank my family and girlfriend for supporting me throughout my studies and helping me stay sane during the challenging parts of my education.

Table of Contents

Abstract ii

Acknowledgements iii

Table of Contents iv

List of Figures xii

List of Tables xvii

List of Acronyms and Symbols xviii

1 Introduction 1

1.1 Background 1

1.2 Research Objectives 3

1.3 Research Scope 3

1.4 Contributions and Novelty of the Study 4

1.5 Publications 5

1.6 Outline of the Thesis 5

2 Literature Review 7

2.1 Debris Impact Loads 7

2.1.1 Single Degree of Freedom Models 7

2.1.1.1 Haehnel and Daly (2002 and 2004) 8

2.1.1.2 Matsutomi (2009) 10

2.1.1.3 Riggs et al. (2013) 11

2.1.1.4 Aghl et al. (2014) 15

2.1.1.5 Aghl et al. (2015) . . . 17
2.1.1.6 Ko et al. (2015) . . . 20
2.1.1.7 Ikeno et al. (2016) . . . 21
2.1.1.8 Derschum et al. (2018) . . . 23
2.1.1.9 Stolle et al. (2018a) . . . 24
2.1.1.10 Code Provisions . . . 25
2.1.1.11 Discussion of Key Points and Limitations to the Single Degree of Freedom Models . . . 27
2.1.1.12 Comparison Between Various Approaches for SDOF Models 28
2.1.2 Two Degree of Freedom Model . . . 30
2.1.2.1 Stolle et al. (2019) . . . 31
2.1.2.2 Discussion of Key Points and Limitations to the Two Degree of Freedom Model . . . 34
2.1.3 Beam / Column Response to Impacts . . . 35
2.1.3.1 Khowitar et al. (2014) . . . 35
2.1.3.2 Khowitar et al. (2015) . . . 36
2.1.3.3 Discussion of Key Points and Limitations to the Impact Response Analyses Studies . . . 38
2.1.4 Energy Method . . . 39
2.1.4.1 Discussion of Key Points and Limitations to the Energy Method . . . 40
2.2 Debris Damming Loads . . . 40
2.2.1 ASCE 7 (2016) . . . 40
2.2.2 Stolle et al. (2018c) . . . 41
2.2.3 Discussion of Key Points and Limitations to Debris Damming Studies 41
2.2.3.1 Key Points . . . 41
2.2.3.2 Limitations . . . 41
2.3 Summary of Limitations in the Literature and Code Provisions . . . 42
2.4 Structural Response to Impact Loads . . . 43
2.4.1 Cotsovos et al. (2008) . . . 43
2.4.2 Fujikake et al. (2009) . . . 45
2.4.3 Imbeau (2012) . . . 47
2.4.4 Cowan et al. (2015) . . . 50

2.4.5 Das Adhikary and Li (2018) 54
2.4.6 Discussion of Key Points and Limitations in the Literature on Structural Response to Impact Loads 57
2.4.6.1 Key Points 57
2.4.6.2 Limitations 59
2.5 Review of ASCE 7 (2016) Chapter 6 Guidelines for Debris Impact Loads . 59
2.5.1 Current Guidelines 60
2.5.2 Comparison to Other Analytical Methods 62
2.5.3 Structural Response Comparison 64
2.5.3.1 Structural Model Description 65
2.5.3.2 Structural Dynamic Characteristics 66
2.5.3.3 Earthquake Record 68
2.5.3.4 Debris Impact Load 68
2.5.3.5 Structural Comparison 69
2.5.4 Discussion of Key Points and Limitations of the Review 72
2.5.4.1 Key Points 72
2.5.4.2 Limitations 72
2.6 Conclusions 73

3 Estimating Impact Force Histories **75**
3.1 Objectives and Description of Methodology 75
3.2 Description of Experimental Data 75
3.3 Impact Forcing Functions 78
3.3.1 Half-Sine Impact Shape 78
3.3.2 Rectangular Impact Shape 78
3.3.3 Triangular Impact Shape 79
3.3.4 Trapezoidal Impact Shape 79
3.3.5 Parabolic Impact Shape 79
3.4 Single-Degree-of-Freedom Method 80
3.4.1 SDOF Impact Shape Study 81
3.5 Multiple-Degree-of-Freedom Method 88
3.5.1 Mass Matrix Formulation 89
3.5.2 Stiffness Matrix Formulation 93

3.5.3 Damping Matrix Formulation 94
3.5.4 Mesh Refinement Study 98
3.5.5 Time Step Study 100
3.5.6 MDOF Impact Shape Study 103
3.6 Analytical Method 110
3.7 Results and Discussion 111
3.8 Conclusions 119

4 Parametric Study on the Influence of Impact Shape on Response Parameters 121
4.1 Objectives and Description of Methodology 121
4.2 Results and Discussion 122
4.2.1 Shear Response 122
4.2.2 Deflection Response 128
4.3 Conclusions 132

5 Parametric Study on the Influence of the Structural Stiffness on Response Parameters 135
5.1 Objectives and Description of Methodology 135
5.2 Reinforced Concrete Design 136
5.3 Development of Impact Force Histories 136
5.4 Modelling Parameters 139
5.4.1 Load Location and Analysis Type 139
5.4.2 Damping Model 140
5.4.3 Mass Definition 143
5.4.4 Concrete Model 143
5.4.5 Reinforcing Steel Model 145
5.4.6 Section Model 146
5.4.6.1 Mesh Refinement Study - Section Fibers 147
5.4.7 Element Type 150
5.4.8 Geometric Transformation Method 151
5.4.9 System of Equations Solver and Convergence Test 152
5.4.9.1 System of Equations Solver 152
5.4.9.2 Convergence Test 153

5.4.10 Time Integration Method and Solution Algorithm 153
5.4.10.1 Time Integration Method 153
5.4.10.2 Solution Algorithm 154
5.4.11 Mesh Refinement Study - Elements 154
5.4.12 Time Step Study 159
5.4.13 Yield Deflection Study 162
5.5 Results and Discussion 164
5.5.1 Shear Response 165
5.5.2 Bending Moment Response 167
5.5.3 Midspan Deflection Response 168
5.6 Conclusions 170

6 Numerical Modelling of Dam-Break Wave Generated Debris Impacts 173
6.1 Introduction and Objective 173
6.2 Numerical Modelling Methods in LS-DYNA 173
6.2.1 Lagrangian Method 174
6.2.2 Eulerian Method 174
6.2.3 Arbitrary Lagrangian-Eulerian Method 175
6.3 Physical Model Reference 176
6.4 Computational Domain 177
6.5 General ALE Description of Navier-Stokes Equations 179
6.6 Time Integration Method 181
6.6.1 Time Step Control 183
6.7 ALE Advection Schemes 185
6.8 Turbulence Modelling 186
6.9 ALE Model 187
6.9.1 Section Types 187
6.9.2 Material Modelling 187
6.9.2.1 Rigid and Elastic Material Models 188
6.9.2.2 Null Material Model 189
6.9.2.3 Vacuum Material Model 190
6.9.3 Equation of State Model 190
6.9.4 Boundary and Loading Conditions 190

6.9.5 Contact Modelling . . . 192
6.9.5.1 Debris-Structure Contact . . . 192
6.9.5.2 Fluid-Structure Interaction . . . 193
6.10 Mesh Sensitivity Analyses . . . 195
6.10.1 ALE Mesh Sensitivity Analysis . . . 195
6.10.1.1 Water Surface Elevation . . . 195
6.10.1.2 Hydrodynamic Force . . . 199
6.10.1.3 Conclusions . . . 200
6.10.2 Debris FEM Mesh Sensitivity Analysis . . . 201
6.10.2.1 Debris Transport . . . 202
6.10.2.2 Debris Impact Force . . . 203
6.10.2.3 Conclusions . . . 205
6.11 Rigid vs Elastic Structure . . . 206
6.11.1 Water Surface Elevation . . . 207
6.11.2 Hydrodynamic Force . . . 209
6.11.3 Debris Transport . . . 210
6.11.4 Debris Impact Force and Top Deflection . . . 211
6.11.5 Conclusions . . . 213
6.12 Multi-Debris Study . . . 215
6.12.1 Water Surface Elevation . . . 216
6.12.2 Hydrodynamic Force . . . 220
6.12.3 Debris Transport . . . 221
6.12.4 Debris Impact Force . . . 222
6.12.5 Conclusions . . . 225
6.13 Conclusions and Recommendations . . . 227

7 General Conclusions and Recommendations for Future Work 229
7.1 General Conclusions . . . 229
7.2 Recommendations for Future Work . . . 231

References 233

APPENDICES 239

A Example Calculations **240**
A.1 Debris Impact . . . 240
A.1.1 Haehnel and Daly (2004) . . . 240
A.1.1.1 Contact Stiffness Method . . . 240
A.1.1.2 Work Energy Method . . . 241
A.1.1.3 Impulse Momentum Method . . . 241
A.1.2 Matsutomi (2009) . . . 241
A.1.3 Riggs et al. (2013) . . . 242
A.1.4 Aghl et al. (2015) . . . 242
A.1.5 Ikeno et al. (2016) . . . 243
A.1.6 Stolle et al. (2018a) . . . 243
A.1.7 ASCE 7 (2016) . . . 244
A.1.8 AASHTO (2012) . . . 244
A.1.9 FEMA P646 (2012) . . . 244
A.1.10 Stolle et al. (2019) . . . 244
A.2 Response to Impacts . . . 246
A.2.1 Khowitar et al. (2014) . . . 246
A.2.2 Khowitar et al. (2015) . . . 247
A.3 Energy Method . . . 248
A.3.1 Clause 6.11.8 of ASCE 7 (2016) . . . 248
A.4 Debris Damming . . . 248
A.4.1 ASCE 7 (2016) . . . 249
A.4.2 Stolle et al. (2018c) . . . 249

B *OpenSees* Modelling Decisions - NCREE Structure **250**
B.1 Nodal Mass . . . 250
B.2 Geometric Transformation . . . 250
B.3 Steel Model . . . 251
B.4 Concrete Model . . . 251
B.5 Section Model . . . 252
B.6 Analysis Type and Damping Model . . . 252
B.7 System of Equations Solver . . . 253
B.8 Convergence Test . . . 253
B.9 Integrator . . . 253
B.10 Solution Algorithm . . . 254

C Numerical Solution Algorithms **255**

C.1 Duhamel's Integral Solution Algorithm 255

C.2 Newmark's Constant Average Acceleration Solution Algorithm for Linear Systems 256

List of Figures

1.1 Global and Local Structural Damage (Palermo et al., 2012) 2
1.2 Concrete Debris and Marine Vessel Impacts (Photos Taken by Jacob Stolle) 2

2.1 SDOF Model 8
2.2 Longitudinal Impact of a Rod (Riggs et al., 2013) 11
2.3 Transverse Impact of a Beam (Riggs et al., 2013) 13
2.4 In-Water and In-Air Impact Force History (Riggs et al., 2013) 14
2.5 Wooden Utility Pole Impact Force and Duration (Aghl et al., 2014) 16
2.6 Steel Tubes and Shipping Containers Impact Force and Duration (Aghl et al., 2014) 17
2.7 Inelastic Impact Force Definition (Aghl et al., 2015) 18
2.8 Impact Force and Duration Comparison (Aghl et al., 2015) 20
2.9 Dynamic Response Factor (Aghl et al., 2015) 20
2.10 Impact Force versus Velocity (Stolle et al., 2018a) 25
2.11 Comparison between SDOF Models 29
2.12 Two-Degree-of-Freedom Model 31
2.13 Impact Force versus Velocity for Various Methods (Stolle et al., 2019) . . . 33
2.14 Duhamel Integral Estimate (Stolle et al., 2019) 34
2.15 Column / Beam and Pole Interaction (Khowitar et al., 2014) 35
2.16 Column Pole Interaction (Khowitar et al., 2015) 37
2.17 Effective Length of a Beam (Cotsovos et al., 2008) 45
2.18 Model for Drop Impact Experiments (Fujikake et al., 2009) 46
2.19 SDOF Model for Elastic Deformation (Imbeau, 2012) 49
2.20 SDOF Model for Inelastic Deformation (Imbeau, 2012) 50
2.21 Linear and Nonlinear Response-Spectrum Analysis (Cowan et al., 2015) . . 52
2.22 Time-History Analysis versus IRSA Method (Cowan et al., 2015) 53

2.23 Idealized SDOF System (Das Adhikary and Li, 2018) 56
2.24 SDOF Estimate of Midspan Deflection History (Das Adhikary and Li, 2018) 57
2.25 Dynamic Response Ratio (ASCE 7, 2016) 60
2.26 Clause 6.11.2 of ASCE 7 (2016) versus Other Analytical Models 64
2.27 *OpenSees* Structural Model 65
2.28 Mode Shapes 67
2.29 Earthquake Ground Motion History 68
2.30 Debris Impact Load History 69
2.31 Peak Column Displacements 70
2.32 Residual Column Displacements 71

3.1 Example Force Response History 77
3.2 Duhamel Integration Process 81
3.3 Example Force Response for SDOF Fitting 82
3.4 Example Impact History from SDOF Fitting 83
3.5 SDOF Fitting Half-Sine Impact Histories 84
3.6 SDOF Fitting Rectangle Impact Histories 84
3.7 SDOF Fitting Triangle Impact Histories 85
3.8 SDOF Fitting Trapezoid Impact Histories 85
3.9 SDOF Fitting Parabola Impact Histories 86
3.10 SDOF Fitting Maximum Force Response Comparison 88
3.11 MDOF Solver Process 89
3.12 Example Impact Force History 90
3.13 Shear Response at Maximum Base Shear 91
3.14 Moment Response at Maximum Base Moment 92
3.15 Deflection Response at Maximum Top Deflection 93
3.16 Modal Analysis Comparison - Maximum Base Shear Force 95
3.17 Modal Analysis Comparison - Maximum Base Moment 96
3.18 Modal Analysis Comparison - Maximum Top Deflection 96
3.19 Rayleigh Damping Curve 98
3.20 Mesh Refinement Study - Maximum Base Shear Force 99
3.21 Mesh Refinement Study - Maximum Base Moment 99
3.22 Mesh Refinement Study - Maximum Top Deflection 100

3.23 Time Step Study - Maximum Base Shear Force 101
3.24 Time Step Study - Maximum Base Moment 102
3.25 Time Step Study - Maximum Top Deflection 103
3.26 Example Force Response for MDOF Fitting 104
3.27 Example Impact History from MDOF Fitting 105
3.28 MDOF Fitting Half-Sine Impact Histories 106
3.29 MDOF Fitting Rectangle Impact Histories 106
3.30 MDOF Fitting Triangle Impact Histories 107
3.31 MDOF Fitting Trapezoid Impact Histories 107
3.32 MDOF Fitting Parabola Impact Histories 108
3.33 MDOF Fitting Maximum Force Response Comparison 110
3.34 Measured Maximum Force Response vs Measured Impact Velocity 111
3.35 SDOF and MDOF Fitting Methods Compared to the Experimental Data . 112
3.36 Impact Force Histories for All Methods 113
3.37 Force Response for All Methods 114
3.38 Impact Force History Suite for ASCE 7 (2016) Method Using k_d 115
3.39 Impact Force History Suite for ASCE 7 (2016) Method Using k_s 115
3.40 Impact Force History Suite for SDOF Method 116
3.41 Impact Force History Suite for MDOF Method 116
3.42 Maximum Experimental vs Maximum Modelled Force Response 117

4.1 Example Impact Histories for Parametric Study 122
4.2 Shear Force Diagram at Point in Time When Base Shear is Maximum . . . 123
4.3 Maximum Shear Forces Developed in the Column 124
4.4 Maximum Base Shear, k_s vs k_d 125
4.5 Normalized Maximum Base Shear, k_s vs k_d 126
4.6 Time at Peak Base Shear 127
4.7 Maximum Base Shear vs Impact Force 128
4.8 Deflection Diagram at Point in Time When Top Deflection is Maximum . . 129
4.9 Maximum Deflections Developed in the Column 129
4.10 Time at Peak Top Deflection 130
4.11 Maximum Top Deflection, k_s vs k_d 131
4.12 Maximum Top Deflection vs Impact Force 132

5.1 Reinforced Concrete Cross-Section 136
5.2 Design Debris Impact Force History 139
5.3 Damping Study - Shear Forces 141
5.4 Damping Study - Bending Moment 142
5.5 Damping Study - Midspan Deflection 143
5.6 Concrete Material Models 145
5.7 Longitudinal Reinforcement Material Model 146
5.8 Fiber Model Cross-Section 147
5.9 Fiber Study - Shear Forces 148
5.10 Fiber Study - Bending Moments 149
5.11 Fiber Study - Midspan Deflection 150
5.12 Mesh Study - Shear Forces 155
5.13 Mesh Study - Bending Moments 157
5.14 Mesh Study - Midspan Deflection 158
5.15 Time Step Study - Shear Forces 160
5.16 Time Step Study - Bending Moments 161
5.17 Time Step Study - Midspan Deflection 162
5.18 Imposed Displacement History 163
5.19 Midspan Force Displacement Curve 164
5.20 Comparison of Shear Reaction Forces to $f_c^{'}$ and $\frac{k_s}{k_d}$ 166
5.21 Normalized Shear Reaction Forces ($\frac{F_x}{F_i}$) vs $\frac{k_s}{k_d}$ 167
5.22 Comparison of Reaction Bending Moments to $f_c^{'}$ and $\frac{k_s}{k_d}$ 168
5.23 Comparison of Midspan Deflections to $f_c^{'}$ and $\frac{k_s}{k_d}$ 169
5.24 Comparison of Time at Yield Displacement (δ_y) to $f_c^{'}$ and $\frac{k_s}{k_d}$ 170

6.1 University of Ottawa Dam-Break Wave Flume (Units in Meters) 176
6.2 University of Ottawa Dam-Break Wave Flume in LS-DYNA (Units in Meters) 178
6.3 Water Surface Elevation Time Series at WG1 (0.00, -0.10) 179
6.4 LS-DYNA Time Integration Loop 183
6.5 Influence of Time Step Scale Factor on Hydrodynamic Force in Y-Direction 184
6.6 Influence of Time Step Scale Factor on Time Step 185
6.7 Advection Methods in LS-DYNA 186

6.8 Fluid Material Swelling 189
6.9 Rigid Walls in Computational Domain 191
6.10 ALE Mesh Sensitivity - Water Surface Elevation at WG1 196
6.11 ALE Mesh Sensitivity - Water Surface Elevation at WG2 197
6.12 ALE Mesh Sensitivity - Water Surface Elevation at WG3 198
6.13 ALE Mesh Sensitivity - Water Surface Elevation at WG4 199
6.14 ALE Mesh Sensitivity - Hydrodynamic Force 200
6.15 Debris FEM Mesh Sensitivity - Debris Transport 203
6.16 Debris FEM Mesh Sensitivity - Pressure on Debris 203
6.17 Debris FEM Mesh Sensitivity - Debris Impact Force 204
6.18 Debris FEM Mesh Sensitivity - Debris Impact Velocity 205
6.19 Elastic Structure Study - Water Surface Elevation at WG1 207
6.20 Elastic Structure Study - Water Surface Elevation at WG2 208
6.21 Elastic Structure Study - Water Surface Elevation at WG3 208
6.22 Elastic Structure Study - Water Surface Elevation at WG4 209
6.23 Elastic Structure Study - Hydrodynamic Force 210
6.24 Elastic Structure Study - Debris Transport 211
6.25 Elastic Structure Study - Pressure on Debris 211
6.26 Elastic Structure Study - Debris Impact Force 212
6.27 Elastic Structure Study - Debris Impact Velocity 213
6.28 Elastic Structure Study - Top Deflection 213
6.29 Example Debris Layout 216
6.30 Multi-Debris Study - Water Surface Elevation at WG1 217
6.31 Multi-Debris Study - Water Surface Elevation at WG2 218
6.32 Multi-Debris Study - Water Surface Elevation at WG3 219
6.33 Multi-Debris Study - Water Surface Elevation at WG4 220
6.34 Multi-Debris Study - Hydrodynamic Force 221
6.35 Multi-Debris Study - Debris Transport 222
6.36 Multi-Debris Study - Debris Impact Forces 224
6.37 Multi-Debris Study - Initial Debris Impact Velocities 224
6.38 Multi-Debris Study - Debris Impact Orientations 225

B.1 Force-Displacement History Comparison 252

List of Tables

2.1 *OpenSees* Structural Dynamic Characteristics 66

3.1 SDOF Fitting Results 86
3.2 Modal Analysis Comparison Summary Table 97
3.3 Mesh Refinement Study Summary Table 100
3.4 Time Step Study Summary Table 103
3.5 MDOF Fitting Results 108
3.6 Impact History Properties 113
3.7 Statistics for Each Impact Force History Suite 117

4.1 Percentage Increase in Top Deflection from k_s to k_d 132

5.1 Debris Impact Force Parameters 139
5.2 Mesh Refinement Study Summary Table - Shear Forces 156
5.3 Mesh Refinement Study Summary Table - Bending Moments 158
5.4 Mesh Refinement Study Summary Table - Midspan Deflection 159
5.5 Yield Displacements and Forces 164

6.1 Reservoir Length Study 179
6.2 ALE Mesh Sensitivity - Simulation Details 195
6.3 Debris FEM Mesh Sensitivity - Simulation Details 202
6.4 Elastic vs Rigid Structure - Simulation Details 207
6.5 Multi-Debris Study - Simulation Details 216

List of Acronyms and Symbols

Acronyms

2DOF	Two degrees of freedom
ALE	Arbitrary Lagrangian-Eulerian Method
CQC	Complete-Quadratic-Combination
DEM	Discreet Element Method
DOFs	Degrees-of-Freedom
EEMD	Ensemble Empirical Mode Decomposition's
EOS	Equation of State
FEM	Finite Element Method
FSI	Fluid Structure Interaction
FVM	Finite Volume Method
HIS	Half Index Shift
IRSA	Impact Response-Spectrum Analysis
MDOF	Multiple degree of freedom
NCREE	National Centre for Research on Earthquake Engineering
RMSE	Root-Mean-Squared-Error
SDOF	Single degree of freedom
SPH	Smoothed Particle Hydrodynamics
SRSS	Square-Root-of-the-Sum-of-the-Squares

Symbols

$\mathbf{:}$	Double inner product	–
$[\boldsymbol{c}]$	Damping matrix	–
$[\boldsymbol{k}]$	Stiffness matrix	N/m
$[\boldsymbol{m}]$	Mass matrix	kg
$\boldsymbol{\beta_i}$	Obliqueness	deg
$\boldsymbol{\ddot{u}}$	Acceleration	m/s^2
$\boldsymbol{\Delta t}$	Time step	s
$\boldsymbol{\delta_{max}}$	Maximum midspan deflection	m
$\boldsymbol{\nabla\cdot}$	Divergence	–
$\boldsymbol{\dot{P}}$	Static loading rate	N/s
$\boldsymbol{\dot{u}}$	Velocity	m/s
$\boldsymbol{\epsilon_0}$	Distance from the COG of the debris to the point of impact	m
$\boldsymbol{\gamma_d}$	Unit weight of the debris	kg/m^3
$\boldsymbol{\nabla}$	Gradient	–
$\boldsymbol{\kappa}$	Shear coefficient	–
$\boldsymbol{\lambda(\theta_c)}$	Kinetic to rotational energy function	–
$\boldsymbol{\mu}$	Coefficient of friction	–
$\boldsymbol{\nu_d}$	Poisson's ratio for the debris	–
$\boldsymbol{\nu_s}$	Poisson's ratio for the structure	–
$\boldsymbol{\nu}$	Poisson's ratio	–
$\boldsymbol{\omega_1}$	First natural frequency	rad/s
$\boldsymbol{\omega_2}$	Second natural frequency	rad/s
$\boldsymbol{\omega_d}$	Damped natural frequency	rad/s
$\boldsymbol{\omega_{v0}}$	Rotational velocity	rad/s
$\boldsymbol{\phi_i}$	Angle of impact relative to the debris surface	deg
$\boldsymbol{\rho_f}$	Density of fluid	kg/m^3

$\boldsymbol{\rho}$	Density	kg/m^3
$\overline{\overline{\boldsymbol{\nabla}}}$	Second order tensor	–
$\boldsymbol{\sigma_{df}}$	Debris yield stress	MPa
$\boldsymbol{\tau}$	Elapsed time since impact	s
$\boldsymbol{\theta'_c}$	Collision velocity vector	m/s
$\boldsymbol{\theta_c}$	Collision angle	deg
$\boldsymbol{\tilde{E}}$	Effective Young's modulus	MPa
$\boldsymbol{\xi}$	Damping ratio	%
$\boldsymbol{\{\ddot{u}\}}$	Acceleration vector	m/s^2
$\boldsymbol{\{\dot{u}\}}$	Displacement vector	m
$\boldsymbol{\{\dot{u}\}}$	Velocity vector	m/s
$\boldsymbol{a_0}$	Mass coefficient for Rayleigh damping	–
$\boldsymbol{a_1}$	Stiffness coefficient for Rayleigh damping	–
$\boldsymbol{A}$	Cross-sectional area	m^2
$\boldsymbol{B_b}$	Overall building width	m
$\boldsymbol{C_0}$	Impact orientation coefficient	–
$\boldsymbol{C_d}$	Drag coefficient	–
$\boldsymbol{C_e}$	Coefficient of restitution	–
$\boldsymbol{C_f}$	Added mass coefficient	–
$\boldsymbol{c_{cr}}$	Critical damping	$N/(m/s)$
$\boldsymbol{C_{cx}}$	Closure Ratio	–
$\boldsymbol{C_{MA}}$	Matsutomi (2009) Mass Coefficient	–
$\boldsymbol{C_{R0}}$	Resistance coefficient	–
$\boldsymbol{C_R}$	Mean resistance coefficient	–
$\boldsymbol{c}$	Inherent damping	%
$\boldsymbol{d_s}$	Debris stopping distance	s
$\boldsymbol{D_w}$	Diameter of the driftwood	m

$\boldsymbol{E_b}$	Bending deformation energy	J
$\boldsymbol{E_c}$	Energy stored in the contact region	J
$\boldsymbol{E_d}$	Modulus of elasticity for the debris	MPa
$\boldsymbol{E_m}$	Membrane-stiffening energy	J
$\boldsymbol{E_p}$	Secondary modulus	MPa
$\boldsymbol{E_s}$	Modulus of elasticity for the structure	MPa
$\boldsymbol{E_s}$	Shear deformation energy	J
$\boldsymbol{E_{rc}}$	Energy loss due to perfectly plastic collision	J
$\boldsymbol{E}$	Modulus of Elasticity	MPa
$\boldsymbol{e}$	Eccentricity	$-$
$\boldsymbol{F_y}$	Yield strength	MPa
$\boldsymbol{F_{cap}}$	Force capacity of the structure	N
$\boldsymbol{F_i}$	Impact force	N
$\boldsymbol{F_{nd}}$	Drag force	N
$\boldsymbol{F_{ni}}$	Nominal impact force	N
$\boldsymbol{G}$	Shear modulus	MPa
$\boldsymbol{g}$	Gravity	m/s^2
$\boldsymbol{h(t-\tau)}$	Impulse response function	N
$\boldsymbol{h_{drop}}$	Drop height	m
$\boldsymbol{h_{in}}$	Inundation depth	m
$\boldsymbol{I_{tsu}}$	Importance factor for structures subjected to tsunami loads	$-$
$\boldsymbol{I}$	Moment of inertia	m^4
$\boldsymbol{k_d}$	Debris stiffness	N/m
$\boldsymbol{k_e}$	Effective stiffness	N/m
$\boldsymbol{K_m}$	Membrane stiffness	N/m
$\boldsymbol{k_s}$	Structural stiffness	N/m
$\boldsymbol{K_{bs}}$	Bending and shear stiffness	N/m

k_{de}	Equivalent elastic stiffness	N/m
k_{dp}	Secondary equivalent stiffness	N/m
k_{HD}	Haehnel and Daly structure stiffness	N/m
k_{sp}	Spring stiffness	N/m
L_T	Distance between the COG of the debris and the point of contact	m
L_w	Length of the driftwood	m
L_{eff}	Effective length of a beam	m
L	Length	m
m_d	Mass of the debris	kg
m_f	Added mass of fluid	$-$
m_s	Mass of the structure	kg
$m_{contents}$	Mass of shipping container contents	kg
n_c	Hertzian contact stiffness	N/m
$P(\delta)$	Force deformation function	N
$p(\tau)$	Impact forcing function	N
P_s	Static load carrying capacity	N
$R(t)$	Structural Response function	N
R_d	Dynamic response facto r	$-$
r_{0d}	Radius of the debris	m
r_{id}	Radius of gyration of the debris	m
R	Inertial motion radius	m
T_1	First natural period	s
t_d	Impact duration	s
T_n	Natural period	s
t_s	Time since impact	s
T_{comp}	Computation time	hrs
t_{dLogs}	Impact duration for logs and poles	s

$t_{dShipping}$	Impact duration for shipping containers	s
T_{sim}	Simulation time	s
T_{step}	Time step	s
t	Time	s
u_d	Debris velocity	m/s
u_w	Stress wave velocity	m/s
u_{flow}	Tsunami flow velocity	m/s
u_{max}	Maximum debris velocity	m/s
u	Displacement	m
v_y	Yield velocity	m/s
v_{A0}	Debris collision velocity	m/s
v_{ia}	Beam deformation velocity	m/s
v_{ib}	Hammer impact velocity	m/s
v_{in}	Initial velocity at the impact point	m/s
v	Current velocity	m/s
x_d	Displacement of debris in 2DOF model	m
x_s	Displacement of structure in 2DOF model	m

Chapter 1

Introduction

1.1 Background

Recent devastation caused by extreme coastal inundation events, such as the 2010 Tsunami in Chile, 2011 Tohoku Tsunami in Japan, and the 2018 Indonesian Tsunami, have increased awareness about the effectiveness of design codes used to estimate loads generated during such extreme events. Due to the proximity of the Canadian West Coast to the Circum-Pacific Belt, this region is vulnerable to the potential impact of tsunamis, which can have severe economic, social, and environmental impacts on coastal communities. Hence, it is essential for the engineering design community to better understand how to account for loads that are generated during these types of extreme events and how to apply these loads in the design of critical infrastructure. Chapter 6 of ASCE 7 (2016) classifies tsunami loads into the following three categories:

1. Hydrostatic load - a load applied onto a structure due to a standing mass of water.
2. Hydrodynamic load - a load applied onto a structure due to water flowing against or around it.
3. Impact load - a load applied onto a structure due to debris or other objects being transported by the design tsunami.

Observing post-tsunami field surveys, each of these loading conditions can be seen to have caused extensive damage to coastal communities (Palermo et al., 2012; Naito et al., 2014; Syamsidik et al., 2019; Stolle et al., 2020a). Specifically, during the 2018 Indonesian Tsunami the damaged caused by debris impacts was seen in most of the inundated areas (Syamsidik et al., 2019), highlighting the importance of understanding these types of loads for structural design. Palermo et al. (2012) presents specific examples of structural damage experienced during the 2010 Tsunami in Chile and the 2011 Tohoku Tsunami. The damage ranges from local member failure to global structural damage as is shown in Figure 1.1.



(a) Global Structural Damage

(b) Local Structural Damage

Figure 1.1: Global and Local Structural Damage (Palermo et al., 2012)

Stolle et al. (2020a) presents further examples of structural damage due to various types of debris impacts during the 2018 Indonesian Tsunami. The author shows that debris impacts can be due to a wide range of debris types such as concrete debris and marine vessels as shown in Figure 1.2. Additionally, the damaged caused by debris impacts can vary widely; the authors show that structural damage can range from concrete spalling to complete failure of exterior columns, as shown in Figure 1.2.



(a) Concrete Debris Impact

(b) Marine Vessel Impact

Figure 1.2: Concrete Debris and Marine Vessel Impacts (Photos Taken by Jacob Stolle)

Observing post-tsunami field studies, the conclusion can be made that an important design consideration for tsunami-resilient infrastructure is debris impact loading. However, this type of loading has not seen significant attention (Nistor et al., 2017a; Stolle et al., 2020a) and hence debris impact loads will be the focus of this study.

1.2 Research Objectives

The intent of this thesis is twofold: (1) To investigate how the current design standards for debris impact loads outlined in Chapter 6 of ASCE 7 (2016) influence structural response parameters; and (2) investigate the validity and practicality of numerically simulating dam-break wave generated debris impacts. The overall objectives for each chapter of this thesis are outlined as follows:

1. The main objective of Chapter 3 is to investigate alternative methods for estimating debris impact force histories and to compare the resulting modelled force history from these methods to experimental force response data to determine their validity. Furthermore, how loads generated from a single-degree-of-freedom method translate to a multiple-degree-of-freedom system is also investigated.

2. The main objective of Chapter 4 is to investigate the significance that the shape of the debris impact force history has on structural response parameters. The results will be compared to the guidelines outlined in Chapter 6 of ASCE 7 (2016), where the use of a rectangular pulse impact shape is required.

3. The main objective of Chapter 5 is to investigate the influence that the structural stiffness has on how a column responds to the design debris impact load as defined in Chapter 6 of ASCE 7 (2016).

4. The main objective of Chapter 6 is to present the validity and practicality of using a numerical model for simulating dam-break wave generated debris impact events.

1.3 Research Scope

One of the objectives of this thesis is to enhance the understanding and investigate the assumptions made about debris impact loads in the guidelines outlined in Chapter 6 of ASCE 7 (2016). This is achieved by comparing how Chapter 6 of ASCE 7 (2016) defines debris impact loads to alternative methods and also investigating how the assumptions made in Chapter 6 ASCE 7 (2016) about debris impact loads influence structural response parameters. Furthermore, another objective of the thesis is to highlight the validity of using a numerical model to simulate debris impact events generated from extreme hydrodynamic conditions. This is achieved by developing a numerical model in LS-DYNA that simulates dam-break wave generated debris impact events and comparing the numerically modelled results to experimental data.

The development of the structural models used in Chapters 3 and 4 was restricted to linearly elastic models as the physical structure in Stolle et al. (2019) did not exhibit nonlinear behavior. These numerical models were then used to estimate debris impact loads generated from the experimental program outlined in Stolle et al. (2019). Furthermore, how these loads compared to those generated by following Clauses 6.11.2 and 6.11.8 of ASCE 7 (2016) was determined to investigate how the standard compares to these alternative

methods. A numerical model was then subjected to the impact loads generated from all of the methods investigated in Chapter 3. The resulting force response history from the numerical model was then compared to the experimental data outlined in Stolle et al. (2019), to determine which method for estimating the debris impact force history resulted in the closest fit to the experimental data. Furthermore, how the impact shape influenced the response of the numerical model was also investigated by subjecting the numerical model to debris impact force histories with varying impact shapes. The objective of studying the impact shape is to provide a better understanding of the significance of assuming a rectangular pulse impact shape as defined in Clause 6.11.8 of ASCE 7 (2016).

The study in Chapter 5 numerically models a full-scale reinforced concrete column subjected to a point load at the midspan. The point load is used to approximate the debris impact force from a shipping container, where the impact magnitude, duration, and shape are defined by Clauses 6.11.2, 6.11.6, and 6.11.8 of ASCE 7 (2016). During this study the influence of the structural stiffness on how a column responds to the debris impact load was investigated.

A numerical model was then developed to study the validity of using a numerical model to simulate dam-break wave generated debris impact events. The numerical model simulates the dam-break wave generated debris impact events outlined in Stolle et al. (2019, 2020b). The validity of the model was determined by comparing the numerical water surface elevation, hydrodynamic force, debris impact force, debris impact velocity, and debris transport to the experimental data outlined in Stolle et al. (2019, 2020b).

1.4 Contributions and Novelty of the Study

Section 2.1 outlines previous studies and current design standards for estimating debris impact loads. As can be seen in the majority of these studies, the debris impact force equations have been developed based on the assumption that the debris impact event can be treated as a single-degree-of-freedom (SDOF) system. As such, the novelty of this study lies in investigating the assumption that a debris impact event can be treated as a SDOF system and also investigating how the loads developed by a SDOF method translate to a multiple-degree-of-freedom (MDOF) system. Furthermore, Chapter 4 aims to further the understanding of how the assumptions made about debris impact loads in Chapter 6 of ASCE 7 (2016) influence the response of a structure. Additionally, Chapter 5 aims to further the understanding how structures with different stiffnesses influence both the debris impact force as per Chapter 6 ASCE 7 (2016) and how the structures responds to these debris impact forces.

As part of this thesis, a novel numerical model in LS-DYNA was developed to simulate dam-break wave generated debris impact events. Previous studies, as shown in Chapter 2, have primarily focused on quantifying tsunami generated debris impact loads through scaled-down experimental studies. Alternatively, full-scale experimental and numerical studies that do not include the transient hydrodynamic conditions associated with tsunami generated debris impacts were also investigated. As such, the novelty of this study lies in

investigating the validity and practicality of using a numerical model to estimate debris impacts under transient hydrodynamic conditions. With the ability to numerically simulate debris impacts under transient hydrodynamic conditions, full-scale debris impacts that cause extreme deformations and failures in structures can be studied without costly experimental setups.

1.5 Publications

At the time of writing this thesis, the author of the thesis (Patrick Joynt) has not been published. However, two manuscripts are currently being prepared for publication. The first manuscript is focused on the studies completed in Chapters 3 and 4. The second manuscript is focused on the numerical modelling of dam-break wave generated debris impact events as presented in Chapter 6.

1.6 Outline of the Thesis

To address the objectives of this thesis as outlined in Section 1.2, the thesis was divided into the following chapters:

- Chapter 2 outlines a literature review that presents the state-of-the-art in regards to estimating debris impact and damming loads resulting from extreme inundation events. Additionally, how debris impact and damming loads are defined in current standards and guidelines is also presented. Furthermore, a literature review is presented that highlights the general structural response to impact loads. Finally, a brief study is presented that analyzes a structures response to a load combination of an earthquake and a debris impact defined by the formulas in Chapter 6 of ASCE 7 (2016).
- In Chapter 3, a study is performed that examines alternative methods for estimating debris impact force histories and also examines how these methods compare to experimental data. The objective of the study is to investigate the validity of using each of the methods presented to estimate debris impact force histories and to compare them to how Chapter 6 of ASCE 7 (2016) defines debris impact force histories.
- In Chapter 4, a parametric study is performed to investigate the influence that the shape of the debris impact force history has on response parameters of a column. The objective of the study is to highlight the significance of assuming a rectangular impact force history for debris impact loads as defined in Clause 6.11.8 of ASCE 7 (2016).
- In Chapter 5, a parametric study is performed to investigate the influence that the structural stiffness has on response parameters of a column. The objective of the study is to highlight the significance that the structural stiffness has on both the

response of a column and the debris impact loads generated by following Clause 6.11.2 of ASCE 7 (2016).

- In Chapter 6, a novel numerical model is presented that simulates dam-break wave generated debris impact events. The objective of the study is to investigate the validity of using a numerical model to predict debris impact loads by comparing the results from the numerical model to experimental data.

- Chapter 7 summarizes the thesis by outlining the general conclusions drawn from the studies completed. Additionally, recommendations for future work in the field of estimating debris impact loads is proposed.

- The Appendices include a section that describes different analytical formulations for debris impact loads, *OpenSees* numerical modelling decisions for the study presented in Chapter 2, and two numerical algorithms for solving the equation of motion.

Chapter 2

Literature Review

2.1 Debris Impact Loads

The following sections focus on studies that outline various procedures for estimating debris impact loads. The procedures can be broken down into four main categories:

1. Single Degree of Freedom Models
2. Two Degree of Freedom Models
3. Beam and Column Response Models
4. Energy Methods

2.1.1 Single Degree of Freedom Models

A single degree of freedom (SDOF) model is a model where the structure is assumed to be fully rigid and the debris is modelled as a point mass with a certain velocity, as shown in Figure 2.1. In this SDOF model the following properties can be outlined:

1. The mass of the structure is not accounted for when deriving the impact force, only the mass of the debris is accounted for.
2. The stiffness of the structure and debris is typically accounted for by taking the effective stiffness between the two bodies. This effective stiffness represents the contact stiffness between the two bodies.
3. Any inherent damping associated with the structure and debris is not accounted for and any viscous damping associated with the impact occurring in a fluid is also not accounted for. Damping is typically not accounted for as the impact occurs over a short duration of time (Haehnel and Daly, 2004).

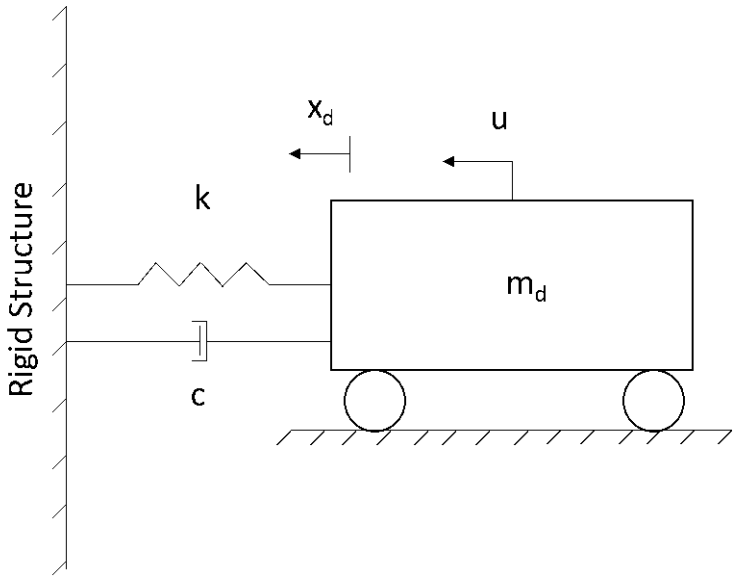


Figure 2.1: SDOF Model

2.1.1.1 Haehnel and Daly (2002 and 2004)

In Haehnel and Daly (2002) a woody debris was collided with structures to investigate the maximum impact force that flood-plain structures could be exposed to during flooding events. The experiments concluded that the maximum impact force could be defined by a SDOF model termed the contact-stiffness approach. Where the impact force is a function of the velocity of the debris, mass of the debris, and the stiffness of the debris, the equation below outlines this relationship:

$$F_{ni} = u_{max}\sqrt{k_d m_d} \tag{2.1}$$

Additionally, the authors outline two other methods that are equivalent to the contact-stiffness approach outlined above. The second method is termed the work-energy approach which assumes that the impact force is a function of the velocity of the debris, mass of the debris, and the stopping distance of the debris. The stopping distance of the debris is defined as the distance the debris travels from the point of contact until the motion of the debris is reduced to zero, the equation below outlines this relationship:

$$F_{ni} = \frac{m_d u_{max}^2}{d_s} \tag{2.2}$$

The third method is termed the impulse-momentum approach which equates the impulse acting on the debris that is in contact with the structure to the momentum change of the debris. This method is a function of the velocity of the debris, the mass of the debris, and the impact duration. The impact duration is defined as the duration of time required to reduce the momentum of the debris to zero, with the start time being defined

at the initial contact between the debris and structure, the equation below outlines this relationship:

$$F_{ni} = \frac{\pi}{2} \frac{m_d u_{max}}{t_d} \tag{2.3}$$

As per Haehnel and Daly (2002), all three of these methods are theoretically equivalent however, due to the typical treatment of the impact duration and stopping distances as constants, these three formulas often lead to different maximum impact forces. The authors show that the impact duration is a function of the mass of the debris and the stiffness of the debris. Similarly, the stopping distance of the debris is a function of the velocity of the debris, the mass of the debris, and the stiffness of the debris. The following equations outline these relationships:

$$t_d = \frac{\pi}{2} \sqrt{\frac{m_d}{k_d}} \tag{2.4}$$

$$d_s = u_{max} \sqrt{\frac{m_d}{k_d}} \tag{2.5}$$

In Haehnel and Daly (2004), the same test data from 2002 was investigated again, however, the stiffness of the debris was replaced with the effective stiffness of the system. The effective stiffness of the system is a function of the local stiffness of the structure at the contact point and the stiffness of the debris, the equation below outlines this relationship:

$$k_e^{-1} = \frac{1}{k_s} + \frac{1}{k_d} \tag{2.6}$$

The benefit of using the effective stiffness when compared to using the debris stiffness is that the response of the structure due to the impact now has an influence on the force exerted onto the structure, which is important for non-rigid impacts. Regardless, in Haehnel and Daly (2002) the structure was assumed to be rigid such that no displacement in the structure occurred.

Haehnel and Daly (2004), go on to state that due to the impact occurring in water there should be a term that addresses the added mass of the displaced fluid by the debris, this is termed the added mass coefficient. The revised equation for the maximum impact force is outlined below to include the added mass coefficient:

$$F_{ni} = u_{max} \sqrt{k_e (m_d + C_f m_f)} \tag{2.7}$$

The value of the added mass coefficient is related to the debris' geometry, submergence, orientation relative to the direction of acceleration, and the natural period of the debris. The authors outline various values for the added mass coefficient based on the impact angle and type of debris as follows:

- $C_f = 0.00$ for full-size cylindrical logs with an impact angle of 0°
- $C_f = 0.22$ for small rectangular timbers with an impact angle of 0°

- $C_f = 1.00$ for long cylindrical logs with an impact angle of 90°
- $C_f = 2.40$ for square timbers with an impact angle of 90°
- $C_f = 3.50$ for rectangular timbers with an impact angle of 90°

The authors add on two more parameters that account for the eccentricity and obliqueness of the impact. These parameters are functions of the angle of the impact relative to the debris surface, distance from the center of gravity of the debris to the point of impact, radius of gyration of the debris, coefficient of the friction between the structure and debris, and the radius of the debris. The equations for eccentricity and obliqueness are defined below, along with the general form of the impact equation:

$$e = \frac{1}{\sqrt{1 + \left(\frac{\epsilon_0}{r_{id}}\right)\left(1 + \mu(\frac{r_{0d}}{\epsilon_0})\right)}} \tag{2.8}$$

$$\beta = \sin\phi_i \tag{2.9}$$

$$F_{ni} = e\beta u_{max}\sqrt{k_e(m_d + C_f m_f)} \tag{2.10}$$

It should be noted that the effect of eccentricity and obliquity are to reduce the impact force due to eccentric and oblique impacts. For a more conservative estimate of the impact force these parameters are typically not included.

Finally, the authors go on to conclude that the peak impact force occurred for debris impacts where the longitudinal axis of the debris was parallel with the flow and hence, the effects of the added mass coefficient are negligible. Additionally, the authors conclude that based on the experimental data in their study, the contact-stiffness approach provides an upper-bound estimate for the debris impact load. Applying these conclusions, the maximum impact force equation takes the form of Eq. 2.1, however, the stiffness of the debris is replaced with the effective stiffness of the structure and debris.

2.1.1.2 Matsutomi (2009)

In Matsutomi (2009) a method for estimating the maximum impact force for a single debris entrained in a tsunami inundation flow is presented. The author experimentally studied the impact force in-water induced by small-scale driftwood onto a rigid structure. The author noted that the added mass of the displaced fluid by the driftwood needs to be accounted for in the force equation, as this volume of water is decelerated along with the driftwood when the impact occurs. The force equation that the author proposes is a function of the unit weight of the debris, the diameter of the driftwood, the length of the driftwood, the debris collision velocity, the yield stress of the driftwood, gravity, and the added mass coefficient. The following relationship is outlined below:

$$\frac{F_{ni}}{\gamma_d D_w^2 L_w} = 1.6 C_{MA}\left(\frac{v_{A0}}{\sqrt{gD_w}}\right)^{1.2}\left(\frac{\sigma_{df}}{\gamma_d L_w}\right)^{0.4} \tag{2.11}$$

The author states that the mass coefficient depends on the size and shape of the driftwood, the type of structure it collides with, and the type of flow. For driftwood located at the tip of the inundated flow the mass coefficient ranges from 1.1-1.7, for driftwood located at the tip of a strong bore the mass coefficient ranges from 0.5-1.7, for driftwood in a steady or quasi-steady flow a mass coefficient of 1.9 is suggested. In order to be conservative a mass coefficient of 1.9 would generate the highest impact force when compared to all other mass coefficients suggested and would yield a force formula as follows:

$$F_{ni} = 3.04 \left(\frac{v_{A0}}{\sqrt{gD_w}} \right)^{1.2} \left(\frac{\sigma_{df}}{\gamma_d L_w} \right)^{0.4} \left(\gamma_d D_w^2 L_w \right) \tag{2.12}$$

The author also suggests a formula for the duration of the impact which is a function of the length of the driftwood, the diameter of the driftwood, the collision velocity, and gravity. The equation is outlined below:

$$t_d = 0.48 \left(\frac{L_w}{D_w} \right)^{0.24} \left(\frac{v_{A0}}{\sqrt{gD_w}} \right)^{0.42} \sqrt{\frac{D_w}{g}} \tag{2.13}$$

2.1.1.3 Riggs et al. (2013)

In Riggs et al. (2013) a theoretical solution is developed for water-driven debris impact forces on structures, which is based off of analytical models for longitudinal and transverse impacts. The theoretical solution is validated by full-scale impact tests of a wooden utility pole and a shipping container for both in-air tests and $1:5$ scale prototype tests in-water. The objective of the study was to validate the theoretical models and quantify the effect of the added mass due to the impact occurring in-water.

The theoretical models assume that the impact occurs only in the elastic range, that the debris impacts a spring with a certain stiffness which represents the structural member, and that the added mass of the displaced fluid is not significant and as such is not included in the model. The theoretical models are broken down into two categories, the first being a longitudinal impact model and the second being a transverse impact model.

Longitudinal Impact Model The longitudinal impact model is described as a continuous rod traveling with an initial velocity that impacts a spring with a certain stiffness associated to the structural stiffness. The longitudinal impact model can be seen below in Figure 2.2:

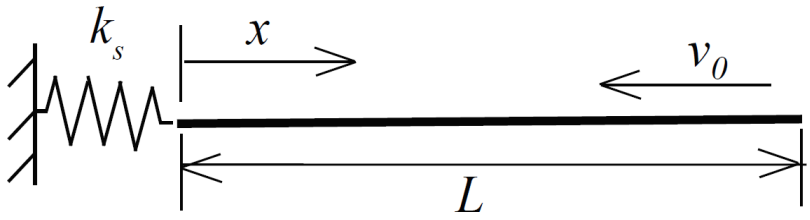


Figure 2.2: Longitudinal Impact of a Rod (Riggs et al., 2013)

One of the key assumptions in this model is that the rod responds uniaxially implying that the displacement of the rod only occurs in the direction of the longitudinal axis of the debris. The assumption of a uniaxial response is used to ensure that the one-dimensional wave equation governs the behaviour of the impact. The force induced by the longitudinal impact model is a function of the initial velocity of the impact, the stiffness of the rod, and the mass of the rod. The stiffness of the rod is a function of the modulus of elasticity of the rod, the cross-sectional area of the rod, and the length of the rod. For a rigid impact, the time history of the force is described as a rectangular pulse such that at the end of the impact the rod separates away from the rigid spring. The duration of the impact is described as function of the mass of the rod and the stiffness of the rod, theoretically it is the duration of time for a stress wave to propagate the length of the rod and back. The following formulas outline the stiffness, impact force, and impact duration:

$$k_s = \frac{EA}{L} \tag{2.14}$$

$$F_{ni} = -v_{in}\sqrt{k_s m_d} \tag{2.15}$$

$$t_d = 2\sqrt{\frac{m_d}{k_s}} \tag{2.16}$$

Observing the above formulas, they take a similar form to those suggested by Haehnel and Daly (2004), however, a different definition of the contact stiffness is used. The authors go on to state that as the stiffness of the rod increases closer to the stiffness of the spring, the impact duration increases but the peak impact force decreases noticeably, eventually reaching the half-sinusoidal shape associated with a rigid mass hitting a spring. This behaviour is significant, as the stiffness of the rod becomes closer to the stiffness of the spring, both bodies will be experiencing elastic behaviour. This implies that the elastic deformation of both the rod and the spring absorb a portion of the impact energy which decreases the impact force and increases the duration of the impact. In the case of a rigid mass hitting a flexible spring the impact force and impact duration can be described as follows:

$$F_{ni} = -v_{in}\sqrt{k_{sp} m_d} \tag{2.17}$$

$$t_d = \pi\sqrt{\frac{m_d}{k_{sp}}} \tag{2.18}$$

Transverse Impact Model The transverse impact model is described as a continuous beam traveling with an initial velocity at the center of mass of the beam and a uniform rotational velocity along the beam. The beam then impacts a spring with a certain stiffness associated to the structural stiffness. The authors state that as the beam is being impacted in shear, shear deformation becomes an important mechanism and hence, Timoshenko's beam theory is adopted for the formulation of the transverse impact model. The transverse impact model can be seen below in Figure 2.3:

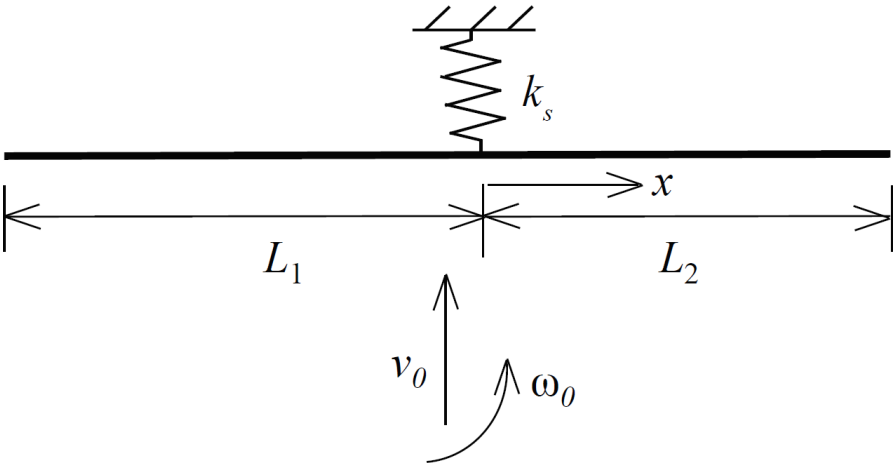


Figure 2.3: Transverse Impact of a Beam (Riggs et al., 2013)

For a rigid spring impact, the force induced by the transverse impact model is a function of the initial velocity at the point of impact, the stiffness of the beam, and the mass of the beam. The stiffness of the beam is a function of the shear coefficient, shear modulus, cross-sectional area, and the length of the beam. The authors note that the impact duration is governed by the shear wave speed in the beam and hence is a function of the length of the beam, shear coefficient, shear modulus, and the density of the beam. These formulas can be described as follows:

$$k_s = \frac{\kappa G A}{L} \tag{2.19}$$

$$F_{ni} = -v_{in}\sqrt{k_s m_d} \tag{2.20}$$

$$t_d = \frac{L}{\sqrt{\frac{\kappa G}{\rho}}} \tag{2.21}$$

The authors go on to further explain that for many cases of impacting debris, the longitudinal impact model will produce the larger peak force as the longitudinal and transverse models are related to each other by the following relationship:

$$\frac{F_{peak_{Longitudinal}}}{F_{peak_{Transverse}}} = \frac{\sqrt{\tau}}{2} \tag{2.22}$$

Where τ for isotropic materials is a function of Poisson's ratio and the shear coefficient associated with the debris material and cross-section as shown below:

$$\tau = \frac{2(1+\nu)}{\kappa} \tag{2.23}$$

For example, a square steel tube has a shear coefficient equal to 0.5 and if the Poisson's ratio is assumed to be 0.30, this would yield a force ratio of 1.14. The authors go on to state that due to this force ratio, it is anticipated that for many debris types the peak

longitudinal force will be larger than the peak transverse force. Additionally, the peak longitudinal force is likely to occur over a longer period of time when compared to the peak transverse force. Hence, this would suggest that the peak longitudinal force provides the more critical impact case for design.

Physical Experiments and Added Mass Factor The in-air and in-water experiments were completed to determine if the impact models mentioned above represent the experimental data well and to determine if the added mass due to displaced water has a significant effect on the impact force. The authors came to the conclusion that Eq. 2.15 can reasonably estimate the peak impact forces for a wooden hydro-pole and a steel shipping container. However, the impact duration is not adequately estimated by the above equations. The authors stipulate that this is due to the fact that the entire mass of the debris was used to calculate the duration of the impact. Using the entire mass would correlate to an underestimation of the shear wave speed and hence the calculated impact duration becomes longer than those recorded during the in-air experiments. The results from the in-water experiments show that there is a slight increase in the peak impact force generated by the debris impact as show in Figure 2.4:

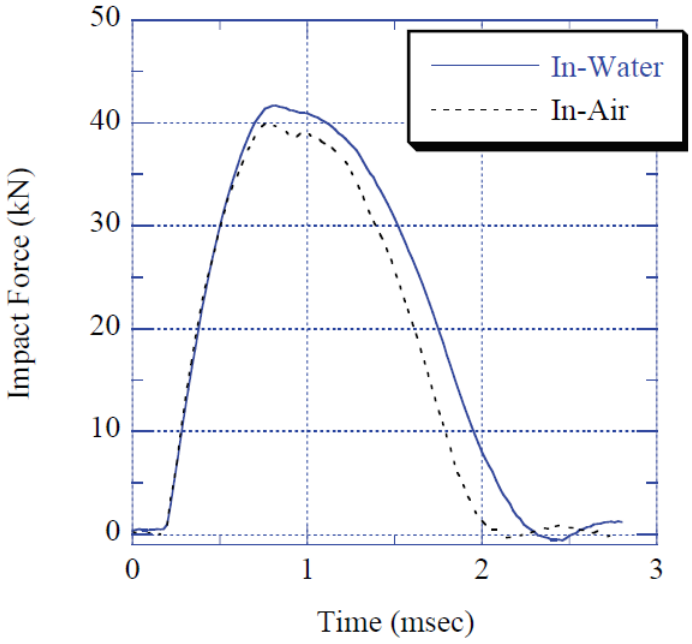


Figure 2.4: In-Water and In-Air Impact Force History (Riggs et al., 2013)

Observing the figure, the peak in-air impact occurs at approximately $40kN$ whereas the peak in-water impact occurs at approximately $42.5kN$, which represents a peak in-water impact force that is approximately 6.25% greater than the peak in-air impact force. The authors state that this increase in the impact force may be negligible for design purposes as the effect of the added mass of water comes secondary to the purely structural response

of the impact, which for this specific event accounts for 93.75% of the peak impact force that occurs in water.

2.1.1.4 Aghl et al. (2014)

In Aghl et al. (2014) a full-scale in-air experimental study was conducted on debris impacts for wood utility poles, ISO shipping containers, and steel tubes which represent structural supports inside the shipping containers. The goal of the experimental study was to quantify the impact forces induced by debris and to study how inelastic impacts influence the duration and magnitude of the force. Additionally, the influence of the contact area ratio and contact stiffness on the impact load and duration were also examined. The contact area ratio is defined as the ratio between the area of the impact region to the cross-sectional area of the debris. The contact stiffness is the stiffness of the impacted material between the debris and the load cell.

Wooden Utility Pole Results The wooden utility pole experiments were completed such that both the small and large ends of the poles were impacted to remain in the elastic range. The small end of the pole was then impacted past the elastic capacity and into the inelastic range (permanently damaged state). Results from the wooden utility pole impact tests concluded that the impact force varies linearly with the impact velocity when the poles capacity was not extended beyond the elastic capacity, as theorized and shown by Haehnel and Daly (2004) and Riggs et al. (2013). The authors go on to state that as the impact velocity increases, the impact duration decreases which is attributable to an increase in the stress wave propagation speed in the wooden pole, which is a strain-rate sensitive material.

Additionally, the authors concluded that the peak impact force does not depend on the contact area ratio of the impact. The authors do not provide an inclination of why this behaviour was noted but it could be due to the fact that the small and large ends of the debris do not vary much in size, there is a difference of only $5.1cm$ (21.1%) between the two ends. Further studies would have to be completed for larger varying cross-sections to determine if the contact area ratio has an effect on the peak impact force.

The authors show that the elastic impact force decreased and the impact duration increased as the wooden poles were loaded into an inelastic state. As can be seen in Figure 2.5 the impact force of the two inelastic tests tapers down and away from the line of best fit as the impact velocity increases. This trend suggests that as impact velocity increases the wooden poles become more damaged and hence the impact force decreases as more energy is absorbed by the deformation of the pole. Additionally, in Figure 2.5 the opposite trend is visible where the impact duration tapers up and away from the line of best fit as the impact velocity increases. Comparing these two graphs the conclusion can be made that if wooden utility poles are impacted passed the elastic capacity, the peak impact force will decrease but the impact duration will increase.

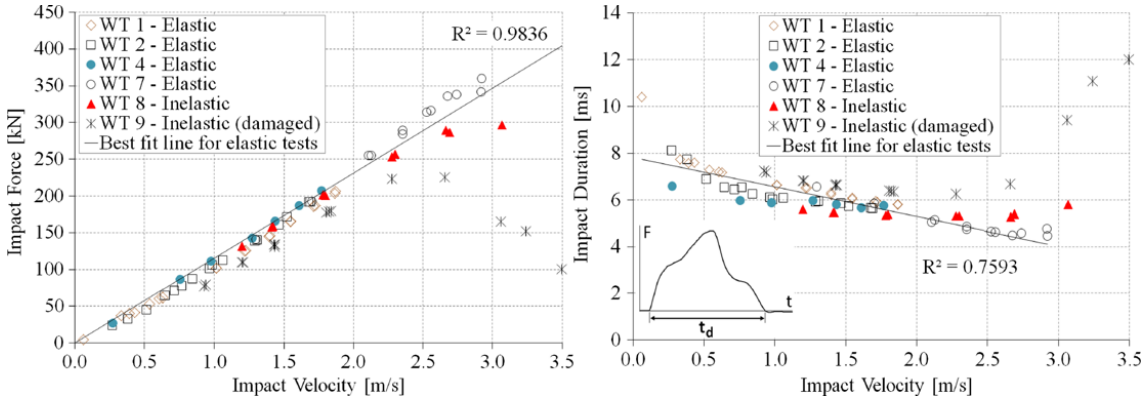


Figure 2.5: Wooden Utility Pole Impact Force and Duration (Aghl et al., 2014)

The effect of contact stiffness was also examined by the authors, where the conclusion was made that for wooden utility poles, as the contact stiffness was decreased (from rigid), the impact force also decreased but the impact duration increased. This is expected behaviour as when the contact stiffness decreases a portion of the impact energy is absorbed and dissipated by the impacted material. Whereas a fully rigid contact, in theory, would reflect the impact energy in its entirety back to the debris.

Steel Tube and Shipping Container Results Similar to the wooden utility pole impact tests, in the elastic range the steel tubes and shipping containers exhibited the behaviour that the peak impact force increased linearly with the impact velocity. However, unlike the wooden utility poles the impact duration for the steel tubes and shipping containers was found to stay constant for an increase in impact velocity. The authors go on to state that similar to the wooden utility poles as the impact area is reduced (everything else constant) the peak impact force decreases but the impact duration increases. The single corner impact of the shipping containers provided the highest duration and lowest peak force.

For the inelastic tests, the peak impact force and impact duration were shown to both increase with an increase in impact velocity. The impact force does not appear to taper away from the linear trend like the behaviour experienced by the wooden poles. This could be due to the wooden poles having a lower elastic and ultimate capacity when compared to the steel tubes and shipping containers. This would imply that the wooden poles would reach a more damaged state at lower impact velocities when compared to the steel tubes and shipping containers. Perhaps if even larger impact velocities were used the trend of the impact force tapering down and away from the linear trend would be experienced by the steel tubes and shipping containers. The peak impact force and impact duration by impact velocity can be seen below in Figure 2.6.

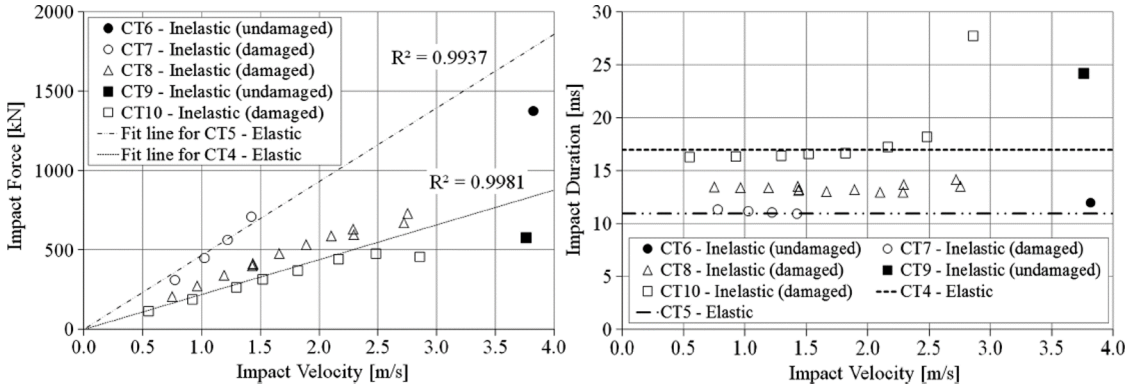


Figure 2.6: Steel Tubes and Shipping Containers Impact Force and Duration (Aghl et al., 2014)

Steel Tube and Shipping Container Results The authors state that in order to relate the dynamic impact event to a statically equivalent force, a dynamic response factor should be determined based on the impact time histories. The dynamic response factor is determined by taking the ratio of two quantities. The first quantity is described as the maximum response (displacement) of an undamped SDOF system subjected to the impact history. The second quantity is described as the equivalent static displacement from the system subjected to the peak impact force. The dynamic response factor ranges from zero to two. The dynamic response factor is then used as a scale-factor for the peak impact force specified by the solution of the 1D wave equation outlined in Riggs et al. (2013), the proposed force equation can be seen below:

$$F_{ni} = R_d v_{in} \sqrt{k_s m_d} \tag{2.24}$$

The authors go on to state that the proposed force equation is conservative for single corner shipping container impacts and utility poles, but not for multi-corner shipping container impacts.

2.1.1.5 Aghl et al. (2015)

In Aghl et al. (2015) inelastic response of debris was studied through the use of a numerical model and physical results obtained from Aghl et al. (2014). The objective of the study was to obtain a better estimate of debris impact forces on a rigid structure when the debris is stressed into the inelastic state. The results from the study show that as the response of debris changes from elastic to inelastic the duration of the impact increases along with the peak impact force. However, the peak impact force will only increase to a limit equal to the ultimate strength of the debris material after which the force will decrease as the material fails.

Equivalent One-Dimensional Inelastic Bar Model Observing the previous debris impact models, they all share very similar looking solutions as they all solve the one-dimensional wave equation to produce the simple one-dimensional bar model (Riggs et al. (2013), Aghl et al. (2014)). The authors in this study examine the extension of this one-dimensional bar model to cover the inelastic response of the bar. The authors then compare this model to a few experimental results and several non-linear numerical results.

The 1D inelastic bar model is defined as a piecewise function made up of two components. The first component is the component that describes the impact force up until the elastic limit is reached for the material. The second component is the component of the impact force due to the impact velocity exceeding the velocity that will cause yielding in the debris. The following schematic, Figure 2.7, outlines the relationship for how the piecewise function is formed. Theoretically, the piecewise function to describe the impact force can be made up of as many components as used to describe the post-yielding behaviour of the material. Meaning, if the material model is defined as bilinear then the impact force piecewise function consists of two components.

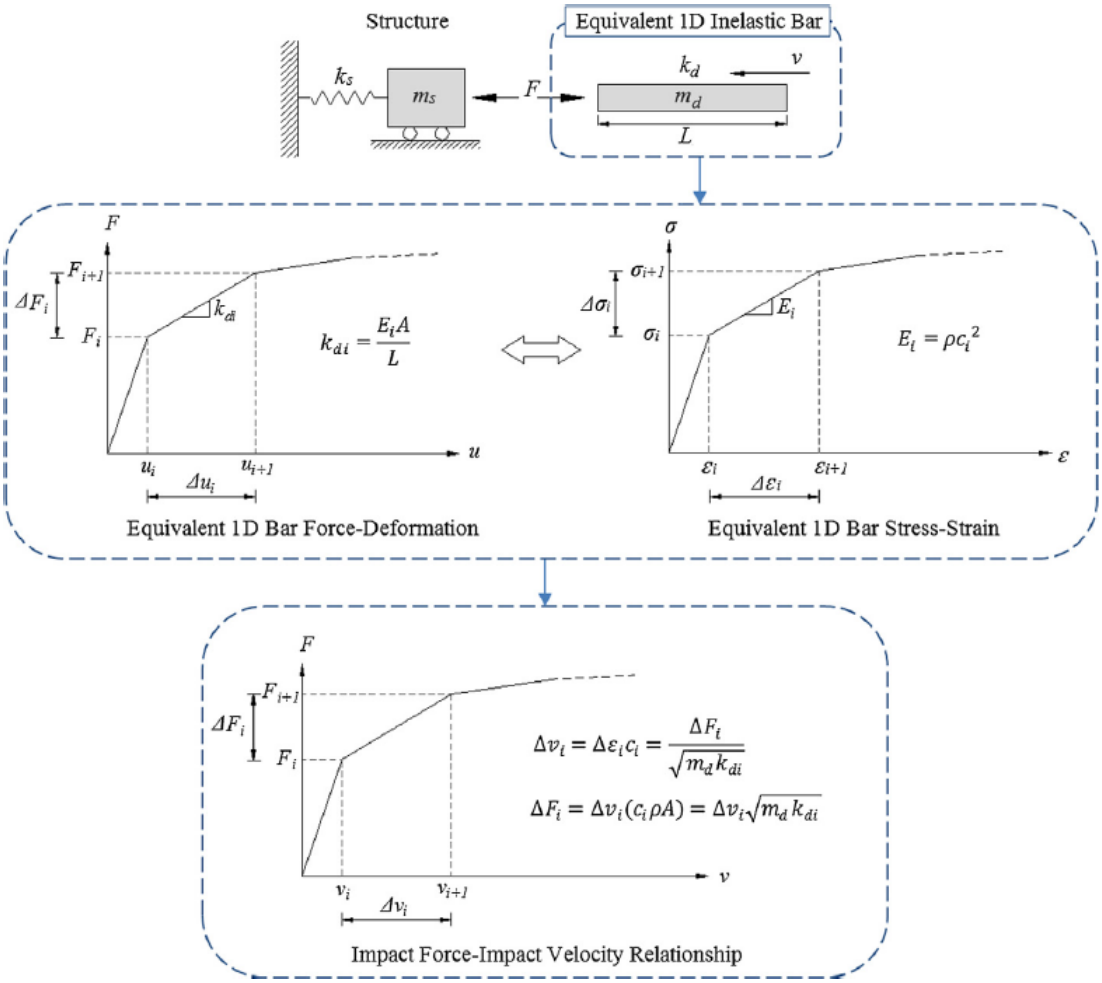


Figure 2.7: Inelastic Impact Force Definition (Aghl et al., 2015)

Based on this model definition the authors define the peak impact force using a bilinear force-deformation curve for the bar element. The piecewise formula is function of the velocity of the impact, the velocity that causes the debris to yield, the mass of the debris, the elastic equivalent stiffness, and the secondary equivalent stiffness. The elastic equivalent stiffness is a function of the modulus of elasticity of the material, the cross-sectional area of the debris, and the length of the bar. The secondary equivalent stiffness is a function of the secondary modulus, the cross-sectional area of the debris, and the length of the bar. The velocity that will cause yielding in the bar is a function of the yield strength of the material, the mass of the debris, and the elastic equivalent stiffness. The equations below outline these relationships:

$$k_{de} = \frac{EA}{L} \tag{2.25}$$

$$k_{dp} = \frac{E_p A}{L} \tag{2.26}$$

$$v_y = \frac{F_y}{\sqrt{m_d k_{de}}} \tag{2.27}$$

$$F_{ni} = \begin{cases} v\sqrt{m_d k_{de}} & v \leq v_y \\ v_y\sqrt{m_d k_{de}} + (v - v_y)\sqrt{m_d k_{dp}} & v > v_y \end{cases}$$

To calculate the duration of the impact the authors state that for simplicity the duration is assumed to be a rectangular pulse and is calculated based off of impulse-momentum theory. This implies that the impact duration is a function of the impact velocity, mass of the debris, and the impact force. In order to account for both elastic and inelastic impacts the impact duration is modified by a coefficient of restitution, which is typically defined as the ratio between the final and initial relative velocities between two bodies. The authors state that for an inelastic response the coefficient of restitution is equal to zero, whereas, for elastic impacts it is assumed to be one. The equation below outlines the impact duration formula:

$$t_d = \frac{(1 + C_e)vm_d}{F_{ni}} \tag{2.28}$$

The authors go on to show that the above formula can predict accurately the peak impact force in the elastic and inelastic range for a shipping container (four corner impact, three corner impact, two corner impact, and single corner impact) when compared to finite element models of simulated impacts and a few experimental data points. Additionally, the authors show that for inelastic impacts the average coefficient of restitution equated to 0.12. However, for simplicity the authors assumed a coefficient of restitution of zero for all test cases, which means that the impact duration was underestimated. The comparison between these developed formulas, experimental data, numerical models, and two code defined solutions are presented below in Figure 2.8 for both impact force and impact duration.

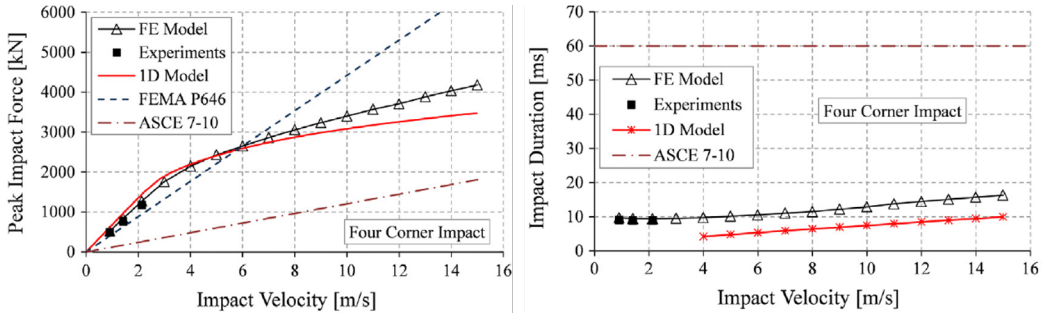


Figure 2.8: Impact Force and Duration Comparison (Aghl et al., 2015)

Similar to Aghl et al. (2014), a dynamic response factor is developed to provide a multiplier to the force equation in order to capture the dynamic response of the physical impact event. The dynamic response factor ranges from zero to two based on the ratio between the impact duration and the natural period of the response of an undamped linear SDOF system. The variation of the dynamic response factor against the ratio of t_d and T_n is presented below in Figure 2.9.

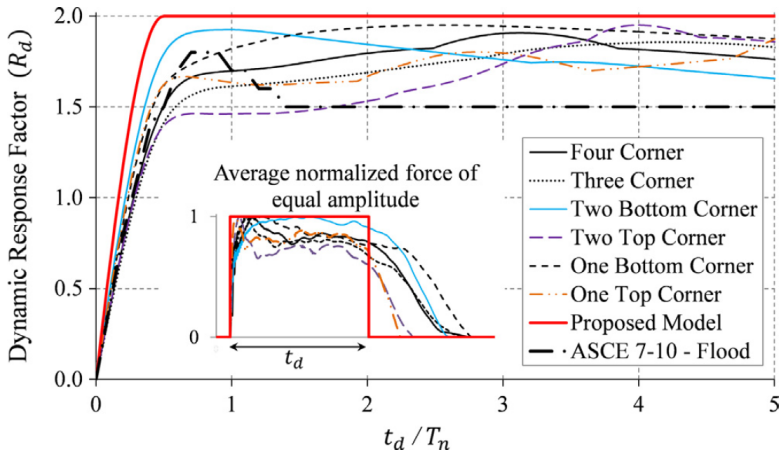


Figure 2.9: Dynamic Response Factor (Aghl et al., 2015)

2.1.1.6 Ko et al. (2015)

Ko et al. (2015) present a study on in-water impacts of an idealized 1 : 5 scale shipping container impacting a rigid column. The purpose of the study was to examine the hydrodynamic effects on impact loads and durations, the study compliments the in-air impact experiments completed by Aghl et al. (2014). Additionally, the authors examined the effect of non-structural mass in shipping containers on the impact force.

The authors outline various methods in design standards that describe how the impact force can be modified to take into account the hydrodynamic effects of the impact occurring in a fluid. Typically, the hydrodynamic effects are taken into account by an added mass

coefficient or a hydrodynamic mass coefficient. The former is used as a multiplication factor for the one-dimensional bar model, whereas, the latter is used as a multiplier for the terms under the square root of the one-dimensional bar model. The authors go on to state that the difference between in-air and in-water impacts is not significant and that the difference between the two peaks fall within the 90% confidence interval of the average impact force time history for in-air impacts.

In order to investigate the difference between the in-air and in-water impacts, both results were normalized by the one-dimensional bar model. From the normalized force plot against the Froude number, the maximum difference between the in-air and in-water peak impact force was 17%. However, the majority of the differences were not greater than 15%. This suggests that the hydrodynamic component of the impact force only makes up a small portion of the peak impact force, potentially up to 17%. For impact durations, the authors noted that the in-water impacts resulted, on average, a 20% increase in the impact duration when compared to the in-air experiments. The authors go on to state that due to only a modest increase in the peak impact force for in-water impacts, for design purposes, it appears to be acceptable to ignore the hydrodynamic effects.

The authors also examined the effect of non-structural mass in shipping containers on the peak impact force and duration. The conclusion that the authors provided is that if the non-structural mass is unsecured then the peak impact force is not significantly influenced by the added mass of the non-structural mass. As such, the non-structural mass should not be added to the mass term in the one-dimensional bar model if it is unsecured. However, if the non-structural mass is secured in the shipping container then the non-structural mass should be added to the mass of the debris in the one-dimensional bar model. The authors do note that the impulse was influenced by the unsecured non-structural mass in the shipping container. The unsecured mass would slide around in the shipping-container during the impact event which would lead to additional impact spikes increasing the overall impulse experienced by the column.

2.1.1.7 Ikeno et al. (2016)

In Ikeno et al. (2016), the authors present an improvement to the collision force formula typically used for woody debris and validate the formula by in-air and in-water physical modelling. The improvement that the authors want to implement into the collision force formula is a parameter that is used to capture the influence of oblique impacts. Additionally, both in-air and in-water experiments were completed to capture any effects associated with water cushioning the impact between the woody debris and the structural wall. The in-air impacts were tested at four different angles 90° (longitudinal collision), 70°, 30°, and 0° (transverse collision). For the in-water impact tests the initial angle used for the woody debris was 90° and 0° (longitudinal and transverse), after which the debris was allowed to freely move down the flume.

Some of the key conclusions that the authors came to is that the in-water experiments indicated that the force trend increased at a slower rate when compared to the in-air experiments as impact velocity was increased. The authors attribute this to water cushioning

the impact force as mentioned above. The authors also noted for the in-air impact tests, if the collision angle was less than 20° when compared to the longitudinal impact, then the impact force was not significantly reduced due to the oblique impact. For collision angles greater than 20°, the impact force was reduced down to less than half of the longitudinal impact force.

The modification to the impact force formula that the authors suggest is the inclusion of a term to capture how the magnitude of the impact force changes with oblique impacts. The theory behind reducing the magnitude of the impact force for oblique impacts is that as the collision angle veers away from a straight longitudinal impact, some of the direct impact energy is transformed into rotational energy, which directly reduces the maximum impact force. This transfer of energy from kinetic to rotational energy is captured by the term λ, which is a function of the collision angle, the inertial motion radius, and the distance between the center of gravity of the debris and the point of contact. The collision angle is defined as 90° minus the angle between the collision velocity vector and the center of gravity of the debris. The inertial motion radius is defined as a function of the moment of inertia and the mass of the debris. The following relationships are outlined below:

$$\theta_c = 90^\circ - \theta_c' \tag{2.29}$$

$$R = \sqrt{\frac{I}{m_d}} \tag{2.30}$$

$$\lambda(\theta_c) = \sqrt{\frac{1 + \left(\frac{L_T}{R}\right)^2 \sin^2\theta_c}{1 + \left(\frac{L_T}{R}\right)^2}} \tag{2.31}$$

The authors then go on to state that the reduction term can be applied to the collision impact formula suggested by Ikeno et al. (2013). In Ikeno et al. (2013), the collision impact formula takes the form of Hertz's equation developed from Hertzian contact mechanics, however, it is modified by using results from their experimental studies. The collision force formula is a function of a dimensionless coefficient equal to 0.243 (based off of large-scale experiments), the mass of the debris, the added mass of the fluid, the width or diameter of the debris, the effective Young's modulus, and the collision speed of the debris. The effective Young's modulus is defined as a function of the modulus' of elasticity and Poisson's ratios for both the debris and structure. The formulas described above are outlined below:

$$\tilde{E} = \frac{E_d E_s}{E_s(1-\nu_d^2) + E_d(1-\nu_s^2)} \tag{2.32}$$

$$F_{ni} = 0.243\left(C_{MA} m_d\right)^{0.6} V_{A0}^{1.2} D_w^{0.2} \tilde{E}^{0.4} \tag{2.33}$$

Based on this above formula the authors suggest that the collision force be modified by the reduction term for oblique impacts:

$$F_{ni} = 0.243\left(C_{MA} m_d\right)^{0.6} V_{A0}^{1.2} D_w^{0.2} \tilde{E}^{0.4} \lambda(\theta_c) \tag{2.34}$$

The authors conclude that while the modified collision formula still overestimates the experimental results of this study, the formula does capture the effect of a decrease in impact force magnitudes as the impact angle becomes more oblique with respect to a purely longitudinal impact.

2.1.1.8 Derschum et al. (2018)

Derschum et al. (2018) present the first part of a two-part study on dam-break wave generated debris impacts on a structure. The first study focuses on the influence of hydrodynamics on debris impact conditions and impact geometry.

Derschum et al. (2018) showed that the typical assumption that the debris impact velocity is equal to the flow velocity is not reflective of what was noted during their experimental studies. The debris impact velocity was shown to be on average 63% less than the flow velocity which can be attributed to several factors. One reason there can be a discrepancy is that the estimation of the flow velocity was completed upstream of the structure and due to bed resistance, the flow velocity would be expected to decrease the further down the flume the velocity reading was estimated. Another factor outlined by the authors that played a role in the debris impact velocity being less than the flow velocity was that the debris experienced grounding. Debris grounding would reduce the velocity of the debris as it experiences contact and friction with the bed of the flume; a larger water depth would reduce the amount of grounding a debris would experience. The authors do state that the debris was shown to not travel with the wave front but rather behind the wave front and hence, the velocity of the wave front would represent the maximum velocity the debris could be traveling at.

Another key point that the authors outlined is the influence that a stagnation zone at the base of the structure has on the impact force. A stagnation zone at the base of the structure is a flow feature generated by the rapid reduction of flow velocity after the wave front has impacted the structure. The area of approximately zero flow velocity represents a water cushioning effect as mentioned in Ikeno et al. (2016). The water cushioning acts to reduce the forward momentum of the debris which can decrease the overall velocity of the debris impact and hence the load. The authors noted that the effect of the stagnation zone was only realized when small impoundment depths were used for the dam-break wave. This is due to the flow velocity being less for smaller impoundment depths which allowed for the full formation of the stagnation zone by the time the debris had impacted the structure. For larger impoundment depths the debris was traveling at a higher velocity and hence the stagnation zone was not fully realized before the debris had impacted the structure. This would suggest that the water cushioning effect may only be relevant for small flow velocities or the quasi-steady flow stage of a tsunami event. The authors also outline the formation of streamlines that split at the face of the structure during the formation of the stagnation zone. These streamlines caused lateral flow velocity at the face of the structure which resulted in a reduction in the forward momentum of the debris and hence the impact force. The authors also noted that as the impoundment depth increased so did the lateral flow velocity at the face of the structure which resulted in more oblique debris impacts.

After the initial wave front impact on the structure a surface roller was formed that influenced the impact geometry of the debris. The authors showed that the debris followed the movement of the surface roller which resembled a circular motion rotating around the axis perpendicular to the flow. This motion caused the debris to rotate and impact the structure repeatedly, this behaviour is similar to the high frequency pounding outlined in Khowitar et al. (2015). If the structure is subjected to multiple impacts, be that in a short

period of time or throughout the entire inundation event, the hysteretic performance of the structure becomes important.

2.1.1.9 Stolle et al. (2018a)

In Stolle et al. (2018a), the authors present the second part of a two-part study on dam-break wave generated debris impacts on a structure. The second study focuses on single debris impacts on a non-rigid structure. The outcome of the study is a new formulation on how to estimate debris impact loads while considering the elasticity of the structure being impacted. The study of non-rigid impacts is important for understanding how the absorption of energy due to structural deformations effects debris impact forces.

The authors in this study present the results from a debris impact onto a structure that is not completely rigid, meaning the structure can deform due to the impact event. The authors stated that during their study the structure did displace and deflect due to the impact load. The occurrence of displacement and deflection indicates that potentially rigid body impact equations are not adequate in accurately estimating the impact force and hence, could overestimate the impact load. The authors compare their experimental results to other impact models such as the ones outlined in Haehnel and Daly (2004) and Ikeno et al. (2016). They go on to discuss different ways that the impact formula can be developed such as, the solution of the 1D wave equation producing the single-degree-of-freedom model outlined in various studies (Riggs et al. (2013), Aghl et al. (2014), Aghl et al. (2015)) and the equations developed using Hertzian contact mechanics (Ikeno et al. (2013), Ikeno et al. (2016)). The models developed using the 1D wave equation generally assume that the impacted structure is large enough such that the rigid impact assumption is valid. Hence, most of the equations developed using this solution do not directly include the influence of the structural properties on the impact force and will typically over-estimate the impact force from debris. The Hertzian contact models were shown to more accurately estimate the impact forces as the properties of the structure are included in their formulation to estimate how much a debris penetrates into a structure.

In this study, the conclusion that material properties of the debris and the structure are key in accurately estimating the impact forces is made. The authors proposed a new parameter to modify the formula of Haehnel and Daly (2004) to capture the effect of a non-rigid structure. The parameter is the dimensionless factor b_s, which is a function of the stiffness of the structure in the current study and the stiffness of the structure in Haehnel and Daly (2004). The impact force estimate is then defined as a function of the dimensionless factor (b_s), the velocity of the impact, the mass of the debris, and the effective contact stiffness. The effective contact stiffness is a function of the debris stiffness and the structure stiffness. The following equations outline these relationships:

$$k_e^{-1} = \frac{1}{k_s} + \frac{1}{k_d} \tag{2.35}$$

$$b_s = \frac{k_s}{k_{HD}} \tag{2.36}$$

$$F_{ni} = u_{max}\sqrt{b_s k_e m_d} \tag{2.37}$$

The authors show that this new formula can better estimate the experimental data gathered from this study when compared to other impact force formulations as shown in Figure 2.10. The figure outlines how the impact force varies with velocity for several types of debris impact formulations and for the measured data from the experiment study. The dotted line, Eq. (14), in the plot below is the impact force estimated with the new proposed method outlined by the authors in this study. As can be seen, this formulation better estimates the impact force when the structure is considered to be non-rigid or flexible.

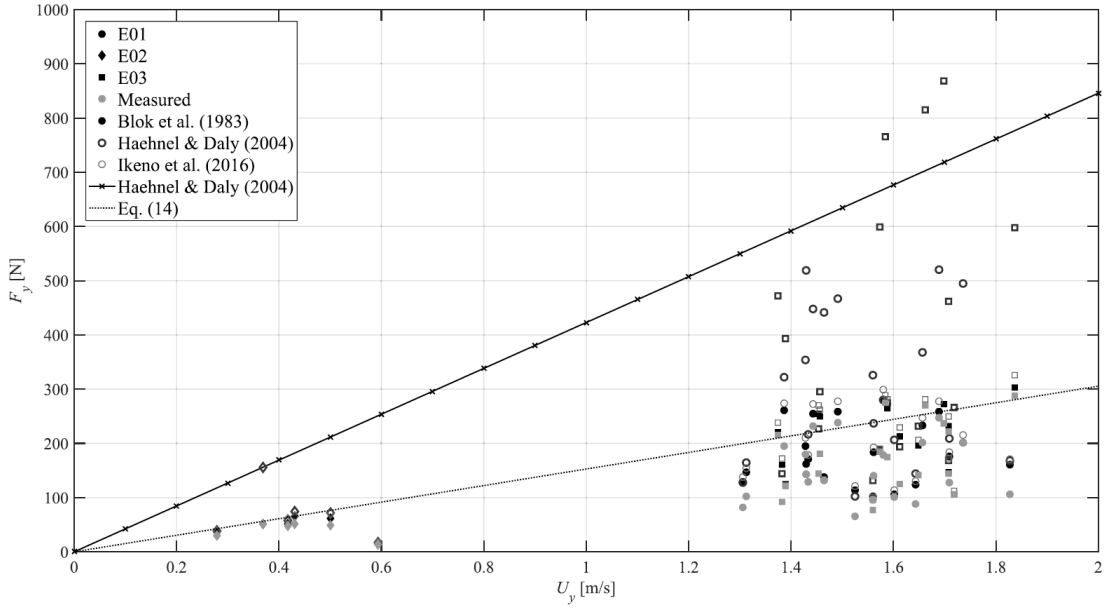


Figure 2.10: Impact Force versus Velocity (Stolle et al., 2018a)

2.1.1.10 Code Provisions

The following sections will outline the methods proposed by three code provisions for calculating debris impact loads.

ASCE 7 (2016) The approach taken by the ASCE 7 (2016) Chapter 6 is based off of the contact-stiffness method outlined in Haehnel and Daly (2004). The nominal impact force is a function of the velocity of the debris, mass of the debris and the lesser of the effective stiffness of the impacting debris or lateral stiffness of the structural element, the equation below outlines this formula:

$$F_{ni} = u_{max}\sqrt{k m_d} \tag{2.38}$$

The duration of the impact for logs and poles is defined as a function of the mass of the debris, velocity of the debris, and the nominal impact force. For empty shipping

containers the impact duration is assumed to be the same as for logs and poles. If the shipping container is not empty, then the mass of the debris is modified by adding the mass of the contents in the container. The following equations outline these relationships:

$$t_{dLogs} = \frac{2m_d u_{max}}{F_{ni}} \tag{2.39}$$

$$t_{dShipping} = \frac{(m_d + m_{contents})u_{max}}{F_{ni}} \tag{2.40}$$

For other types of debris, the standard states that for impacts by vehicles the impact force should be taken as $130kN$ multiplied by the importance factor of the structure. For submerged boulders or concrete debris an impact force of $36kN$ multiplied by the importance factor of the structure is suggested. For extraordinary impacts the standard suggests that the equation following the approach of Haehnel and Daly (2004) should be used, however, the stiffness should be set equal to the structural element stiffness suggesting that the debris is large enough to remain completely rigid during the impact.

Alternatively, instead of calculating the load based on the type of debris, the standard states that the following approximation of the impact force can be made:

$$F_{ni} = 1470 C_0 I_{tsu} \ [kN] \tag{2.41}$$

The variable C_0 represents the orientation coefficient and the standard recommends a value of 0.65. I_{tsu} is the importance factor of the structure and ranges from 1.00 to 1.25. The standard states that this force should be applied to critical flexure and shear sections for structural elements within the inundation depth.

AASHTO (2012) The approach taken by AASHTO (2012) follows a similar method to the impulse-momentum approach outlined in Haehnel and Daly (2004). This method estimates the impact force as a function of the mass of the debris, the maximum flow velocity, and the impact duration. The following equation outlines this relationship:

$$F_{ni} = \frac{m_d u_{max}}{t_d} \tag{2.42}$$

FEMA P646 (2012) The approach taken in FEMA P646 (2012) follows the same approach outlined in Haehnel and Daly (2004) for the contact-stiffness method. The impact force is a function of the added mass coefficient, which is the added mass of the water due to the impact occurring in water, the maximum flow velocity, the mass of the debris, and the effective stiffness of the debris; the standard recommends using an added mass coefficient of 2. The following relationship is outlined below:

$$F_{ni} = C_f u_{max} \sqrt{m_d k_e} \tag{2.43}$$

2.1.1.11 Discussion of Key Points and Limitations to the Single Degree of Freedom Models

This section will outline some key points from the literature presented about SDOF models and also identify some of the limitations to the SDOF models.

Key Points Key points from the presented literature on SDOF models are listed below:

1. Inherent damping associated with the debris or structural response is neglected.
2. The SDOF model can be derived from solving the one-dimensional wave equation or by using Hertzian contact mechanics. The models derived from Hertzian contact mechanics were shown to better represent experimental results (Stolle et al., 2018a).
3. Due to the uncertainty in estimating debris stopping distance and impact duration, the contact-stiffness approach for estimating debris impact loads is typically used (Haehnel and Daly (2002), Haehnel and Daly (2004), Riggs et al. (2013), Aghl et al. (2014), Aghl et al. (2015), Stolle et al. (2018a), ASCE 7 (2016)), FEMA P646 (2012)).
4. There are conflicting studies on whether the added mass of the displaced fluid needs to be accounted for in the debris impact load formulation (Riggs et al. (2013) vs Ikeno et al. (2016)). Stolle et al. (2018a) suggest that as the draft of the debris increases so does the effect of the added mass of the fluid.
5. The maximum impact force occurs for a perfectly longitudinal impact (impact angle = 90°). However, as the impact angle skewed away from >20° the impact force increased until the impact was transverse (impact angle = 0°). This would suggest that the peak impact force occurs for a perfectly longitudinal impact, however, if the impact is not perfectly longitudinal then the transverse impact would govern (Derschum et al., 2018).
6. For inelastic impacts, the impact duration increases along with the impact force up until the impact causes the debris to reach its ultimate capacity. At which point the impact force decreases due to material failure, but the impact duration continues to increase (Aghl et al., 2015).
7. Debris was shown to not travel with the wave front and hence, the maximum velocity a debris could be traveling at is the wave front velocity (Derschum et al., 2018).
8. A formation of a stagnation zone and lateral streamlines at the face of a structure both caused the impact force to decrease (Derschum et al., 2018).
9. Formation of a surface roller can lead to multiple impacts over a short period of time (Derschum et al., 2018). This phenomenon could be important for hysteretic performance of a structure in the inundation zone.
10. Structural deformation plays an important role in reducing peak impact loads as energy is dissipated through deformations (Stolle et al., 2018a).

Limitations Some limitations of the methods mentioned above is that they all focus or are derived from debris impacting a rigid structure. This implies that the structure will not experience any deformations due to impact loads. This may be a reasonable assumption if the debris stiffness is small and the structural stiffness is high. Stolle et al. (2019) suggested that if the structural stiffness is 100 times larger than the debris stiffness then the rigid body assumption holds true. However, the assumption of a rigid structure is a conservative assumption as any damping behavior associated with the structural response is neglected. This damping due to structural response from the impact would work to reduce the maximum impact force by absorbing energy through deformation defined by the ductility of the structure. By taking into consideration the ductility of the structure lower impact forces can be designed for, which is the same approach taken for earthquake engineering. However, the structure must be designed to have the ductility capacity to allow for deformation.

Another limitation to the above methods is that all of these methods consider debris impact loads as singular events when in practice multiple debris impacts can occur at the same time and over the time span of the inundation event. Hence, it would be important to look at the consequences of multiple debris impacts over time on the hysteretic performance of the structure. Another key limitation to these studies is that there is no clear conclusion on if the added mass of the fluid needs to be considered into the force equation. Further studies of debris with larger drafts would have to be completed in order to quantify the added mass effect on the impact force (Stolle et al., 2018a).

2.1.1.12 Comparison Between Various Approaches for SDOF Models

In this section a plot of impact force versus velocity will show how the approaches to calculating these impact forces mentioned above vary. Additionally, any assumptions made in order to calculate the impact forces will be clearly outlined and their significance on the impact force will be inferred.

Figure 2.11 outlines the comparison between the models. Observing the figure, the formulas outlined in Clause 6.11.2 of ASCE 7 (2016) it can be seen that the results provide a very similar solution to those outlined in Haehnel and Daly (2004). Observing the figure, for the formulas outlined in Haehnel and Daly (2004) it can be seen that if the stopping distance and duration of impact are calculated by following the formulas outlined by the authors, then all three-methods for estimating the impact force are equivalent. The formula used for Riggs et al. (2013) only considers the debris stiffness, hence from the plot, it can be seen that the impact force is slightly higher than those outlined by the formulas in Haehnel and Daly (2004). This is expected behaviour as in Haehnel and Daly (2004) the effective stiffness is used to calculate the impact force, which means that a fully rigid structure is not assumed unlike in Riggs et al. (2013). This suggests that Riggs et al. (2013) provides an upper bound for the impact force as a fully rigid structure is assumed. Observing the plot, following the formulas outlined in Matsutomi (2009) and Ikeno et al. (2016), it can be seen that the impact force does not increase linearly with the velocity, as for both formulations the velocity is to the exponent of 1.2. The formula outlined in Ikeno et al. (2016) appears to be approaching the line outlined in Riggs et al. (2013) however,

the formula by Ikeno et al. (2016) does not cross the line until an impact velocity of $90\frac{m}{s}$ is reached. This further enforces that assuming a fully rigid structure produces the highest-impact force as expected. Observing the force velocity relationship for the formula outlined in Aghl et al. (2015), it can be seen that the velocity that causes the debris to yield is approximately $7\frac{m}{s}$. After $7\frac{m}{s}$ the slope of the force velocity line decreases significantly, this is expected as a bi-linear relationship for the debris material properties was assumed. This would suggest that if a more complex stress-strain relationship was defined the impact force velocity relationship would follow the same trends as the stress-strain relationship. In Stolle et al. (2018a) a parameter is defined to capture the ductility of the structure which would correlate to a reduction in the impact force when compared to those outlined for a fully rigid structure, this behaviour is noted in the plot. This phenomenon is due to the ductility of the structure absorbing some impact energy and also highlights the importance of capturing the influence that structural ductility has on the impact force.

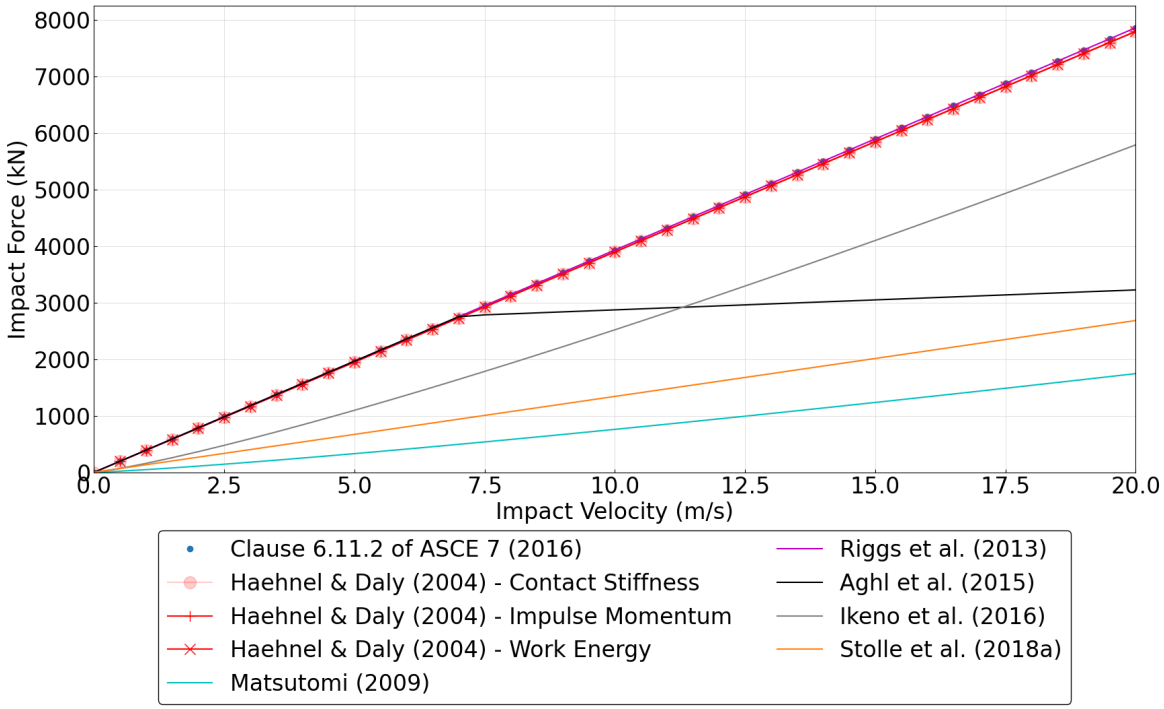


Figure 2.11: Comparison between SDOF Models

The following is a list of assumptions made in order to plot the SDOF models and other notes about the models:

- Debris properties:
  - Northern white cedar pole
  - Impact angle = 90°(longitudinal)
  - Modulus of elasticity, $E_d = 5.52 \times 10^9 \frac{N}{m^2}$ (Wood Handbook, 1999)

- Poisson's ratio, $\nu_d = 0.34$ (Wood Handbook, 1999)
- Unit weight, $\gamma_d = 350\frac{kg}{m^3}$ (Wood Handbook, 1999)
- Diameter, $D_d = 0.6m$
- Length, $L_d = 20m$
- Stiffness, $k_d = 7.80 \times 10^7 \frac{N}{m}$
- Mass, $m_d = 1980kg$
- Compressive yield stress, $\sigma_f = 9.79 \times 10^6 \frac{N}{m^2}$ (Wood Handbook, 1999)
- Shear modulus, $G_d = 1.14 \times 10^9 \frac{N}{m^2}$ (Wood Handbook, 1999)
- Modulus of rupture, $E_p = 4.45 \times 10^7 \frac{N}{m^2}$ (Wood Handbook, 1999)
- Shear coefficient, $\kappa_d = 0.9$

- Structure properties:
  - Column size, $800mm \times 800mm$
  - Length, $L_s = 3.65m$
  - Concrete strength, $f\prime_c = 35\frac{N}{mm^2}$
  - Modulus of elasticity, $E_s = 2.66 \times 10^{10} \frac{N}{m^2}$
  - Poisson's ratio, $\nu_s = 0.15$
  - Shear modulus, $G_s = 1.16 \times 10^{10} \frac{N}{m^2}$
  - Stiffness, $k_s = 4.67 \times 10^9 \frac{N}{m}$
  - Shear coefficient, $\kappa_s = 0.833$

- General notes:
  - Ikeno et al. (2016) use an added mass factor but do not suggest a value hence a value of 1.0 was assumed
  - Stolle et al. (2018a) state that a scale of 1 : 40 was used in their experiments and that the scale factor for the stiffness should be 40^2

2.1.2 Two Degree of Freedom Model

A two degree of freedom model (2DOF) model is a model where the impacted structure and debris are considered as two separate bodies. Figure 2.12 graphically outlines the properties of the 2DOF model and the following remarks can be made about the model:

1. The mass of the structure and debris are both accounted for.
2. The stiffness of the structure and debris are both accounted for.
3. Displacement of the structure and debris are accounted for.

4. Any inherent damping associated with the structure and debris is not accounted for and any viscous damping associated with the impact occurring in a fluid is also not accounted for. Damping is typically not accounted for as the impact occurs over a short duration of time (Haehnel and Daly, 2004).

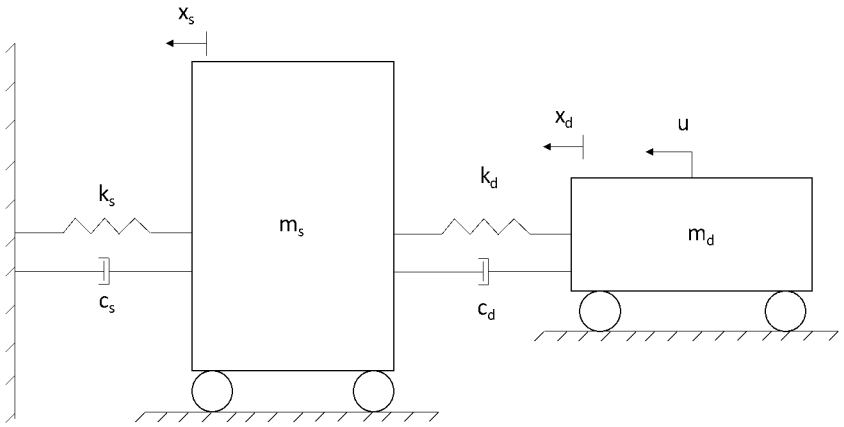


Figure 2.12: Two-Degree-of-Freedom Model

2.1.2.1 Stolle et al. (2019)

In Stolle et al. (2019), the authors present a study on debris impact forces on a flexible structure. The study presents a 2DOF model to represent the debris-structure impact which was validated by experimental results. The experimental program consisted of dam-break wave generated debris impacts, where the debris was 1 : 40 scaled shipping containers, which were allowed to freely move down the flume.

The 2DOF model simulated the debris and structure impact by a two-mass spring and damper system as shown in Figure 2.12. This model implies that both the structure and debris displacements, along with their associated stiffness can be accounted for. The authors state that due to the impact duration being very small, damping can be neglected for both the structure and debris components. Another key point that the authors outline is that the structure should only be modelled as fully rigid when the stiffness of the structure is 100 times larger than the stiffness of the debris.

The authors used d'Alembert's principle to solve the system of equations defining the 2DOF model. This leads to a final solution for the maximum impact force as a function of the effective stiffness of the system and the displacements of the structure (x_s) and debris (x_d):

$$F_{ni} = max\left(k_e\left((\frac{k_s}{k_d}+1)x_s - x_d\right)\right) \tag{2.44}$$

The displacement of the structure and debris are functions of the first and second natural frequencies of the system, the velocity of the debris, the time since impact, and

four constants ($A,\ B,\ C,\ D$) which represent values associated with the mass (a) and stiffness (b) ratios:

$$a = \frac{m_s}{m_d} \tag{2.45}$$

$$b = \frac{k_s}{k_d} \tag{2.46}$$

$$A = \frac{(a+b+1) + \sqrt{(a+b+1)^2 - 4ab}}{2a} \tag{2.47}$$

$$B = \frac{(a+b+1) - \sqrt{(a+b+1)^2 - 4ab}}{2a} \tag{2.48}$$

$$\omega_1 = \sqrt{A\frac{k_e}{m}} \tag{2.49}$$

$$\omega_2 = \sqrt{B\frac{k_e}{m}} \tag{2.50}$$

$$C = \frac{1-B}{A-1}\frac{1}{(\frac{1-B}{A-1}+1)\omega_1} \tag{2.51}$$

$$D = \frac{1}{(\frac{1-B}{A-1}+1)\omega_2} \tag{2.52}$$

$$\begin{bmatrix} x_s \\ x_d \end{bmatrix} = u\left(C\begin{bmatrix} 1-A \\ 1 \end{bmatrix}\sin\omega_1 t_d + D\begin{bmatrix} 1-B \\ 1 \end{bmatrix}\sin\omega_2 t_d\right) \tag{2.53}$$

The authors go on to show that this method for estimating peak debris impact forces proved to be more accurate when compared to the experimental data and other methods such as those provided by Haehnel and Daly (2004) and Ikeno et al. (2016). Figure 2.13 demonstrates that the 2DOF model accurately estimated the peak impact forces from the measured data as it closely resembles the line of best fit to the dataset. The authors note that theoretically the 2DOF model would be expected to overestimate the peak impact force as no corrections for eccentric or oblique impacts have been considered. However, clearly this is not seen in Figure 2.13, where the model underestimates some of the measured data points. The authors state that this is likely due to the challenging nature of estimating the impact stiffness which is a function of the impact velocity, impact geometry, and material properties.

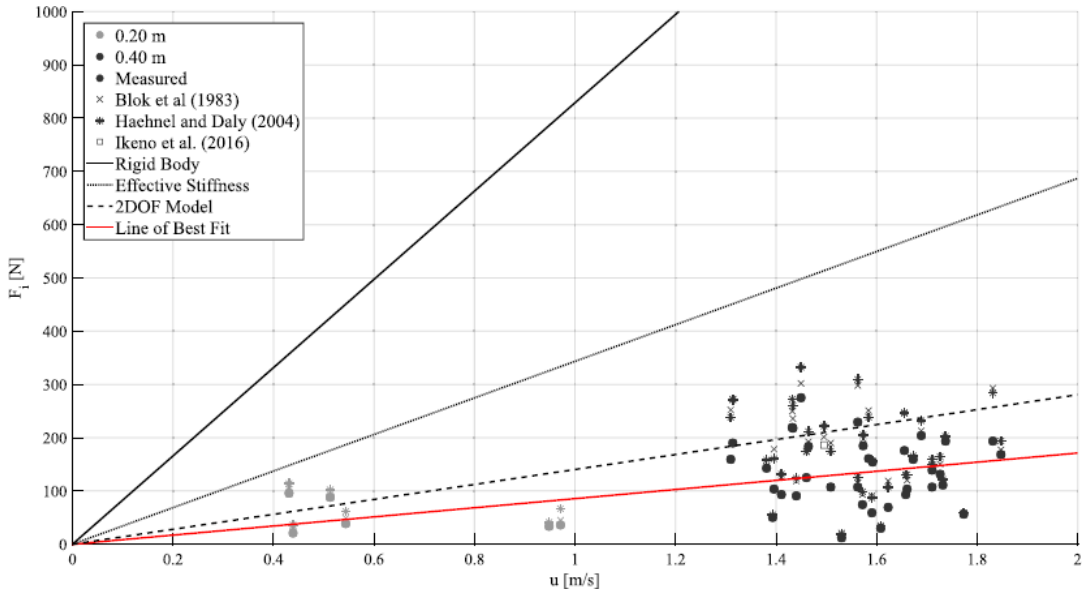


Figure 2.13: Impact Force versus Velocity for Various Methods (Stolle et al., 2019)

Additionally, the authors present a method for estimating the impact load history by means of Duhamel's integral. Duhamel's integral was used to estimate the structural response by integrating the differential responses from an estimated loading history and an assumed shape function of the impact time history. ASCE 7 (2016) states that a step function is assumed for the impact time history, however, Aghl et al. (2014) performed full-scale in-air shipping container impact tests where it was found that the time history was more representative of a half-sine shape. Stolle et al. (2019) assumed a half-sine shape function for the Duhamel integral which did represent well the measured force response in the experimental testing as shown in Figure 2.14. The filtered data tag represents the removal of instrument noise and hydrodynamic loads from the raw data as stated by the authors.

The Duhamel integral is a function of the damped frequency of the structure, the mass of the structure, the impact stiffness of the system, the elapsed time since impact, the impact forcing function, and the damping ratio:

$$R(t) = \frac{k}{m_s \omega_d} \int_0^t p(\tau) \sin \omega_d (t-\tau) e^{-\xi \omega_d (t-\tau)} dt \tag{2.54}$$

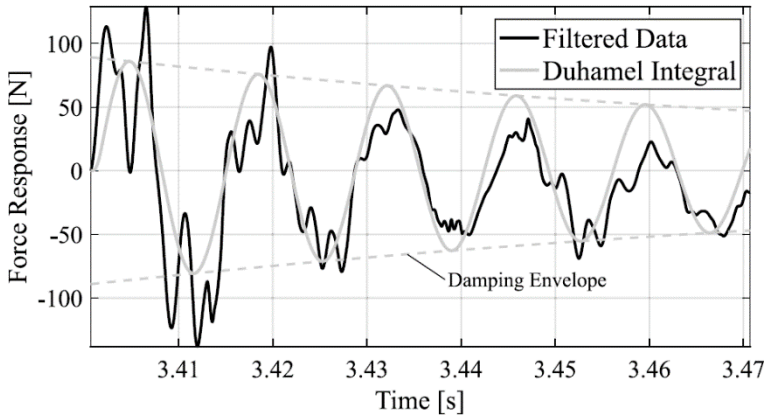


Figure 2.14: Duhamel Integral Estimate (Stolle et al., 2019)

The authors do note that the estimation of the damping coefficient for Duhamel's integral is challenging to determine. The authors state that this is because the damping coefficient can vary based on the water depth around the structure and due to the highly unsteady nature of a dam-break wave it is not feasible to get an accurate estimate of the varying damping coefficient with water depth.

2.1.2.2 Discussion of Key Points and Limitations to the Two Degree of Freedom Model

This section will outline some key points from the literature presented about the 2DOF and also identify some of the limitations to the 2DOF model.

Key Points Key points from the presented literature on the 2DOF model are listed below:

1. Inherent damping associated with debris or structure is neglected.
2. The 2DOF model allows for the assumption of both a rigid and non-rigid structure. Meaning the deformation of the structure can be included into the estimation of the maximum debris impact force. This becomes important with larger debris as to design for structures to remain elastic during the impact event is uneconomical.
3. The 2DOF models proved to be more accurate when compared to experimental data and other proposed methods such as those in Haehnel and Daly (2004) and Ikeno et al. (2016).
4. Duhamel's integral was able to capture the force-time history of the impact event. However, the damping coefficient can be difficult to estimate due to the unsteady nature of a dam-break wave.

Limitations One of the limitations of the two degree of freedom model is that both the masses of the debris and structure were assumed to be point masses. This assumption may be a valid assumption if the contact area is small when compared to the dimensions of the structure. However, as debris is random in its nature, the size of debris will also vary and hence, the assumption of point masses may not be valid for all debris types (Stolle et al., 2019). Additionally, a linear elastic stiffness was assumed for both of the springs which may not be valid for high impact loads where plastic effects / permanent damage may be experienced for both the debris and structure. Another assumption with this model is that the impact does not occur within a fluid. This assumption neglects damping effects due to the fluid reaction forces between the debris and structure along with neglecting any added mass effects due to the displaced fluid. Hence, it would be important to further investigate the effects of assuming point masses for larger debris, the added mass due to the fluid, damping effects, and nonlinearity in spring stiffness.

2.1.3 Beam / Column Response to Impacts

2.1.3.1 Khowitar et al. (2014)

Khowitar et al. (2014) present an analytical solution for a linear impact response of a pole impacting a column or a beam as presented below in Figure 2.15.

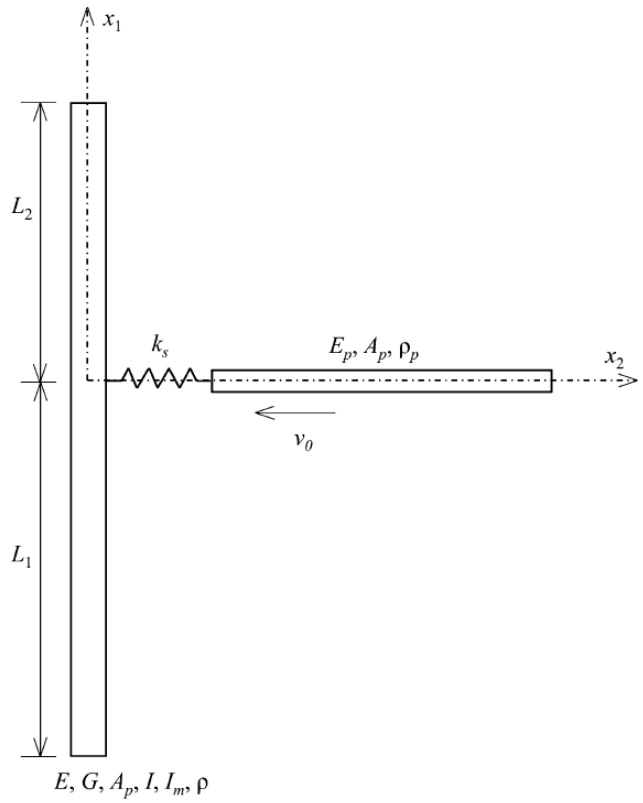


Figure 2.15: Column / Beam and Pole Interaction (Khowitar et al., 2014)

The solution is based off of Timoshenko's beam theory as when the column properties become significant the initial response is dominated by shear behavior and Euler-Bernoulli beam theory no longer applies. The initial peak impact force (F_0) is predicted by a formula which is a function of the two parameters, F_{cR} and F_{pR}. F_{cR} is a function of the modulus of elasticity of the pole, the cross-sectional area of the pole, the initial translational velocity (v_0), and the wave speed in the pole (c_{0p}). The wave speed in the pole is a function of the modulus of elasticity of the pole, and the density of the pole. F_{pR} is a function of the shear coefficient of the column, the shear modulus of the column, the cross-sectional area of the column, the initial translational velocity, and the shear wave speed in the column (c_s). The shear wave speed in the column is a function of the shear coefficient of the column, the shear modulus of the column, and the density of the column. The following formulas are outlined below:

$$c_s = \sqrt{\frac{\kappa G}{\rho}} \tag{2.55}$$

$$c_{0p} = \sqrt{\frac{E_p}{\rho_p}} \tag{2.56}$$

$$F_{pR} = \frac{E_p A_p}{c_{0p}} v_0 \tag{2.57}$$

$$F_{cR} = \frac{2\kappa G A}{c_s} v_0 \tag{2.58}$$

$$F_0 = \frac{F_{cR} F_{pR}}{F_{cR} + F_{pR}} \tag{2.59}$$

This peak impact force assumes that the contact stiffness has approached infinity. Khowitar et al. (2014) state that in no case is the total mass of the projectile significant to the initial peak force. The authors further go on to state that the impact duration is governed by either the longitudinal wave speed in the pole (for stiff columns) or the shear wave speed in the column (for stiff poles). They also conclude that rotary inertia does not play a role in the initial peak impact force but can have an effect on the impact force time history after shear waves in the beam return back to the impact point.

2.1.3.2 Khowitar et al. (2015)

Khowitar et al. (2015) present an analytical solution for the transverse impact of a uniformly translating beam hitting a fixed-fixed column as presented in Figure 2.16.

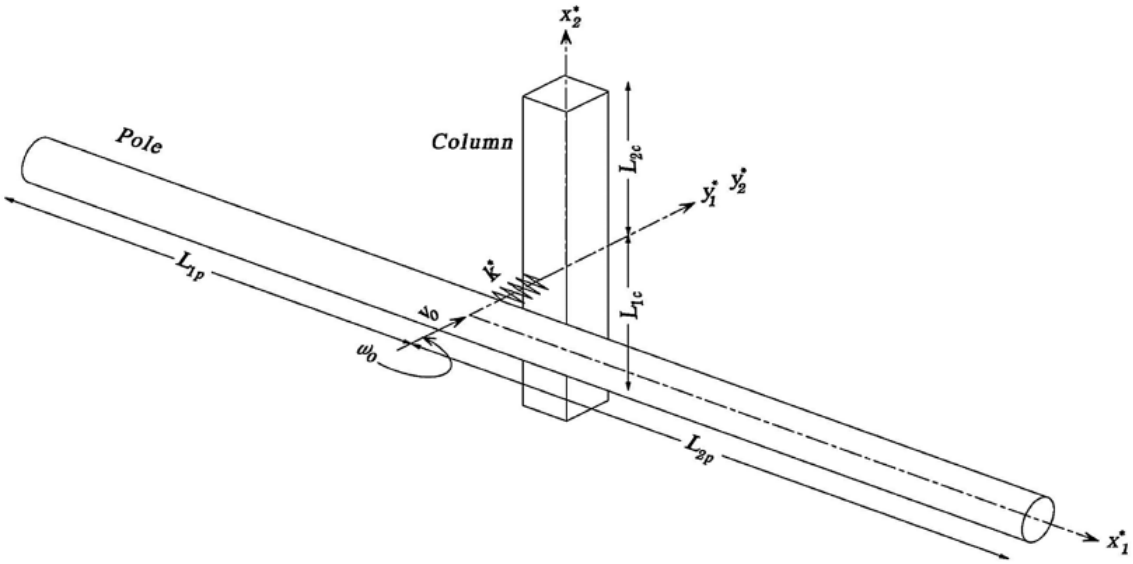


Figure 2.16: Column Pole Interaction (Khowitar et al., 2015)

As with the previous analytical solution, the impact force is dominated by shear deformations and hence, Timoshenko's beam theory was used. The initial peak impact force was predicted by a formula which is a function of the density of the column and the pole, the cross-sectional area of the column and the pole, the initial translational velocity of the pole, and the shear wave speeds in the column (c_{sc}) and the pole (c_{sp}). The shear wave speeds are a function of the shear coefficient for the column and the pole, the shear modulus of the column and the pole, and the density of column and the pole. These formulas are outlined below:

$$c_{sp} = \sqrt{\frac{\kappa_p G_p}{\rho_p}} \tag{2.60}$$

$$c_{sc} = \sqrt{\frac{\kappa_c G_c}{\rho_c}} \tag{2.61}$$

$$F_{pR} = 2\rho_p c_{sp} v_o A_p \tag{2.62}$$

$$F_{cR} = 2\rho_c c_{sc} v_o A_c \tag{2.63}$$

$$F_0 = \frac{F_{cR} F_{pR}}{F_{cR} + F_{pR}} \tag{2.64}$$

Khowitar et al. (2015) state that while the initial peak force is well predicted by this equation, the maximum impact force can reach 1.5 times larger than the initial peak force. Additionally, for most impact cases the pole experienced a high-frequency pounding after a fairly larger separation phase from the initial impact, which could be the reasoning behind the maximum impact force not corresponding to the initial peak force. This conclusion

is inferred as the authors show that the maximum impact occurs after an initial larger separation phase. The authors also go on to state that the governing parameter for the initial peak force is the mass ratio of the column to the pole. They also state that midspan impacts produced the highest impact force and duration when compared to off-centre impacts.

Another point that the authors make is that the total impulse for both the concrete and steel columns are almost 1.6 times the initial momentum of the pole and for wood columns this value is almost 1.8. This phenomenon can be associated with the high-frequency pounding experienced by the pole after the initial impact phase, this high-frequency pounding would increase the total impulse experienced by the column. The authors go onto to suggest that since the total impulse experienced by the columns is larger than the initial momentum of the pole, the rebound velocity of the pole is about 40% less than the initial impact velocity for the concrete and steel columns and about 20% less for wood columns. This would suggest that a denser column absorbs more of the impact energy when compared to a less dense column, which can be important for material selection of structures in the inundation zone.

2.1.3.3 Discussion of Key Points and Limitations to the Impact Response Analyses Studies

This section will outline some key points from the literature presented about impact response models and also identify some of the limitations to the models.

Key Points Key points from the presented literature on the impact response analyses studies are listed below:

1. Timoshenko's beam theory governs the impact response.
2. The pole and column were assumed to stay in the elastic range. This assumption may only be valid for poles (debris) that are of similar size, stiffness, and mass to the column (structure). For larger poles this assumption of an elastic impact may not longer be valid.
3. These studies presented are motivated by in-water impacts but are derived for in-air impacts.
4. For a longitudinal impact of a pole on a column, the impact duration is either governed by the longitudinal wave speed in the pole or the shear wave speed in the column. This suggests that both the properties of the column and pole have to be accurately determined in order to have a proper understanding of the impact duration and hence, the associated impulse of the impact event.
5. For a transverse impact of a pole on a column:
    - A high-frequency pounding occurred after the initial separation phase between the pole and the column.

- The initial peak impact force may not provide the maximum impact force which was shown to be as large as 1.5 times the initial peak impact force. Khowitar et al. (2015) state that the maximum impact force occurred after the initial separation phase which would imply that it is induced by the high-frequency pounding.
- A dense column would absorb more impact energy then a less dense column.

Limitations One of the assumptions that the authors use in this study is that the contact between the two bodies is frictionless. This assumption would have an effect on the impact duration between the two bodies as friction would cause the bodies to interact and stick together for longer. This interaction would increase the impact duration of the event and hence, the associated total impulse of the event would also increase; which is important for understanding ductility requirements for structural members. Another limitation to the studies is that the impacts were considered to be in-air but were motivated by water-driven debris impacts. Hence, any effects associated with added mass of the water or damping due to the water were not evaluated.

2.1.4 Energy Method

Commentary C6.11.8 of the ASCE 7 (2016) allows the designer to use the provided work energy method in the commentary or a nonlinear time history analysis to solve the structural response from a debris impact. The work-energy method provided in the commentary is suitable for impact by large, essentially rigid debris and considers the ductility of the impacted structure. The formula provided in the commentary calculates the force capacity of the structure and is based off of the coefficient of restitution, two mass terms (M_e, M_m), the mass of the debris, the initial elastic stiffness of the structure at the impact point, the maximum flow velocity, and the permissible ductility ratio (μ, as per Appendix C, Section C.3.7 of ACI 349-13 (2013)).

$$F_{cap} = u_{max} \frac{1 + C_e}{(1 + \frac{M_m}{m_d})\sqrt{2\mu - 1}} \sqrt{k_e M_e} \tag{2.65}$$

The mass term M_e is defined as the effective mass of the structure at the impact point which equates to the sum of the masses multiplied by the squared static displacements of the structure at each node i. Similarly, the mass term M_m is defined as the sum of the masses multiplied by the static displacement of the structure at each node i. The displacement values are scaled to have a value of one at the impact point. The following formulas outline these relationships:

$$M_e = \sum m_i \Delta_i^2 \tag{2.66}$$

$$M_m = \sum m_i \Delta_i \tag{2.67}$$

The standard notes that this method for estimating the force capacity of the structure is based off of a study on impacts generated from wind missiles completed by Kuilanoff and Drake (1991).

2.1.4.1 Discussion of Key Points and Limitations to the Energy Method

This section will outline some key points about the energy method presented and also identify some of the limitations to the energy method in commentary C6.11.8 of the ASCE 7 (2016).

Key Points Key points from the presented energy method in C6.11.8 of the ASCE 7 (2016):

1. The method takes into account the ductility of the structure.
2. The commentary allows the designer to do a full non-linear dynamic time-history analysis of the impact event.
3. The method is derived from impacts generated by wind missiles.

Limitations A limitation to the energy method is that the equation is based on an elastic-perfectly plastic force displacement relationship, meaning any post-yield strength gain in the structure is ignored. The commentary does mention in lieu of a full nonlinear time history analysis the secant stiffness can be used to linearize the model response based on a performance point in the inelastic range.

Additionally, the mass terms and stiffness terms are based on the impact point and the static displacement of the structure at the impact point, which can be quite hard to determine due to the random nature of debris impacts. This implies that the solution is dependent on where the impact point is selected, which to be conservative, should be selected as the critical location of the member in shear; as the impact force depends on the local shear deformation (Khowitar et al., 2014, 2015). Additionally, in order to estimate the static displacements, a static analysis has to be conducted which requires an accurate or conservative estimate of the impact force.

2.2 Debris Damming Loads

2.2.1 ASCE 7 (2016)

A debris damming load is a load that is generated when debris agglomerate together at a surface, the load is typically defined by the drag equation (Stolle et al., 2018d). The approach taken by ASCE 7 (2016) follows from the drag equation, where the overall drag force on a building is function of the density of the fluid, drag coefficient, the closure ratio, overall building width, inundation depth, and the tsunami flow velocity:

$$F_{nd} = \frac{1}{2}\rho_f C_d C_{cx} B_b \left(h_{in} u_{flow}^2\right) \tag{2.68}$$

Additionally, ASCE 7 (2016) also specifies a similar formula but for components of the building, where the width subject to the force or the width of the debris dam (b) and the inundated height of an individual element (h_e) are considered:

$$F_{nd} = \frac{1}{2}\rho_f C_d b \left(h_e u_{flow}^2\right) \tag{2.69}$$

2.2.2 Stolle et al. (2018c)

As noted by Stolle et al. (2018d), the classical definition of the drag coefficient refers to the case where the debris is fully submerged in flow. However, the authors state that due to the unsteady and highly dynamic nature of the flow during the experiments, the drag coefficient cannot be determined for the study. Hence, in this study the authors replaced the drag coefficient in the drag formula with a resistance coefficient that was a function of the mean resistance coefficient in the first five seconds after the wave arrival, the width of the channel (w), and the breadth of the debris dam perpendicular to the flow (b) as shown below:

$$C_{R0} = C_R \left(1 + \frac{C_R b}{w}\right)^2 \tag{2.70}$$

2.2.3 Discussion of Key Points and Limitations to Debris Damming Studies

This section will outline some key points and limitations about the debris damming load formulations.

2.2.3.1 Key Points

1. In unsteady flow the classical definition of the drag coefficient no longer applies as it is derived for fully submergent debris.

2. A resistance coefficient was defined to replace the drag coefficient in the drag formula.

2.2.3.2 Limitations

Stolle et al. (2018d) noted that due to the unsteady hydrostatic pressure acting on the dam the drag coefficient could not be directly measured. Following Arnason et al. (2009) the resistance coefficient, which is function of the Froude number and blockage ratio, was estimated based off of the width of the dam. Stolle et al. (2018d) noted that the dam is not a solid object and therefore had an associated porosity that was not accounted for in this study which could lead to an overestimation of the drag coefficient. Some limitations of this study are that the material properties were not scaled down which resulted in the debris maintaining integrity, whereas, based on field surveys this is not the case (Esteban et al.,

2015). Additionally, frictional aspects between the contact of the debris and structure were not considered, which could influence the dam formation and hence associated loads. The authors also go on the state that the influence of negatively and neutrally buoyant debris was not considered but should be as they can influence the formation of the dam and hence the loads experienced by the structure.

2.3 Summary of Limitations in the Literature and Code Provisions

Reviewing the literature and code provisions outlined in this literature review some key limitations with respect to debris impacts are as follows:

- Most debris impact equations do not take into account the structural response to the loading.
  - Structural response can work to reduce the force experienced by the structure, assuming the structure has the ductility capacity to dissipate the impact energy. This is the same principle employed for earthquake engineering where accounting for structural ductility allows for the design of smaller forces and more economical structures.
  - ASCE 7 (2016) C6.11.8 outlines a work-energy method to analyse the structural capacity, however, the method assumes that the behavior is elastic-perfectly-plastic. This means that any post-yield stiffness of the structure is ignored, which can be critical in determining if the structure has the ductility capacity to dissipate the impact energy. Additionally, the method requires that an impact point is selected which can be quite challenging in selecting as debris motion is random (Stolle et al., 2018c).
  - ASCE 7 (2016) C6.11.8 does allow the designer to perform a full non-linear time history analysis of the debris impact event.
- Debris impacts are considered as singular events.
  - In practice multiple debris impacts can occur at once and over the time span of the tsunami event. The effect of multiple debris impacts over time may be critical for analysing the performance of a tsunami evacuation structure throughout the entire event.
  - A performance-based design guideline similar to guidelines for earthquake engineering would be required to define the required performance of structures to tsunami loads.
- Most debris impact equations do not take into consideration that the impact occurs in water.

  - There are contradicting studies on whether or not the added mass of water needs to be accounted for in the impact equation.
  - With the impacts occurring in water there would be fluid reaction forces that are not accounted for. As per Stolle et al. (2019), this phenomenon is usually represented with added mass terms. Additionally, damping in the system is not captured and ignored in any of the above-mentioned equations.
  - An accurate estimation of the added effects of the impact occurring in water would have to be studied in order to modify the impact formulas to account for these effects.

- Debris damming loads are heavily influenced by the formation of the debris dam which is reliant on frictional aspects between the contact of the debris and negatively and neutrally buoyant debris. How a debris dam is formed / the size of the debris dam has a direct relation to the load the structure experiences, hence, it is critical to understand how the debris dam is formed (Stolle et al., 2018d). Additionally, the affect that damaged debris has on the formation of a debris dam is not studied and could be influential on the capture rate as debris becomes more deformed and irregular.

2.4 Structural Response to Impact Loads

The following sections focus on studies that outline key failure mechanisms, considerations for modelling, and various procedures for estimating the structural response to impact loads.

2.4.1 Cotsovos et al. (2008)

In Cotsovos et al. (2008), the authors present a study on the behavior of simply-supported reinforced concrete beams that are subjected to concentrated loads at varying loading rates. The authors propose that material properties of reinforced concrete (i.e. concrete and steel) are independent to the loading rate and that the effects of the loading rate are mostly attributed to the inertial forces that develop within a beam. The study makes use of a general-purpose finite element modelling package for nonlinear static and dynamic analysis, which was compared to experimental data.

The authors conclude that dynamic analysis becomes more important as the rate of the impact load is increased. This is due to the divergence away from a state solution as the impact rate is increased, which causes the member to increase in stiffness and load carrying-capacity while also decreasing in ductility. The authors show that as the impact rate is increased, the damaged section of a beam becomes smaller and more concentrated at the location of the point load. This phenomenon causes a discontinuity point in the deflected shape of the beam which is not characteristic of the expected deflection shape for a simply-supported beam as shown in Figure 2.17. The authors claim that the portion of the beam

between the discontinuity points acts as a fixed-fixed support condition which generates the discontinuity points, the section of the beam between the discontinuity points is termed the effective length of the beam. Ultimately, the authors state that the discontinuity points are generated from the inertial load distribution along the beam, which highlights the importance of performing a dynamic analysis for impact analysis.

The authors also analyse how the crack patterns of the beams change as the rate of impact loading increases. As the loading rate increased it was observed that the cracks primarily consisted of diagonal cracks extending from the impact point down to the tension face of the beam, this would suggest that these cracks are shear cracks. Also observed with an increase in loading rate was that the crack propagation, outwards from the midspan, tended to become more narrow around the impact point, reducing the effective length of the beam. Additionally, under very high loading rates cracks were generated in the compression face of the beam at the discontinuity points in the deflected shape. Comparatively for the static load case, mainly flexural cracks were observed which appear as vertical cracks along the midspan of the beams. This would suggest that as the impact loading rate increases so does the importance of shear behavior in the beam. Additionally, the presence of a discontinuity in the deflected shape also highlights that local member failure could be expected for impact loads with a high loading rate.

The finite element model used for the reinforced concrete beam did not include the effects of loading-rate sensitivity in the material models. This is because the hypothesis of the study is that these effects are primarily due to the inertial forces that are developed because a dynamic analysis is being conducted and not due to the material models. The authors showed that despite loading-rate sensitivity not being included in the material models, under high impact loading rates the numerical model presented similar results to the experimental. The numerical results showed that there was an increase in stiffness and load-carrying capacity but a decrease in ductility as the rate of impact loading increased. Additionally, the authors demonstrated through the numerical model that as the loading-rate increased the effective beam length decreased, similar to the behavior recorded from the experimental results. The results from the numerical model suggest that loading-rate sensitivity may not be a function of only the material models but rather a function of the inertial effects present during a dynamic analysis.

The authors also go on to present the loading-rate at which the analysis can be considered static for a linear elastic simply-supported beam. It is stated that if the loading-rate is greater than or equal to the first dominating mode of vibration then the beam exhibits a load-carrying capacity similar to the static case. For a loading-rate less than the first dominating mode, the failure in the beam occurs before the entire length of the beam is able to oscillate. This phenomenon generates the so-called effective length of the beam, where the beam is assumed to behave as if there is a fixed-fixed support condition at the discontinuity points between the simple-supports as shown in Figure 2.17.

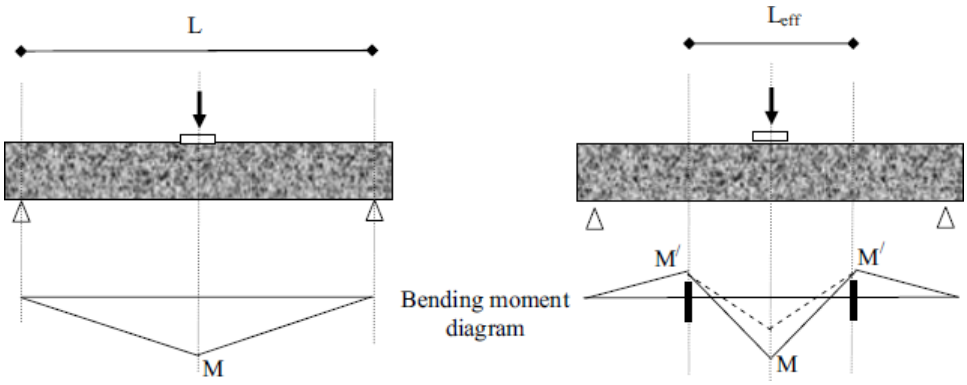


Figure 2.17: Effective Length of a Beam (Cotsovos et al., 2008)

The authors state that the effective length of the beam is a function of the impact duration and the stress-wave velocity (u_w). The authors also outline the loading rate at which the analysis can be considered static, this rate is a function of the static load-carrying capacity and the first natural period. These formulas are outlined below:

$$L_{eff} = 2u_w t_d \tag{2.71}$$

$$\dot{P} = \frac{P_s}{T_1} \tag{2.72}$$

With these formulas for the effective length of the beam and the loading-rate at which the analysis can be considered static, a designer can have a better estimate as to when a full dynamic analysis of an impact problem is required.

2.4.2 Fujikake et al. (2009)

Fujikake et al. (2009) present a study on the analytical evaluation of the impact response for a reinforced concrete beam. The study uses experimental results to develop an analytical expression to predict the maximum midspan deflection and maximum impact load. The experimental program consists of drop impact tests onto a simply-supported reinforced concrete beam. The objective was to study the effects of drop impact height and the amount of longitudinal reinforcement on the response of the beam. The authors state that the response of a reinforced concrete beam subjected to a drop impact can consists of mainly two components. The first being the local response due to the stress-wave propagation at the impact point over a very short period of time and the second being the overall impact response which includes effects of free-vibration and deformation.

The authors classify the impact load as an initial pulse waveform with a high amplitude which is followed by a continuous waveform with a smaller amplitude. The initial pulse waveform was shown to increase in amplitude as the drop height increased however, the duration stayed constant with increasing drop height. This result is similar to the shipping container impacts presented by Aghl et al. (2014), where it was shown that the impact

duration did not change with an increase in impact velocity. The opposite behavior was noted for the continuous waveform, the amplitude did not change with increasing drop height, but the duration increased. The authors also note that there was a lag time between the initial rise of the pulse waveform and the midspan deflection.

The authors develop a 2DOF model consisting of a mass, spring, and damper system. The 2DOF model simulates the drop of a hammer with an initial impact velocity onto the midspan of a reinforced concrete beam as shown in Figure 2.18. The initial impact velocity is assumed to be a function of the acceleration of gravity and the drop height as defined below:

$$v_{ib} = \sqrt{2gh_{drop}} \tag{2.73}$$

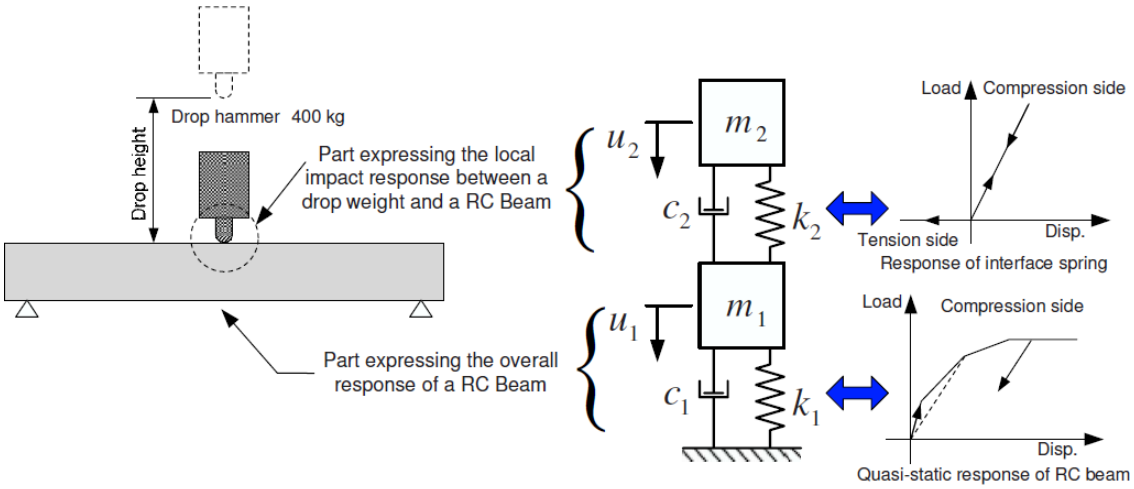


Figure 2.18: Model for Drop Impact Experiments (Fujikake et al., 2009)

This model takes into consideration the contact stiffness of the hammer and the beam (k_2), the nonlinear stiffness of the beam (k_1), and damping (c_1 and c_2). The authors state that the velocity at which the beam deforms is a function of the initial impact velocity, the mass of the hammer (m_2), and the equivalent mass of beam (m_1). The equivalent mass of the beam is defined as a function of the density of the reinforced concrete, the cross-sectional area of the beam, and the span length of the beam as shown below:

$$m_1 = \frac{17\rho AL}{35} \tag{2.74}$$

$$v_{ia} = \frac{m_2}{m_1 + m_2} v_{ib} \tag{2.75}$$

The damping coefficient of the beam (c_1) is assumed to be 0, while the damping coefficient of the contact (c_2) is assumed to be a function of the effective mass of the beam, the mass of the hammer, and contact stiffness as shown below. The authors state that the contact stiffness (k_2) is assumed to be $120,000 \frac{kN}{m}$.

$$c_2 = \sqrt{\frac{m_1 m_2}{m_1 + m_2}} k_2 \tag{2.76}$$

The authors then show that solving this 2DOF system can model the experimental results adequately when the reinforced concrete beams displayed only flexural failure. When local failure was observed the model overestimated the impact force and midspan deflection when compared to the experimental results. The authors state that the local failure likely occurs from the initial peak impact load which results in a large absorption of impact energy that is not captured in the 2DOF model. Hence, when the authors compare the 2DOF model to the experimental results that contained local failure, they show that the maximum midspan deflection from the experimental results are 33% and 18% smaller than those estimated by the 2DOF model. This suggests the importance of capturing local member response of the impact in order to accurately model the impact event, which could be done with a more sophisticated impact model such as modelling the beam as a multiple-degree-of freedom (MDOF) system.

The authors also present an analytical model to determine the maximum midspan deflection that is based on the conservation of energy and a perfectly plastic collision. A perfectly plastic collision is defined as a collision where two bodies stay in contact after the initial impact. The energy loss due to the perfectly plastic collision is defined as a function of the effective mass of the beam, the mass of the hammer, and the initial impact velocity as described below:

$$E_{rc} = \frac{m_1 m_2}{2(m_1 + m_2)} v_{ib}^2 \tag{2.77}$$

Following the conservation of energy, the authors demonstrate that the relationship for the maximum midspan deflection is a function of the energy loss, mass of the hammer, initial impact velocity, the effective mass of the beam, gravitational acceleration, and the area under the force deformation graph for the midspan section.

$$\frac{m_2 v_{ib}^2}{2} - E_{rc} + (m_1 + m_2) g \delta_{max} = \int_0^{\delta_{max}} P(\delta) d\delta \tag{2.78}$$

Once again, the authors show that using this relationship the maximum midspan deflection can be adequately estimated when compared to the experimental data for failure modes that are mainly flexural. For local failure modes this formula, similar to the 2DOF model, overestimated the maximum midspan deflection. This highlights once again the importance of considering local failure for impact events.

2.4.3 Imbeau (2012)

Imbeau (2012) presents a study on reinforced concrete columns subjected to impact loading. The study consists of an experimental program of drop-impact tests on reinforced concrete columns and SDOF analysis to compare analytical results to experimental data. One of the objectives of the study was to analyse how beams, columns, and retrofitted members respond to drop-impact loads. The analysis includes studying the effects of support conditions and axial loads on the response of the members, the crack patterns for dynamic loads, and analytical modeling of the impact event.

The support condition developed for this study resembled a pin and roller boundary condition, meaning the member was restrained against motion in the horizontal and vertical directions at the pin boundary condition and restrained to move in the vertical direction at the roller boundary. The author notes that negative moments were experienced during the initial impact load which is uncharacteristic of the pin and roller boundary condition. Similar behavior was noted in Cotsovos et al. (2008), where they showed that for high impact loading rates a portion of the beam entitled the effective length of the beam, behaves like a fixed-fixed support boundary condition which would induce negative moments in the member. The author notes that after the initial negative reactions, a positive reaction load was recorded which is the typical behavior expected for a pin and roller boundary condition. The author then goes on to explain how the magnitude of the peak positive reaction loads is dependent on the stiffness of the member. This means that for a stiffer member the peak positive reaction load would be greater when compared to a less stiff member. This phenomenon makes physical sense as a less-stiff member (i.e. more flexible) would absorb more of the impact energy through deformation when compared to a stiffer member. The author also explains that the more damage the member experienced correlated to a lower peak positive reaction load, suggesting that more of the impact energy is absorbed through deformation.

An axial load was applied to several of the specimens in order to study the effect of axial load on the response of the members. Observations made during the experimental program were that axially loading members resulted in the member having a higher lateral stiffness when compared to members that did not have an axial load applied. As such, these members experienced large peak positive reaction forces as the stiffness increased with axial load, however, the negative reaction forces remained nearly constant. The author also states that as the axial load increased, the time until peak response decreased, meaning that wave speed increased with increased stiffness of the member as expected. Additionally, the author notes that there was an increase in the inherent damping of the member as the axial load increased. This behavior is expected as the damping of a system is typically defined as a percentage of the critical damping, which for a SDOF system is a function of the stiffness of the system and the mass of the system as shown below (Biggs, 1964):

$$c_{cr} = 2\sqrt{km} \tag{2.79}$$

It is hypothesized by the author that there is a threshold for the axial load limit after which point the additionally axial load would decrease the performance of a member subjected to impact loads. The author hypothesizes that this phenomenon could be due to the pre-compressed member being close to material failure, the addition of an impact load would provide the tipping point for the material to fail. The author states that this point at which the axial load decreases the performance of the member could be a significant factor for designed members for impact loads.

The author also outlined the differences between the crack patterns developed for dynamic and static loads. For the static load experiments a typical flexure failure crack pattern was developed where cracks extend vertically from the tension face (bottom side) of the concrete upwards. For the dynamic experiments (i.e. drop-impact tests) the crack

pattern that was developed is quite different when compared to the static tests. For the dynamic loads the crack pattern consisted of the formation of diagonal shear cracks which formed a shear-plug, punching out of the opposite face of the impact surface (bottom side), and tension cracks developed near the support regions. The author states that the shear cracks were fully developed in the member almost immediately after the initial contact ($1ms$) and before the member started to deflect, which suggests that there is a significant difference in how a member responds to dynamic loads when compared to static loads causing the same peak deflection. The author also notes that flexural cracks developed in the compression face of the member (top side) at locations where negative moments were experienced, these cracks were not developed for the static load case which highlights an important difference between static and dynamic loads. This behavior is consistent with the study completed by Cotsovos et al. (2008), where the member formed a fixed-fixed support condition generating the negative moments causing a discontinuity in the bending shape and cracks on the compression side of the beam.

The applicability of a SDOF model to simulate impacts against reinforced concrete columns is discussed by the author in this study. The author concluded that SDOF models are not adequate to capture the behavior of reinforced concrete columns subjected to impact loads. The author analysed two cases: (1) response from a column that experienced inelastic deformation and (2) response from a column that only experienced elastic deformation. For the column that experienced only elastic deformation, the deflection-time history was well represented by the SDOF model as shown in Figure 2.19. However, for the column that experienced inelastic deformation, the SDOF model did not represent well the deformation-time history as shown in Figure 2.20.

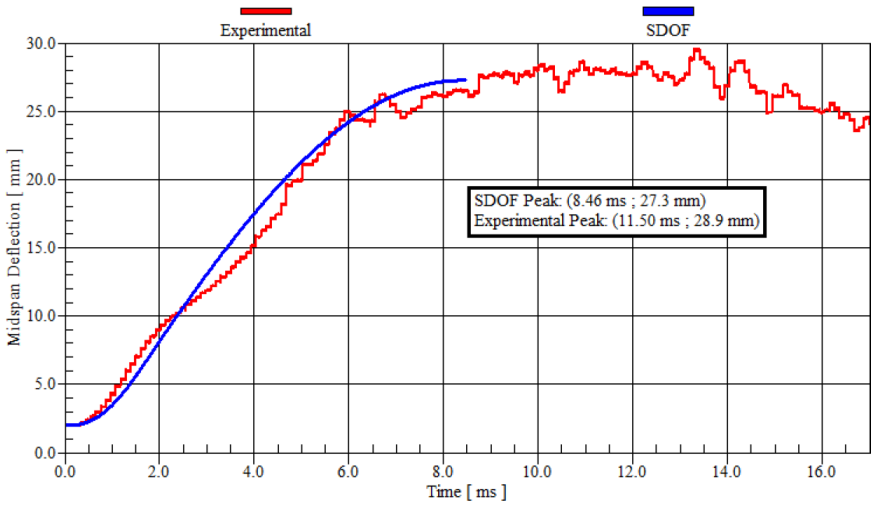


Figure 2.19: SDOF Model for Elastic Deformation (Imbeau, 2012)

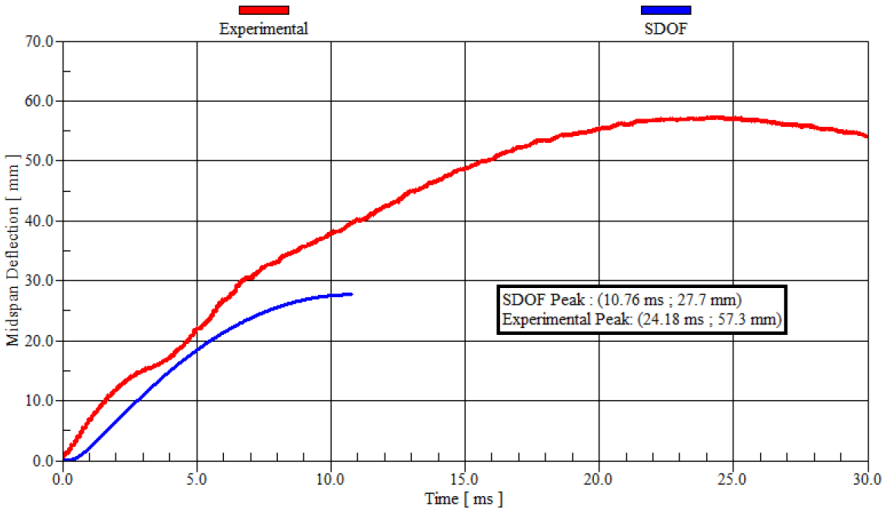


Figure 2.20: SDOF Model for Inelastic Deformation (Imbeau, 2012)

The author goes on to explain that the poor representation by the SDOF model for the member that experienced inelastic deformation is partly due to the formation of a shear plug which increased the midspan deflection. The author states that the effect of the formation of the shear plug cannot be captured by the SDOF model. Additionally, the author speculates that for impact events on a member with distributed mass and stiffness experiencing inelastic deformations, the first mode of bending might not be the dominate mode. This means that higher modes of vibration might be significant for impact events where the member experiences plastic deformation and hence, a SDOF model is not adequate to capture the member response. However, if the member only experienced elastic deformations then the author shows that the SDOF model is adequate in capturing the deflection-time history of the impact event.

2.4.4 Cowan et al. (2015)

Cowan et al. (2015) presents a study on response-spectrum analysis for barge impacts onto bridge piers. Response-spectrum analysis is a form of dynamic analysis where the maximum response of all possible linear one-degree of freedom systems (i.e. all modes of vibration) are calculated for a particular input forcing history (Biggs, 1964). This means that the maximum dynamic response of the system can be estimated without performing a full time-history analysis. The objective of the study, as presented by the authors, is to develop a response-spectrum analysis procedure to model barge impacts on bridges. The results of the analysis were compared to full-scale barge-bridge impact tests where it was shown that the proposed response-spectrum analysis procedure provided conservative results.

The impact response-spectrum analysis (IRSA) procedure outlined by the authors consisted of the following components: (1) perform a modal analysis, (2) extract maximum

response parameters, and (3) determine the dynamic magnification spectrum. Modal analysis is used to calculate the vibration characteristics of a structure such as the natural frequencies and mode shapes. These characteristics are used to transform the system into modal coordinates such that individual modal contributions to overall structural displacements, velocities, and accelerations can be computed for each mode shape. The structures response can then be determined through modal superposition, where each mode contribution is summed together to obtain the structural response. The authors state that in order to determine the maximum overall structural response, the modal contributions should be combined using the complete-quadratic-combination (CQC) method. The authors select this method as it allows for the combination of closely spaced natural frequencies for three-dimensional models where other methods may not be adequate, such as direct superposition and square-root-of-the-sum-of-the-squares (SRSS) methods (Tedesco et al., 1999). Once, the modal superposition has been completed the dynamic magnification factor should be determined. The dynamic magnification factor is determined by two steps outlined by the authors: (1) perform a dynamic analysis of one modal frequency for a SDOF model subjected to the time-varying loading history and extract the maximum response. (2) Perform a static analysis of the same SDOF system subjected to the peak load outlined in the time-varying load history and extract the response. Finally, the dynamic magnification factor is defined as the ratio of the maximum response of the SDOF model due to dynamic analysis to the response due to static analysis. This procedure is repeated for all modal frequencies determined from the modal analysis which produces a dynamic magnification factor for each structural period, this relationship between dynamic magnification factor and structural period is then plotted to produce a dynamic magnification spectrum. From this spectrum the designer can see what structural period is most influenced by dynamic effects and scale the static solution accordingly. The authors outline graphically the procedure for how to calculate linear and nonlinear event-specific response-spectrum analysis based on a known loading-history and dynamic magnification spectrum as shown in Figure 2.21.

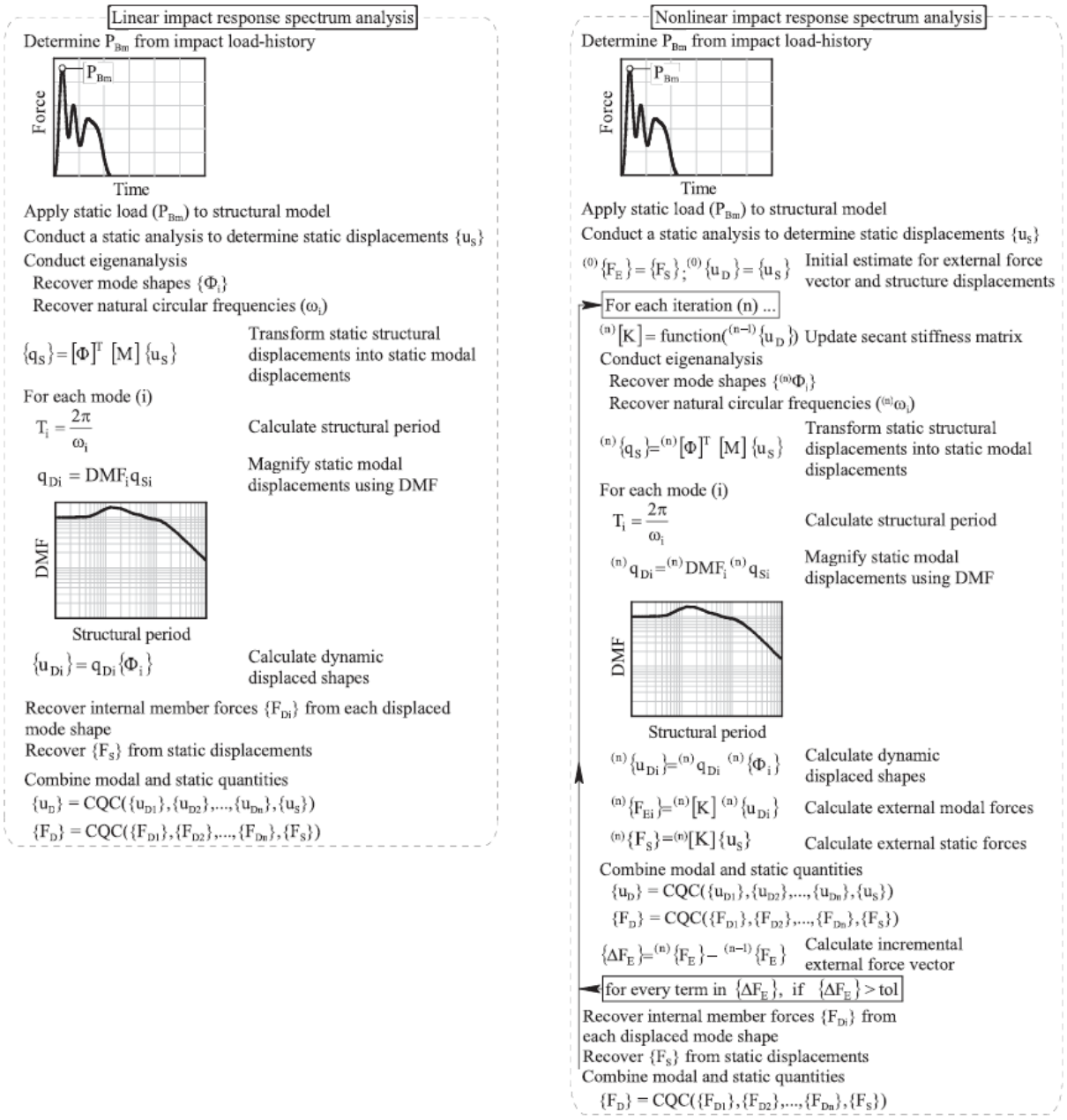


Figure 2.21: Linear and Nonlinear Response-Spectrum Analysis (Cowan et al., 2015)

In order to validate the procedure outlined by the authors, they compare their results to those determined from a software package titled *FB-MultiPier* (Bridge Software Institute, 2008). Both analysis procedures used force data from full-scale bridge-pier impact testing conducted by Consolazio et al. (2005) to ensure a realistic force-time history was used for the models. Using the software package *FB-MultiPier* (Bridge Software Institute, 2008), the authors performed a full dynamic time-history analysis of the impact event and extracted the maximum moment the bridge pile was subjected to. The authors then developed an event specific dynamic magnification spectrum for each impact load-history

considered. The dynamic magnification spectrum was developed by performing dynamic analysis for a certain impact load-history applied to many SDOF systems, each having a different natural period. From this analysis the dynamic magnification factor was calculated by dividing the maximum dynamic displacement with the static displacement for each SDOF system, this relationship was then plotted to produce the dynamic magnification spectrum. Using the dynamic magnification spectrum, the bridge pile was analysed by using the procedures outlined in Figure 2.21. From this analysis, the authors showed that the IRSA method provided conservative results for the bending moment when compared to the time-history analysis as shown in Figure 2.22. They also show that the method was able to accurately predict where the maximum moments occur with respect to the pile elevation. The authors state that the discrepancies between the IRSA method and the time-history method are likely due to the approximate nature of modal combination methods such as the CQC method. The method attempts to estimate the maximum dynamic response of the system by combining modal responses together that may not maximize at the same time. Therefore, the method can lead to differences in response when compared to a full time-history analysis.

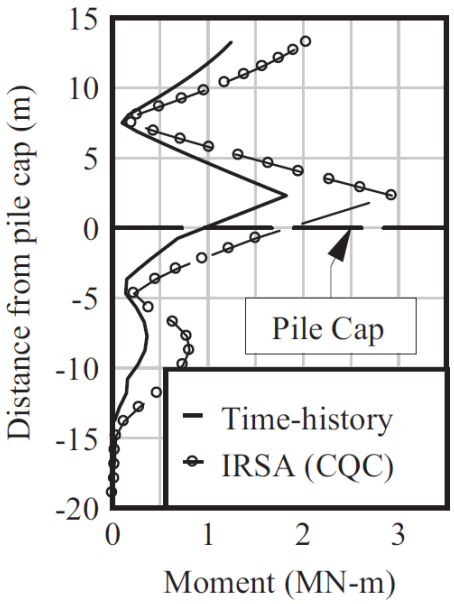


Figure 2.22: Time-History Analysis versus IRSA Method (Cowan et al., 2015)

The authors then go on to explain that the event-specific dynamic magnification spectrum can be extended to a general design-oriented dynamic magnification spectrum. This can be done by computing the event-specific dynamic magnification spectrum for many impact load-histories and providing an upper envelope for all of the spectrum's, which is designated as the design-oriented dynamic magnification spectrum.

The authors also comment on the number of modes to include in the IRSA method. Typically, the number of modes used for response-spectrum analysis for seismic design requires the designer to include enough modes such that the total mass participation of

the modes sums up to 90% of the total mass of the structure in each orthogonal horizontal direction of response (ASCE 7, 2016). The authors of this study suggest that the number of modes selected should sum to a mass participation factor of 99% of the total mass of the structure in the direction of the applied impact loading in order to capture the dynamic response of the structure.

2.4.5 Das Adhikary and Li (2018)

Das Adhikary and Li (2018) present a study on analytical models to predict low-velocity impact response of reinforced concrete beams. The models consist of those based on energy-balance principles and SDOF models that can be used as a precursor to finite-element modelling. The models were used to estimate maximum midspan deflection and were compared to experimental results. The authors state that midspan deflection can be an important performance index for evaluating the damage state of a member.

The energy balance model is based on the theory that the initial kinetic energy of the impactor is used to deform the member. When the maximum deflection is reached for the member, the velocity of the impactor is reduced to zero. This assumption means that all of the kinetic energy of the impactor is being used to deform the member, which implies that the structure is behaving quasi-statically as no dynamic effects are included in the model. The authors outline that the overall deformation of the member can be broken down into several components: (1) bending deformation, (2) shear deformation, and (3) membrane-stiffening effects for large deflections. Additionally, local deformation effects are also considered in the model, however, the energy needed to induce damage in the member is neglected. The energy balance equation can be defined as a function of the mass of the impactor, velocity just before impact, bending deformation energy, shear deformation energy, membrane-stiffening energy, and energy stored in the contact region during indentation. The velocity just before impact is estimated as a function of the drop height of the impactor, effective mass of the beam (m_e), mass of the impactor (m_i), and gravitational acceleration, both equations are outlined below:

$$v = \frac{m_i\sqrt{2gh_{drop}}}{m_e + m_i} \tag{2.80}$$

$$\frac{1}{2}mv^2 = E_b + E_s + E_m + E_c \tag{2.81}$$

The authors outline the bending, shear, and membrane energies as a function of the stiffness of the member, including both bending and shear deformation effects, the membrane stiffness, and the maximum deflection at the impact point (W_{max}):

$$E_b + E_s + E_m = \frac{1}{2}K_{bs}W_{max}^2 + \frac{1}{4}K_mW_{max}^4 \tag{2.82}$$

The contact energy is defined by Hertzian contact law and is a function of the contact stiffness, the stiffness including bending and shear deformation, the membrane stiffness,

and the maximum deflection at the impact point. The contact stiffness is a function of the radius of the impactor, Poisson's ratio of the impactor, the modulus of elasticity of the impactor ($E_{impactor}$), and the modulus of elasticity of the beam (E_{beam}). These formulas are outlined below:

$$n = \frac{4}{3} r_{impactor}^{\frac{1}{2}} \left[\frac{1 - \nu_{impactor}^2}{E_{impactor}} + \frac{1}{E_{beam}} \right]^{-1} \tag{2.83}$$

$$E_c = \frac{2}{5} n^{-\frac{2}{3}} \left(K_{bs} W_{max} + K_m W_{max}^3 \right)^{\frac{5}{3}} \tag{2.84}$$

The authors then sub these formulas back into the main energy balance equation and assuming that membrane effects are negligible, the energy balance is reduced to the following equation:

$$\frac{1}{2} m v^2 = \frac{1}{2} K_{bs} W_{max}^2 \left[1 + \frac{4}{5} \left(\frac{K_{bs} W_{max}}{n} \right)^{\frac{2}{3}} \right] \tag{2.85}$$

The maximum impact load (P_{max}) can also be estimated from that equation if you assume that it follows the load-deflection relationship below. This allows the energy balance equation to be written in terms of the maximum impact load:

$$P_{max} = K_{bs} W_{max} + K_m W_{max}^3 \tag{2.86}$$

$$\frac{1}{2} m v^2 = \frac{1}{2} \left(\frac{P_{max}^2}{K_{bs}} \right) + \frac{4}{5} \left(\frac{P_{max}^{5/3}}{n^{2/3}} \right) \tag{2.87}$$

The authors show that the energy balance model was able to reasonably estimate the maximum midspan deflection for low drop heights. However, as drop heights increased the model underestimated maximum midspan deflections when compared to experimental results. The authors speculate that the model performed poorly for the higher drop heights due to the assumption of a quasi-static beam response. As the drop height increased so does energy lost due to large plastic deformation, heat, and noise which alters the energy balance equation resulting in poor deflection estimates when compared to experimental results.

The SDOF model that the authors propose is an idealized system of the drop impact event, where the two bodies are treated as one at the initial contact as shown in Figure 2.23. As can be seen from the model, damping is neglected. Additionally, the mass of the system is considered to be equal to the mass of the impactor plus the effective mass of the beam. The stiffness of the SDOF model is equal to the stiffness of the beam, meaning that the impactor is assumed to be rigid and the collision is perfectly plastic.

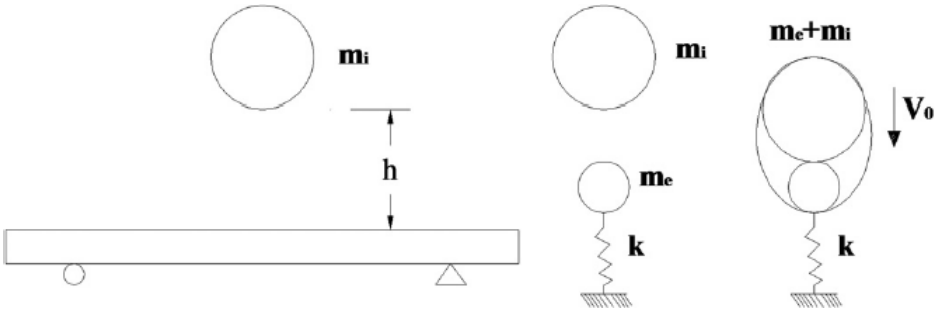


Figure 2.23: Idealized SDOF System (Das Adhikary and Li, 2018)

The authors state that a simple elastic-SDOF model cannot predict the midspan deflection history of a beam under impact and hence the model developed utilizes an elastic-plastic material model. The authors outline the equations of motion for both the elastic response of the beam and the plastic response. The equations of motion are a function of the effective mass of the beam, mass of the impactor, acceleration, initial elastic stiffness, the resistance force causing yielding of the beam (R_m), displacement, elastic limit displacement (u_e), and the maximum deflection. The authors show that the effective mass of the beam for the elastic stage is one-half the mass of the beam and for the plastic stage it is one-third the mass of the beam:

Elastic Response:

$$\left\{ (m_e + m_{impactor})\,\ddot{u} + ku = 0 \quad 0 < u < u_e \right.$$

Plastic Response

$$\begin{cases} (m_e + m_{impactor})\,\ddot{u} + R_m = 0 & u_e < u < u_{max} \\ (m_e + m_{impactor})\,\ddot{u} + R_m - k(u_{max} - u) = 0 & (u_{max} - 2u_e) < u < u_{max} \end{cases}$$

The authors examine both cases where strain-rate effects are included in the material model and when they are not included. They show that when strain-rate effects are included in the SDOF model, the maximum midspan deflection was underestimated when compared to experimental results. However, when they were not included in the model the maximum midspan deflection was always greater than the experimental results. The authors compare the SDOF model to results from Fujikake et al. (2009), where they show that the SDOF model was able to predict the midspan deflection history adequately, as shown in Figure 2.24.

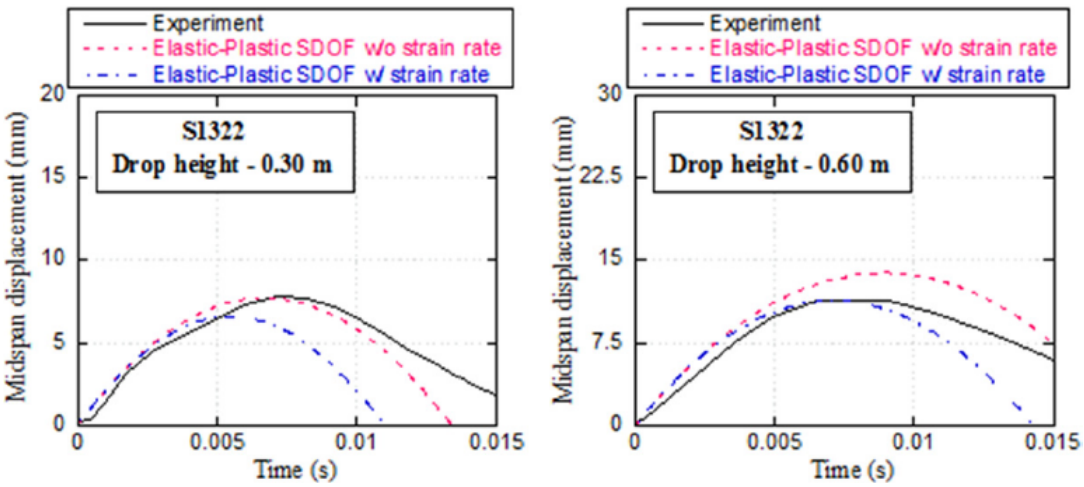


Figure 2.24: SDOF Estimate of Midspan Deflection History (Das Adhikary and Li, 2018)

In conclusion, the authors state that the energy balance model was accurate for low drop heights, however, as the drop height increased so did the inaccuracies of the model. On the other hand, the SDOF model proved to be accurate for both low and high drop heights but to be on the conservative side the authors suggest not including strain-rate effects in the material models.

2.4.6 Discussion of Key Points and Limitations in the Literature on Structural Response to Impact Loads

This section will outline key points and limitations in the literature presented about the structural response to impact loads.

2.4.6.1 Key Points

1. The cause of strength gain in dynamic loading scenarios is not fully understood and could be due to inertial effects and / or strain-rate sensitivity in the material model (Imbeau, 2012). However, Cotsovos et al. (2008) acknowledged that for practical design procedures modification of the effective material properties to account for loading rate effects is practical, especially for analysis that does not include inertial effects.

2. Cotsovos et al. (2008) concluded that dynamic analysis becomes more important as the rate of impact loading increases. The authors showed that as the impact loading rate increased the damaged section of the beam becomes smaller and more concentrated.

3. If the member is dominated by the first mode of vibration, then the load-carrying capacity is similar to that determined from a static analysis (Cotsovos et al., 2008).

4. If higher mode effects are present, inertial properties of the member become more important and hence a dynamic analysis is required (Cotsovos et al., 2008; Imbeau, 2012).

5. A member will increase in stiffness and load-carrying capacity but will decrease in ductility as the impact loading rate increases (Cotsovos et al., 2008).

6. As the impact loading rate increases so does the importance of shear behavior of the member (Cotsovos et al., 2008; Imbeau, 2012).

7. A SDOF or 2DOF model may not be adequate to simulate impacts events:

    - Local member failure is not captured in a 2DOF model (Fujikake et al., 2009).
    - A SDOF model is not capable of capturing the effects of the formation of a shear plug, which leads to additional member deformation (Imbeau, 2012).
    - A SDOF model cannot capture the influence of higher mode effects (Imbeau, 2012).

8. Cotsovos et al. (2008) state that if the loading rate is less than the ratio of the static load-carry capacity to the first mode of vibration then the problem can be considered static.

9. The response of a member during an impact load consists of two components: (1) the local response due to stress-wave propagation and (2) the overall response which includes free-vibration and deformation (Fujikake et al., 2009).

10. The energy-balance method was not an accurate solution for high drop heights (fast loading-rates) due to energy loss from large plastic deformation, heat generation, and noise (Das Adhikary and Li, 2018). The method also assumes a quasi-static response of the member which may not adequate for high loading rates (Cotsovos et al., 2008; Imbeau, 2012).

11. Applying an axial load increased the lateral stiffness of a member, which correlated to a larger positive peak in the reaction forces and a lower time until peak response (Imbeau, 2012).

    - Imbeau (2012) hypothesised that an axial load can decrease the performance of a member if it pre-compresses the member close to material failure.

12. An IRSA procedure was shown to be conservative for barge-bridge impact events (Cowan et al., 2015). This type of method could be useful for classifying the range of loads a structure could be subjected to during a tsunami event.

    - Cowan et al. (2015) suggests that the complete-quadratic-combination method should be used for modal superposition.

13. When performing modal superposition, the number of modes used for analysis should sum to a mass participation factor of 99% in the direction of the impact (Cowan et al., 2015).

14. Strain-rate effects included in the SDOF model outlined by Das Adhikary and Li (2018) where shown to provide unconservative results for higher drop-impact heights. As such, Das Adhikary and Li (2018) suggests not including strain-rate effects in the SDOF analysis to be conservative.

2.4.6.2 Limitations

1. Most of the methods outlined in this literature review do not explicitly include the deformation of the impactor in the formulation or analysis.
    - Deformation of the impactor becomes important for high velocity or low stiffness impactors, where plastic deformations can be expected. Plastic deformation of the impactor could lead to reduced impact forces due to energy loss, which is important to capture for accurately estimating impact forces and structural response.
    - Cowan et al. (2015) implicitly included the deformation of the impactor as the force-time histories used were generated from full-scale barge-bridge impacts. Meaning neither the barge nor bridge were constrained to behave like a rigid body.
2. Only one-dimensional analytical analysis is presented in the literature discussed.
    - Discussion about if analytical MDOF methods can capture key aspects of an impact event are not presented in any of these studies.

2.5 Review of ASCE 7 (2016) Chapter 6 Guidelines for Debris Impact Loads

When designing structures for debris impacts Clause 6.11 of ASCE 7 (2016) states the following:

- Debris impact loads do not need to be combined with other tsunami-related loads outlined in Chapter 6 of ASCE 7 (2016).
- Debris impact loads do not need to be designed for unless the inundation depth is great than or equal to $0.914m$.
- Debris impact loads should be applied to all members in the inundation depth at points of critical flexure and shear. However, the members do not have to be all loaded simultaneously.
- Perimeter gravity-load-carrying structural components whose principle structural axis is perpendicular to the inflow and outflow directions shall be designed for the most severe effect of debris impact loads.

2.5.1 Current Guidelines

Clause 6.11.1 of ASCE 7 (2016) states that the following force can be applied as a maximum static load at points of critical flexure and shear for all members in the inundation depth. This load can be used instead of defining loads based on the type of debris impacting the structure. While this load is not debris specific, it is derived from full-scale in-air shipping container impact tests multiplied by a dynamic amplification factor of 1.5. The force is a function of a constant, the importance factor, and the orientation coefficient as shown below:

$$F_i = 1470 C_0 I_{tsu} \ [kN] \tag{2.88}$$

The importance factor ranges from 1.00 to 1.25 and the orientation coefficient is equal to 0.65. The clause also states that if the site is not in an impact zone with risk for impacts from shipping containers, ships, and barges, then this impact load can be reduced by 50%.

Clause 6.11.2 of ASCE 7 (2016) outlines the impact load and duration to account for debris from wooden logs and poles. The impact force is a function of the importance factor, the orientation coefficient, the maximum flow velocity, the minimum between the effective stiffness of the impacting debris or the lateral stiffness of the impacted structural member, and the mass of the debris. The impact duration is a function of the mass of the debris, maximum flow velocity, and the impact force. These formulas are defined below:

$$F_{ni} = u_{max} \sqrt{k m_d} \tag{2.89}$$

$$F_i = I_{tsu} C_0 u_{max} \sqrt{k m_d} \tag{2.90}$$

$$t_d = \frac{2 m_d u_{max}}{F_{ni}} \tag{2.91}$$

Clause 6.11.2 of ASCE 7 (2016) also states that for an equivalent static analysis the impact force should be multiplied by the dynamic response ratio outlined in Figure 2.25.

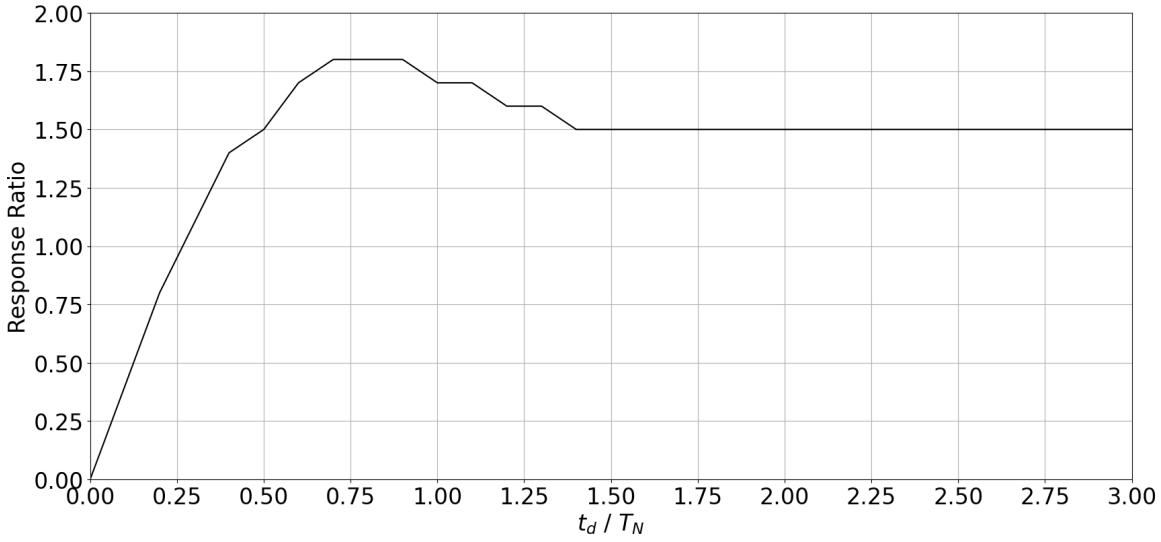


Figure 2.25: Dynamic Response Ratio (ASCE 7, 2016)

Clause 6.11.3 of ASCE 7 (2016) outlines the impact force due to vehicles. The impact force is taken as a constant value derived from data of aerial and on-ground surveys from the 2011 Tohoku Tsunami (Naito et al., 2014). Additionally, the standard requires the assumption that this type of impact occurs if the inundation depth is at least $0.914m$, which equates to the inundation depth required to float a vehicle. This force is outlined below:

$$F_i = 130 I_{tsu} \ [kN] \tag{2.92}$$

Clause 6.11.4 of ASCE 7 (2016) outlines the impact force due to tumbling boulders and concrete debris. The impact force is taken as a constant value derived from a simplified static approach of a boulder with a relative maximum velocity of $4\frac{m}{s}$ multiplied by a dynamic amplification factor of 2 (Chau and Bao, 2010). Additionally, the standard requires the assumption that this type of impact occurs if the inundation depth is at least $0.61m$, which is the depth required to capture the tumbling motion of the boulder. This force is outlined below:

$$F_i = 36 I_{tsu} \ [kN] \tag{2.93}$$

Clause 6.11.6 of ASCE 7 (2016) outlines the load for shipping container impacts. The impact force takes the same form as specified in Clause 6.11.2 of ASCE 7 (2016), where the mass of the debris is equal to the mass of the empty shipping container. Additionally, for empty shipping containers the impact duration is the same as specified in Clause 6.11.2 of ASCE 7 (2016). The impact duration for loaded shipping containers is a function of the mass of the empty shipping container, the mass of the contents of the shipping container, the maximum flow velocity, and the nominal impact force. The nominal impact force (i.e. the impact force not including the importance factor and orientation coefficient) does not need to exceed $980kN$ and the mass of the contents should be taken as 50% of the maximum rated content capacity of the shipping container. The impact duration formula for loaded shipping containers is defined below:

$$t_d = \frac{(m_d + m_{contents}) u_{max}}{F_{ni}} \tag{2.94}$$

The clause also states that for an equivalent static analysis, the impact force should be amplified by the dynamic response ratio as defined in Figure 2.25.

Clause 6.11.7 of ASCE 7 (2016) outlines the load for extraordinary debris impacts, which are classified as impacts by a $39,916kg$ or larger marine vessel. Additionally, the standard requires that the maximum inundation depth must exceed $3.66m$ in order for these types of impacts to occur. The impact force is calculated based off of the formula outlined in Clause 6.11.2 of ASCE 7 (2016), where the stiffness is defined as the transverse structural member stiffness and the mass is defined as the Lightship Weight plus 30% of the Deadweight Tonnage. This definition assumes that the vessel's stiffness is greater than the structural stiffness. If the impact load is to exceed the structural member capacity, then the standard allows for it to be accommodated through alternative load path progressive collapse provisions in Section 6.8.3.5.3 of ASCE 7 (2016). The standard outlines that the analysis should be applied to all framing levels from the base of the structure up to 1.3 times the inundation depth plus the freeboard of the vessel.

Clause 6.11.8 of ASCE 7 (2016) outlines alternative methods that the standard allows for response analysis. For dynamic analysis the standard specifies that a rectangular pulse be applied with a load and duration equal to that specified in Clause 6.11.2 of ASCE 7 (2016). The standard states that if inelastic response is considered the impact force can be reduced by considering the ductility of the structure. The standard allows for the inelastic response to be estimated through time-history analysis and work-energy methods. Additionally, a work-energy method is outlined by the standard that is based off of an impact by large, essentially rigid debris and an elastic-perfectly plastic force-displacement relationship. The yield force is defined as a function of the maximum flow velocity, the coefficient of restitution (e, equal to one unless otherwise substantiated), the effective mass of the structure at the impact point (M_e), the initial elastic stiffness of the structure at the impact point, the permissible ductility ratio (μ), and the mass term M_m. Both mass terms are a function of the mass (m_i) and static displacements (Δ_i) at a node i, the displacements are scaled to have a value of one at the impact point. These formulas are outlined below:

$$F_{cap} = u_{max} \left[\frac{1+e}{\left(1 + \frac{M_m}{m_d}\right)\sqrt{2\mu - 1}} \right] \sqrt{k_e M_e} \tag{2.95}$$

$$M_e = \sum m_i \Delta_i^2 \tag{2.96}$$

$$M_m = \sum m_i \Delta_i \tag{2.97}$$

Additionally, the standard states that care should be taken on selecting the impact duration. For a very short impact duration, the entire structure may not have time to respond and hence only a portion of the structure must be analysed. Whereas, for longer impact durations such as those from extraordinary debris, the entire structure might respond to the event and hence the entire structure should be analysed. However, the standard provides no guidance on how to determine if the entire structure should be analysed or not.

2.5.2 Comparison to Other Analytical Methods

This section will outline how the loads specified in Clause 6.11.2 of ASCE 7 (2016) compare to other analytical models. This section will use all of the same assumptions outlined from the SDOF model comparison in Section 2.1.1.12 to generate debris impact forces versus impact velocity curves for various methods outlined in Figure 2.26.

Observing Figure 2.26, it can be seen that the method outlined in Clause 6.11.2 of ASCE 7 (2016) produces the very similar results as all three of the methods outlined in Haehnel and Daly (2004); assuming the stopping distance and duration of impacts are calculated by following the formulas outlined by Haehnel and Daly (2004). This result is expected as the method outlined in Clause 6.11.2 of ASCE 7 (2016) is derived from the stress wave propagation which produces the same formula as the contact-stiffness approach outlined in Haehnel and Daly (2004). With this conclusion the comparison of Clause 6.11.2 of ASCE 7 (2016) to all other SDOF models is the same as those outlined previously in the SDOF model section. A summary of the conclusions made is outlined as follows:

- Matsutomi (2009) provides a formula for debris impact that does not increase linearly with velocity as the velocity term is to the exponent of 1.2. This method provides much lower impact forces compared to the standard and could be due to the sensitivity of the formula to the debris yield stress.

- Riggs et al. (2013) only use the debris stiffness in the formulation of the impact force. Hence this impact force is slightly larger than those outlined by Clause 6.11.2 of ASCE 7 (2016) as the standard uses lesser of the structure or debris stiffness, which means a fully-rigid structure is not necessarily assumed.

- Aghl et al. (2014) provide a debris impact force formula that is not presented in the figure as it only multiplies the formula outlined in Clause 6.11.2 of ASCE 7 (2016) by a factor of two to account for dynamic effects.

- Aghl et al. (2015) provide a debris impact force estimate that follows the same relationship as the debris material properties. Hence, the debris impact force becomes very sensitive to the debris material properties that were selected. From the figure, the formula outlined in Aghl et al. (2015) provides the same impact force as the standard up until the debris yields, at which point the formula provides a much smaller estimate of the debris impact force when compared to the standard. This is due to the debris material being pushed past the elastic limit and into a plastic state.

- Ikeno et al. (2016) provide a formula for debris impact that does not increase linearly with velocity as the velocity term is to the exponent of 1.2. This method considers both the properties of the debris and the structure through Hertzian contact mechanics, which means the structure is not assumed to be fully rigid. Hence, this method provides a smaller debris impact force than those estimated by the standard. However, as this method is derived from material properties of both the structure and debris, the impact force becomes sensitive to the selected material properties.

- Stolle et al. (2018a) provide a parameter to capture the ductility of the structure which would work to convert impact energy into deformation energy of the structure. This parameter is a modifier to the formula outlined in Clause 6.11.2 of ASCE 7 (2016) which correlates to a reduction in the impact force as noted in the figure.

Khowitar et al. (2015) provide a formula for beam / column impacts of debris on a fixed-fixed column. The method estimates the initial peak impact force which may not correlate to the maximum impact, which can be 1.5 times larger than the initial peak force as stated by the authors. This method considers the local shear deformation in the debris and structure which differs from the standard, which just considers the lesser of the stiffnesses. This means that the method outlined by Khowitar et al. (2015) relies heavily upon the debris and structure properties selected such as the shear modulus and shear coefficient, which can be challenging to estimate. For these particular material properties selected, this method provided debris impact forces that were smaller than those estimated by the standard. It should be noted though that this method only estimates the initial peak impact force which may not represent the maximum impact force as stated by the authors.

Stolle et al. (2019) provide a method for estimating the debris impact force that is based on a 2DOF model that takes into account the displacements of the debris and the structure. From Figure 2.26, it can be seen that this method provides a debris impact force that is significantly smaller than that outlined by the standard. This suggests that for this particular structure and debris, the structure displaced a notable amount which decreased the overall impact force. Further highlighting the importance of including the structural response when developing debris loads for flexible structures.

In conclusion, the method outlined in Clause 6.11.2 of ASCE 7 (2016) provides an upper-bound estimate of the impact force for this particular debris and structure combination when compared to the other methods outlined in this study. The method is able to include the affects of structural stiffness through the formulation of using the lesser of the debris or structure stiffness. However, this method does not explicitly include the affects of structural deformation which would decrease the impact force and hence, this method may provide unnecessarily large impact forces for extraordinary debris impact events.

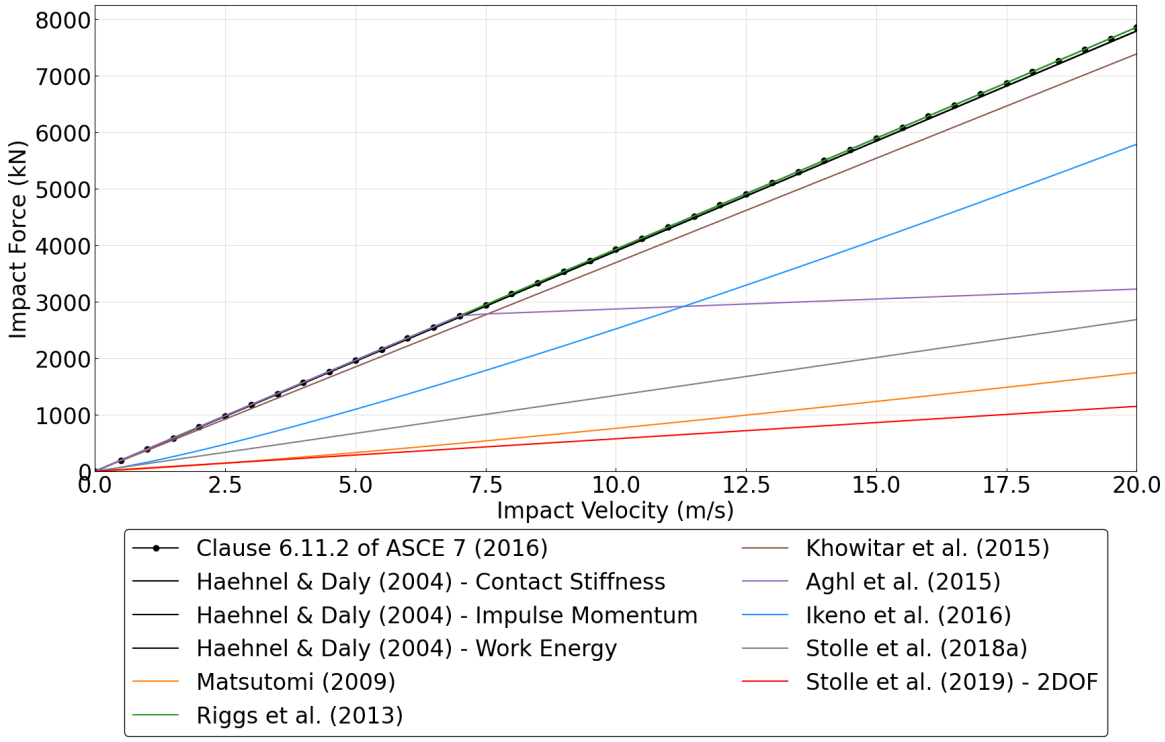


Figure 2.26: Clause 6.11.2 of ASCE 7 (2016) versus Other Analytical Models

2.5.3 Structural Response Comparison

This section will outline a comparative analysis of three different loading cases: (1) a damaged structure due to an earthquake being subjected to a shipping container impact (damaged impact loading scenario), (2) a structure that has no previous damage being subjected to a shipping container impact (undamaged impact loading scenario), and (3)

the earthquake loading exclusively (earthquake scenario). The goal is to highlight the importance of including previous structural damage when performing debris impact analysis outlined in Chapter 6 of ASCE 7 (2016). It should be noted that the loading scenario for applying the hydrostatic and hydrodynamic loads outlined in Section 6.9 and Section 6.10 of ASCE 7 (2016) to the damaged structure was also investigated, however, the structure failed and no meaningful results could be extracted. Additionally, Clause 6.11 of ASCE 7 (2016) states that debris impact loads do not need to be combined with other tsunami-related loads outlined in Chapter 6 of ASCE 7 (2016).

2.5.3.1 Structural Model Description

The structural model can be seen below in Figure 2.27 and is based off the structure used for the National Centre for Research on Earthquake Engineering (NCREE) blind analysis competition in Taiwan (2019). The nonlinear time history analysis was completed using *OpenSees* (McKenna et al., 2010) and the modelling parameters are outlined in Appendix B. The first story is $2.8m$ tall, stories two to seven are each $1.5m$ tall, and the bay width is $3.5m$. Each frame is connected by a constraint that ensures the displacements are the exact same between the frames, this ensures the structure acts as a single structure instead of three separate frames. The bottom nodes are fixed in all degrees of freedom in order to simulate a fixed foundation and the cross-members seen in frames one and three represent infill reinforced concrete walls. Additionally, note that this structure will exhibit soft-story behaviour in the first and second story as these stories will have considerably less stiffness compared to the third to seventh story due to the absence of a wall. This is important to note as this means these stories are not capable of sustaining large lateral loads.

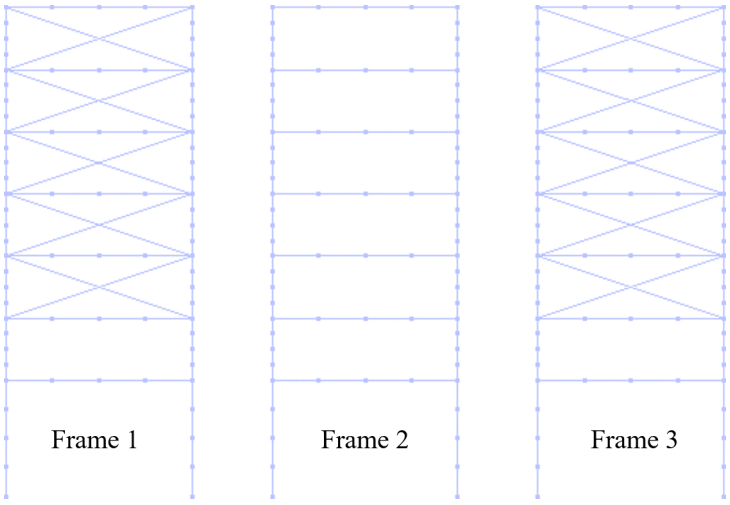


Figure 2.27: *OpenSees* Structural Model

2.5.3.2 Structural Dynamic Characteristics

The dynamic characteristics of the structure include the first five natural periods of vibration and the corresponding mode shapes. The periods of vibration were calculated by solving the eigenvalue problem and extracting the natural frequencies and mode shapes. The natural periods of vibration can be seen below in Table 2.1:

Mode Shape	**Period (s)**
1^{st}	0.265
2^{nd}	0.062
3^{rd}	0.026
4^{th}	0.017
5^{th}	0.012

Table 2.1: *OpenSees* Structural Dynamic Characteristics

For each period of vibration, the corresponding mode shape was plotted and labelled with the displacement for each floor level in the x-direction only. The modes shapes can be seen below in Figure 2.28:

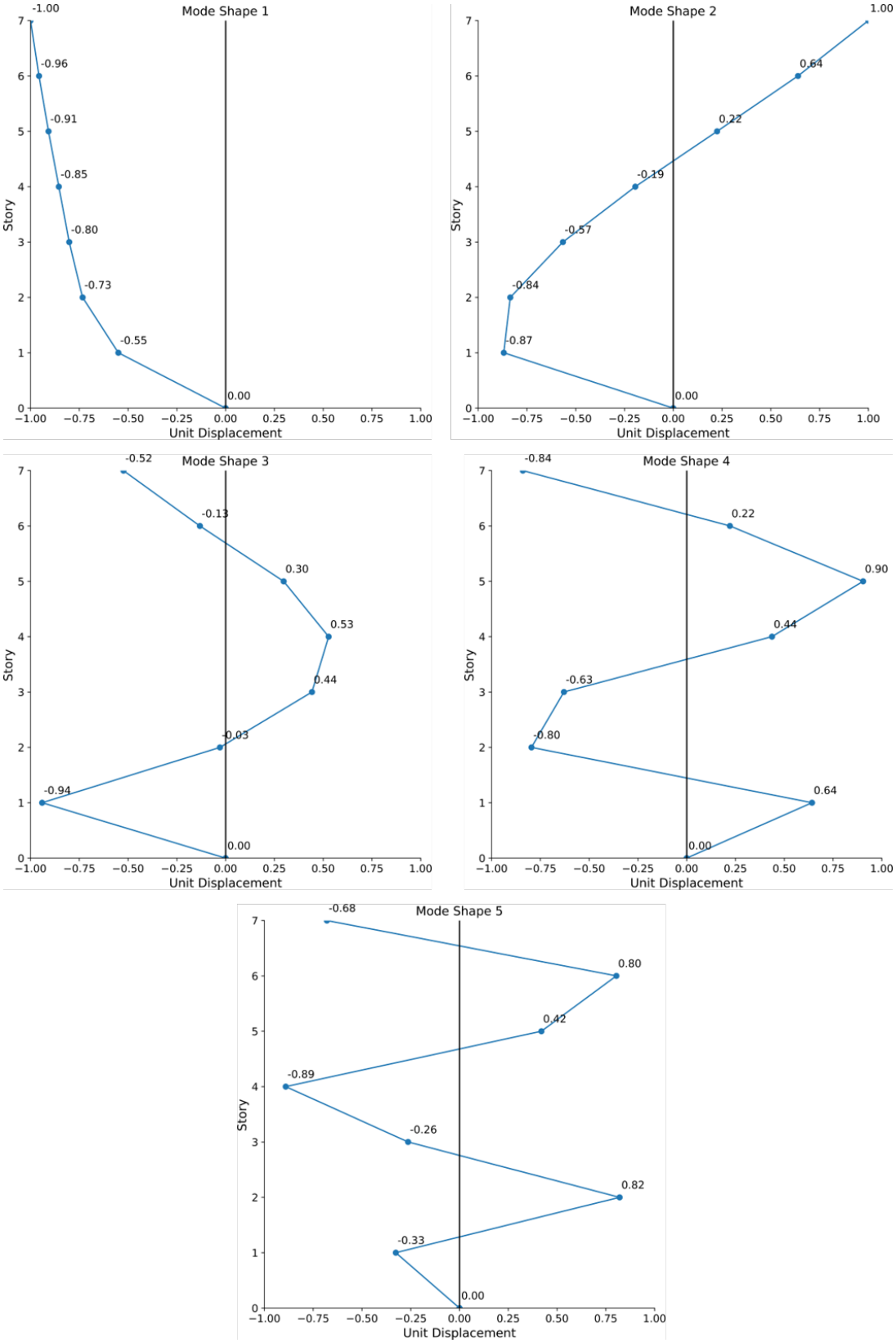


Figure 2.28: Mode Shapes

2.5.3.3 Earthquake Record

One earthquake record was used as input for the ground motion analysis of the structure. It should be noted that Clause 16.2.2 of ASCE 7 (2016) requires that a minimum of 11 ground motions be used to determine structural performance. However, as this study is a simple comparison, only one ground motion record was selected. The record selected is a near field acceleration history for the 1999 Chi-Chi earthquake in Taiwan, the earthquake had a magnitude of 7.62 (Ancheta et al., 2013). The acceleration history used as input into the model can be seen below in Figure 2.29, it is classified as a record that is $74.834s$ long with a maximum acceleration of $0.42g$, the record was applied at a 100% hazard level.

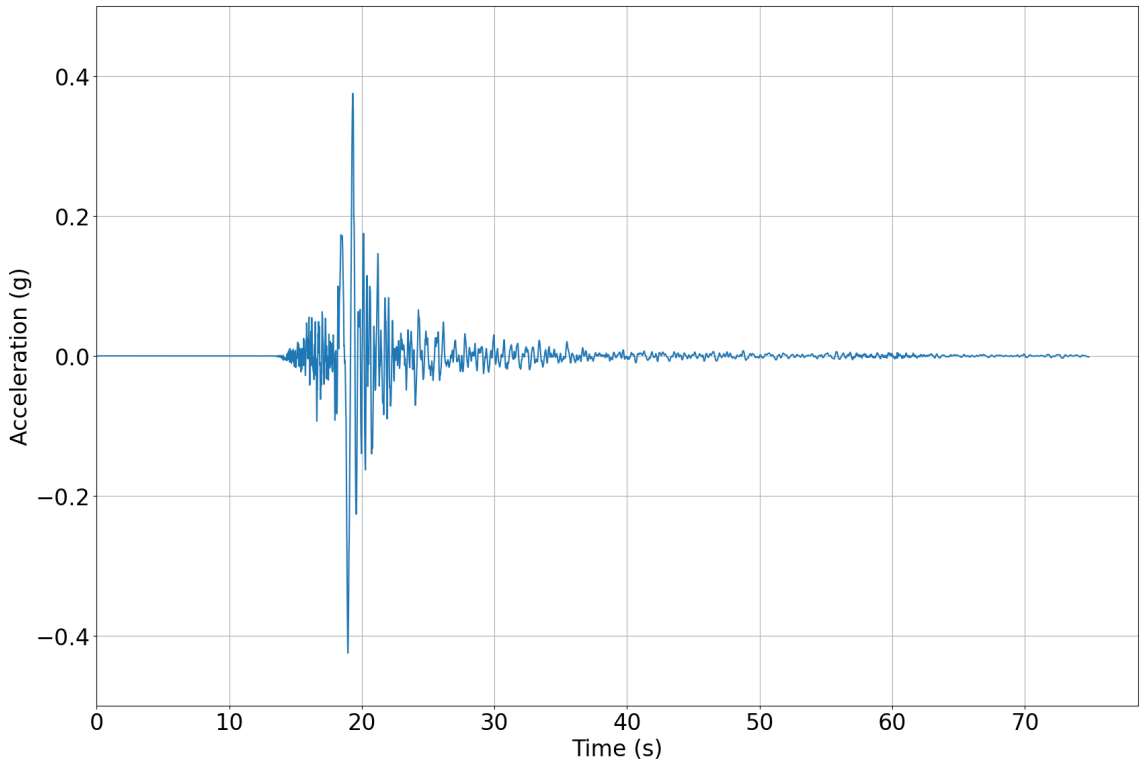


Figure 2.29: Earthquake Ground Motion History

2.5.3.4 Debris Impact Load

The debris impact load was generated by following the guidelines in Clause 6.11.6 of ASCE 7 (2016). This clause outlines the impact force and duration for shipping container impacts. An empty shipping container was used to generate the impact force, the mass of the shipping container was assumed to be $2,300kg$ with a stiffness of $65,300\frac{kN}{m}$ (Aghl et al., 2014). The inundation depth and maximum flow velocity was assumed to be $5.1m$ and $2.5\frac{m}{s}$ respectively, these parameters are taken from aerial and ground surveys after the 2011 Tohoku Tsunami in Japan (Naito et al., 2014). The inundation depth provided the height at which the impact load was applied, which corresponded to the exterior column in frame

one located half-way between the second and third stories. Following these parameters, the impact force was determined to be $969kN$ with an impact duration of $0.012s$, as seen in Figure 2.30.

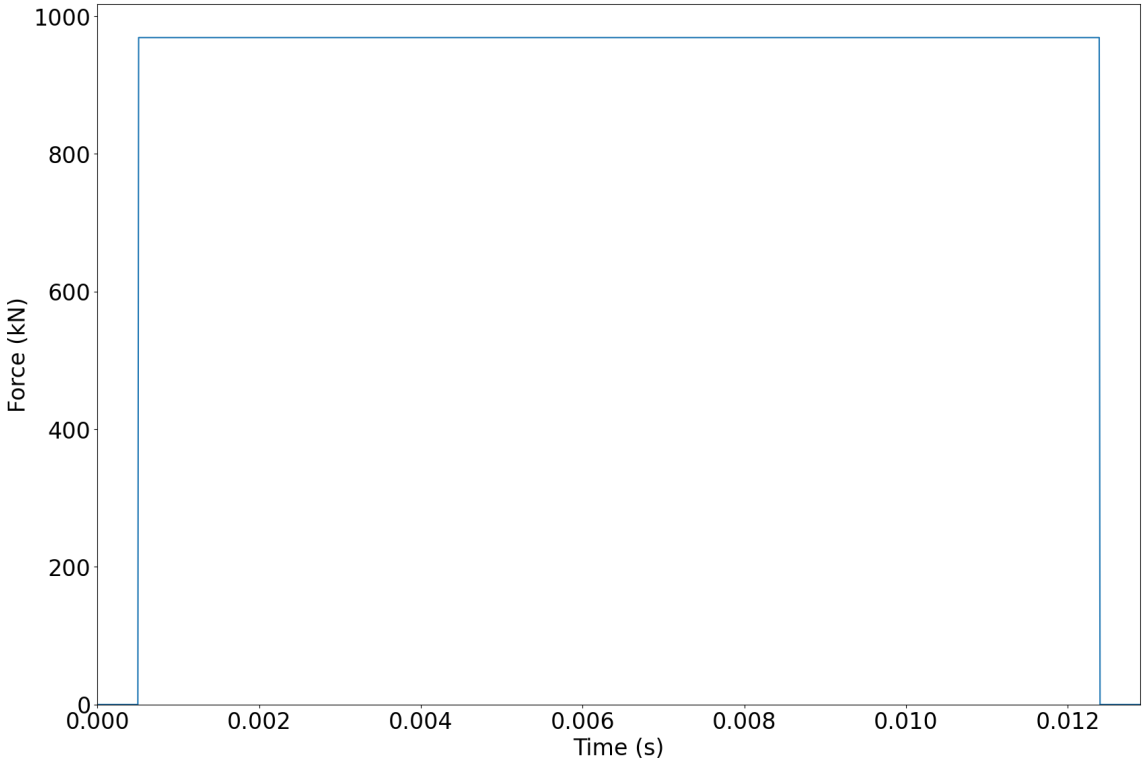


Figure 2.30: Debris Impact Load History

2.5.3.5 Structural Comparison

This section will discuss the comparison between the three loading cases by comparing the exterior column peak and residual displacements.

Peak Column Deflections This section will outline the peak column deflections for the exterior column (left) in frame one. As can be seen below in Figure 2.31, the damaged impact loading scenario resulted in larger peak column displacements when compared to the undamaged impact loading scenario and earthquake scenario. The peak displacement for the damaged loading scenario was $25.13mm$ and the peak displacement for the undamaged impact loading scenario was $8.96mm$. This resulted in an increase of 64% in peak displacements. The peak displacement for the earthquake scenario was $20.61mm$ which is 57% larger than the undamaged impact loading scenario. From these results it can be inferred that a structure that is damaged due to an earthquake and then subjected to a debris impact will display larger peak displacements when compared to the other two loading scenarios.

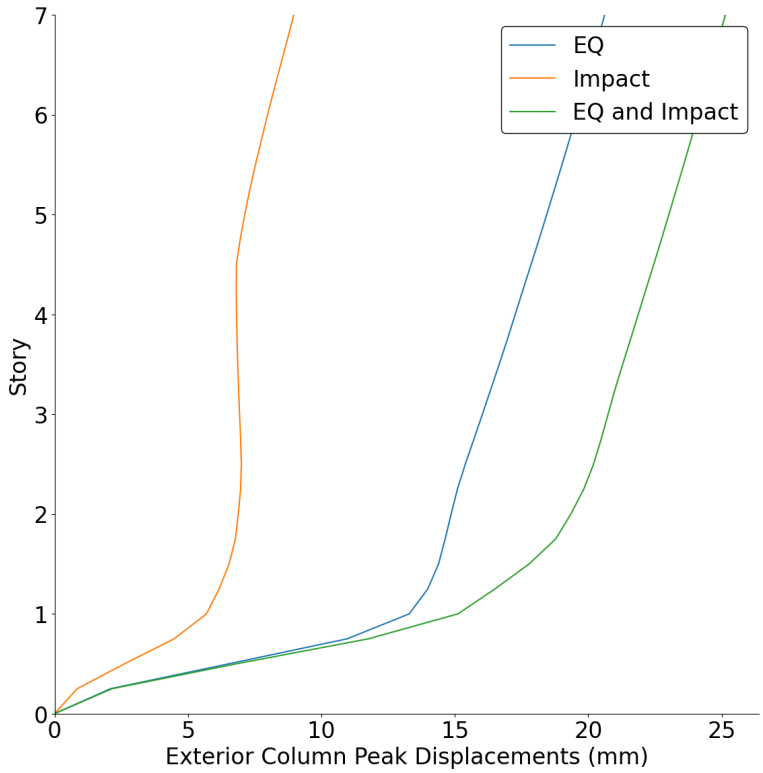


Figure 2.31: Peak Column Displacements

Residual Column Deflections This section will outline the residual column deflections for the exterior column (left) in frame one. As can be seen below in Figure 2.32, the damaged impact loading scenario resulted in larger residual column displacements when compared to the undamaged impact loading scenario and earthquake scenario. The maximum residual displacement for the damaged impact loading scenario was $1.90mm$ and the maximum residual displacement for the undamaged impact loading scenario was $0.55mm$. This resulted in an increase of 71% in residual displacements. The earthquake scenario resulted in a maximum residual displacement of $0.56mm$ which is only 2% larger than the undamaged impact loading scenario. This suggests that a structure that is damaged due to an earthquake and then subjected to a debris impact will result in more damaged members when compared to the undamaged loading scenario and earthquake scenario. Due to the members having a residual displacement, this suggests that these members have been loaded past their elastic capacity, which highlights the importance of including nonlinear material behavior in the model.

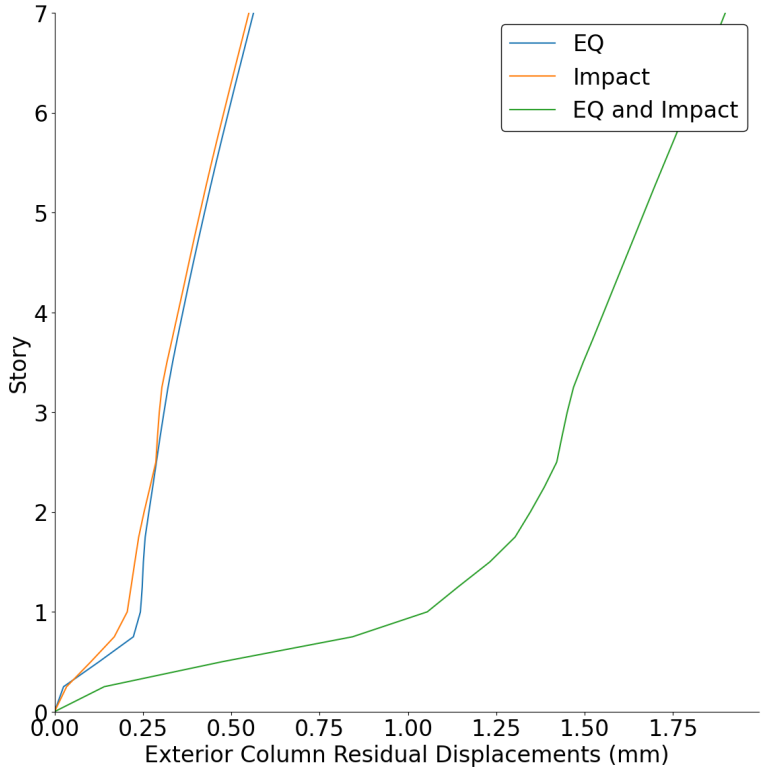


Figure 2.32: Residual Column Displacements

Summary of Comparison Three loading scenarios were investigated to study the importance of including a damage state in the structural model when performing debris impact analysis following Section 6.11 of ASCE 7 (2016). The three loading scenarios considered were: (1) analysing the structure due to an earthquake load, (2) analysing the structure for a debris impact load, and (3) analysing the structure for an earthquake event, keeping the damage history and then subjecting the structure to a debris impact load. These three loading scenarios are denoted as the earthquake scenario, undamaged impact loading scenario and the damaged impact loading scenario.

Observing the first frame exterior column displacements, it can be seen that for both the peak and residual displacements, the damaged impact loading scenario resulted in larger displacements when compared to the undamaged loading scenario and earthquake scenario. Additionally, from the peak displacement figure, it can be inferred that most of the peak displacements occur due to the earthquake load. This is inferred as both of the earthquake loading scenarios resulted in larger peak displacements when compared to the undamaged impact loading scenario. It should also be noted that the residual displacements for both the undamaged impact loading and earthquake scenario are smaller than the damaged impact loading scenario. This suggests that the impact load pushed the member capacity further into the plastic state where smaller force gradients lead to much larger displacements when compared to the elastic state. This suggests that including previous damaged history in a structure when performing debris impact analysis as per Clause 6.11

of ASCE 7 (2016) becomes important for high impact loading events. A final note is that all three loading scenarios resulted in some residual column displacements, which highlights the importance of including elastic-plastic material models when performing debris impact analysis.

To conclude, the damaged impact loading scenario resulted in the structure experiencing larger peak and residual displacements when compared to the undamaged impact loading scenario and the earthquake scenario. This previous damaged history could play a large role in determining if a structure is going to collapse due to a tsunami generated debris impact and hence, should be a key consideration when designing a structure for tsunami loads.

2.5.4 Discussion of Key Points and Limitations of the Review

This section will outline some key points and limitations from the review of the debris impact loads outlined in Chapter 6 of ASCE 7 (2016).

2.5.4.1 Key Points

Key points from the review of debris impact loads are listed below:

1. The standard does not outline any guidelines for when an entire structure should be included in the analysis for debris impact loads or when just a structural member needs to be considered. The standard suggests that for longer impact durations the entire structure should be considered, however, the difference between a short and long impact duration is not defined.

2. Clause 6.11.2 of ASCE 7 (2016) seems to provide an upper-bound impact force when compared to other analytical impact models outlined in the literature.

    - Riggs et al. (2013) provided the largest impact force as the debris stiffness is used and not the lesser of the structure and debris stiffness.

3. A previously damaged structure that is subjected to debris impact loads outlined from Clause 6.11.2 of ASCE 7 (2016) resulted in a structure that experienced much larger peak and residual displacements, when compared to the same structure without previous damage history. This suggests that previous damage history could play a large role in determining if a structure is adequately designed to resist tsunami generated debris impact loads.

2.5.4.2 Limitations

Some limitations of the review mentioned above are outlined below:

1. Only one type of debris and structure combination was used to compare Clause 6.11.2 of ASCE 7 (2016) to other analytical models. More types of debris and structure combinations should be investigated in order to conclude that the standard provides an upper bound solution to the debris impact force.

2. The debris was not explicitly modelled in the nonlinear time history analysis. Only the time history of the force was input into the analysis, which means that any impact force reduction due to debris deformation is not captured (Aghl et al., 2015). The debris would have to be explicitly included as a body in the simulation in order to capture this effect.

2.6 Conclusions

In this report, three different studies were completed: (1) a literature review of debris impact loads, (2) a literature review of structural response to impact loads, and (3) a review of the current design guidelines for debris impacts outlined in Chapter 6 of ASCE 7 (2016).

The first section of this report outlined a review of current literature and code provisions for debris impact loads. Reviewing the literature and code provisions, one of the key limitations is that most of the debris impact equations do not take into account how structural ductility affects the impact load. How structural ductility affects the debris generated impact force becomes important as designing a structure to remain fully elastic under large debris impacts is uneconomical. By taking into consideration the ductility of the structure, smaller impact forces can be designed for, which is the same design philosophy employed in earthquake engineering. Another key aspect of debris impact loads that is typically neglected from literature and code provisions is that debris impacts are not always singular events. In practice, multiple debris impacts can occur at once and over the time span of the tsunami event. Hence, it is important to understand how debris impacts influence the hysteretic performance of the structure. Finally, most debris impact equations do not take into consideration that the impact occurs in water. Additionally, there are contradicting studies on whether it needs to be accounted for. Ko et al. (2015) state that there was a maximum difference in peak impact forces of up to 17% for impacts in-water when compared to in-air impact tests. Stolle et al. (2019) state that this increase in impact forces is typically included by adding a mass term to the impact equation. Conversely, other studies such as Riggs et al. (2013) state that this increase may be negligible for design purposes and the current design standard does not explicitly include an added mass term in the debris impact force formula (Chapter 6 of ASCE 7 (2016)). Further studies should be conducted to determine when including in-water effects are important for the debris impact formula.

The second section of this report outlined a review of current literature on structural response to impact loads. Reviewing the literature, one of the key conclusions noted is that dynamic analysis becomes more important as the impact loading rate increases (Cotsovos et al., 2008). This suggests that as the debris impact velocity increases the

importance of capturing dynamic effects also increases. Another important conclusion is that single-degree-of-freedom (SDOF) models may not be adequate for simulating impact events (Imbeau, 2012). Imbeau (2012) showed that SDOF models are not capable of capturing local member failures and higher mode effects, which suggests that SDOF models can result in an inaccurate structural response to the impact load. Imbeau (2012) also showed that when local member failures such as shear plugs are experienced, the SDOF model is not capable of capturing the additional deformation in the system. Inferring from this information, the conclusion can be made that if local member failures or higher mode effects are expected, then a SDOF model may not be adequate for modelling a debris impact event. This is an important conclusion as Clause 6.11.8 of ASCE 7 (2016) states that a SDOF mass-spring system with nonlinear stiffness can be used to model a structure if the impact is large enough to cause inelastic behavior in the structure. Meaning if a debris impact event is large enough to cause inelastic behavior in the structure, key structural response parameters such as local member failure and higher mode effects will not be captured by the SDOF model and could lead to an inaccurate structural response.

The third section of this report outlined a review of current design guidelines for debris impacts in Chapter 6 of ASCE 7 (2016). One key conclusion made during this review is that the impact formulas outlined in Clause 6.11.2 of ASCE 7 (2016) seem to provide an upper-bound impact force when compared to other analytical models. However, a wide range of varying structural stiffnesses and debris properties would have to be examined in order to say conclusively that Clause 6.11.2 of ASCE 7 (2016) always provides an upper-bound impact force. From the structural analysis section, the conclusion that a damaged structure subjected to a debris impact performs differently then an undamaged structure subjected to a debris impact was made. The study showed that the damaged structure experienced larger peak and residual displacements when compared to the undamaged structure. Concluding that previous hysteretic damage in a structure can play a large role in determining the performance of a structure subjected to tsunami generated debris impact loads.

Chapter 3

Estimating Impact Force Histories[1]

3.1 Objectives and Description of Methodology

The objective of this study is to analyse and compare the validity of three different methods for approximating debris impact force histories, the three methods are: (1) a SDOF method; (2) a MDOF method; and (3) an analytical method based on Clauses 6.11.2 and 6.11.8 of ASCE 7 (2016). By comparing these three different methods the validity of using each method to approximate debris impact force histories can be concluded. The validity of each method will be determined by applying the debris impact force histories for each method to the same MDOF model and comparing the force response from the model to experimental data from Stolle et al. (2019).

3.2 Description of Experimental Data

The experimental data analysed in this study was obtained from Stolle et al. (2019), who performed the experimental program in the Hydraulics Laboratory at the University of Ottawa. The facility houses a dam-break wave flume with a length of $30m$, a width of $1.5m$, and a maximum impoundment depth of $0.7m$. The reservoir of water has a length of $21.55m$, which was impounded behind a swing-gate at various inundation depths for the experimental study of Stolle et al. (2019).

The experimental program consisted of a structural column subjected to dam-break wave-generated debris impact events. The debris used in the experimental study were $1:40$ geometrically scaled $20-ft$ shipping containers constructed of positively buoyant polyethylene with dimensions of $0.06 \times 0.06 \times 0.15m$, a wall thickness of $0.005m$, and a mass of $0.236kg$. The structure used in the experimental study had a square hollow cross-section which was constructed from acrylic with dimensions of $0.20 \times 0.20 \times 0.80m$ and a wall thickness of $0.005m$.

[1]This Chapter forms a portion of a manuscript being prepared for submission to the Journal of Structural Engineering.

From the experimental study, the modulus of elasticity of the structure was determined to be $2.50GPa$. Other parameters required for the numerical modelling of the structure are the mass density of the structure, Poisson's ratio, and the shear coefficient. As these parameters were not provided in the experimental study, the ANSYS GRANTA material selector (ANSYS®, 2018) was used to define these parameters. The mass density of the structure was assumed to be $1200kg/m^3$ with a Poisson's ratio of 0.375 for an acrylic structure, and the shear coefficient was assumed to be equal to 0.50 for a thin walled hollow cross section. Key parameters that were recorded during the experimental program included the following:

- Water surface elevation of the dam-break wave.
  - The water surface elevation provided the elevation at which the debris impacted the structure.
- Force response of the structure due to the combined wave and debris impact. The force in the y-direction extracted from the 6-axis force-torque transducer was used for this study, this force is a measurement of the base shear force.
- Debris impact velocity.

Stolle et al. (2019) processed the force response data signal of the structure to remove components associated with instrument noise and hydrodynamic loads using the EEMD method (Huang et al., 1998). The filtered force signal represents the structures response only attributed to the debris impact load. An example of the filtered force signal can be seen below in Figure 3.1. Further information on the experimental program can be found in Stolle et al. (2019).

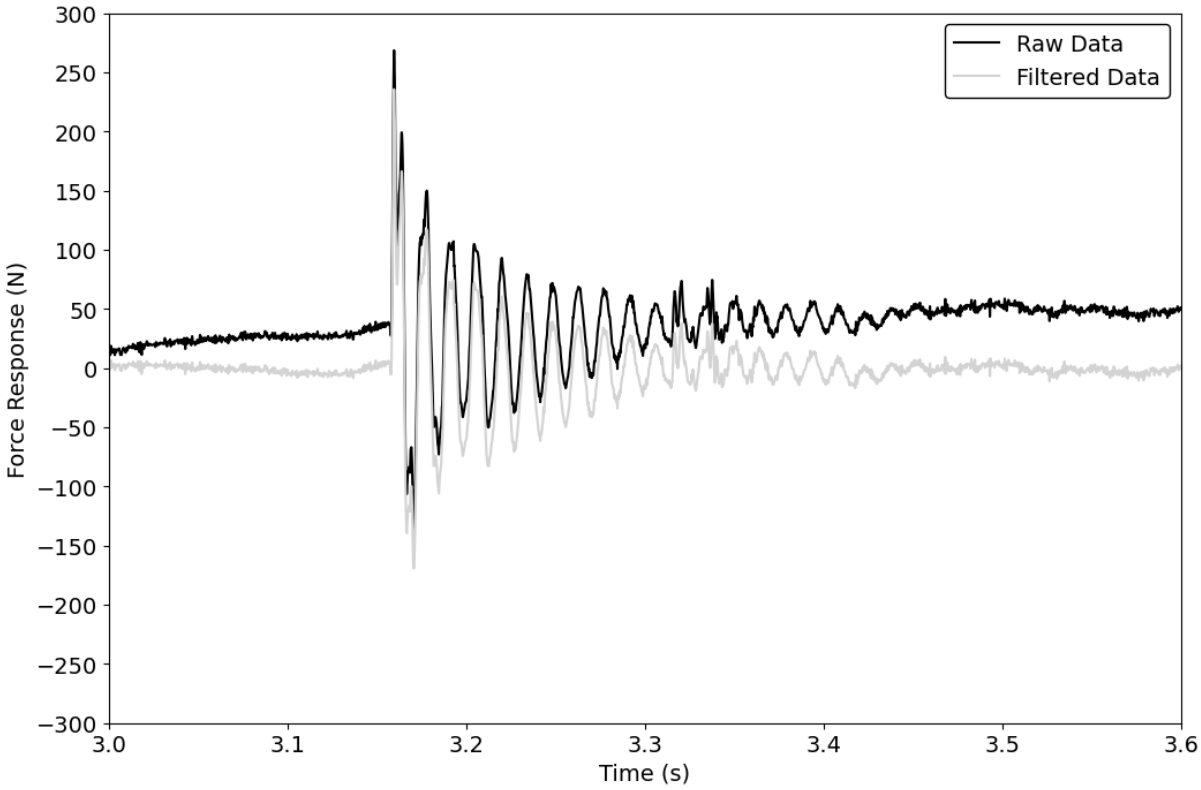


Figure 3.1: Example Force Response History

A total of 22 experiments were analysed in this study from the experimental data set of Stolle et al. (2019). The selection involved removing experiments with bad data, which was defined as experiments where the force response data did not present any obvious impact event. Secondly, experiments where multiple impacts occurred in a very short period of time were removed, as the goal was to extract the initial impact force and not impact forces due to high frequency pounding events. Finally, only single-debris impact events generated from an inundation depth of $0.40m$ were considered, as ASCE 7 (2016) does not provide any guidance for multiple-debris impact events.

This force response data set was then used to estimate the debris impact force through the use of a SDOF method and a MDOF method. In order to estimate the debris impact force through either of these methods, a fit was performed which estimated the impact magnitude and duration by calculating the force response of the system and varying these parameters until difference between the numerical and experimental force response was minimized. Further details on each fitting algorithm are presented in Sections 3.4 and 3.5. Furthermore, the fitting algorithm was performed for five impact shapes defined in Section 3.3 to determine which impact shape resulted in the best fit to the experimental data.

Duhamel's integral was used as the SDOF method to model the force response of the debris impact event. Whereas, Newmark's constant acceleration method was used as the MDOF method to model the force response. Two methods were investigated as Duhamel's

integral provides a general result for evaluating the response of a linear SDOF system to an arbitrary force. Whereas, Newmark's method can be used to evaluate the response of a SDOF or a MDOF system to an arbitrary force. By comparing these two methods the validity of using a SDOF method to estimate debris impact forces can be determined. Furthermore, debris impact histories were generated by following Clauses 6.11.2 and 6.11.8 of ASCE 7 (2016) which outline the debris impact magnitude, duration, and shape. Clauses 6.11.2 and 6.11.8 of ASCE 7 (2016) were investigated to provide a comparative on how Chapter 6 of ASCE 7 (2016) holds up against alternative methods for estimating debris impact loads, which is crucial for understanding the limitations outlined in Chapter 6 of ASCE 7 (2016) for estimating debris impact forces.

3.3 Impact Forcing Functions

As part of this study, five different impact shapes were used in the fitting algorithms outlined in Sections 3.4 and 3.5 to investigate which impact shape resulted in the best approximation of the experimental force response data. The five different impact shapes that were investigated are: (1) Half-Sine; (2) Rectangular; (3) Triangular; (4) Trapezoidal; and (5) Parabolic. How each forcing function was developed is presented in Sections 3.3.1, 3.3.2, 3.3.3, 3.3.4, and 3.3.5.

3.3.1 Half-Sine Impact Shape

The first forcing function was assumed to be a half-sine varying function which peaks at half the impact duration. A half-sine function was used as full-scale in-air impact tests of shipping containers completed by Aghl et al. (2014) showed that the impact history was similar to a half-sine wave. The forcing history is a function of the impact force, impact duration, and the impact time as shown below:

$$p(\tau) = \begin{cases} F_i \sin \frac{\pi}{t_d}\tau & \tau \leq t_d \\ 0 & t_d < \tau \leq t \end{cases}$$

3.3.2 Rectangular Impact Shape

The second function was assumed to be a rectangular pulse varying function based on the requirements of Clause 6.11.8 of ASCE 7 (2016). This forcing history is a function of the impact force and the impact time as shown below:

$$p(\tau) = \begin{cases} F_i & \tau \leq t_d \\ 0 & t_d < \tau \leq t \end{cases}$$

3.3.3 Triangular Impact Shape

The third function was assumed to be a triangular pulse varying function which peaks at half the impact duration. This impact shape results in a quicker rise time to the peak impact force when compared to the half-sine impact shape. Additionally, this impact shape results a smaller amount of impulse being added into the system when compared to the half-sine impact shape. This forcing history is a function of the impact force, impact duration, and the impact time as shown below:

$$p(\tau) = \begin{cases} \frac{2F_i}{t_d}\tau & \tau \leq \frac{t_d}{2} \\ \frac{-2F_i}{t_d}(\tau - t_d) & \frac{t_d}{2} < \tau \leq t_d \\ 0 & t_d < \tau \leq t \end{cases}$$

3.3.4 Trapezoidal Impact Shape

The fourth function was assumed to be a trapezoidal pulse varying function which peaks at one-third the impact duration, at which point it is constant at the peak impact force, and then starts to linearly decrease back to zero at two-thirds the impact duration. This impact shape provides a middle ground between the half-sine and rectangular impact shapes. This forcing history is a function of the impact force, impact duration, and the impact time as shown below:

$$p(\tau) = \begin{cases} \frac{3F_i}{t_d}\tau & \tau \leq \frac{t_d}{3} \\ F_i & \frac{t_d}{3} < \tau \leq \frac{2t_d}{3} \\ \frac{-3F_i}{t_d}(\tau - t_d) & \frac{2t_d}{3} < \tau \leq t_d \\ 0 & t_d < \tau \leq t \end{cases}$$

3.3.5 Parabolic Impact Shape

The fifth function was assumed to be a parabolic pulse varying function which peaks at half the impact duration. This impact shape results in a slower rise time to the peak impact force when compared to the half-sine impact shape. Additionally, this impact shape results a larger amount of impulse being added into the system when compared to the half-sine impact shape. This forcing history is a function of the impact force, impact duration, and the impact time as shown below:

$$p(\tau) = \begin{cases} \frac{-4F_i}{t_d^2}(\tau)(\tau - t_d) & \tau \leq t_d \\ 0 & t_d < \tau \leq t \end{cases}$$

3.4 Single-Degree-of-Freedom Method

Duhamel's integral was used to resolve the force response history of a SDOF system subjected to an arbitrary forcing history (Chopra, 2017). Duhamel's integral is a function of the stiffness of the structure, the mass of the structure, the damped natural circular frequency of the structure, the time elapsed since impact, time, the impact forcing function, and the impulse response of the SDOF system as shown below:

$$R(t) = \frac{k_s}{m_s \omega_d} \int_0^t p(\tau) * h(t-\tau)\, d\tau \tag{3.1}$$

The impulse response of the system is defined as a function of the damping ratio, damped and undamped natural frequencies, time, and the elapsed time since impact:

$$h(t-\tau) = e^{-\xi\omega_n(t-\tau)} \sin \omega_d (t-\tau) \tag{3.2}$$

Substituting Eq. 3.2 into Eq. 3.1 results in the following equation for the force response of a SDOF system subjected to an arbitrary loading history:

$$R(t) = \frac{k_s}{m_s \omega_d} \int_0^t p(\tau)\, e^{-\xi\omega_n(t-\tau)} \sin \omega_d (t-\tau) d\tau \tag{3.3}$$

The solution to Duhamel's integral follows an iterative procedure where the integral is evaluated by using an incremental summation over time as outlined in Navaratnam et al. (2013) and presented in Appendix C.1. The solution of Duhamel's integral represents the force response of the system, this force response was optimized to fit the experimental force response data from Stolle et al. (2019). The Duhamel integral was fit to the experimental force response data by minimizing the difference between the measured and modelled data. This was achieved by iteratively estimating the impact magnitude, impact duration, damping coefficient, structural stiffness, and natural frequency of the structure. The impact loading history used in this method was determined by selecting the impact shape that resulted in the smallest root-mean-squared-error (RMSE) when fitting the numerical result to the experimental as presented in Section 3.4.1. The RMSE was calculated by the following formula as per Stolle et al. (2019):

$$RMSE = \frac{\sqrt{\frac{\sum_{i=1}^{n}(F_{exp}-F_{mod})^2}{n}}}{F_{max}} \tag{3.4}$$

Where:

- n = Number of data points
- F_{exp} = Experimental force response (shear force from 6-axis force-torque transducer)
- F_{mod} = Modelled force response (shear force)

- F_{max} = Maximum experimental force response value

Stolle et al. (2019) stated that the natural frequency of the structure was measured using impact hammer tests and a natural frequency of $70Hz$ ($\pm 2.2Hz$) was determined. The authors also stated that the stiffness of the structure was estimated to be $4.685 \times 10^5 \frac{N}{m}$ with lower and upper bounds of $4.653 \times 10^5 \frac{N}{m}$ and $4.701 \times 10^5 \frac{N}{m}$. These values provided upper and lower bounds for both the natural frequency and the structural stiffness in the fitting algorithm. Stolle et al. (2019) also estimated a damping coefficient of 0.045, however, the water depth around the structure can influence the damping of the structural response (Oumeraci et al., 1993) and hence an error bar of ± 0.005 was assumed. The process diagram for solving Duhamel's integral and fitting it to the experimental data can be seen below in Figure 3.2. The fitting procedure was done using the *LMFIT* package in Python, which is a package for non-linear optimization and curve fitting problems (Newville et al., 2020). The fitting routine read in the measured force response data, assumed initial values for the fitting parameters, solved Duhamel's integral to obtain the modelled force response, calculated the RMSE, and then optimized the fitting parameters using non-linear least-squares minimization until the RMSE was less than $1e^{-7}N$. For the initial fitting values used in the algorithm, the initial impact force was always assumed to be equal to the maximum measured force response for the measured force response history that the model was being fit to. The initial impact duration was assumed to be equal to $0.005s$ and both the impact force and duration did not have upper or lower bounds. The initial values used for the damping coefficient, natural frequency, and structural stiffness were 0.045, $70Hz$, and $4.685 \times 10^5 \frac{N}{m}$ respectively. Furthermore, the influence that the impact shape has on the fitting algorithm is presented in Section 3.4.1.

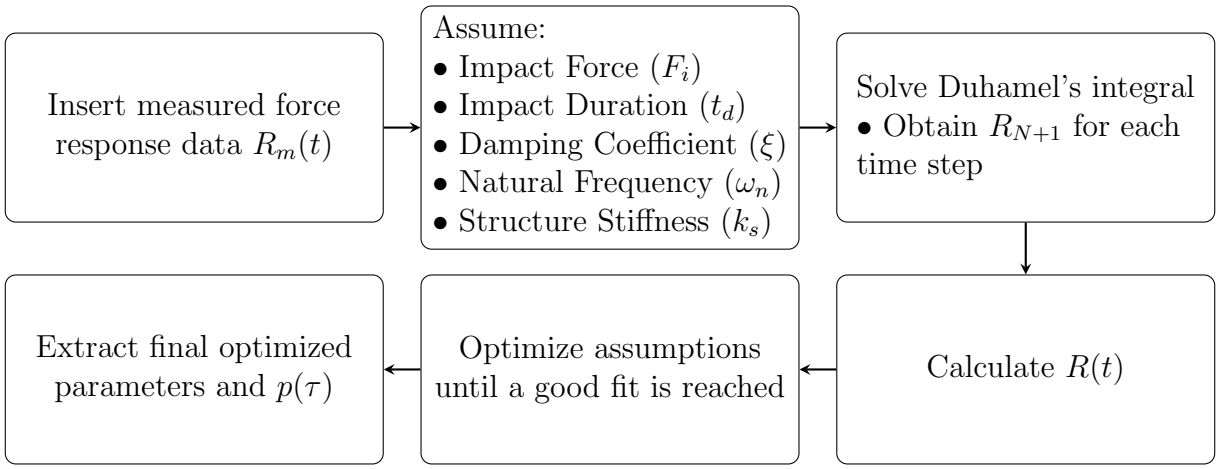


Figure 3.2: Duhamel Integration Process

3.4.1 SDOF Impact Shape Study

One of the key assumptions in the fitting algorithm is the shape of the impact history. The influence that the impact shape has on the fitting algorithm was investigated by calculating

the RMSE following Eq. 3.4 for all 22 experimental data points and the five impact shapes outlined in Section 3.3. The impact shape that resulted in the smallest average RMSE over the entire data set was concluded to be the impact shape that resulted in a force response that best fit the experimental data.

Figure 3.3 presents the force response resulting from the fitting algorithm for one experimental data point. The figure outlines the fitting results for all five impact shapes and compares them to the experimental force response. From Figure 3.3, the impact shape has the largest influence on the initial peak of the force response, after the initial peak the influence of the impact shape diminishes as the structure is in a free-vibration response. Furthermore, it is clear from Figure 3.3 that the SDOF fitting method is not capable of capturing the dual peak behavior present in the experimental data and therefore, is not capable of capturing the peak force response of the system. This is because the dual peak behavior is associated with higher mode effects, which a SDOF method cannot capture.

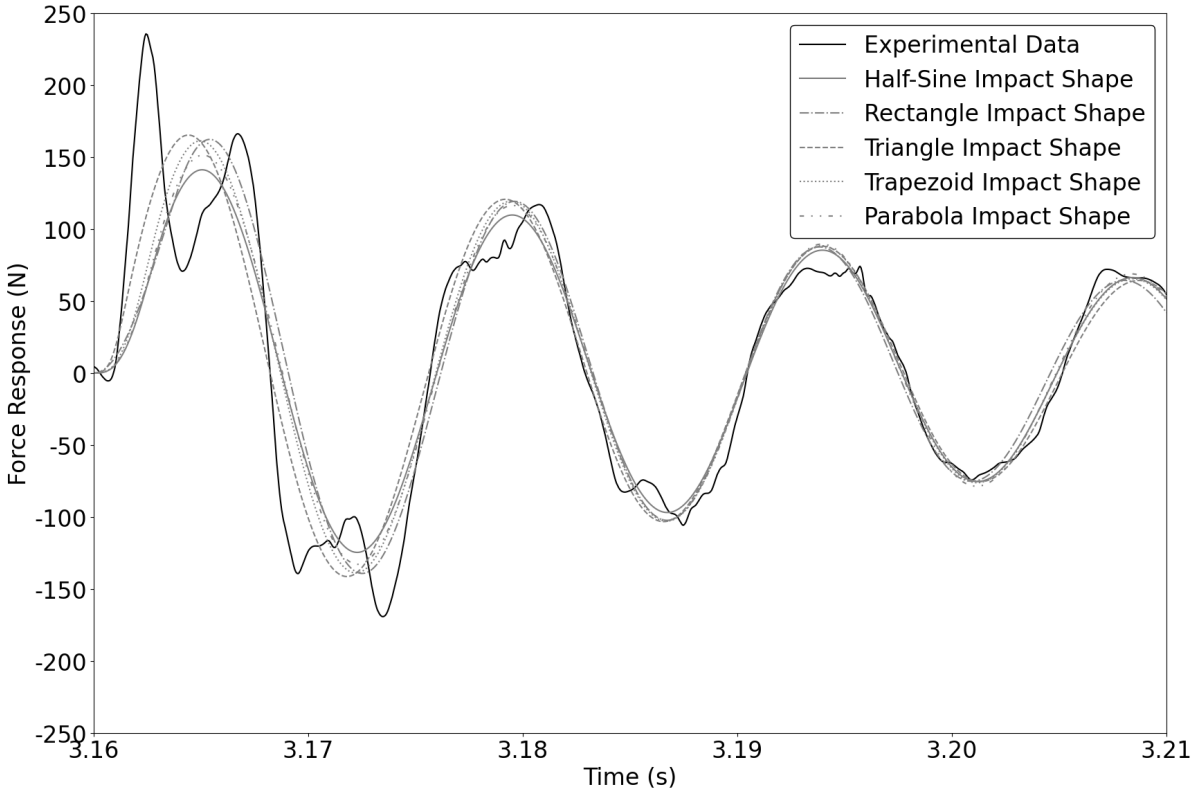


Figure 3.3: Example Force Response for SDOF Fitting

After the fitting algorithm is complete, the impact force histories that developed the fitted force responses are extracted. Figure 3.4 presents the impact force histories that developed the force responses outlined in Figure 3.3. From Figure 3.4, it is apparent that the fitting algorithm produced different impact force histories for each impact shape. A trend that is visible in Figure 3.4 is that as the impact duration increases, the impact magnitude decreases, which suggests that the total impulse into the system for each impact

shape should be similar. The impulse for each impact shape is shown on Figure 3.4 where it can be seen that the impulse for the triangular, trapezoidal, and parabolic impact shapes is similar, with a maximum difference of $0.07Ns$. The half-sine impact shape resulted in the smallest impulse, while the rectangular impact shape resulted in the largest impulse. Observing both Figures 3.3 and 3.4, it is apparent that the experimental force response can be modelled with significantly different impact histories if a SDOF model is used.

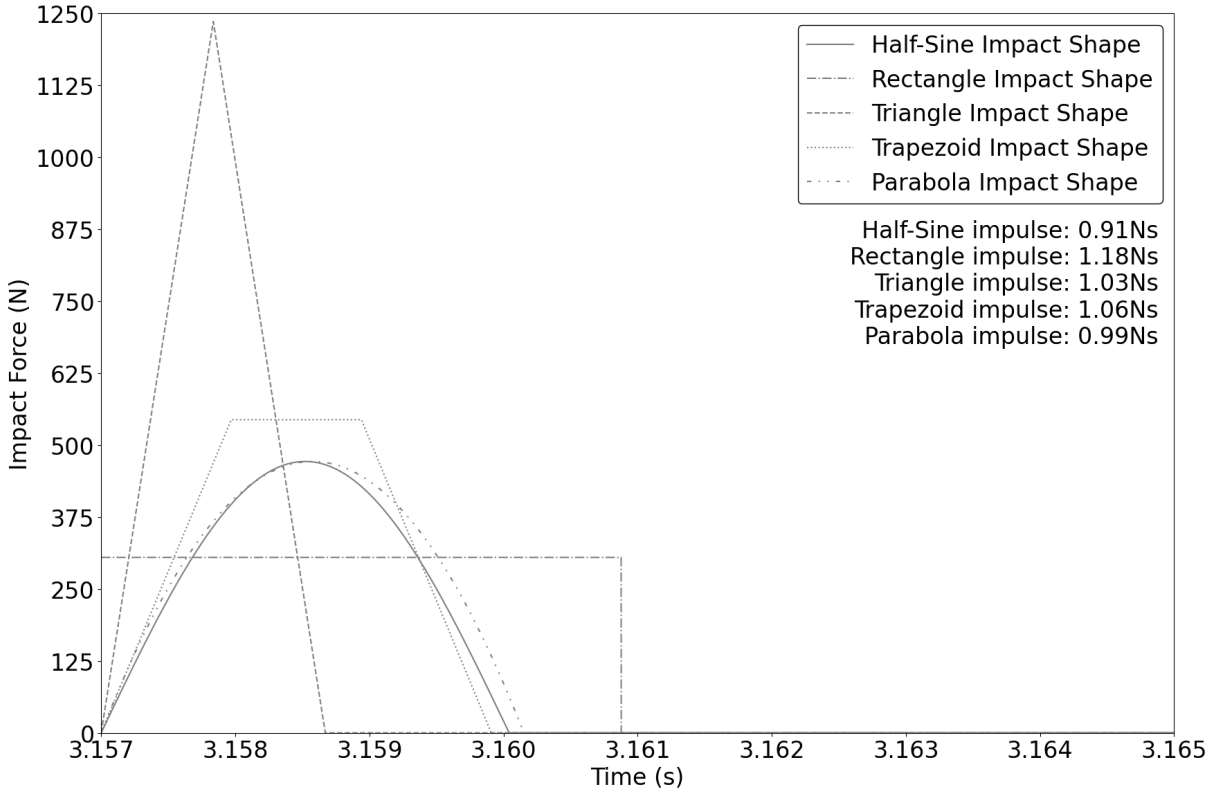


Figure 3.4: Example Impact History from SDOF Fitting

Extending the analysis to all 22 experimental data points, a suite of impact force history curves can be developed for each impact shape. Figures 3.5, 3.6, 3.7, 3.8, and 3.9 present the impact force histories for the half-sine, rectangular, triangular, trapezoidal, and parabolic impact shapes. Furthermore, Table 3.1 presents a summary table of the fitting results for each impact shape. From these figures, the conclusion can be made that the impact shape used in the fitting algorithm has a significant influence on the impact force histories developed.

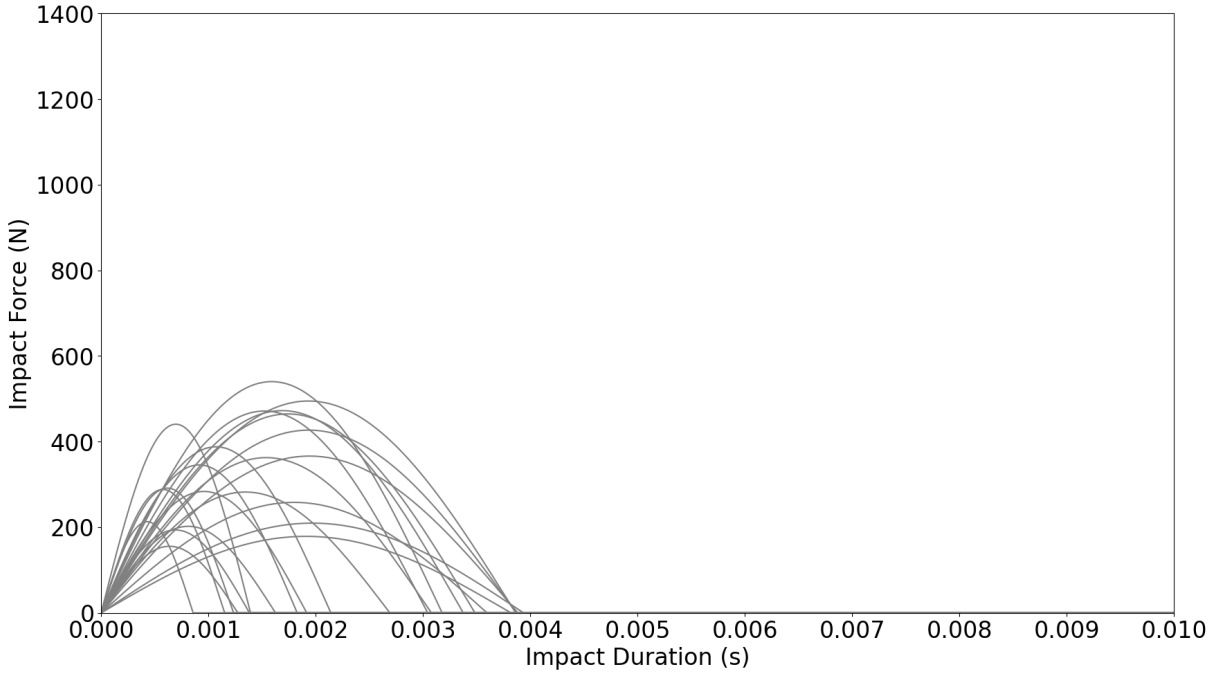


Figure 3.5: SDOF Fitting Half-Sine Impact Histories

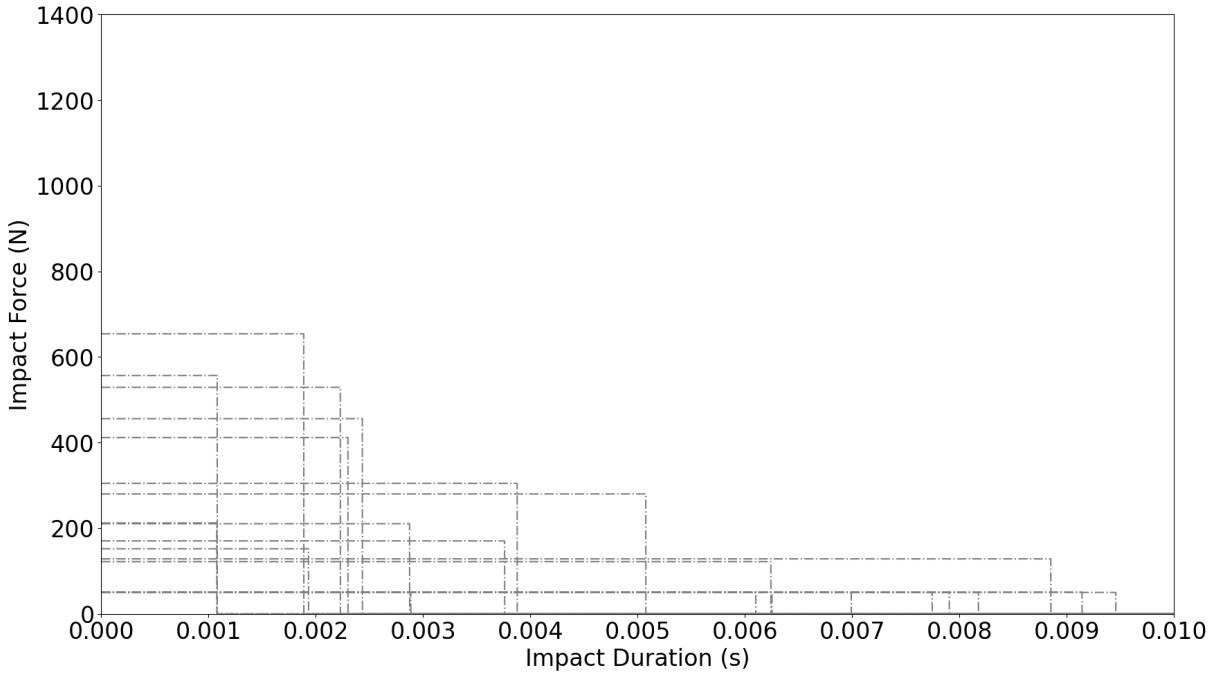


Figure 3.6: SDOF Fitting Rectangle Impact Histories

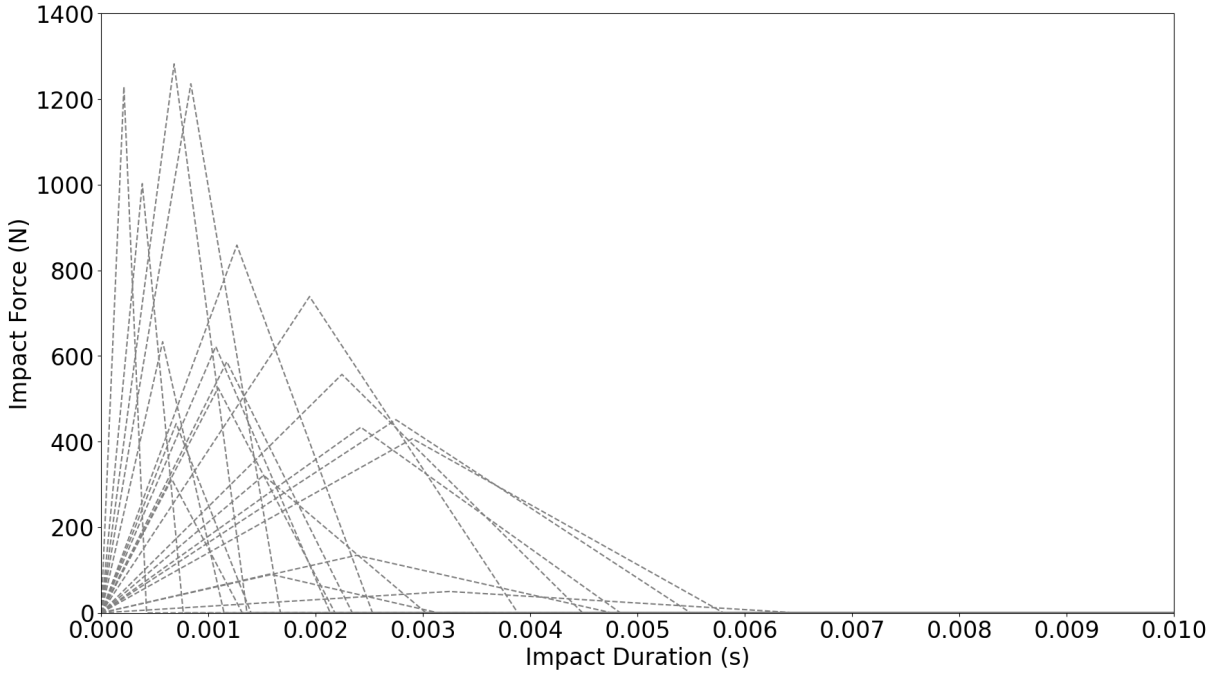


Figure 3.7: SDOF Fitting Triangle Impact Histories

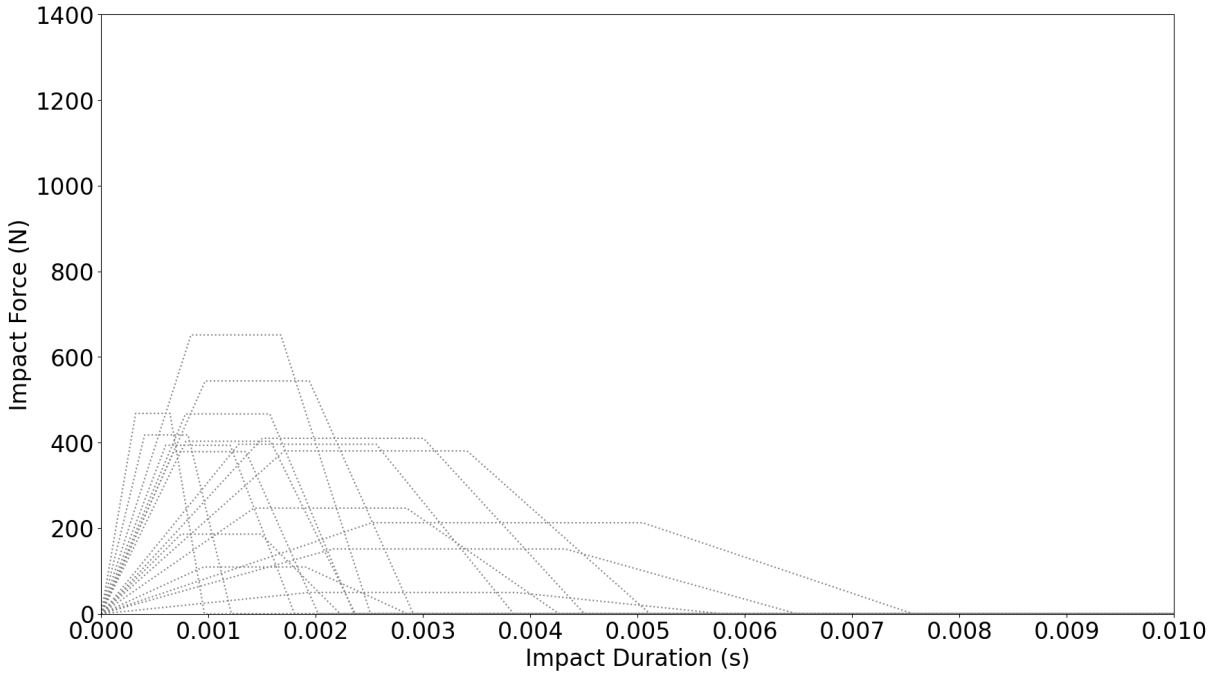


Figure 3.8: SDOF Fitting Trapezoid Impact Histories

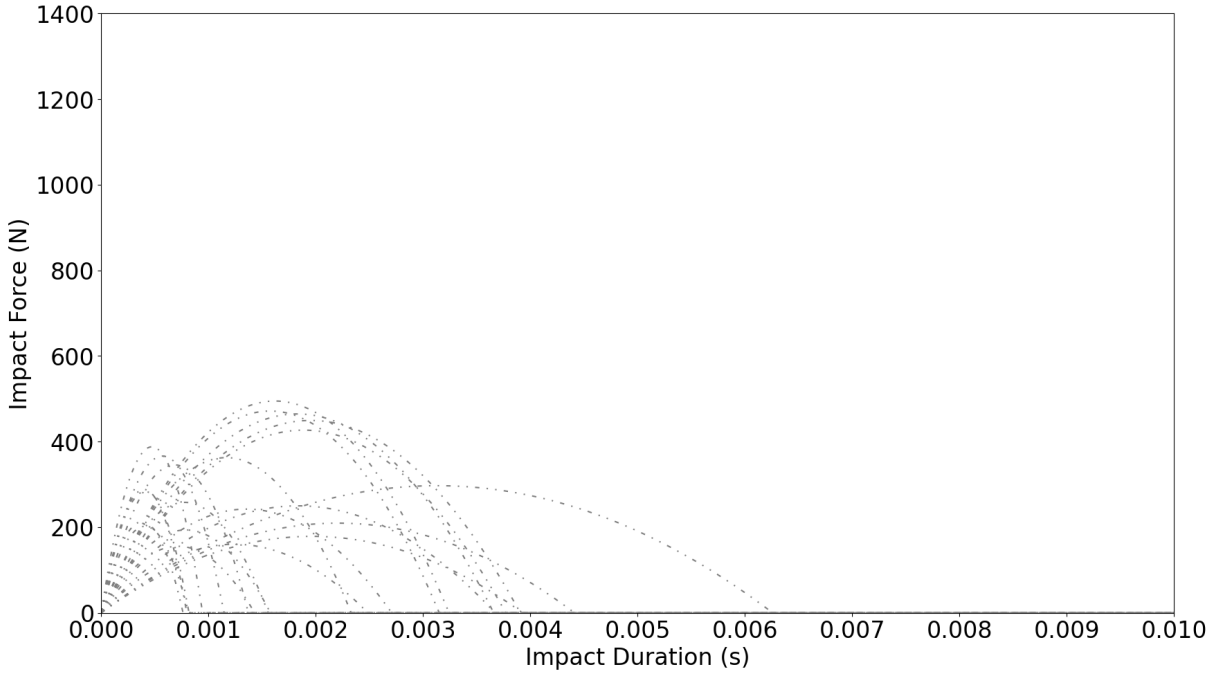


Figure 3.9: SDOF Fitting Parabola Impact Histories

Table 3.1 outlines the mean and standard deviation of the impact magnitude, impact duration, impulse, and the RMSE. Observing the mean and standard deviation of the impact magnitudes for all impact shapes, it is can be seen that there is a wide range of impact magnitudes that change depending on the impact shape. This further supports the conclusion that the experimental force responses can be modelled with a wide range of significantly different impact force histories when a SDOF model is used. Additionally, there is also a wide range in both the impact durations and impulses which highlights the variability of the impact force histories developed using the SDOF method. Observing the RMSE, the half-sine impact shape resulted in the smallest mean and standard deviation of the RMSE, with the parabolic impact shape providing the second smallest. This result implies that the half-sine impact shape resulted in force responses that best fit the experimental data.

Impact Shape	Magnitude (N)		Duration (s)		Impulse (Ns)		RMSE	
	Mean	Std.	Mean	Std.	Mean	Std.	Mean	Std.
Half-Sine	333.16	114.10	0.0026	0.0011	0.58	0.35	0.14	0.02
Rectangle	210.98	188.68	0.0049	0.0028	0.66	0.38	0.21	0.10
Triangle	595.75	358.77	0.0030	0.0018	0.69	0.41	0.15	0.06
Trapezoid	345.24	156.47	0.0035	0.0018	0.69	0.36	0.16	0.06
Parabola	304.64	106.66	0.0025	0.0015	0.53	0.39	0.14	0.03

Table 3.1: SDOF Fitting Results

Figure 3.10 outlines how the maximum force responses developed by the SDOF model

compare to the maximum experimental force responses. From this figure, the conclusion can be made that the SDOF model underestimates the maximum experimental force response for all impact shapes. This is because the SDOF model is not capable of capturing higher mode effects, which cause peaks in the experimental force response as shown in Figure 3.3.

Another metric for assessing which impact shape resulted in the best fit to the experimental data is the coefficient of determination (R^2). The coefficient of determination takes a value from zero to one, meaning a R^2 of one for this analysis implies that the maximum force responses from the SDOF model exactly predict the maximum force responses from the experimental data. The coefficients of determination for all five impact shapes are as follows:

- Half-Sine: $R^2 = 0.71$
- Rectangle: $R^2 = 0.47$
- Triangle: $R^2 = 0.69$
- Trapezoid: $R^2 = 0.67$
- Parabola: $R^2 = 0.61$

Based on the mean RMSE and the coefficient of determination, the conclusion was made that the half-sine impact shape resulted in forces responses that best fit the experimental data when compared to all other impact shapes investigated in this study.

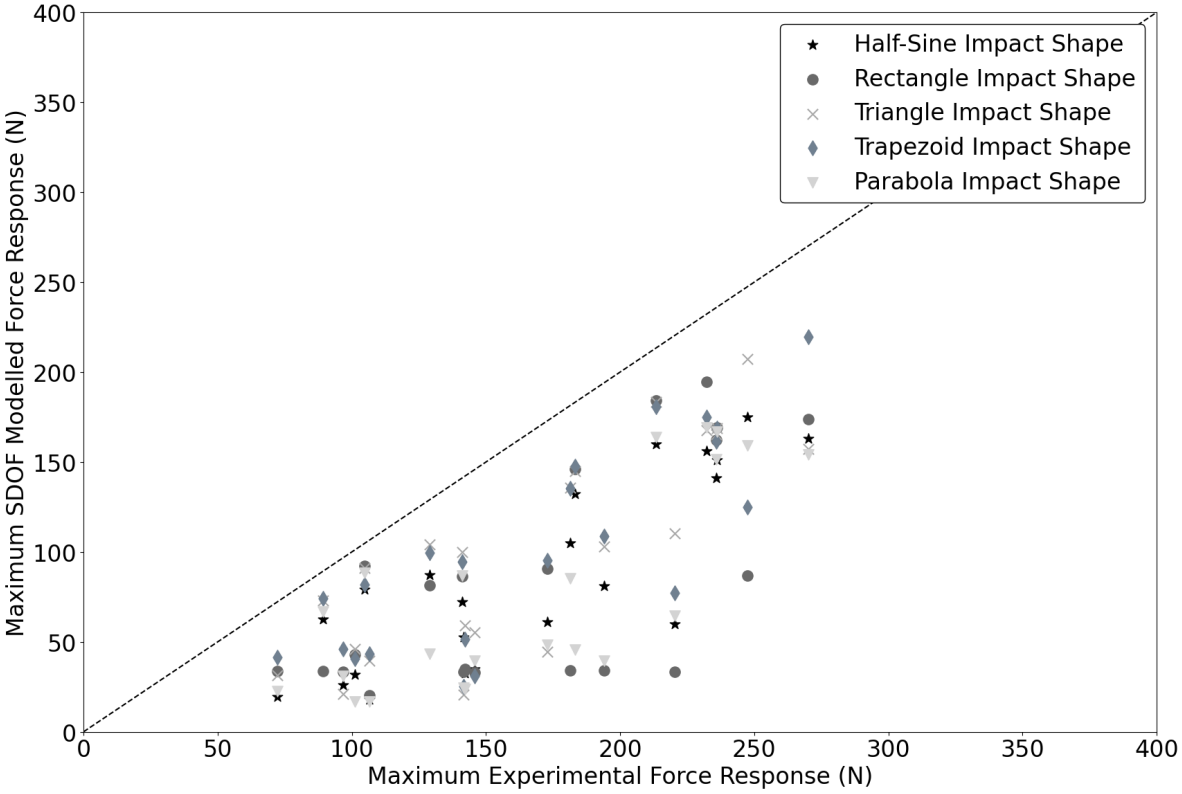


Figure 3.10: SDOF Fitting Maximum Force Response Comparison

3.5 Multiple-Degree-of-Freedom Method

Newmark's constant average acceleration method was used to resolve the force response history of a MDOF system subjected to an arbitrary forcing history. This was done by solving the equation of motion in the time domain. The equation of motion is a function of the mass matrix ($[m]$), damping matrix ($[c]$), stiffness matrix ($[k]$), acceleration vector ($\{\ddot{u}\}$), velocity vector ($\{\dot{u}\}$), displacement vector ($\{u\}$), and the impact forcing function as shown below:

$$[m]\{\ddot{u}\} + [c]\{\dot{u}\} + [k]\{u\} = \{p(t)\} \tag{3.5}$$

Generically, Newmark's method for solving the equation of motion is an implicit time integration scheme meaning, the solution at time $i+1$ is determined from the equilibrium condition at time $i+1$. However, for linear systems, Newmark's original formulation can be modified to directly solve the equation of motion without iterations. Chopra (2017) presents the direct time history integration solution algorithm as it would be implemented on a computer. Furthermore, the solution algorithm as implemented in this study is presented in Appendix C.2. For the analysis in this study the constant average acceleration method was chosen as this method provides an unconditionally stable solution (Chopra,

2017). The structure in Stolle et al. (2019) was chosen to be modelled as a cantilevered beam and used as input into Newmark's method, the stiffness, mass, and damping matrices were defined. The choice to model the column as beam-elements was decided as Stolle et al. (2018a) showed that the force response during experimental debris impacts was governed by shear loading.

Following the development of the mass, stiffness, and damping matrices a similar fitting procedure to that outlined in the SDOF method was followed. The model shear time history response at the force transducer location outlined in Stolle et al. (2019) was fit to the experimental force response data by minimizing the difference between the measured and modelled data as outlined in Section 3.4. For the MDOF analysis this fitting was completed by varying the impact force and impact duration; the mass, stiffness, and damping matrices were all held constant. The initial impact force and duration were selected to be same values used in the SDOF fitting procedure as outlined in Section 3.4. As outlined in the SDOF method, the influence of the impact shape on the fitting results was evaluated for the MDOF method and is presented in Section 3.5.6. Furthermore, the impact shape was selected based on the impact shape that resulted in the smallest RMSE when fitting the numerical result to the experimental. As outlined in the SDOF method, the RMSE was calculated by following Eq. 3.4. The process diagram for solving the MDOF system and fitting it to the experimental data can be seen below in Figure 3.11.

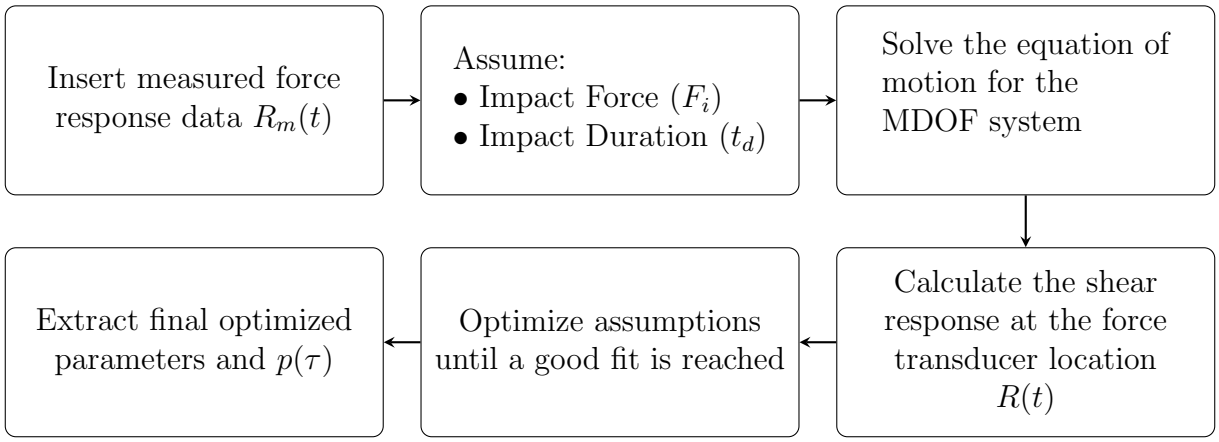


Figure 3.11: MDOF Solver Process

3.5.1 Mass Matrix Formulation

Using beam-elements the mass matrix can be formed through two methods: (1) the lumped-mass matrix; and (2) the consistent-mass matrix. The lumped-mass matrix is a method for defining the mass matrix of a beam element for which the rotational degrees-of-freedom (DOFs) are ignored. Whereas, the consistent-mass matrix is a method for defining the mass matrix of a beam element for which the inertial effects associated with the rotational DOFs are included. The formulation of the local mass matrix for a 2-node beam element using the lumped-mass matrix and the consistent-mass matrix approaches are presented in

Eq. 3.6 and Eq. 3.7, respectively. In order to determine which mass matrix to use for the dynamic analysis the influence of the mass rotational DOFs on the response of the beam was investigated.

$$[m] = \frac{\rho AL}{2} \begin{bmatrix} 1 & 0 & 0 & 0 \\ 0 & 0 & 0 & 0 \\ 0 & 0 & 1 & 0 \\ 0 & 0 & 0 & 0 \end{bmatrix} \tag{3.6}$$

$$[m] = \frac{\rho AL}{420} \begin{bmatrix} 156 & 22L & 54 & -13L \\ 22L & 4L^2 & 13L & -3L^2 \\ 54 & 13L & 156 & -22L \\ -13L & -3L^2 & -22L & 4L^2 \end{bmatrix} \tag{3.7}$$

The influence of the mass rotational DOFs on the response of the column was determined by applying a dynamic load to the free-end of the column with a magnitude of $500N$ and a duration of $0.0005s$, as shown in Figure 3.12. The influence of the mass rotational DOFs was determined by comparing the shear, moment, and deflection responses of the column using either the lumped or consistent mass matrix.

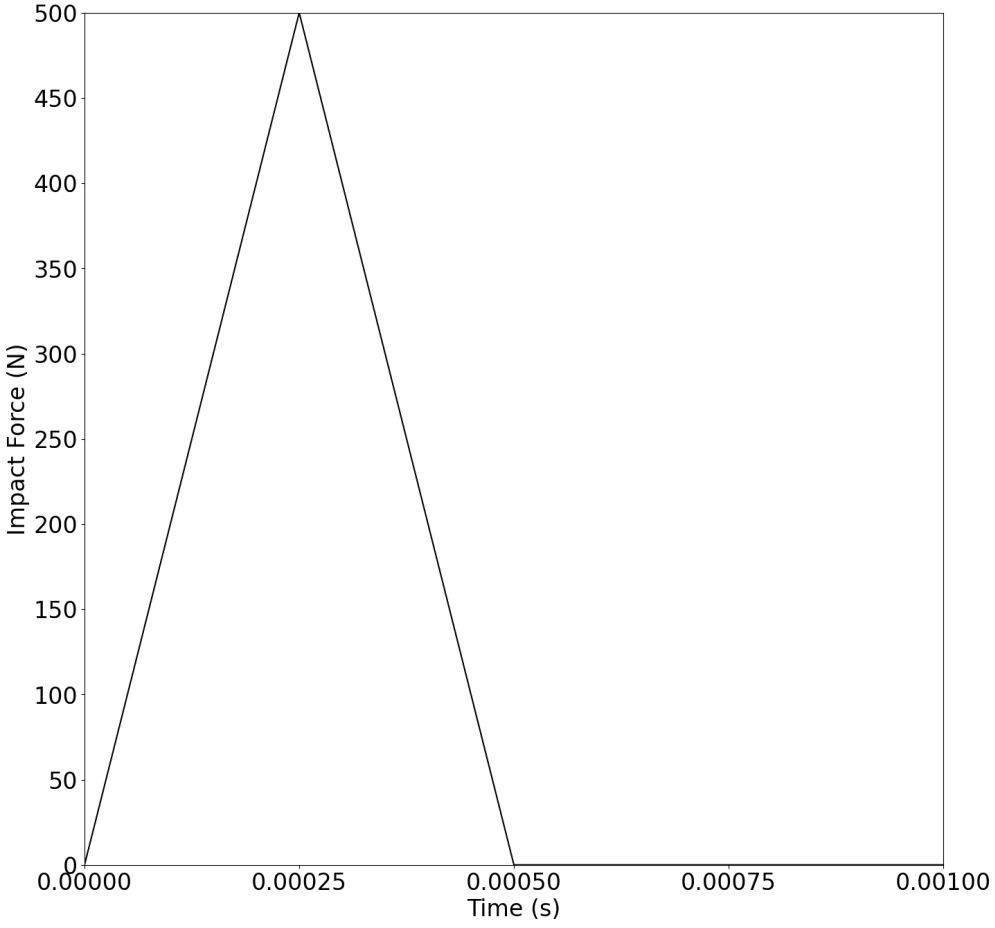


Figure 3.12: Example Impact Force History

Observing Figures 3.13, 3.14, and 3.15 the shear, moment, and deflections responses of the column are presented. Figure 3.13 outlines the shear response in the column at the point in time when the base shear is maximum. From Figure 3.13, it is apparent that when the mass rotational DOFs are not included in the model, the shear forces developed along the height of the column are larger and have an opposite sign than those developed when the mass rotational DOFs are included in the model. Based on this result, the mass rotational DOFs have an influence on the shear response of the column, meaning the consistent mass matrix should be used for the dynamic analysis of this column. Figure 3.14 presents the moment response in the column at the point in time when the base moment is maximum. Observing Figure 3.14, it is apparent that the mass rotational DOFs have an influence on the moment response at approximately the mid-point of the column, the magnitude of the base moments is very similar for both cases. Similar to the other response parameters, Figure 3.15 outlines the deflection response in the column at the point in time when the top deflection is maximum. From Figure 3.15, it is clear that the mass rotational DOFs have an insignificant influence on the deflection response of this column. Based on these results, the consistent-mass matrix was chosen to model the column, as the mass rotational DOFs had an influence on the shear and moment response of the system.

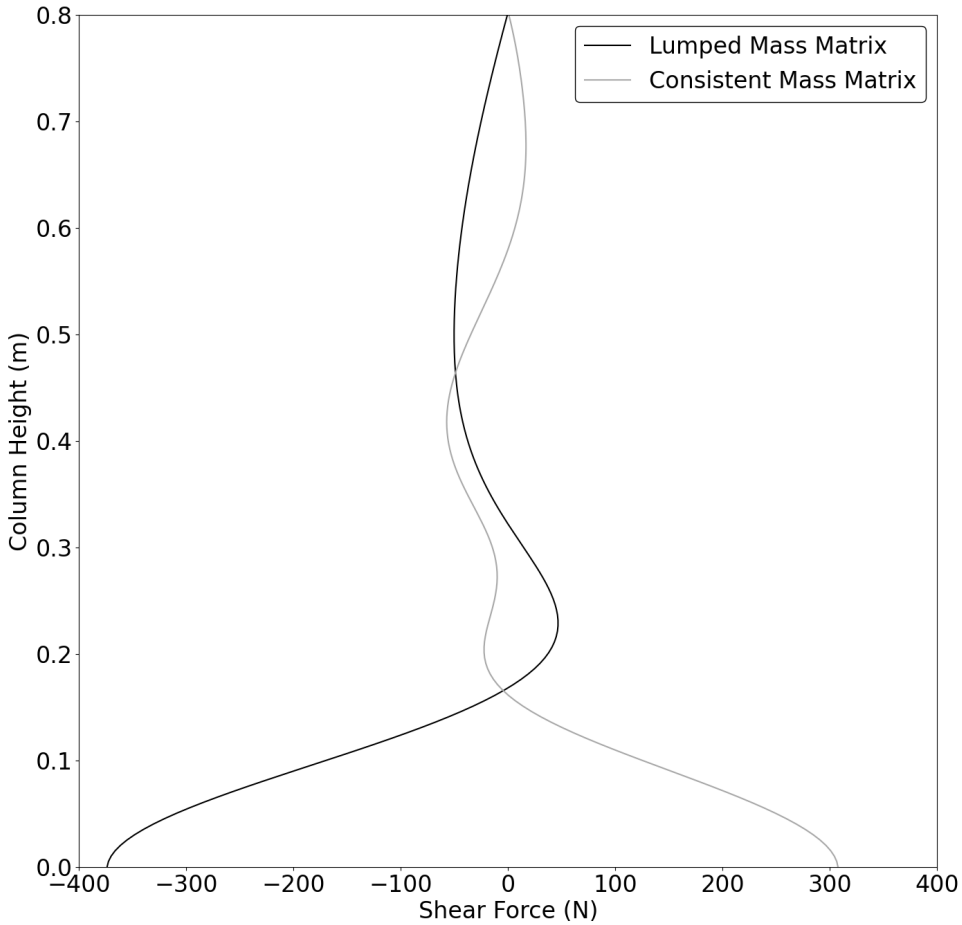


Figure 3.13: Shear Response at Maximum Base Shear

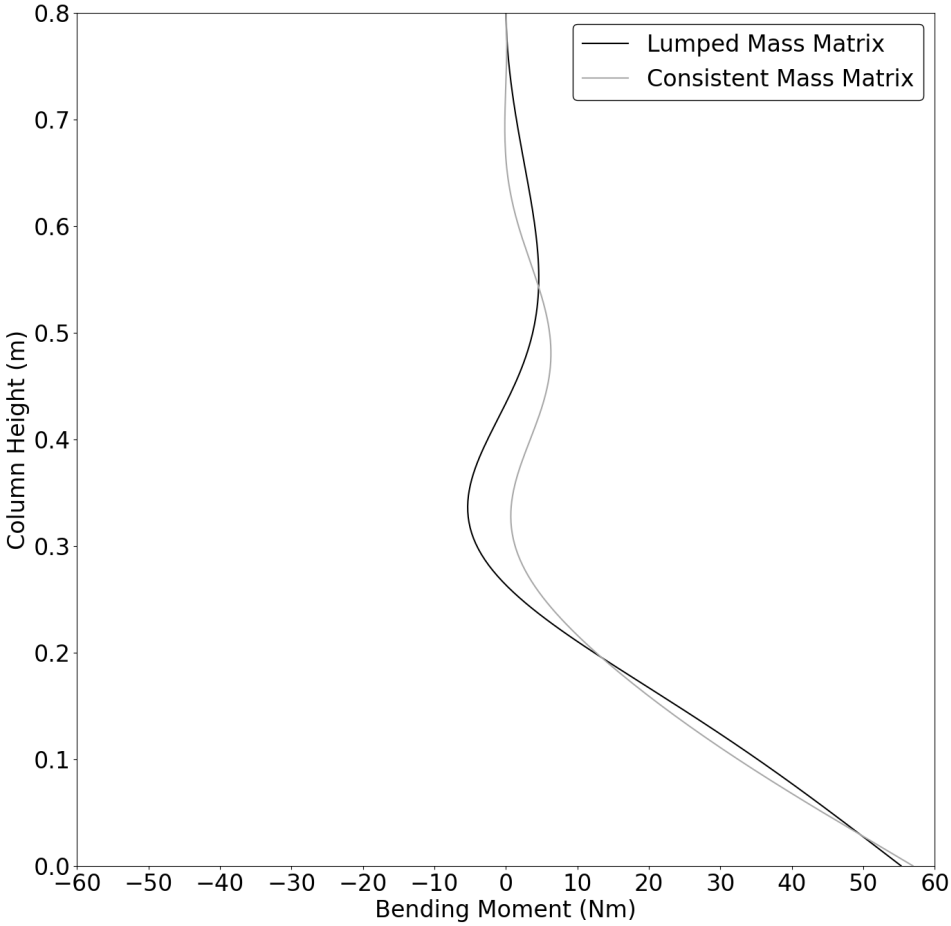


Figure 3.14: Moment Response at Maximum Base Moment

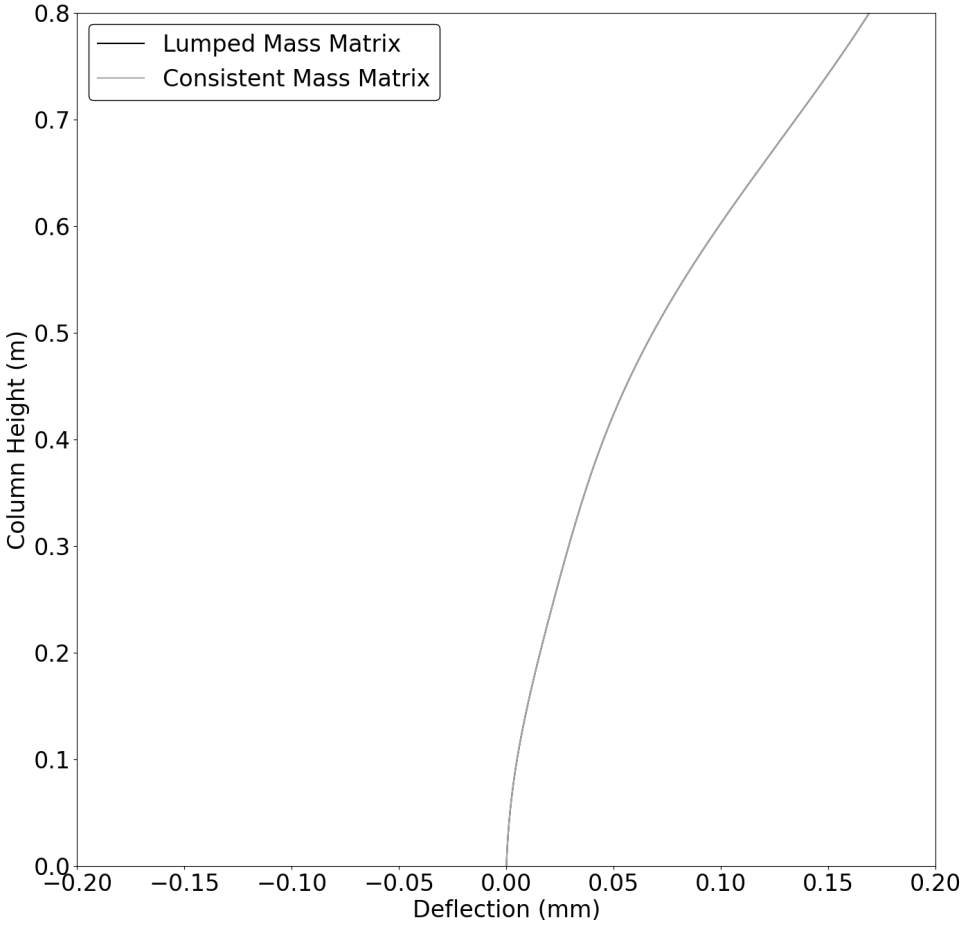


Figure 3.15: Deflection Response at Maximum Top Deflection

3.5.2 Stiffness Matrix Formulation

Using beam-elements the stiffness matrix can be derived through two methods: (1) Euler–Bernoulli beam theory; and (2) Timoshenko beam theory. Both methods use the geometry and material properties of the structure to derive the stiffness matrix, the material properties were outlined in Section 3.2 and the geometry is defined by the number of beam-elements outlined in Section 3.5.4. The difference between the two beam theories is that Timoshenko beam theory allows for the effects of shear deformation to be included in the model, while Euler-Bernoulli beam theory does not. Timoshenko's beam theory is typically used for deep beams where the ratio of the length to the depth of the beam is less than or equal to 10. For the beam outlined in Stolle et al. (2019), the ratio of the length to depth is 4, hence, Timoshenko's beam theory was chosen to derive the stiffness matrix of the column. Additionally, Khowitar et al. (2014) demonstrated that shear behavior dominates the initial response of a pole impacting a column, which suggests that including shear deformation in the response of the column is important. The local stiffness matrix

for a 2-node beam element using Timoshenko's beam theory can be seen below:

$$[k] = \frac{EI}{L^3\left(1+\phi\right)} \begin{bmatrix} 12 & 6L & -12 & 6L \\ 6L & \left(4+\phi\right)L^2 & -6L & \left(2-\phi\right)L^2 \\ -12 & -6L & 12 & -6L \\ 6L & \left(2-\phi\right)L^2 & -6L & \left(4+\phi\right)L^2 \end{bmatrix} \tag{3.8}$$

Where:

$$\phi = \frac{12EI}{k_s AGL^2} \tag{3.9}$$

3.5.3 Damping Matrix Formulation

The damping matrix was derived from Rayleigh damping, which assumes that the damping matrix is a linear combination of the mass and stiffness matrices as shown in Eq. 3.10. The Rayleigh damping matrix is defined by specifying damping coefficients ($\xi_i,\ \xi_j$) at two different frequencies ($\omega_i,\ \omega_j$) and calculating scalar multipliers for the mass (a_0) and stiffness (a_1) matrices as shown below in Eq. 3.11 and Eq. 3.12, respectively. The damping coefficients at the i^{th} and j^{th} frequencies were assumed to be the same and have a value of 0.045 (4.5%) based on the experimental impact hammer tests performed by Stolle et al. (2019).

$$[c] = a_0\,[m] + a_1\,[k] \tag{3.10}$$

$$a_0 = 2\omega_i\omega_j\left(\frac{\xi_j\omega_i - \xi_i\omega_j}{\omega_i^2 - \omega_j^2}\right) \tag{3.11}$$

$$a_1 = 2\left(\frac{\xi_j\omega_i - \xi_i\omega_j}{\omega_i^2 - \omega_j^2}\right) \tag{3.12}$$

In order to determine the two frequencies to be used to approximate 4.5% damping in the structure, a baseline modal time history analysis of the structure was completed using the impact force history in Figure 3.12. Modal time history analysis is a method for solving the dynamic response of the structure by solving the response in each normal mode and superimposing the response in each mode to capture the total response of the structure. The benefit of using modal analysis to solve the response of the structure is that if classical damping is assumed (i.e. Rayleigh damping), then the response at each normal mode may be solved as a SDOF system. Due to this result the damping in each mode can be explicitly defined, whereas in Rayleigh damping, the damping can only be defined at two frequencies (Chopra, 2017). One of the draw-backs to using modal analysis to solve impact problems, is that in order to obtain an accurate response of the structure nearly all of the natural modes of the structure need to be extracted, which can be computationally expensive for large MDOF structures.

In order to determine the two frequencies which should be used in the Rayleigh damping model, the two frequencies (ω_i and ω_j) were varied until the direct time history analysis provided a response that was equal to the response determined from the modal time history analysis. The first frequency was selected to be constant at a value equal to the first natural frequency of the structure ($435\frac{rad}{s}$). The second frequency was then determined by selecting the natural frequency associated with the next mode (i.e. the second, third, fourth, etc. modes) until the solution converged to the modal time history analysis solution. Figures 3.16, 3.17, and 3.18 present the maximum base shear, base bending moment, and top deflections for the modal analysis solution and for when ω_j was assumed to be equal to the frequency associated with the second, fifth, tenth, and fifteenth modes.

From Figure 3.16 and Table 3.2, it is apparent that when ω_j is equal to the frequency of the tenth mode, the modal and direct time history analysis result in a very similar maximum base shear with a difference of $1.17N$. When ω_j is equal to the frequency of the fifteenth mode, the direct time history analysis overestimates the base shear when compared to the modal analysis solution. Whereas, when ω_j is equal to the frequency of the second or fifth mode, the direct time history analysis underestimates the base shear.

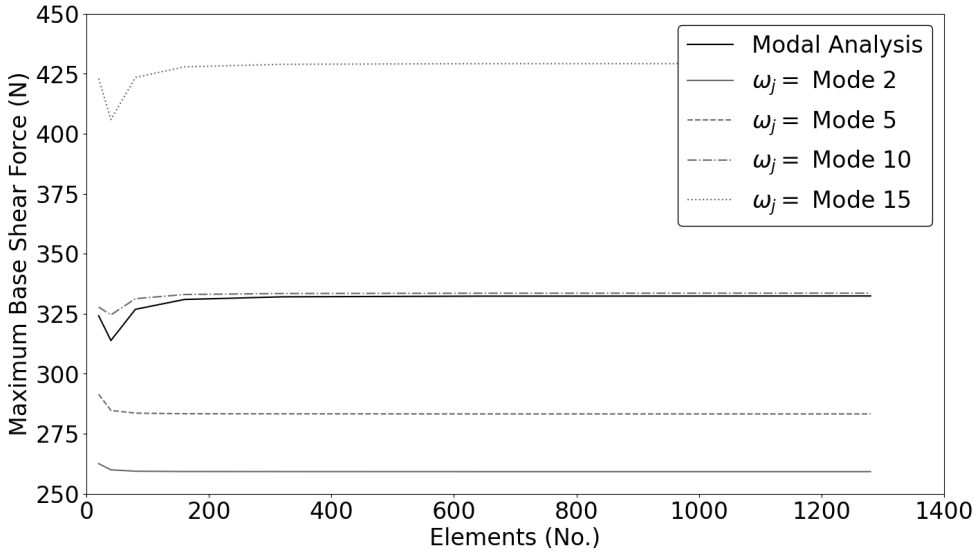


Figure 3.16: Modal Analysis Comparison - Maximum Base Shear Force

From Figure 3.17 and Table 3.2, it is apparent that the modal analysis solution provides the smallest maximum base bending moment. The closest solution to the modal analysis solution is when ω_j is equal to the frequency of the second mode. The difference between the maximum base bending moments for the modal analysis solution and for when ω_j is equal to the frequency of the second mode is $0.41Nm$. All other direct time history analysis solutions overestimated the maximum base bending moment.

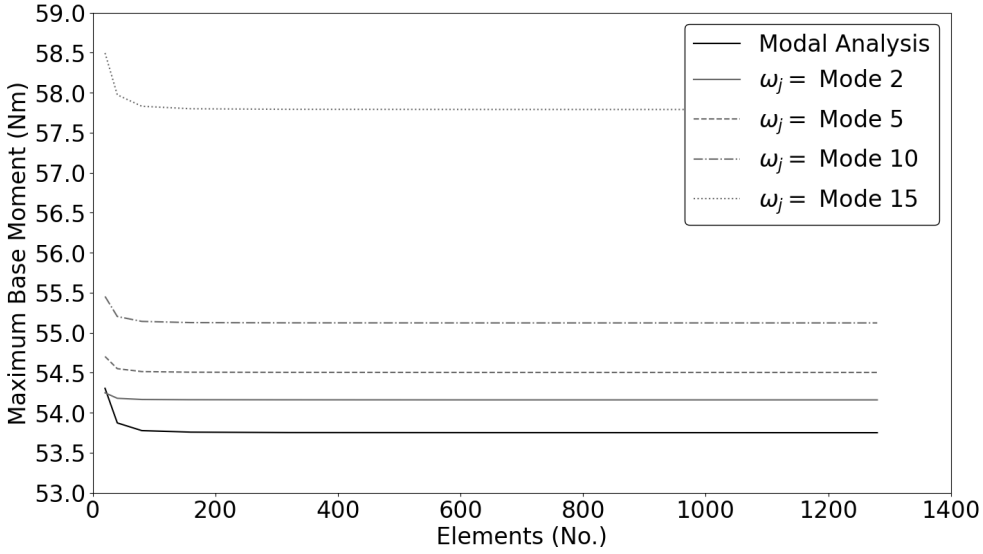


Figure 3.17: Modal Analysis Comparison - Maximum Base Moment

From Figure 3.18 and Table 3.2, it is apparent that the modal analysis solution provides the smallest maximum top deflection. The closest solution to the modal analysis solution is when ω_j is equal to the frequency of the second mode. The difference between the maximum top deflections for the modal analysis solution and for when ω_j is equal to the frequency of the second mode is $0.0002mm$. All other direct time history analysis solutions overestimated the maximum top deflection.

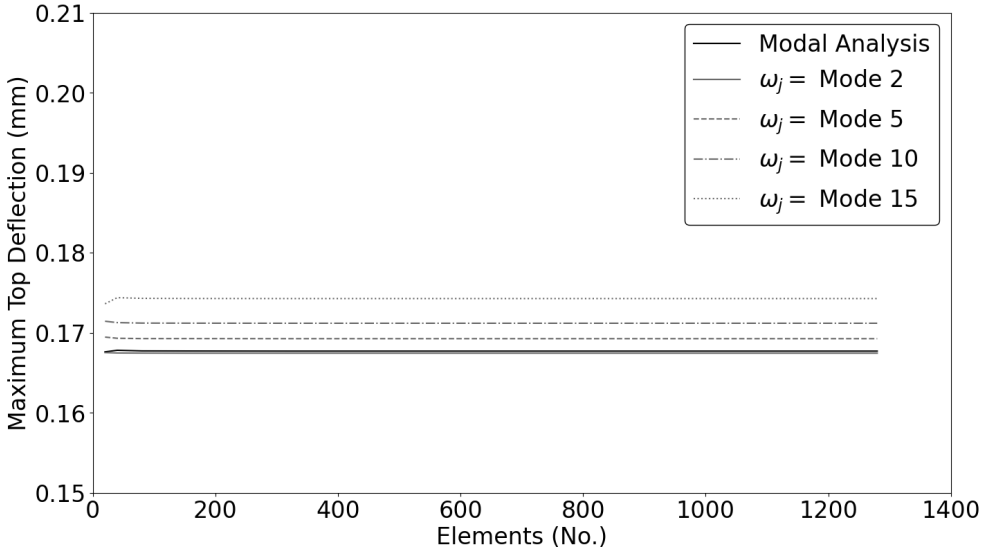


Figure 3.18: Modal Analysis Comparison - Maximum Top Deflection

Based on these results, it can be concluded that when ω_j is equal to the frequency

of the tenth mode, the difference between the modal and direct time history solution is minimal. When ω_j is equal to the frequency of the second mode, the direct time history solution provides a maximum base shear that is $73.17N$ smaller than the modal analysis solution. This suggests that when ω_j is equal to the frequency of the second mode, all higher mode effects are damped out quickly. Conversely, when ω_j is equal to the frequency of the fifteenth mode, the direct time history solution provides a maximum base shear that is $96.85N$ larger than modal analysis solution. This suggests that when ω_j is equal to the frequency of the fifteenth mode, the amount of damping in the lower modes is too small, which causes the maximum base shear to increase. When observing the results in Table 3.2 for the maximum base moment and top deflection, it is apparent that the direct time history solution using ω_j equal to the second mode, provides the closest solution to the modal analysis results. However, as ω_j increases up to the fifteenth mode, the difference between the direct time history analysis solution and the modal analysis solution is still not as significant when compared to the differences for the base shear. For the base moment, the difference between the modal analysis solution and the direct time history solution is at a maximum of $4.04Nm$. While for the top deflection, the difference is at a maximum of $0.0066mm$. Furthermore, as ω_j increases, the differences between the direct time history analysis and modal analysis increases, which suggests that the base moment and top deflection respond mostly in the first and second mode. This can be concluded as when ω_j increases the damping in the second mode decreases causing the magnitude of the response parameters to increase. Based on these results ω_j was selected to be the frequency associated with the tenth mode ($11730\frac{rad}{s}$), as the shear response of the structure was the most sensitive response parameter to damping.

Mode Number	Base Shear (N)		Base Moment (Nm)		Top Deflection (mm)	
	Value	% Change	Value	% Change	Value	% Change
Modal Analysis	332.41	N/A	53.75	N/A	0.1677	N/A
2	259.24	−22.01%	54.16	0.76%	0.1675	−0.16%
5	283.28	−14.78%	54.50	1.40%	0.1693	0.92%
10	333.58	0.35%	55.12	2.55%	0.1712	2.08%
15	429.26	29.14%	57.79	7.51%	0.1743	3.91%

Table 3.2: Modal Analysis Comparison Summary Table

With both frequencies selected for the Rayleigh damping matrix, the mass and stiffness scalar multipliers can be calculated along with the Rayleigh damping curve. The Rayleigh damping curve estimates the damping ratio for the n^{th} mode of a system and is defined as a function of the mass and stiffness scalar multipliers and the frequency at mode n:

$$\xi_n = \frac{a_0}{2}\frac{1}{\omega_n} + \frac{a_1}{2}\omega_n \tag{3.13}$$

Figure 3.19 plots Eq. 3.13 over a range of frequencies using the mass and stiffness scalar multipliers for when ω_i is equal to $435\frac{rad}{s}$ and ω_j is equal to $11730\frac{rad}{s}$. Also plotted on Figure 3.19 are the first ten natural frequencies of the column used in this analysis.

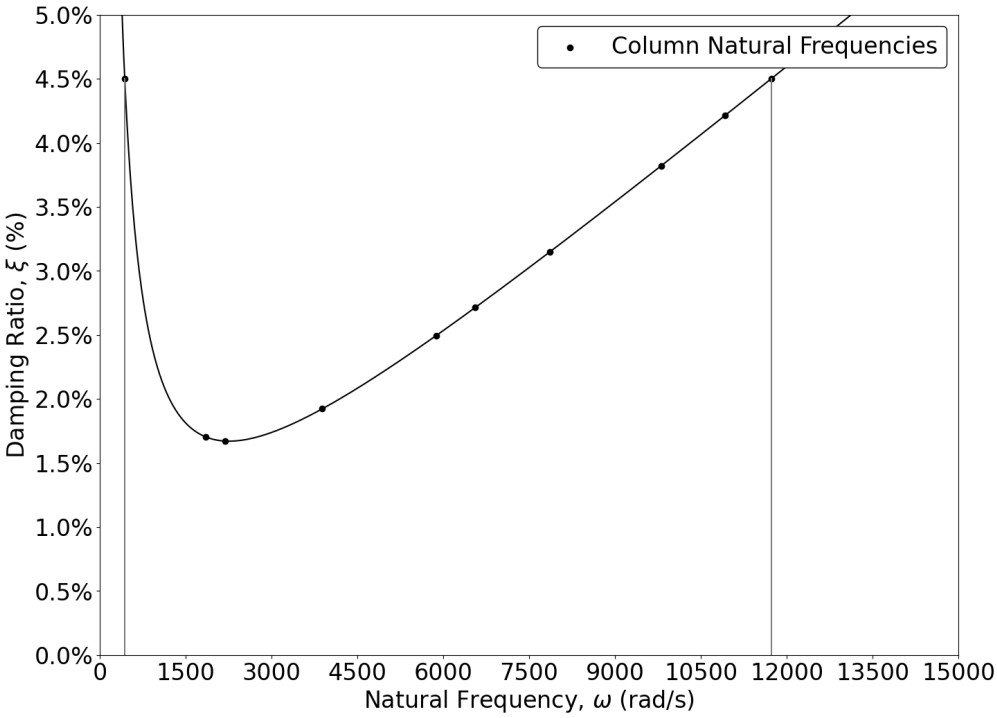


Figure 3.19: Rayleigh Damping Curve

3.5.4 Mesh Refinement Study

This section outlines how sensitive the structural response is to the refinement of the mesh. The mesh refinement consisted of increasing the number of beam elements in the model from 20 elements to 1280 elements and analysing how the maximum base shear, base bending moment, and top deflection changed as a result of the mesh refinement. The influence of the mesh refinement on each response parameter was determined by calculating the percentage change between each mesh refinements. A converged mesh was defined as the number of elements at which the percentage difference between mesh refinements was less than 0.25%.

Figure 3.20 outlines how the maximum base shear changes as the mesh refinement increases. It is apparent in the figure that the maximum base shear converges at approximately 160 elements. Furthermore, Table 3.3 outlines the percentage change in the maximum base shear as refinement increases. From Table 3.3, it can be concluded that the percentage change from 160 elements to 320 elements is 0.13% or a $0.43N$ difference. Concluding that to accurately capture the shear response of the system a minimum mesh refinement of 160 elements should be modelled.

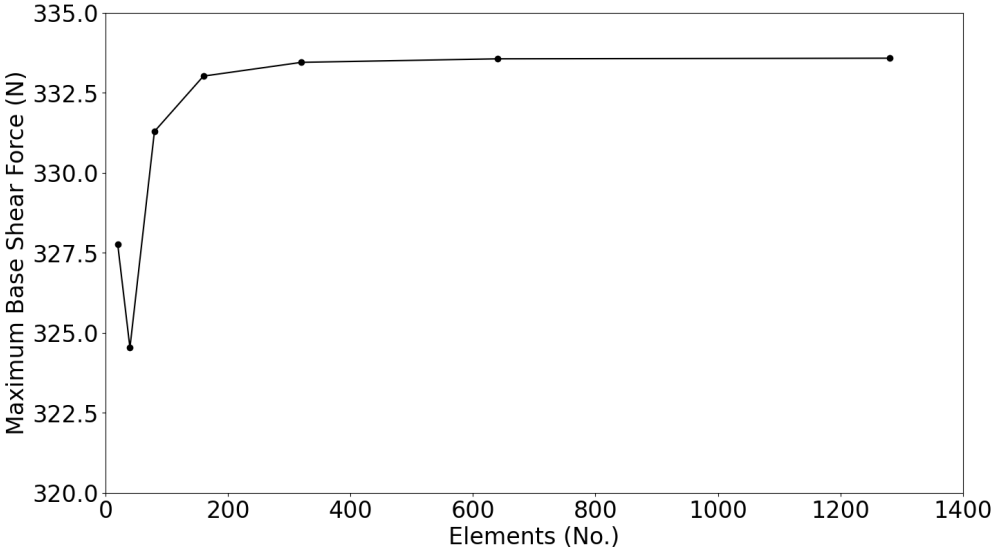


Figure 3.20: Mesh Refinement Study - Maximum Base Shear Force

Figure 3.21 outlines how the maximum base bending moment changes as the mesh refinement increases. It is apparent in the figure that the maximum base moment converges at approximately 40 elements. Furthermore, Table 3.3 outlines the percentage change in the maximum base moment as refinement increases. From Table 3.3, it can be concluded that the percentage change from 40 elements to 80 elements is 0.11% or a $0.06Nm$ difference. Concluding that to accurately capture the moment response of the system a minimum mesh refinement of 40 elements should be modelled.

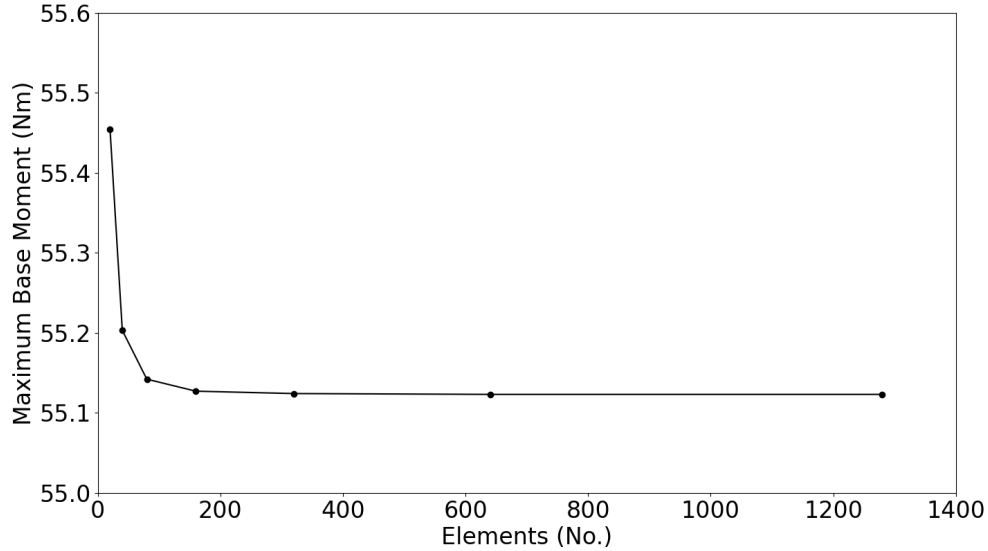


Figure 3.21: Mesh Refinement Study - Maximum Base Moment

Finally, Figure 3.22 outlines how the maximum top deflection changes as the mesh

refinement increases. It is apparent in the figure that the maximum top deflection converges at approximately 20 elements. Furthermore, Table 3.3 outlines the percentage change in the maximum top deflection as refinement increases. From Table 3.3, it can be concluded that the percentage change from 20 elements to 40 elements is 0.10% or a $0.0001mm$ difference. Concluding that to accurately capture the deflection response of the system a minimum mesh refinement of 20 elements should be modelled.

Based on all of these results, the conclusion can be made that a minimum mesh refinement of 160 elements should be used to accurately capture the shear, moment, and deflection responses of this model.

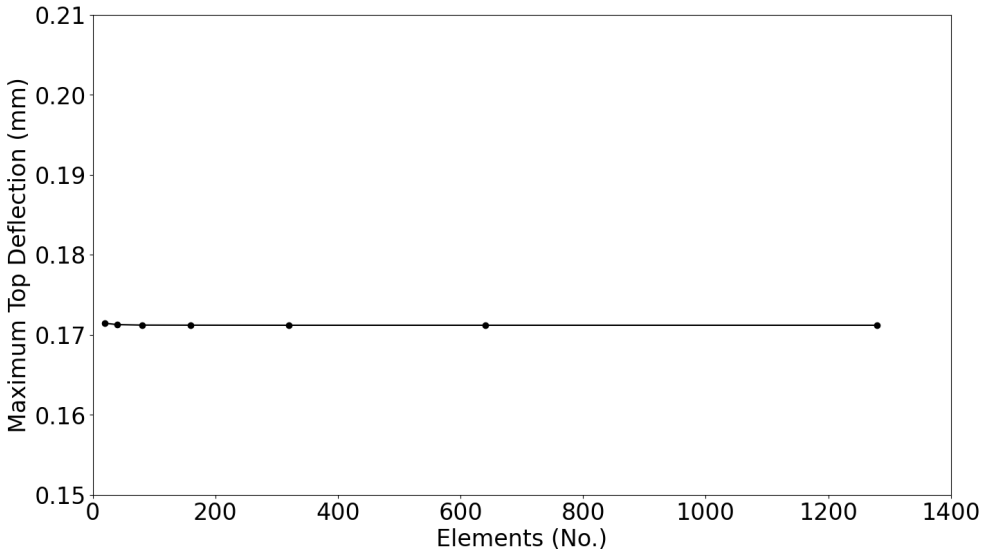


Figure 3.22: Mesh Refinement Study - Maximum Top Deflection

Elements (No.)	Base Shear (N)		Base Moment (Nm)		Top Deflection (mm)	
	Value	% Change	Value	% Change	Value	% Change
20	327.77	N/A	55.45	N/A	0.1714	N/A
40	324.53	−0.99%	55.20	−0.45%	0.1713	−0.10%
80	331.29	2.08%	55.14	−0.11%	0.1712	−0.04%
160	333.02	0.52%	55.13	−0.03%	0.1712	−0.01%
320	333.45	0.13%	55.12	−0.01%	0.1712	−0.01%
640	333.56	0.03%	55.12	0.00%	0.1712	0.00%
1280	333.58	0.01%	55.12	0.00%	0.1712	0.00%

Table 3.3: Mesh Refinement Study Summary Table

3.5.5 Time Step Study

This section outlines how sensitive the structural response is to the time step of the time integration scheme. The time step sensitivity study consisted of decreasing the time step

of the model from $1e^{-5}s$ down to $1e^{-9}s$. A maximum time step of $1e^{-5}s$ was selected as a larger time step was not capable of capturing a half-sine wave impact shape for impact duration's less than $5e^{-4}s$. The influence of decreasing the time step on each response parameter was determined by calculating the percentage change between each refinement. A time step where the solution was deemed converged was defined as the time step at which the percentage difference between refinements was less than 0.25%.

Figure 3.23 outlines how the maximum base shear changes as the time step decreases. It is apparent in the figure that the maximum base shear converges at a time step of approximately $1e^{-5}s$. Furthermore, Table 3.4 outlines the percentage change in the maximum base shear as the time step decreases. From Table 3.4, it can be concluded that the percentage change from a time step of $1e^{-5}s$ to a time step of $1e^{-6}s$ is 0.24% or a $0.79N$ difference. Concluding that to accurately capture the shear response of the system a time step of $1e^{-5}s$ can be used, however, using a time step of $1e^{-5}s$ resulted in a change of base shear bordering 0.25% and hence, a time step of $1e^{-6}s$ should be used.

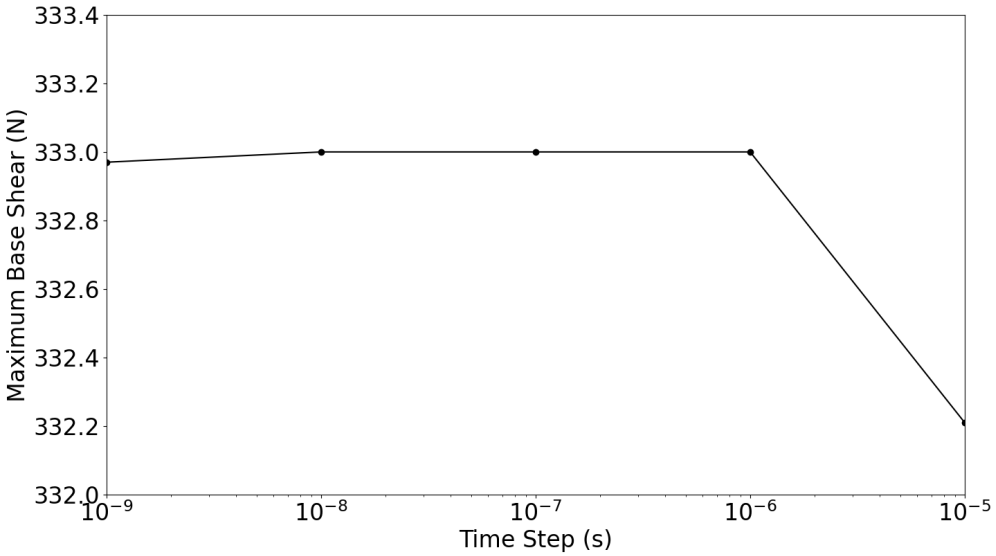


Figure 3.23: Time Step Study - Maximum Base Shear Force

Figure 3.24 outlines how the maximum base bending moment changes as the time step decreases. It is apparent in the figure that the maximum base bending moment converges at a time step of approximately $1e^{-5}s$. Furthermore, Table 3.4 outlines the percentage change in the maximum base moment as the time step decreases. From Table 3.4, it can be concluded that the percentage change from a time step of $1e^{-5}s$ to a time step of $1e^{-6}s$ is 0.05% or a $0.02Nm$ difference. Concluding that to accurately capture the moment response of the system a time step of $1e^{-5}s$ can be used.

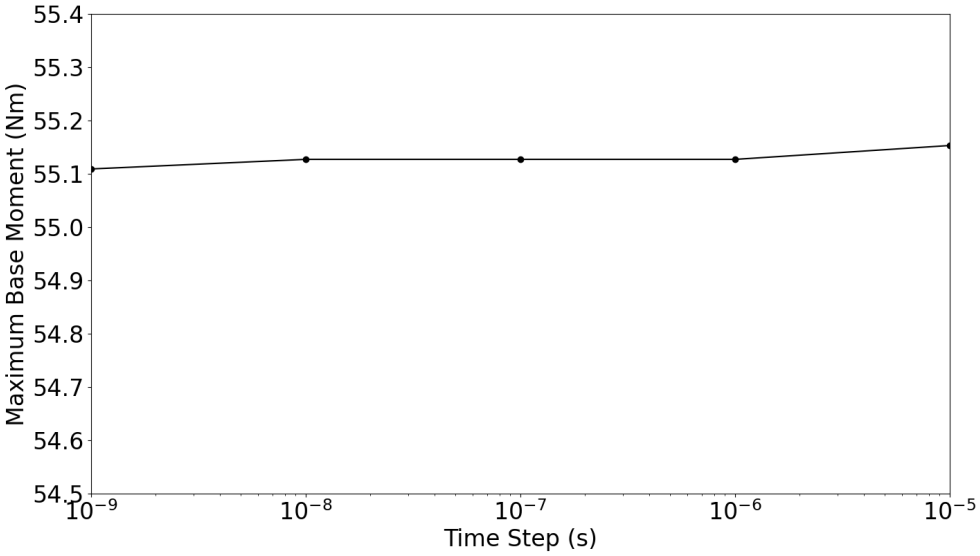


Figure 3.24: Time Step Study - Maximum Base Moment

Figure 3.25 outlines how the maximum top deflection changes as the time step decreases. It is apparent in the figure that the maximum top deflection converges at a time step of approximately $1e^{-5}s$. Furthermore, Table 3.4 outlines the percentage change in the maximum top deflection as the time step decreases. From Table 3.4 it can be concluded that the percentage change from a time step of $1e^{-5}s$ to a time step of $1e^{-6}s$ is 0.01% or a $0.00001mm$ difference. Concluding that to accurately capture the deflection response of the system a time step of $1e^{-5}s$ is adequate for this model.

Based on all of these results, the conclusion can be made that a time step of $1e^{-6}s$ should be used to accurately capture the shear, moment, and deflection responses of this model.

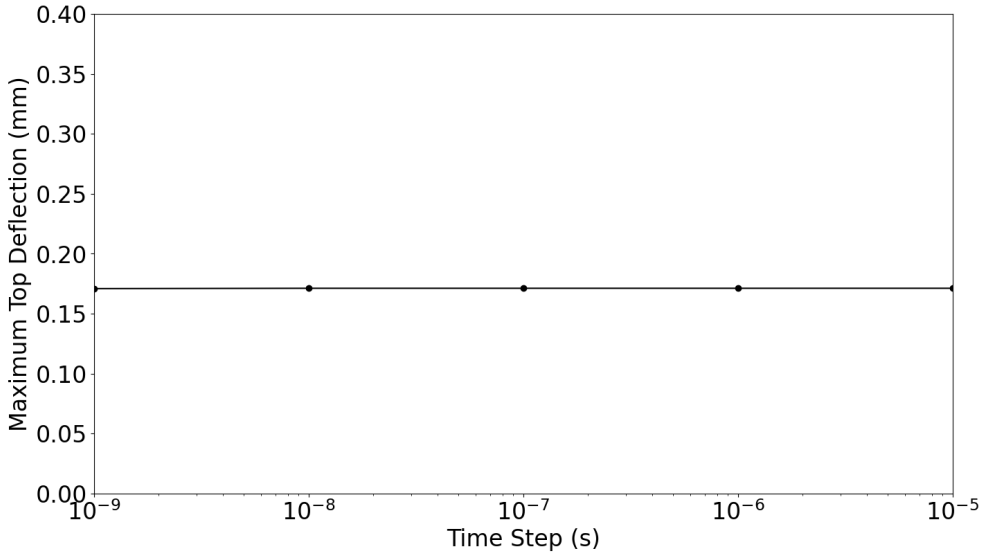


Figure 3.25: Time Step Study - Maximum Top Deflection

Time Step (s)	Base Shear (N)		Base Moment (Nm)		Top Deflection (mm)	
	Value	% Change	Value	% Change	Value	% Change
$1e^{-5}$	332.21	N/A	55.15	N/A	0.1712	N/A
$1e^{-6}$	333.00	0.24%	55.13	−0.05%	0.1712	−0.01%
$1e^{-7}$	333.00	0.00%	55.13	0.00%	0.1712	0.00%
$1e^{-8}$	333.00	0.00%	55.13	0.00%	0.1712	0.00%
$1e^{-9}$	332.97	−0.01%	55.11	−0.03%	0.1709	−0.16%

Table 3.4: Time Step Study Summary Table

3.5.6 MDOF Impact Shape Study

One of the key assumptions in the fitting algorithm is the shape of the impact history. The influence that the impact shape has on the fitting algorithm was investigated by calculating the RMSE following Eq. 3.4 for all 22 experimental data points and the five impact shapes outlined in Section 3.3. The impact shape that resulted in the smallest average RMSE over the entire data set was concluded to be the impact shape that resulted in a force response that best fit the experimental data.

Figure 3.26 presents the force response resulting from the fitting algorithm for one experimental data point. The figure outlines the fitting results for all five impact shapes and compares them to the experimental force response. From Figure 3.26, the impact shape has the largest influence on the initial peak of the force response, after the initial peak the influence of the impact shape diminishes as the structure is in a free-vibration response. Furthermore, it is clear from Figure 3.26 that the MDOF fitting method is capable of capturing the dual peak behavior present in the experimental data and therefore, is capable

of capturing the peak force response of the system. This is because the dual peak behavior is associated with higher mode effects, which a MDOF method can capture, while a SDOF method cannot.

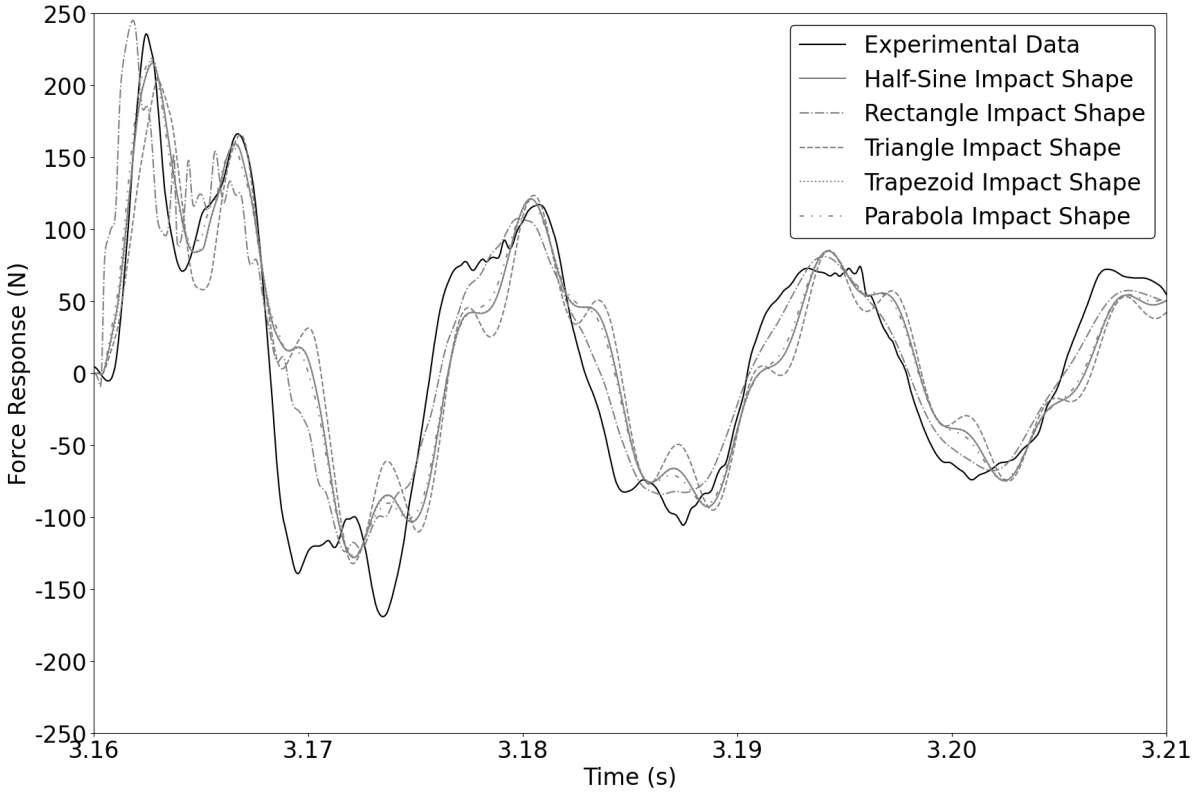


Figure 3.26: Example Force Response for MDOF Fitting

After the fitting algorithm is complete, the impact force histories that developed the fitted force responses are extracted. Figure 3.27 presents the impact force histories that developed the force responses outlined in Figure 3.26. From Figure 3.27, it is evident that the fitting algorithm produced similar impact force histories for each impact shape, aside from the rectangular impact shape. It is apparent that each impact force history peaks at similar magnitude, ends a similar duration, and has a similar total impulse, while the rectangular impact force history resulted in the smallest impact magnitude and duration. Furthermore, comparing the force responses in Figure 3.26, demonstrates that the smaller impact duration associated with the rectangular impact history excited higher modes in the column at the initial peak of the response. This caused the modelled force response from the rectangular impact shape to peak five times instead of two as in the experimental data and all force responses resulting from the other impact shapes. Additionally, as opposed to the force responses and impact force histories developed by the SDOF method for this experimental data point (Figures 3.3 and 3.4), it is clear that the experimental force response cannot be modelled with significantly different impact histories if a MDOF model is used.

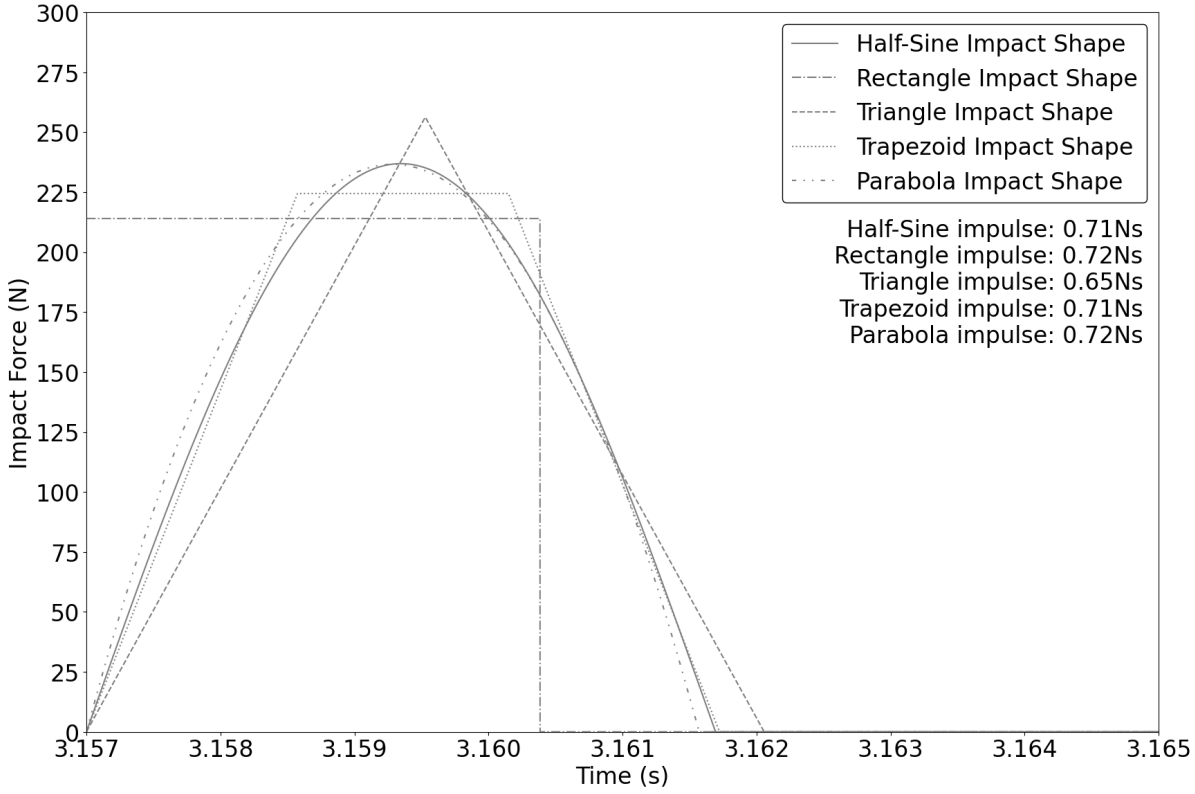


Figure 3.27: Example Impact History from MDOF Fitting

Extending the analysis to all 22 experimental data points, a suite of impact force history curves can be developed for each impact shape. Figures 3.28, 3.29, 3.30, 3.31, and 3.32 present the impact force histories for the half-sine, rectangular, triangular, trapezoidal, and parabolic impact shapes. Furthermore, Table 3.5 presents a summary table of the fitting results for each impact shape. From these figures, the conclusion can be made that the impact shape used in the fitting algorithm has a significantly less influence on the impact force histories developed when compared to the SDOF fitting method. The fitting results for all impact shapes resulted in impact force histories that have similar magnitudes and durations.

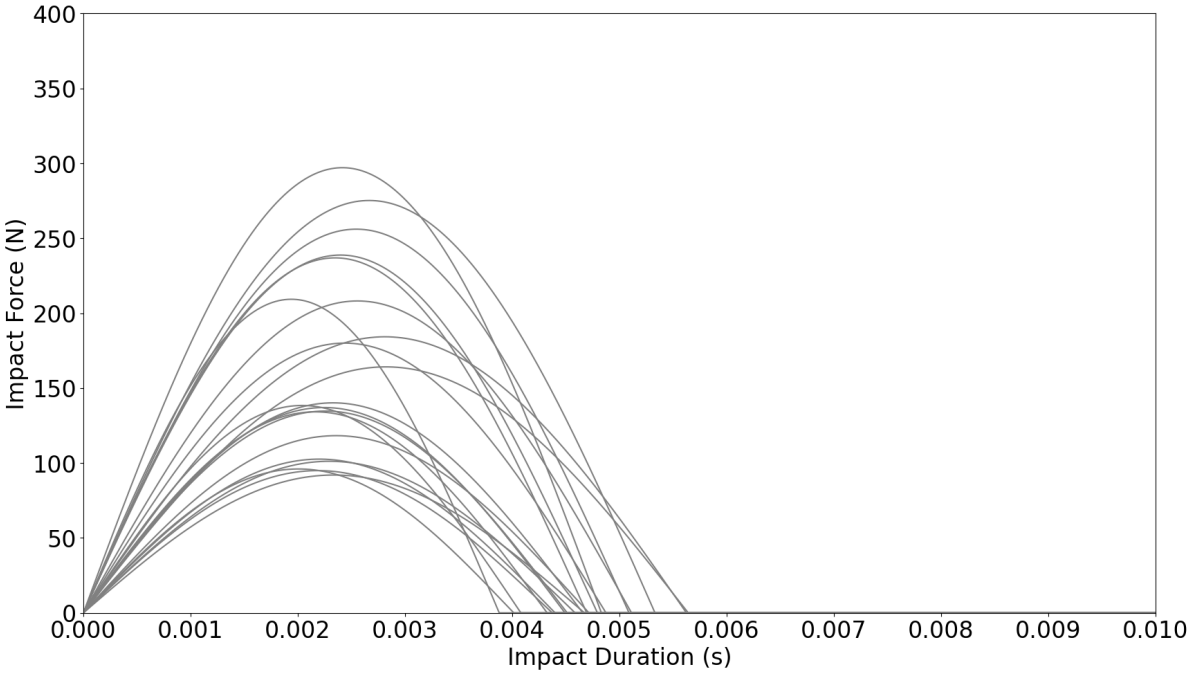


Figure 3.28: MDOF Fitting Half-Sine Impact Histories

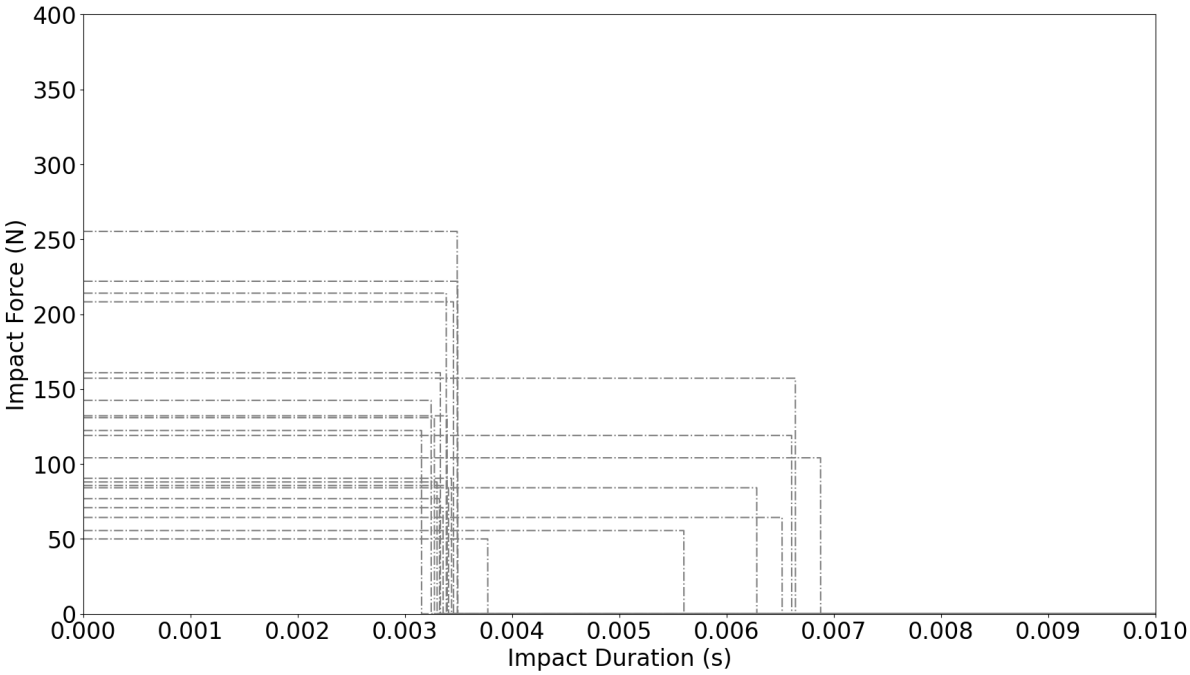


Figure 3.29: MDOF Fitting Rectangle Impact Histories

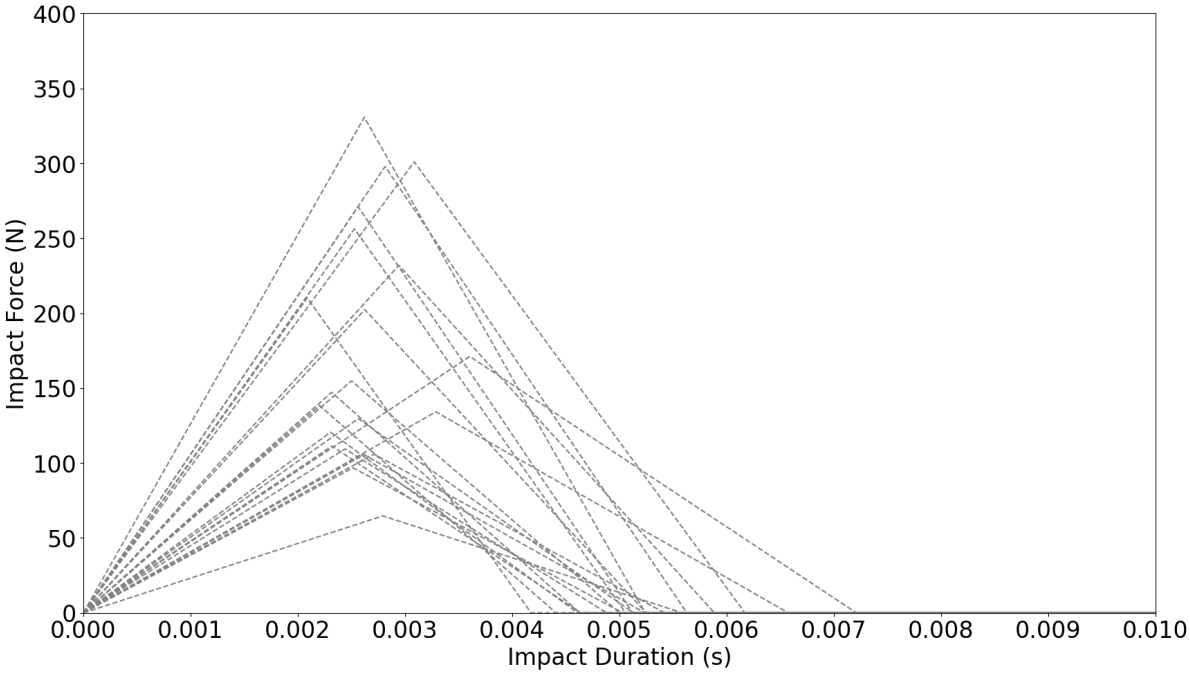


Figure 3.30: MDOF Fitting Triangle Impact Histories

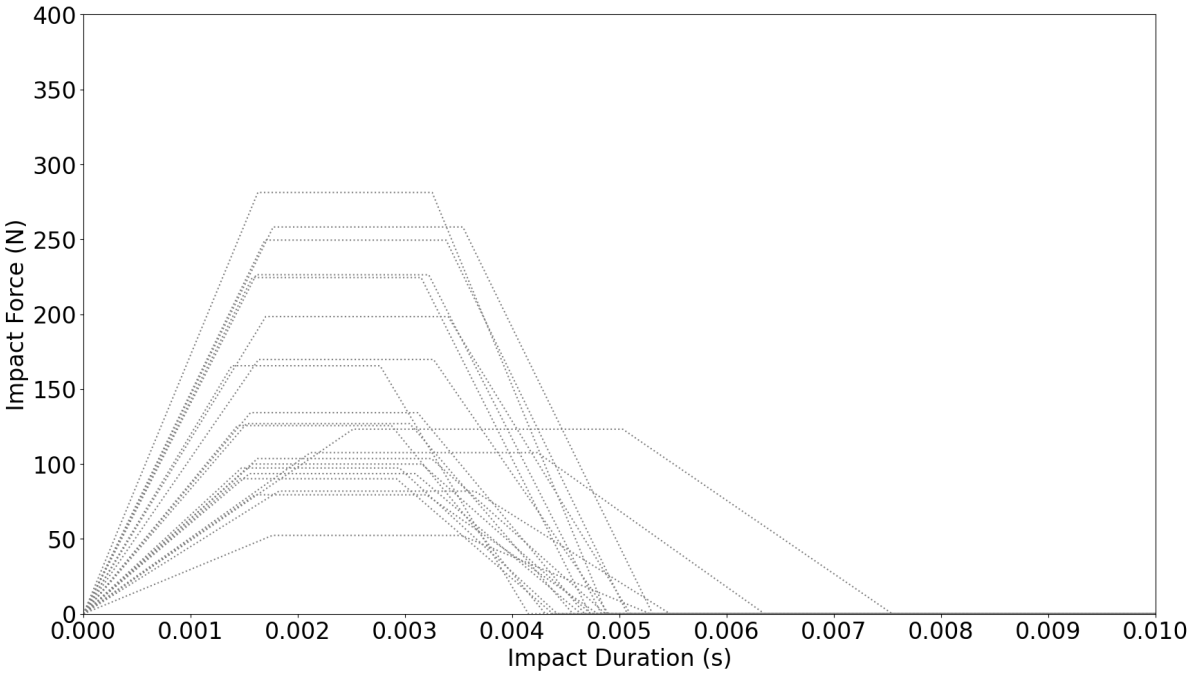


Figure 3.31: MDOF Fitting Trapezoid Impact Histories

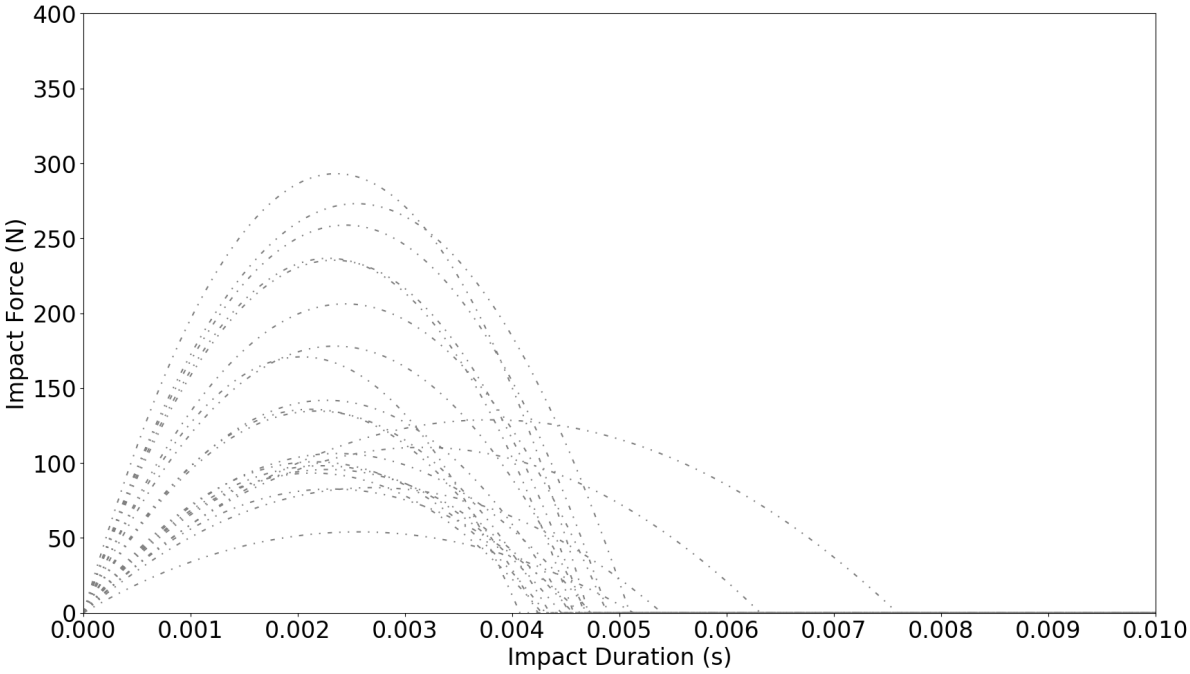


Figure 3.32: MDOF Fitting Parabola Impact Histories

Table 3.5 outlines the mean and standard deviation of the impact magnitude, impact duration, impulse, and the RMSE. Observing the mean and standard deviation of the impact magnitudes for all impact shapes, it is can be seen that there is a small range of impact magnitudes that change depending on the impact shape. This further supports the conclusion that the experimental force responses cannot be modelled with a wide range of significantly different impact force histories when a MDOF model is used. Additionally, there is also small range in mean impact durations for all impact shapes, which suggests that the impact shape does not have a large influence on the impact durations. Furthermore, all impact shapes resulted in a similar mean and standard deviation for the impulse. Observing the RMSE, the parabolic impact shape resulted in the smallest mean and standard deviation of the RMSE, with the half-sine impact shape providing the second smallest. This result implies that the parabolic impact shape resulted in force responses that best fit the experimental data.

Impact Shape	Magnitude (N)		Duration (s)		Impulse (Ns)		RMSE	
	Mean	Std.	Mean	Std.	Mean	Std.	Mean	Std.
Half-Sine	168.55	62.41	0.0047	0.0005	0.51	0.22	0.14	0.04
Rectangle	125.47	57.56	0.0043	0.0014	0.51	0.24	0.15	0.03
Triangle	175.78	76.14	0.0053	0.0007	0.47	0.22	0.15	0.03
Trapezoid	147.14	65.54	0.0050	0.0007	0.49	0.22	0.14	0.04
Parabola	153.26	69.10	0.0049	0.0008	0.49	0.23	0.14	0.03

Table 3.5: MDOF Fitting Results

Figure 3.33 outlines how the maximum force responses developed by the MDOF model compare to the maximum experimental force responses. From this figure, the conclusion can be made that on average, the MDOF model underestimates the maximum experimental force response for all impact shapes. However, the magnitude to which the MDOF model underestimates the maximum experimental force responses is significantly smaller when compared to the SDOF fitting results. For all experimental data points, the maximum experimental force responses are on average 1.19 times larger than the MDOF maximum force responses and on average 2.53 times larger than the SDOF maximum force responses.

Another metric for assessing which impact shape resulted in the best fit to the experimental data is the coefficient of determination (R^2). The coefficient of determination takes a value from zero to one, meaning a R^2 of one for this analysis implies that the maximum force responses from the MDOF model exactly predict the maximum force responses from the experimental data. The coefficients of determination for all five impact shapes are as follows:

- Half-Sine: $R^2 = 0.90$
- Rectangle: $R^2 = 0.85$
- Triangle: $R^2 = 0.84$
- Trapezoid: $R^2 = 0.83$
- Parabola: $R^2 = 0.83$

Based on the mean and standard deviation of the RMSE, the parabolic impact shape resulted in force responses that best fit the experimental data. However, the half-sine impact shape produced the same mean RMSE and a very similar standard deviation when compared to the parabolic impact shape, but with a coefficient of determination closer to one. This implies that the half-sine impact shape is better at predicting the maximum experimental force responses when compared to the parabolic impact shape. Based on these results, the conclusion was made that the half-sine impact shape resulted in force responses that best fit the experimental data when compared to all other impact shapes investigated in this study.

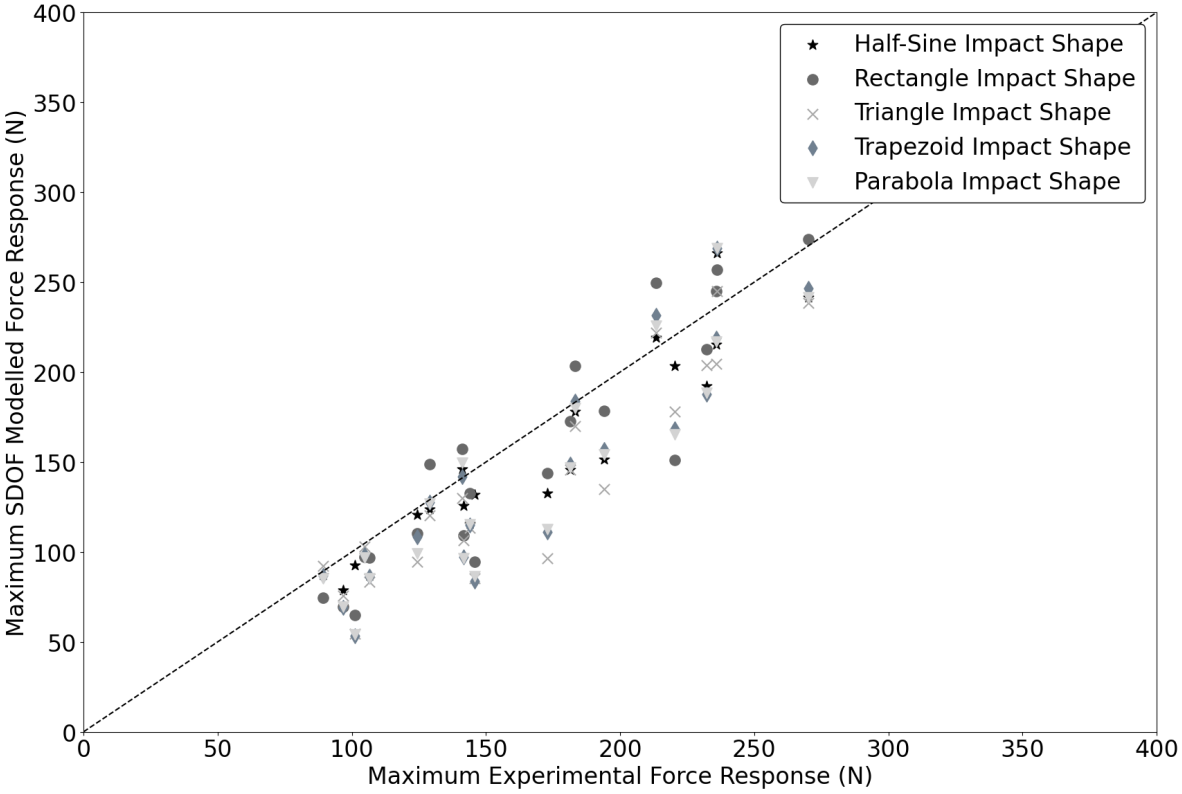


Figure 3.33: MDOF Fitting Maximum Force Response Comparison

3.6 Analytical Method

The analytical method follows the formulas and procedures outlined in Clauses 6.11.2 and 6.11.8 of ASCE 7 (2016) to determine the impact magnitude, duration, and shape. Clause 6.11.2 of ASCE 7 (2016) defines the impact magnitude and duration, which are functions of the building importance factor, orientation coefficient, maximum flow velocity, the lesser of the effective stiffness of the impacting debris or the lateral stiffness of the impacted structural element, and the mass of the debris:

$$F_i = I_{tsu} C_0 F_{ni} \tag{3.14}$$

The nominal impact force is:

$$F_{ni} = u_{max} \sqrt{k m_d} \tag{3.15}$$

For this analysis the importance factor was selected to be one, corresponding to a Tsunami Risk Category of II and following Clause 6.11.6 of ASCE 7 (2016) the orientation coefficient is equal to 0.65 for shipping containers, leading to the following equation for the design debris impact force:

$$F_i = 0.65 * u_{max} \sqrt{k m_d} \tag{3.16}$$

The impact duration was calculated as per Clause 6.11.2 of ASCE 7 (2016) as the scaled shipping containers from Stolle et al. (2019) were empty:

$$t_d = \frac{2m_d u_{max}}{F_{ni}} \tag{3.17}$$

Following Clause 6.11.8 of ASCE 7 (2016) the impact force history will take the shape of a rectangular pulse with magnitude defined by Eq. 3.16 and duration defined by Eq. 3.17. To calculate the impact magnitude and duration, the experimental debris impact velocity, debris material properties, and structure material properties from Stolle et al. (2019) were used. A plot of measured maximum force response and debris impact velocity is shown in Figure 3.34.

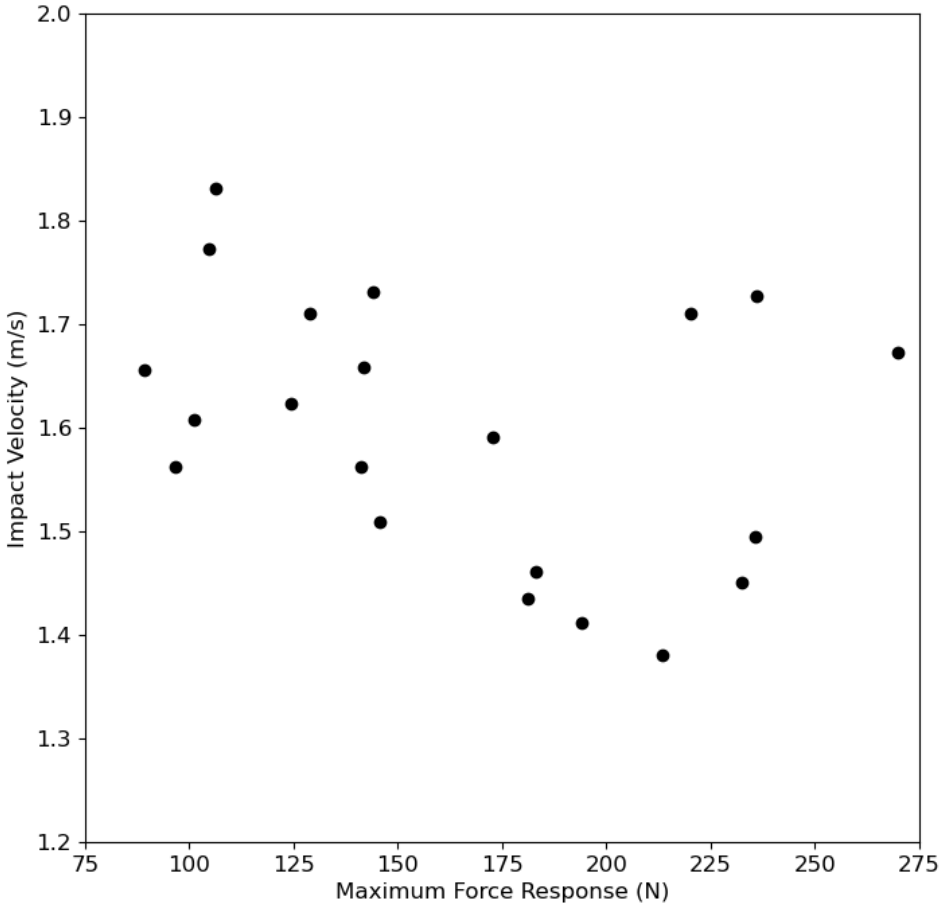


Figure 3.34: Measured Maximum Force Response vs Measured Impact Velocity

3.7 Results and Discussion

This section presents and discusses the debris impact force histories generated for each method and how these debris impact force histories influence the force response of the

column modelling the structure outlined in Stolle et al. (2019). Figure 3.35 presents the fitting results from the SDOF method for one of the experimental force response histories. From Figure 3.35, the conclusion can be made that the SDOF fit resulted in a force response that is in phase with the experimental data. Furthermore, after the initial peak of the force response, the SDOF method captured the magnitude of the subsequent peaks but underestimated the maximum measured force response by 40.0%. Additionally, the SDOF method was not able to capture the dual peak behavior in the initial response as the dual peak behavior was attributed to higher mode effects.

From Figure 3.35, the results from the MDOF fitting method can also be observed. Similar to the SDOF fitting method, the MDOF fitting method resulted in a force response that is in phase with the measured force response data. However, the MDOF fitting method was capable of capturing all peaks of the measured response and underestimated the maximum measured force response by 8.7%. Furthermore, the MDOF response captured the dual peak behavior present in the initial response, as the MDOF method allows for higher mode responses to be captured. Comparing the two fitting methods, the conclusion can be made that both methods captured the general response of the system, however, the MDOF method performed better at capturing the maximum measured force response and the higher mode effects.

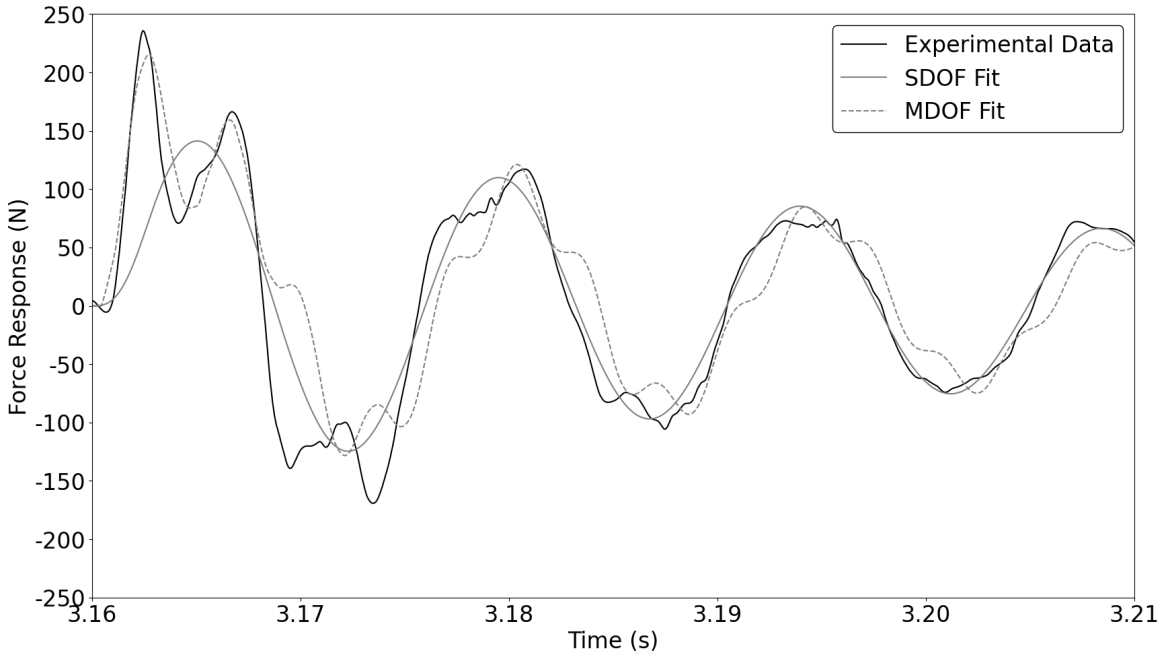


Figure 3.35: SDOF and MDOF Fitting Methods Compared to the Experimental Data

Following the fitting algorithm, the impact force histories that generated the force responses in Figure 3.35 were extracted for both the SDOF and MDOF methods. For the experimental force response history outlined in Figure 3.35, the impact velocity was measured to be $1.50\frac{m}{s}$ and using the debris and structures materials properties as outlined

in Stolle et al. (2019), two impact force histories can be generated by following Clauses 6.11.2 and 6.11.8 of ASCE 7 (2016). The two methods differ by using either the debris or structure stiffness values. All of these impact force histories are plotted in Figure 3.36 and Table 3.6 outlines the impact magnitude, duration, and impulse for each impact history.

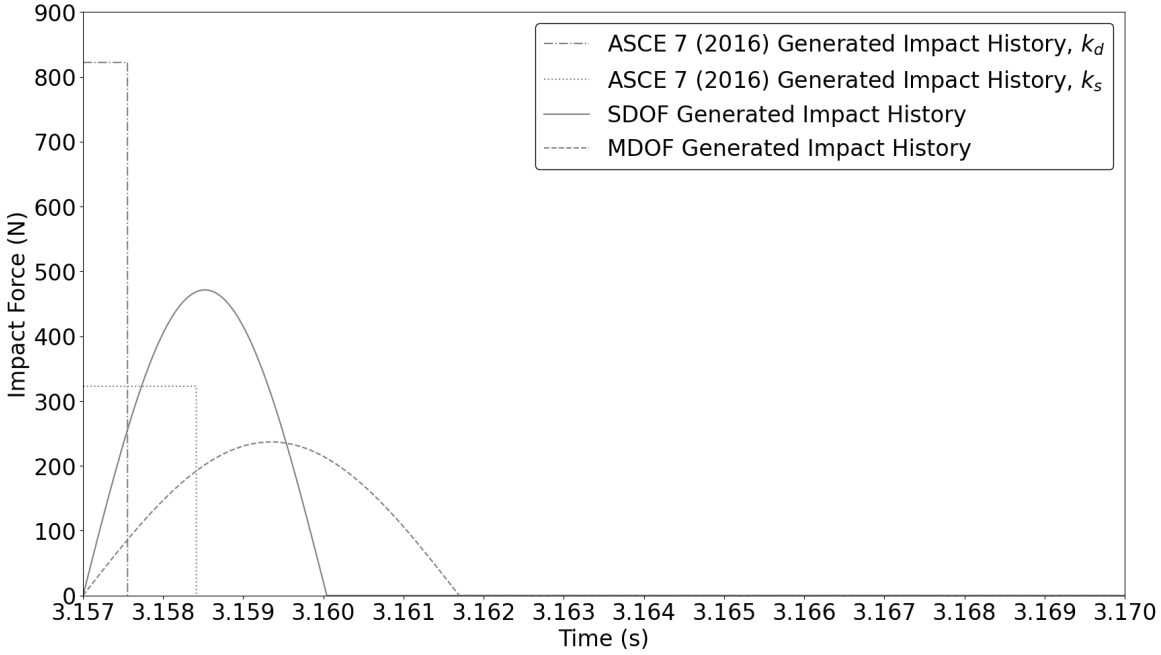


Figure 3.36: Impact Force Histories for All Methods

Method	Magnitude (N)	Duration (s)	Impulse (Ns)
ASCE 7 (2016) using k_d	822.34	0.0006	0.46
ASCE 7 (2016) using k_s	322.83	0.0014	0.46
SDOF	471.49	0.0030	0.91
MDOF	236.93	0.0047	0.71

Table 3.6: Impact History Properties

From Figure 3.36 and Table 3.6 it can be observed that using either the debris or structure stiffness in the debris impact formulation results in a significantly different impact history. This highlights the importance of the stiffness parameter when calculating the debris impact magnitude and duration. Applying these impact force history curves to the MDOF model results in the force responses outlined in Figure 3.37.

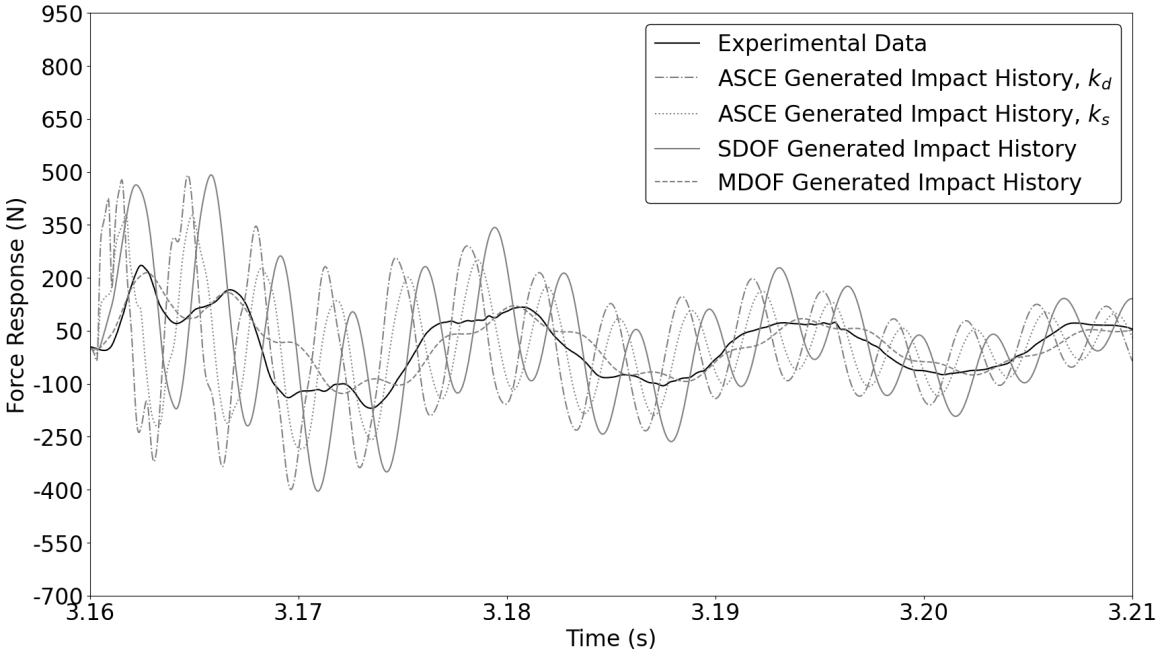


Figure 3.37: Force Response for All Methods

From Figure 3.37, the conclusion can be made that only the MDOF method for generating the impact force history resulted in a response that models the experimental data accurately both in frequency and in magnitude. Additionally, only the MDOF method was capable of capturing the dual peak behaviour present in the initial response. All other methods overestimated the frequency and magnitude of the measured response.

Extending this analysis for all 22 experimental data points, a suite of impact force history curves can be generated for each method as shown in Figures 3.38, 3.39, 3.40, and 3.41.

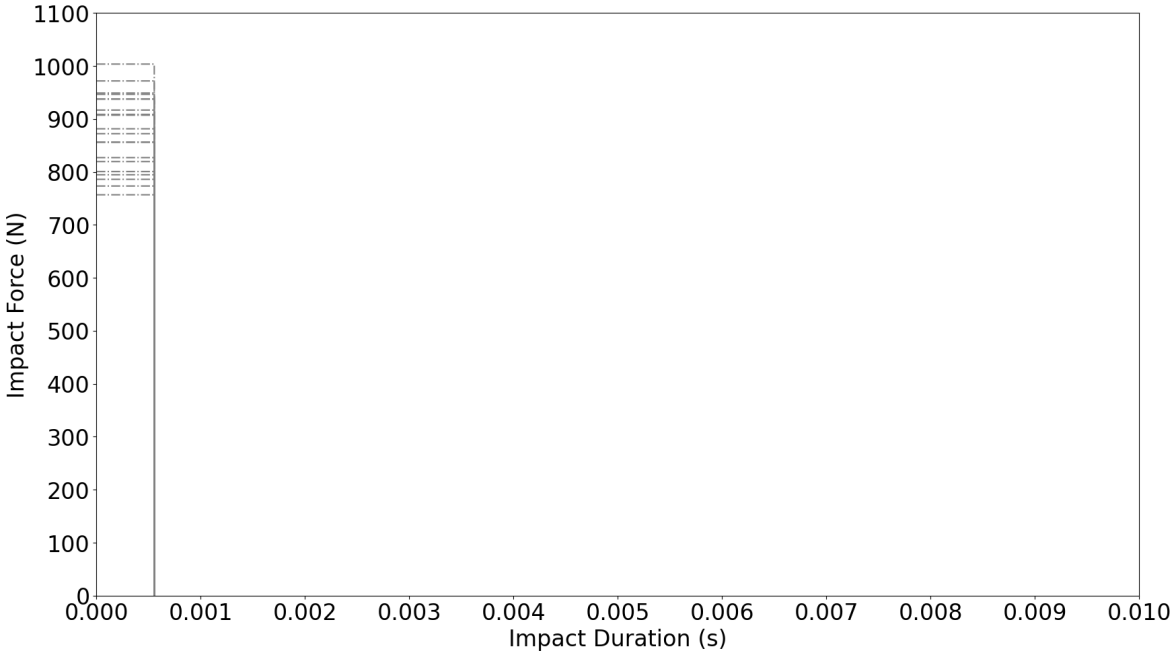


Figure 3.38: Impact Force History Suite for ASCE 7 (2016) Method Using k_d

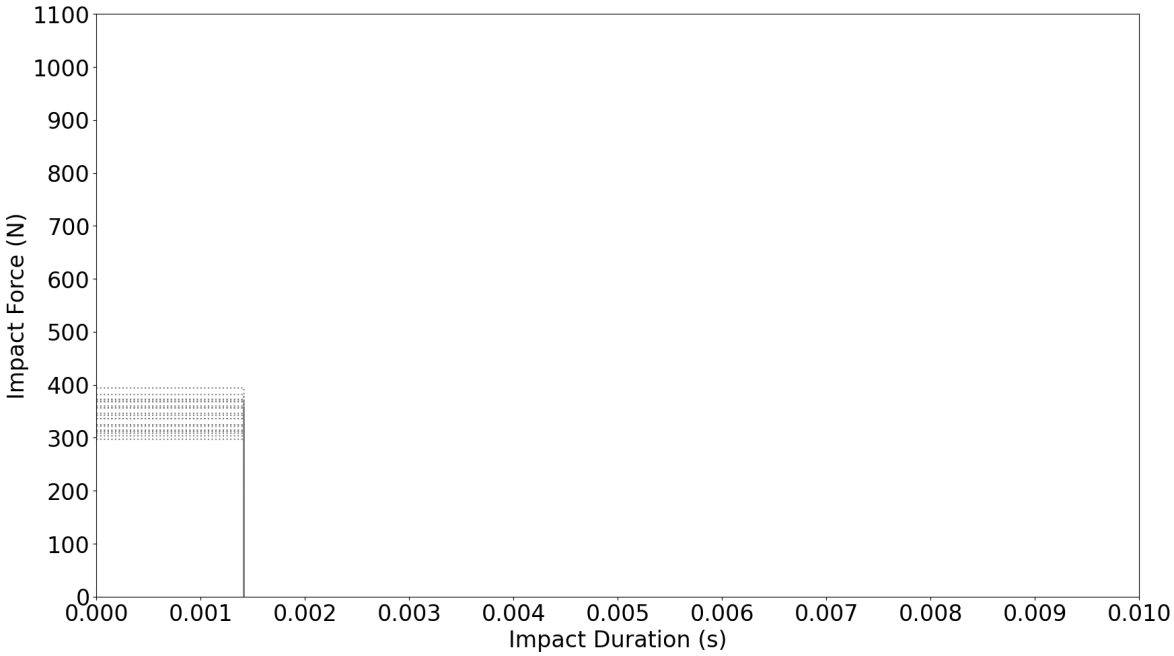


Figure 3.39: Impact Force History Suite for ASCE 7 (2016) Method Using k_s

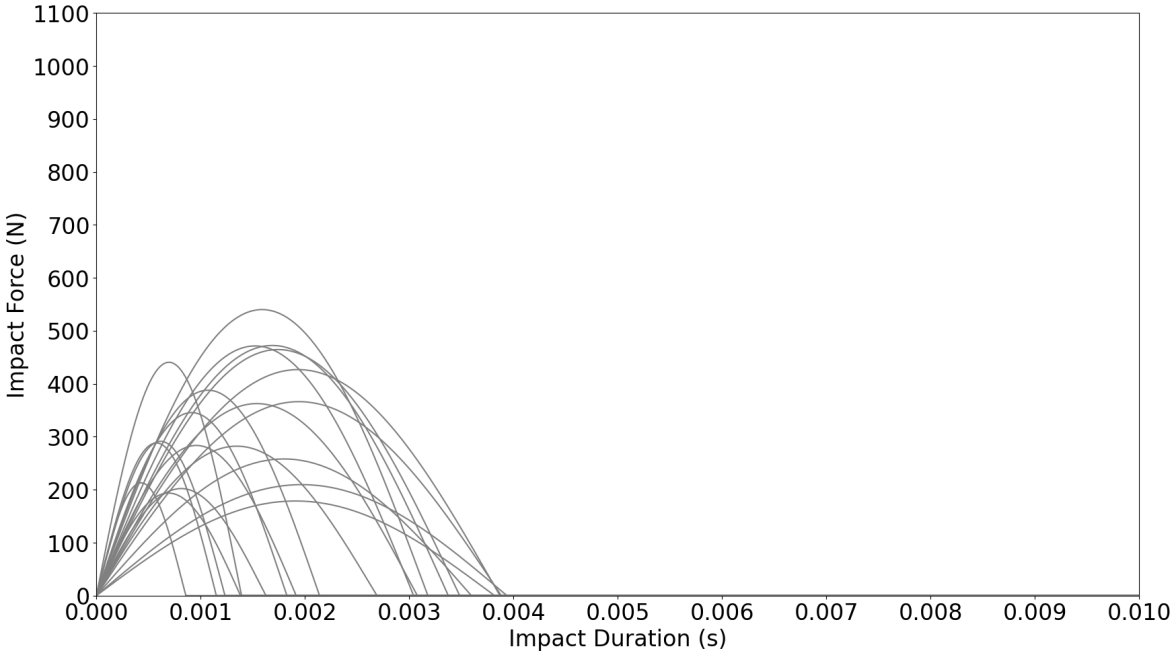


Figure 3.40: Impact Force History Suite for SDOF Method

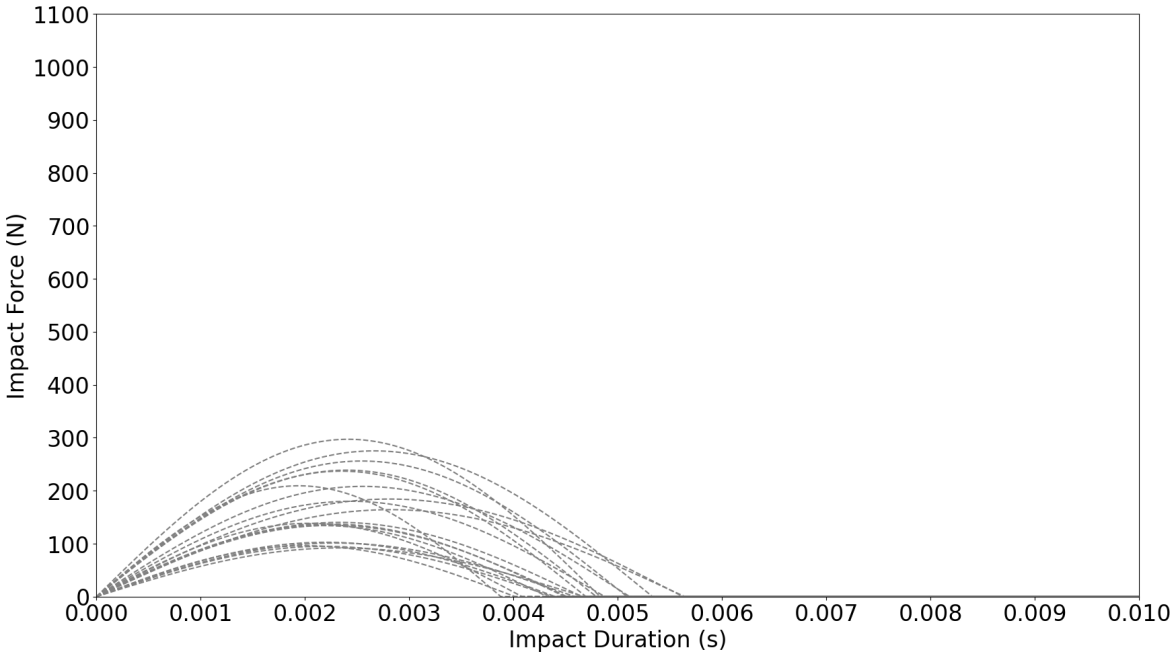


Figure 3.41: Impact Force History Suite for MDOF Method

Table 3.7 outlines the mean and standard deviation of the impact magnitude, duration and total impulse for each impact force history suite.

Method	Magnitude (N)		Duration (s)		Impulse (Ns)	
	Mean	Std.	Mean	Std.	Mean	Std.
ASCE 7 (2016) using k_d	875.25	70.22	0.0006	0.0000	0.49	0.04
ASCE 7 (2016) using k_s	343.60	27.57	0.0014	0.0000	0.49	0.04
SDOF	333.96	106.94	0.0026	0.0010	0.57	0.32
MDOF	171.07	62.91	0.0047	0.0005	0.52	0.22

Table 3.7: Statistics for Each Impact Force History Suite

Observing Figures 3.38, 3.39, 3.40, 3.41, and Table 3.7, the impact force history suites developed using ASCE 7 (2016) resulted in no variation in the impact durations as the impact velocity does not influence the impact duration based on the formulas outlined in Clause 6.11.2 of ASCE 7 (2016). Additionally, it is noted that the stiffness value used in Clause 6.11.2 of ASCE 7 (2016) has a significant influence on the impact magnitude and duration. However, regardless of the type of stiffness value chosen the total impulse into the system will be the same when developing impact force histories by following Clauses 6.11.2 and 6.11.8 of ASCE 7 (2016). Comparing the impact force history suites developed using the SDOF and MDOF fitting methods, it is apparent that the SDOF method resulted in a larger range of impact magnitudes and durations when compared to the MDOF method.

Using the impact force history suites outlined in Figures 3.38, 3.39, 3.40, and 3.41 as input into the MDOF model, the maximum modelled force response can be directly compared to the maximum measured force response as shown in Figure 3.42.

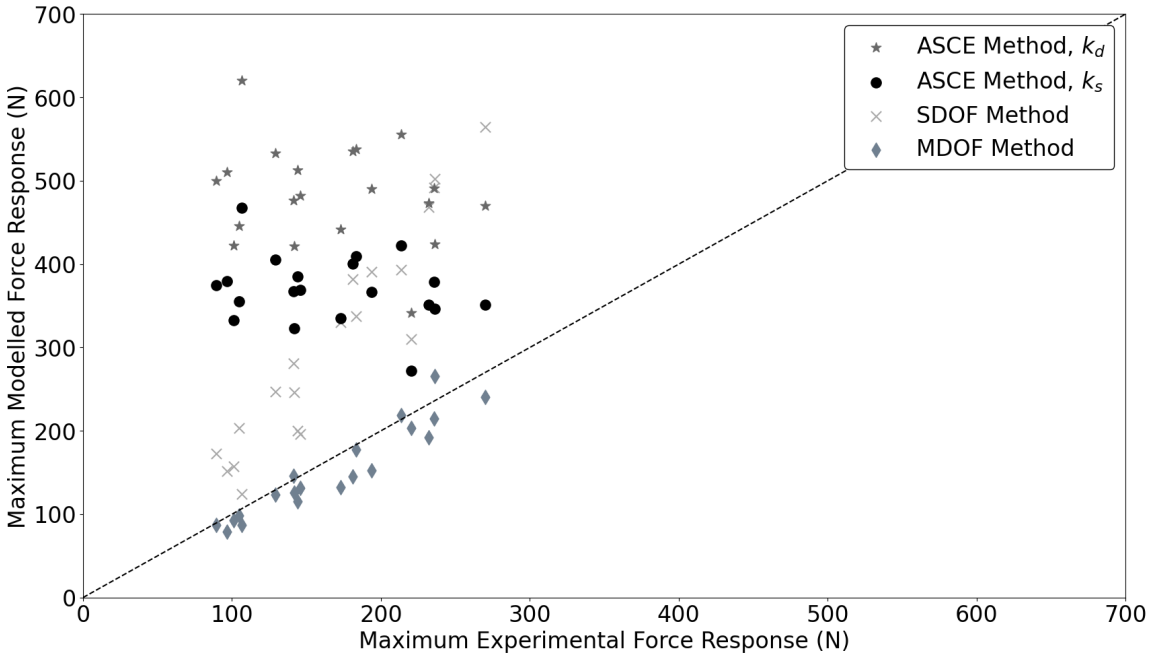


Figure 3.42: Maximum Experimental vs Maximum Modelled Force Response

Observing Figure 3.42, the dashed black line represents the 1 : 1 ratio line which

corresponds to when the maximum modelled shear force response at the force transducer location is equal to the maximum experimental force response. From Figure 3.42, the maximum modelled force responses resulting from the impact histories developed by the SDOF fitting method show a large range in variability, which is directly correlated to the variability of the impact force histories shown in Figure 3.40. For example, using the SDOF method to estimate impact force histories resulted in events that induced a maximum modelled force response at both $300N$ and $500N$ while the measured maximum force response is $225N$. This result indicates that even though a SDOF system subjected to the impact force history may provide a response that is in general agreement with the measured data, when that same impact force history is applied to a MDOF system, the impact force history no longer results in a realistic force response. This is evident in Figure 3.42 as the scatter associated with the SDOF fitting method fall far from the $1:1$ line, meaning the maximum modelled force responses developed in the MDOF model using the impact force histories generated from the SDOF fitting method do not accurately represent the maximum experimental force responses. On average, using the SDOF method for estimating the impact force history resulted in a maximum force response that is 1.8 times larger than the maximum measured force response. However, this value ranges from 1.2 to 2.1 times larger than the maximum measured force response. Furthermore, as the maximum measured force response increases, the amount that the SDOF method overestimates the measured force response also increases. Suggesting that as impact force histories increase in magnitude, the validity of the using a SDOF method to estimate debris impact force histories decreases.

Observing the maximum modelled force responses resulting from the impact histories developed by the MDOF fitting method, it can be concluded that the MDOF fitting method resulted in a good approximation of the maximum measured force responses. This is shown in Figure 3.42 as the scatter associated with the MDOF method fall close to the $1:1$ line, meaning the MDOF method for estimating impact force histories provides realistic impact force histories and force responses. On average the MDOF method for estimating the impact force history resulted in a maximum force response that is nine tenths the maximum measured force response. This highlights that the MDOF method typically underestimates the measured maximum force response. However, this value ranges from four fifths the maximum measured force response to 1.1 times larger than the maximum measured force response.

From Figure 3.42, the maximum force responses induced by the impact force histories developed by following Clauses 6.11.2 and 6.11.8 of ASCE 7 (2016) are also presented. It is apparent from the plot that regardless of the stiffness value chosen, the maximum force response developed using the methods outlined in ASCE 7 (2016) resulted in an overestimation of the maximum measured force response. When the debris stiffness is used, the maximum modelled force responses are larger than when the structure stiffness is used, as the debris stiffness is larger than the structure stiffness, which has a direct correlation to the impact magnitude as per Eq. 3.16. When the debris stiffness is used to generate the impact force histories, the resulting maximum modelled force responses are on average 1.3 times larger than the maximum modelled force responses developed when the structure stiffness is used to generate the impact force histories, however, this value ranges

from a minimum of 1.2 and a maximum of 1.35 times larger. Additionally, on average, when the structure stiffness is used, the maximum modelled force response is 2.5 times larger than the measured value, with a minimum of 1.2 and a maximum of 4.4 times larger than the measured value. Whereas, when the debris stiffness is used this value increases to 3.3, with a minimum of 1.5 and a maximum of 5.8 times larger than the measured value.

3.8 Conclusions

This study outlined different methods for estimating debris impact histories and analysed how these methods approximated experimental force response data. Also presented in this study is how Chapter 6 Tsunami Loads and Effects of ASCE 7 (2016) estimates debris impact histories and how the formulations outlined in the standard compare to alternative methods for estimating debris impact histories. The main conclusions are as follows:

1. The choice of stiffness value in Clause 6.11.2 of ASCE 7 (2016) has a large influence on the impact force histories generated.
    - Assuming the larger stiffness value will always lead to larger impact forces and smaller impact durations. If the smaller stiffness value is chosen the opposite is true.
    - The total impulse into the system will always be the same when either the debris or the structure stiffness is used.
2. Following Clauses 6.11.2 and 6.11.8 in ASCE 7 (2016) resulted in an overestimation of the forces developed in a structural model and an overestimation of the frequency of the response.
    - For the experimental data set presented in this study, the maximum modelled force response when the structure stiffness was used, was on average 2.5 times larger than the maximum measured force response. When the debris stiffness was used, the maximum modelled force response was on average 3.3 times larger than the maximum measured force response.
3. Using a SDOF system to estimate an impact force history may provide a response that is in general agreement with the measured data. However, when that same impact force history is applied to a MDOF system, that impact force history no longer results in a realistic force response.
4. Using a MDOF system to estimate the impact force history resulted in a good approximation of the measured force response data.
5. When all impact force histories were applied to the same MDOF model, only the impact force histories developed from the MDOF fitting method resulted in a response that was in phase and of similar magnitude to the experimental data. All alternative methods for estimating impact force histories resulted in force responses that overestimated the frequency and magnitude of the experimental responses.

Presented in this study is how debris impact loads can be estimated by Clauses 6.11.2 and 6.11.8 in ASCE 7 (2016) and how these loads compare to alternative methods for estimating debris impact loads. It was shown in this study that following the guidelines in Clauses 6.11.2 and 6.11.8 in ASCE 7 (2016) resulted in a force response that overestimated both the frequency and the magnitude of the experimental force response data. One of the requirements for developing debris impact force histories as per Clause 6.11.8 of ASCE 7 (2016) is that the shape of the impact history must be a rectangular pulse. The significance of assuming a rectangular pulse impact shape is investigated in the parametric study outlined in Chapter 4.

One of the limitations to this study is that it was assumed that the structure can be modelled with only elastic beam-elements. A future study could investigate the validity of this assumption by performing a full finite element analysis in three-dimensional space and investigating how the loads generated in each direction compare to the experimental data of Stolle et al. (2019). Another limitation of this study is that the debris was not explicitly modelled, only a point load associated with the debris impact magnitude and duration was applied to the models. A future study could investigate the validity of this assumption by performing a two-body impact simulation that considers the deformation of both the structure and debris.

Chapter 4

Parametric Study on the Influence of Impact Shape on Response Parameters[1]

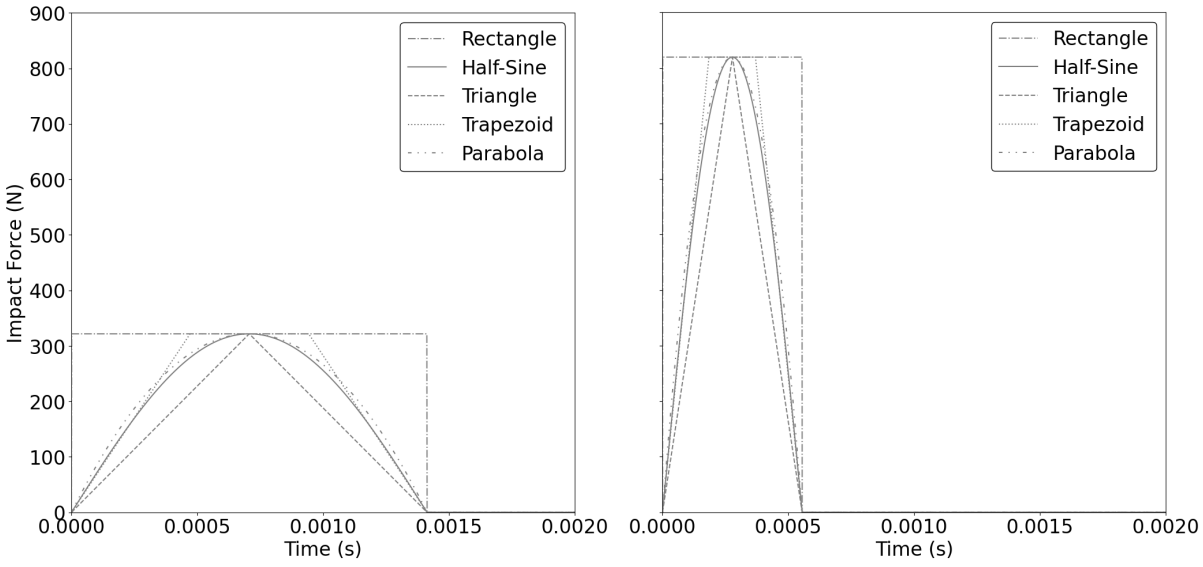
4.1 Objectives and Description of Methodology

Clause 6.11.8 of ASCE 7 (2016) allows a dynamic analysis to be performed in order to calculate the structural response to the impact magnitude and duration defined by Clause 6.11.2 of ASCE 7 (2016). The dynamic analysis is to be performed by applying the impact force as a rectangular pulse, however, previous studies have suggested that for full-scale in-air shipping container impacts the impact force history has a shape more representative of a half-sine wave (Aghl et al., 2014).

The objective of this study is to conduct a parametric analysis on the influence that the impact shape has on the response history of the column outlined in Section 3.5, both the shear and deflection responses are presented. Specifically, the scope of this analysis is bounded to five impact shapes, two stiffness values for calculating the impact magnitudes and durations, and the experimentally determined debris impact velocities outlined in Figure 3.34. The impact force histories are calculated by using the impact magnitudes and durations outlined by Clause 6.11.2 of ASCE 7 (2016) for five different impact shapes: (1) Rectangular; (2) Half-Sine; (3) Triangular; (4) Trapezoidal; and (5) Parabolic. The impact magnitudes and durations are calculated using the experimental data from Stolle et al. (2019). Specifically, the experimentally determined debris impact velocities outlined in Figure 3.34, the structure and debris stiffness, and the debris mass; which were determined to be $4.685 \times 10^5 \frac{N}{m}$, $3.04 \times 10^6 \frac{N}{m}$, and $0.236kg$ respectively (Stolle et al., 2019). The results are presented for both stiffness values to highlight the importance that the stiffness value has on the impact force history and consequently, on the response of the column when following the guidelines outlined in Clause 6.11.2 of ASCE 7 (2016).

[1]This Chapter forms a portion of a manuscript being prepared for submission to the Journal of Structural Engineering.

Following Clause 6.11.2 of ASCE 7 (2016) to estimate the impact magnitude and duration, an impact history can be developed for each impact shape and stiffness value as shown in Figure 4.1. Each impact history is then applied to the MDOF model described in Section 3.5 and the influence of the impact shape is investigated by analysing the shear and deflection responses of the column.



(a) k_s (b) k_d

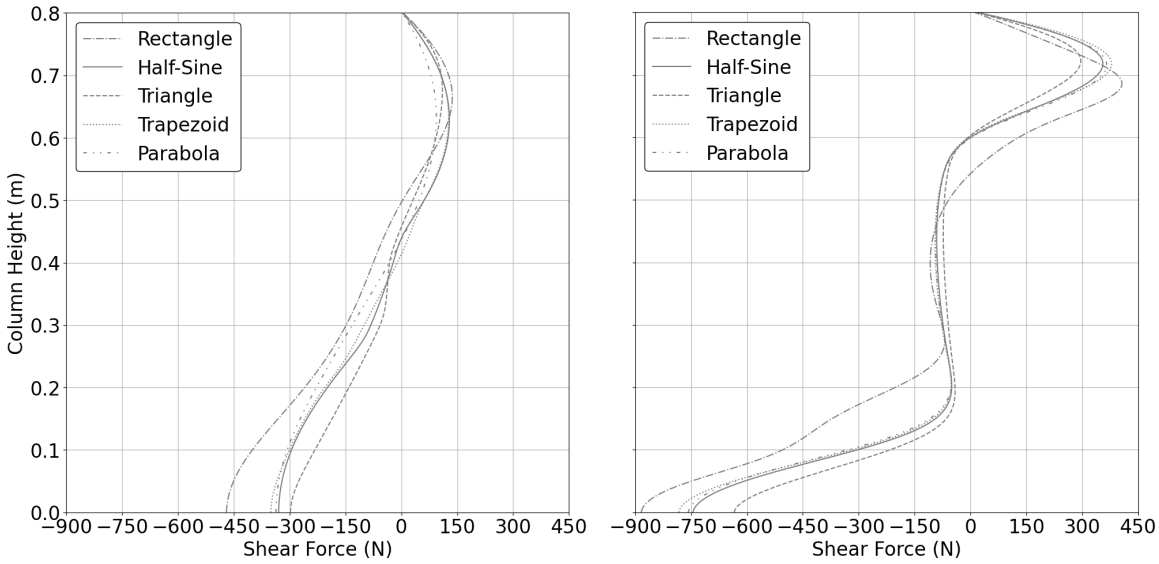
Figure 4.1: Example Impact Histories for Parametric Study

4.2 Results and Discussion

This section presents and discusses how the impact shape influences the response of the column outlined in Section 3.5 by investigating both the shear and deflection responses of the column.

4.2.1 Shear Response

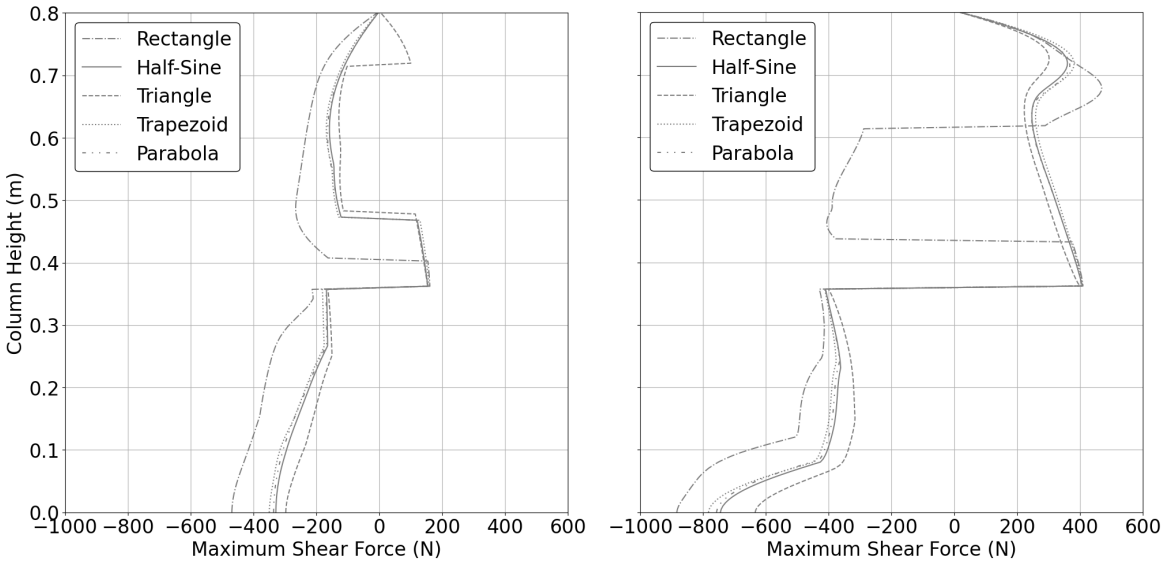
Using the impact force histories outlined in Figure 4.1, the shear force diagrams at the point in time when the base shears are maximum is presented for each impact shape in Figure 4.2.



(a) k_s (b) k_d

Figure 4.2: Shear Force Diagram at Point in Time When Base Shear is Maximum

From Figure 4.2 it is clear that using a rectangular impact shape resulted in the largest shear forces developed in the column, while the triangular impact shape resulted in the smallest shear forces. All other impact shapes resulted in a very similar response and furthermore, the overall shape of the response is similar for each impact shape. It is also evident from Figure 4.2 that the magnitude of the impact force has a direct correlation to the maximum base shear the column developed. When the structure stiffness is used, the maximum base shear ranges from a minimum of $300N$ to a maximum of $470N$, with an impact magnitude of $320N$. When the debris stiffness is used the maximum base shear ranges from a minimum of $635N$ to a maximum of $885N$, with an impact magnitude of $820N$. Furthermore, it can be concluded that assuming one stiffness value over another when developing the impact history has a significant influence on the forces developed in the column. Figure 4.3 presents the maximum shear forces developed in each element at any point in time during the structures response.



(a) k_s (b) k_d

Figure 4.3: Maximum Shear Forces Developed in the Column

From Figure 4.3, it is evident that at the point of impact, which in this particular example is at approximately $0.36m$, large shear forces are developed in the column. This highlights the importance of knowing the impact location along the height of the column. Additionally, note that the point in time when the base shear is maximum does not correlate to when the shear forces are maximum in other parts of the column, this is due to shear wave propagation along the height of the column. Also similar to Figure 4.2, assuming a rectangular impact shape resulted in the largest shear forces developed along the height of the column and assuming a triangular impact shape resulted in the smallest shear forces. All other impact shapes provided similar shear forces that were bounded by the rectangular and triangular impact shape results. Furthermore, it is clear from Figure 4.3 that assuming one stiffness value over another when developing the impact history has a significant influence on the forces developed in the column.

Figure 4.4 extends the analysis to all 22 data points and describes how the maximum base shear changes based on the type of stiffness value chosen when developing the impact history. From Figure 4.4, it can be seen that when the debris stiffness is used to generate the impact force history, the maximum base shear will always be larger than if the structure stiffness is used. This is due to the fact that when the debris stiffness is used, the impact magnitude increases due to the debris stiffness being larger than the structure stiffness. The magnitude of the stiffness has a direct influence on the magnitude of the impact force based on Eq. 3.16. Plotted on Figure 4.4 are the $1:1$ and $1:2$ ratio lines, which correspond to when the maximum base shears are equivalent for both stiffness values and when the maximum base shear resulting from using the debris stiffness is twice as large as the maximum base shear resulting from using the structure stiffness. From Figure 4.4, the maximum base shear resulting from using the debris stiffness and a rectangular impact shape is on average 2.0 times larger than when the structure stiffness is used, but ranges

from 1.9 to 2.4 times larger. When the impact shape is a half-sine, trapezoid, or parabola, the average increases to 2.1 times larger with a range from 2.0 to 2.4 times larger. Finally, when the impact shape is triangular, the average is 2.1 times larger with a range from 2.0 to 2.3 times larger.

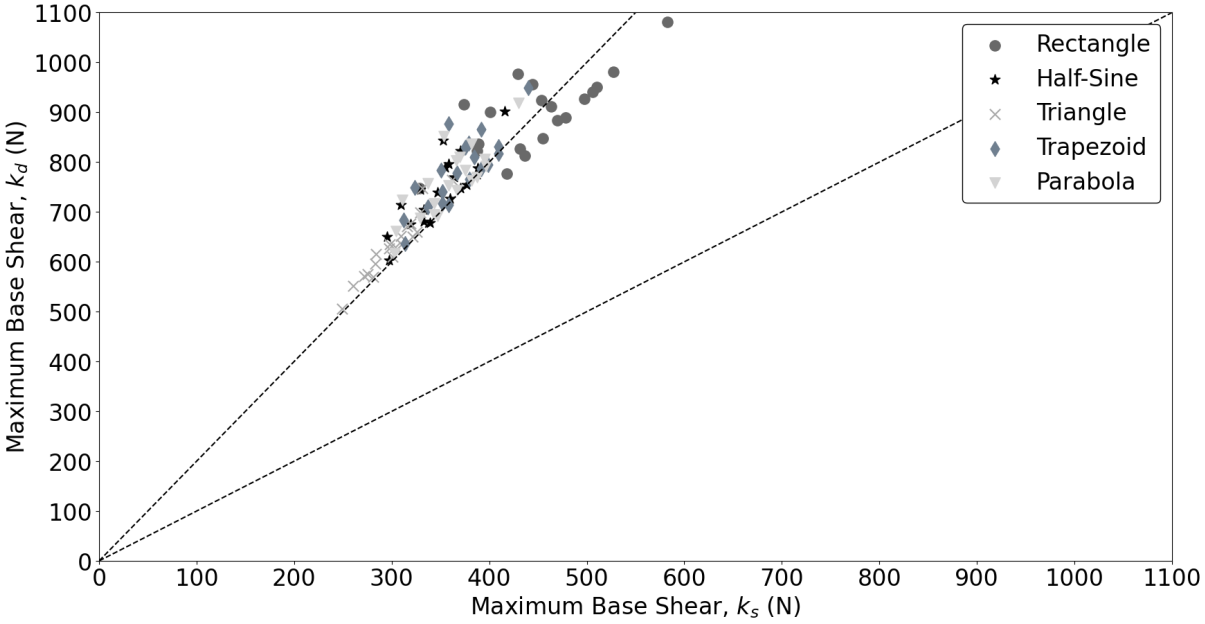


Figure 4.4: Maximum Base Shear, k_s vs k_d

Figure 4.5 nondimensionalizes the maximum base shear by the associated impact magnitude to determine the relative influence that the impact magnitude has on the maximum base shear. From Figure 4.5, it is apparent that the nondimensionalized maximum base shear associated with the impact histories developed using the structures stiffness are larger when compared to the data points using the debris stiffness. This indicates that the ratios of the maximum base shear to the impact magnitude are larger when the structures stiffness is used to develop the impact force history. This result can be interpreted as the impact force histories developed using the structures stiffness produce relatively larger maximum base shears compared to those generated using the debris stiffness. Additionally, in Figure 4.5 the influence of the impact shape on the nondimensionalized maximum base shear can be observed. The rectangular impact force histories produced the largest nondimensionalized maximum base shears and the triangular impact histories produced the smallest nondimensionalized maximum base shears, with all other results from using the alternative impact shapes falling between these two bounds. These results directly support the conclusion that a rectangular impact shape will produce the largest base shear forces when compared to all other impact shapes investigated in this study.

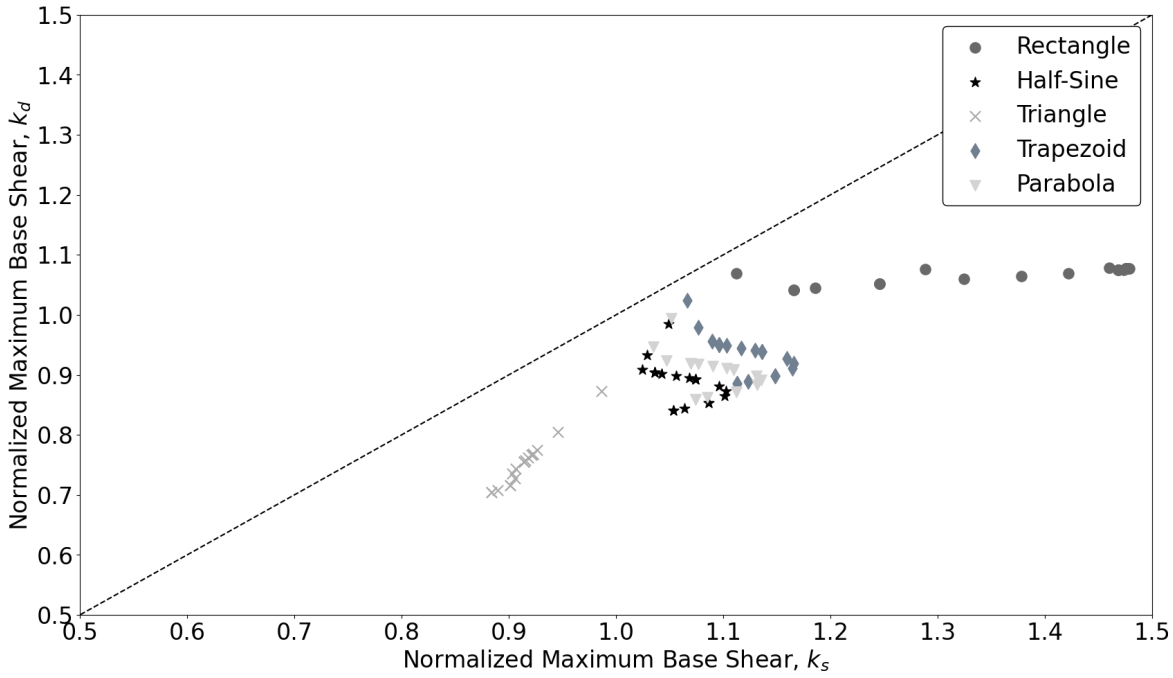
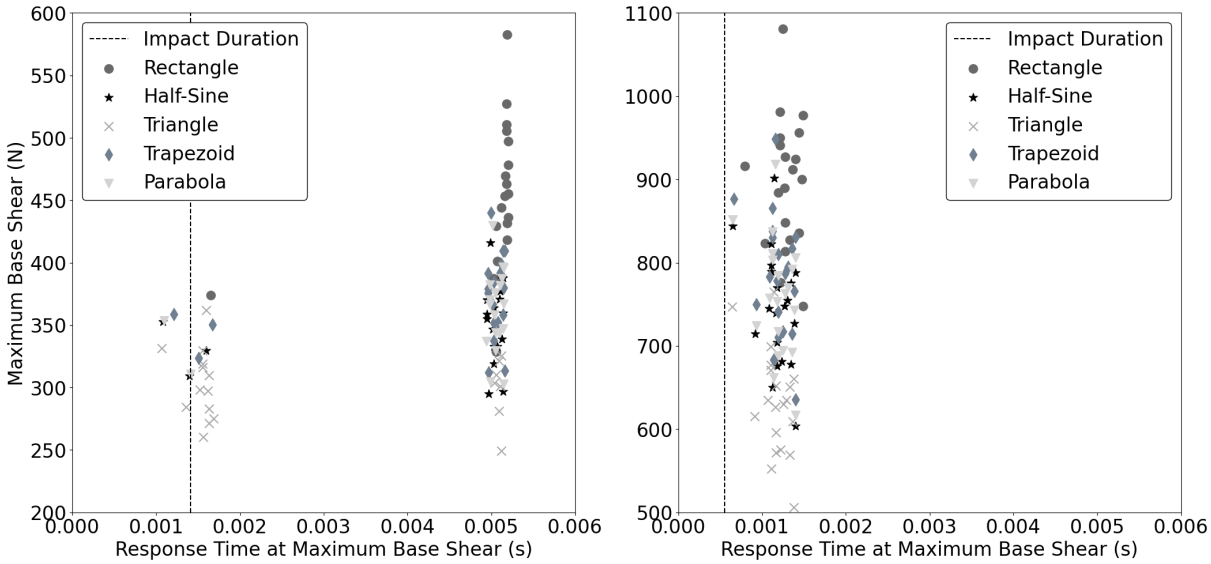


Figure 4.5: Normalized Maximum Base Shear, k_s vs k_d

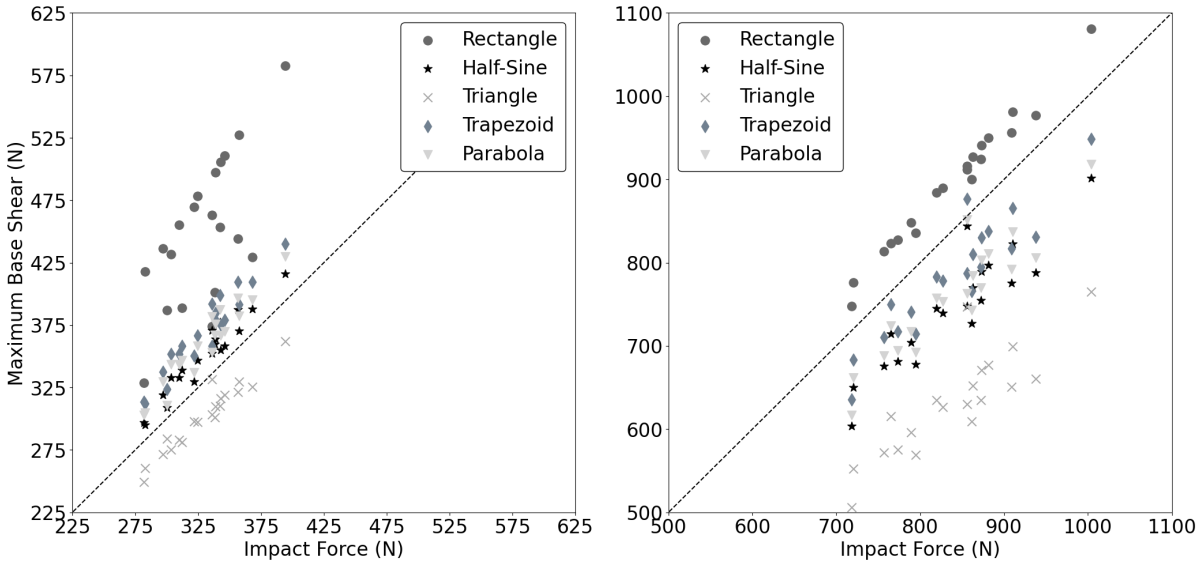
Figure 4.6 outlines the magnitude of the maximum base shear and the time at which it peaked. Also shown in Figure 4.6 is a dashed line defining the end of the impact duration, which for the impact history developed using the structure stiffness is $0.014s$ and for the debris stiffness it is $0.00055s$. Using the structure stiffness to develop the impact histories resulted in two distinct groups of scatter points. The first group of scatter points show that the base shears peaked at approximately the end of the impact duration. Whereas, the second group of scatter points show that the base shears peaked at approximately 3.6 times the impact duration. However, when the debris stiffness is used to develop the impact history, there is only one group of scatter points that are on average 2.1 times the impact duration. These results suggest that when using the smaller stiffness value (i.e. structure stiffness in this study), the impact shape plays a larger role in determining when the base shear peaks when compared to using a higher stiffness value (i.e. debris stiffness in this study). When a higher stiffness value is used, the time at which the base shears peaked becomes less sensitive the impact shape when compared to a lower stiffness value. Furthermore, the importance of including damping in the model is evident as the majority of the base shears in this study peaked after the impact duration, meaning the structure was in a free vibration response.



(a) k_s (b) k_d

Figure 4.6: Time at Peak Base Shear

Figure 4.7 outlines the magnitude of the maximum base shears and the associated impact forces that generated the responses. The dashed line represents the $1:1$ ratio line, which defines when the maximum base shear is equal to the impact force. From Figure 4.7, it is apparent that when the structure stiffness is used the maximum base shear is larger than the impact force for all impact shapes except the triangular impact shape. Whereas, when the debris stiffness is used the maximum base shear is smaller than the impact force for all impact shapes except the rectangular impact shape. This result confirms the conclusion that the impact force histories developed using the structures stiffness produce relatively larger maximum base shears when compared to those generated using the debris stiffness. Additionally, from Figure 4.7, it is clear that the rectangular impact shapes resulted in the largest base shears, the triangular impact shapes resulted in the smallest base shears, and all other impact shapes resulted similar base shears that were bounded by the rectangular and triangular impact shape results.

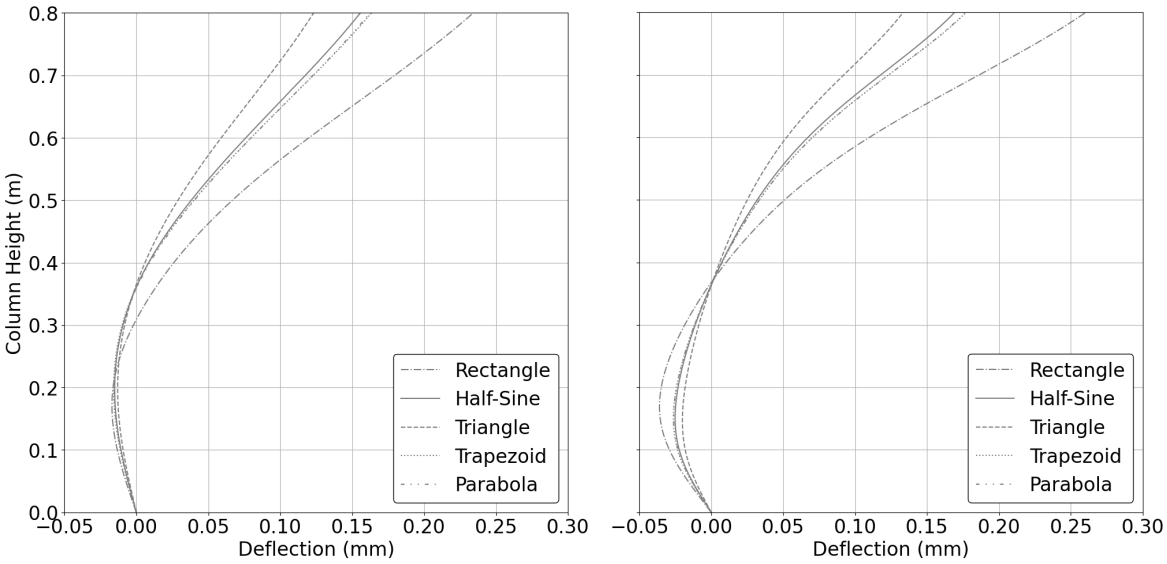


(a) k_s (b) k_d

Figure 4.7: Maximum Base Shear vs Impact Force

4.2.2 Deflection Response

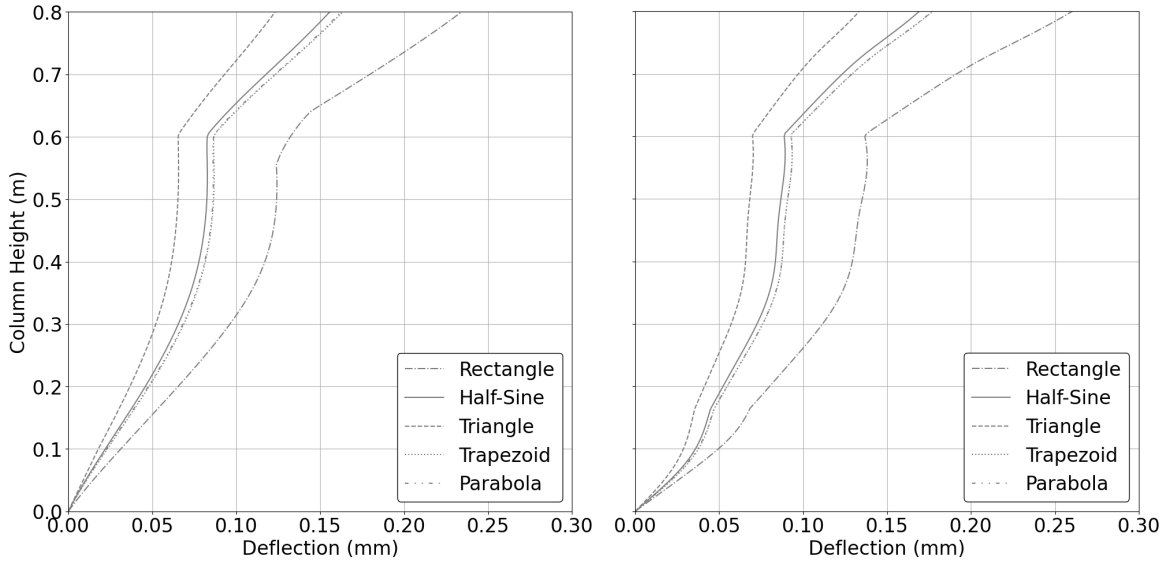
The deflection diagrams for the example impact force histories outlined in Figure 4.1 are presented in Figure 4.8 for all impact shapes at the point in time when the top deflection is maximum during the structures response. From Figure 4.8, it is evident that the rectangular impact shape resulted in the largest deflections along the height of the column and the triangular impact shape resulted in the smallest. All other impact shapes resulted in deflections that are bounded by the rectangular and triangular impact shape results, as also observed with the shear forces. When comparing the response derived from using the debris stiffness to the response derived from using the structures stiffness, it is apparent that using the response derived from the debris stiffness resulted in larger deflections. This is due to the impact magnitude being larger when the debris stiffness is used to develop the impact force history, as shown in Figure 4.1.



(a) k_s (b) k_d

Figure 4.8: Deflection Diagram at Point in Time When Top Deflection is Maximum

Figure 4.9 presents the maximum deflections developed at each node at any point in time during the structures response.



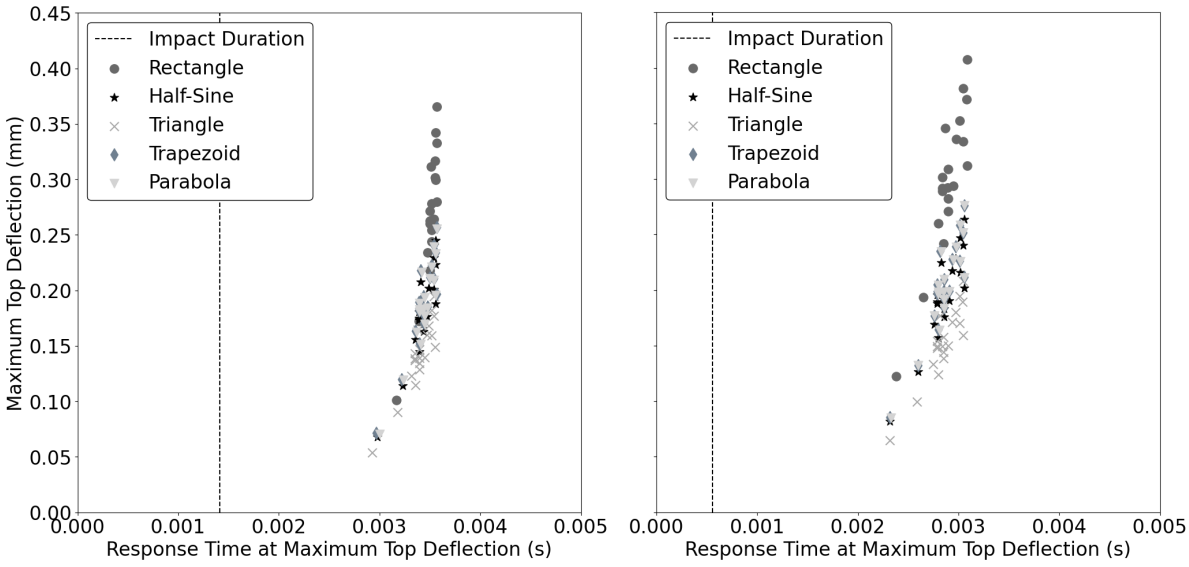
(a) k_s (b) k_d

Figure 4.9: Maximum Deflections Developed in the Column

From Figure 4.9, it is evident that similar to the shear forces, the point in time when the maximum top deflection occurs does not correlate to when the deflection is maximum at other nodes. Also similar to the shear forces, assuming a rectangular impact shape resulted in the largest deflections developed along the height of the column, with the

triangular impact shape resulting in the smallest, and all other impact shapes resulting in deflections that are bounded by those two results.

Comparing the maximum deflections resulting from using the impact histories developed by either the debris or structures stiffness shows that both stiffness values resulted in similar maximum deflections. For example, when the rectangular impact shape is used the maximum top deflection resulting from using the debris stiffness is $0.26mm$, while when the structure stiffness is used a deflection of $0.23mm$ is developed, this is a 10% decrease in maximum top deflection. This result suggests that assuming one stiffness value over another does not influence the deflections in this column significantly. Furthermore, this suggests that the maximum deflection response peaks during the free vibration period, after the impact load has occurred. This is further validated in Figure 4.10 where the magnitude of the maximum top deflection and the time at which it peaked is plotted. When using the structure stiffness to develop the impact history, the impact duration for all data points is $0.0014s$ and the top deflections for all impact shapes peaked on average 2.4 times the impact duration or $0.0034s$. When the debris stiffness is used to develop the impact force history, the impact duration for all data points is $0.00055s$ and the top deflections for all impact shapes peaked on average 5.1 times the impact duration or $0.0028s$. This result implies that the shorter impact duration associated with using the debris stiffness causes the top deflection to peak sooner than when the structure stiffness is used.



(a) k_s (b) k_d

Figure 4.10: Time at Peak Top Deflection

Figure 4.11 outlines how the maximum deflections compare to each other when using either the structure or debris stiffness to develop the impact histories. As stated previously, the maximum top deflections resulting from using impact histories developed by the debris stiffness are slightly larger than when the structure stiffness is used to develop the impact histories. Table 4.1 quantifies how much larger the maximum top deflections are when the

debris stiffness is used compared to when the structure stiffness is used. From Table 4.1, it is clear that for all impact shapes, on average the maximum top deflections when the debris stiffness is used are 9.2% larger than when the structure stiffness is used. Furthermore, the rectangular impact shape resulted in the largest percentage increase in maximum top deflections, while the triangular impact shape resulted in the smallest percentage increase. All other impact shapes resulted in percentage increases that fall within the bounds of those generated from the rectangular and triangular impact shapes. Additionally from Figure 4.11, it is clear that for larger top deflections the difference between using the debris or structure stiffness to develop the impact force history becomes more significant. This suggests that for more severe impact forces that could push the response into the nonlinear range, the choice of the stiffness value becomes more significant. Finally, Figure 4.12 further emphasises that the rectangular impact shape provides the largest top deflections, as the scatter associated with the rectangular impact shape are always above the scatter associated with all other impact shapes.

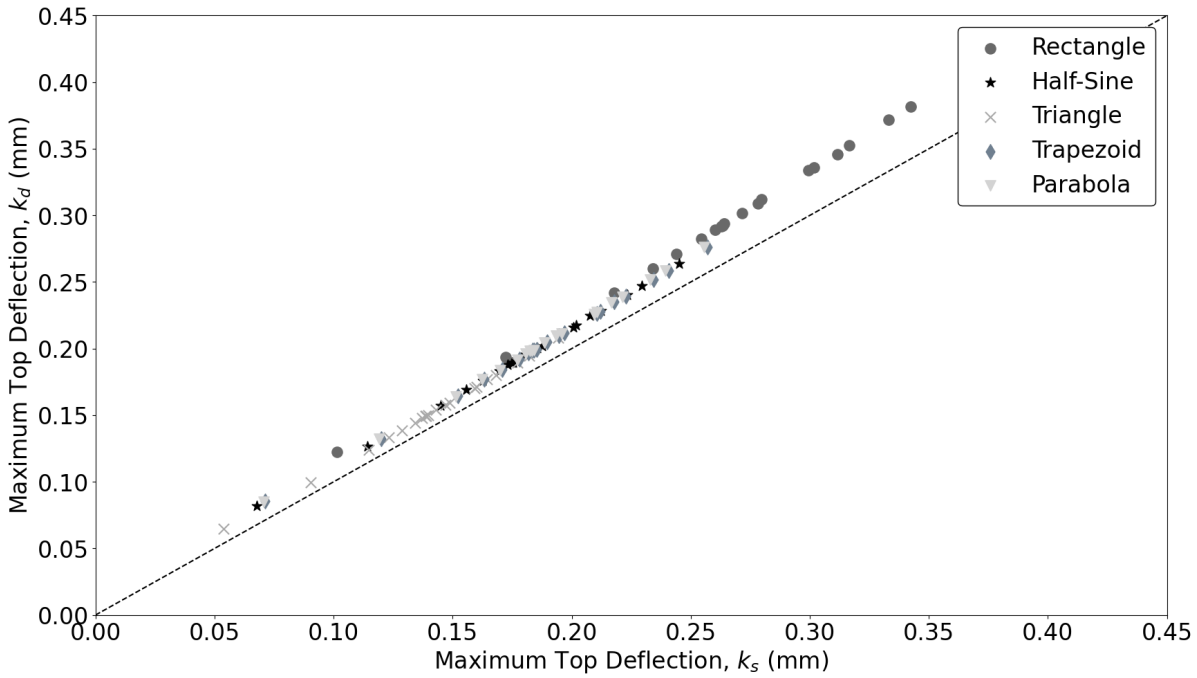
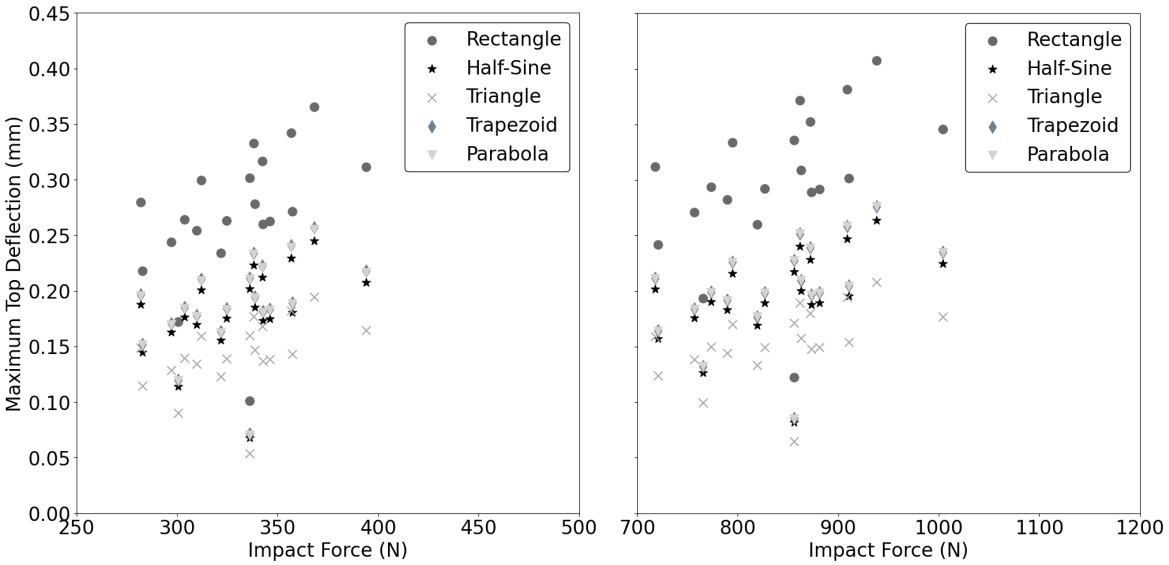


Figure 4.11: Maximum Top Deflection, k_s vs k_d

Impact Shape	Percentage Increase from k_s to k_d			
	Mean (%)	Std. (%)	Max. (%)	Min. (%)
Rectangle	11.8	2.1	20.6	11.1
Half-Sine	8.7	2.9	20.6	7.6
Triangle	8.2	3.0	20.4	6.9
Trapezoid	8.5	2.8	20.1	7.5
Parabola	9.0	2.8	20.7	7.9

Table 4.1: Percentage Increase in Top Deflection from k_s to k_d



(a) k_s (b) k_d

Figure 4.12: Maximum Top Deflection vs Impact Force

4.3 Conclusions

This study outlined how the impact shape influenced the shear and deflection responses of the column outlined in Section 3.5. Additionally, the influence of using either the debris or structure stiffness in developing the impact force history as per Clause 6.11.2 of ASCE 7 (2016) was investigated. The main conclusions are as follows:

1. The choice of stiffness value in Clause 6.11.2 of ASCE 7 (2016) has a significant influence on the shear forces developed along the height of the column. This is because the impact magnitude is directly proportional to the square root of the product of the stiffness and mass as outlined in Eq. 3.16.

2. The choice of stiffness value influences the time at which the base shears peaked. For the larger stiffness value in this study (i.e. debris stiffness), the base shears peaked

at approximately 2.1 times the impact duration. Whereas, when the smaller stiffness value (i.e. structure stiffness) was used, two groups of scatter points emerge at a time approximately equal to the impact duration and at approximately 3.6 times the impact duration.

- When the structure stiffness value is used, the impact shape played a larger role in determining when the base shears peaked compared to when the debris stiffness value was used. This implies that when a larger stiffness value is used, the peak response time becomes less sensitive to the shape of the impact history.

3. Large shear forces are developed at the impact location, which highlights the importance of understanding where the debris impacts the structure.

4. The rectangular impact shape resulted in the largest shear forces, while the triangular impact shape resulted in the smallest shear forces. All other impact shapes resulted in shear forces that were similar to each other and bounded by the results from the rectangular and triangular impact shapes. The rectangular impact shape resulted in the largest shear forces as it transmits the most impulse into the model.

5. The choice of stiffness value had a slight influence on the maximum top deflections the column developed in this study.

   - The influence of the stiffness value is more apparent for larger top deflections, which highlights the importance of understanding the stiffness value for more severe impact histories.
   - Impact histories developed using the debris stiffness always resulted in larger top deflections. On average, for the rectangular impact shape they were 11.8% larger, for the half-sine impact shape they were 8.7% larger, for the triangular impact shape they were 8.2% larger, for the trapezoidal impact shape they were 8.5% larger, and for the parabolic impact shape they were 9.0% larger.

6. The shape of the impact force history has a large influence on the maximum top deflections the column developed.

   - The rectangular impact shape resulted in the largest deflections, while the triangular impact shape resulted in the smallest deflections. All other impact shapes resulted in deflections that were similar to each other and bounded by the results from the rectangular and triangular impact shapes. The rectangular impact shape resulted in the largest deflections as it transmits the most impulse into the model.

7. As both the base shears and top deflections peaked either at or after the impact duration for this study, the influence of damping in the model is important as the structure is in a free vibration response.

Presented in this study is how the shear and deflection responses are influenced by the shape of the debris impact force history. Five impact shapes were investigated in this

study, where it was shown that a rectangular impact shape always resulted in the largest shear forces and deflections developed in the column. Whereas, the triangular impact shape always results in the smallest shear forces and deflections developed in the column. Finally, the half-sine, trapezoidal, and parabolic impact shapes all developed similar shear forces and deflections to each other, which were bounded by the results from the rectangular and triangular impact shapes. Furthermore, results were presented for impact force histories that were generated with two different stiffness values, the debris and structure stiffness from Stolle et al. (2019). These impact force histories were then applied to the same MDOF model outlined in Section 3.5 and hence, the actual stiffness of the model was not changed. This indicates that the influence of the structural stiffness on response parameters was not investigated but it is, however, an important parameter for understanding how a structure responds to debris impact loads. The significance of the structural stiffness on response parameters is investigated in the parametric study outline in Chapter 5.

As this study uses the same structure outlined in Section 3.5, the same limitations are adopted for this study. Mainly, the structure considered was modelled with elastic beam-elements and as such, the results presented are only valid within the elastic range of the structure analysed. A future study could investigate how the impact shape influences the nonlinear response of a structure to see if the same conclusions made in this study also apply within the nonlinear response of a structure. Furthermore, the structure used in this study is a small-scale column and as such, the debris impact magnitudes and durations are relatively small when compared to full-scale impact loads. A future study could investigate if the same conclusions made in this study also apply to a full-scale column.

Chapter 5

Parametric Study on the Influence of the Structural Stiffness on Response Parameters

5.1 Objectives and Description of Methodology

The objective of this study is to conduct a parametric analysis on the influence that the structural stiffness has on the support reaction forces and midspan deflection for a column subjected to a point load. The point load is defined by the debris impact guidelines for shipping containers outlined in Clause 6.11.6 of ASCE 7 (2016). The structural stiffness has a direct influence on the magnitude of the debris impact load outlined in Clause 6.11.6 of ASCE 7 (2016) and Eq. 5.1, it also has a direct influence on how a structure responds to the impact load. Hence, the importance of understanding how the structural stiffness influences the response of the structure is crucial for understanding how to design for tsunami generated debris impact loads.

The column in this study was selected to be a reinforced concrete column that was chosen to be modelled in *OpenSees*, which is a structural analysis software typically used for simulating the seismic response of structures (McKenna et al., 2010). In order to investigate the influence that the structural stiffness has on response parameters and the debris impact force histories, the stiffness of the column needs to be varied. This was achieved by varying the cylinder strength of the concrete from $5MPa$ to $80MPa$, which has a direct influence on the flexural stiffness of the column. The details of the column model are outlined in Section 5.2.

In order to conduct this parametric study, the debris impact force histories have to be defined. The debris impact force histories are generated by following Clauses 6.11.6 and 6.11.8 of ASCE 7 (2016), which define the impact magnitude, duration, and impact shape to be a rectangular pulse. Furthermore, in order to calculate the impact magnitude and duration, the material properties of the debris have to be known. The debris mass and stiffness were assumed to be equal to the values associated with an empty $20 - ft$

standard shipping container, which has a mass of $2,270kg$ and a stiffness of $42,900\frac{kN}{m}$, as outlined in Table 6.11-2 of ASCE 7 (2016). The details of how the impact force histories were developed is outlined in Section 5.3.

5.2 Reinforced Concrete Design

The reinforced concrete model used in this study is a $4.0m$ tall column that has a square cross-section with dimensions of $350mm \times 350mm$ and a concrete cover of $40mm$. The column has two supports at either end that restrict the shear and bending moment DOFs, while the axial DOF is released to simulate a fixed-fixed beam boundary condition. The reinforcement layout consists of 12-$25M$ longitudinal rebars with $10M$ ties spaced $125mm$, which resulted in a reinforcement ratio of 4.9%. This cross-section is based on Table 7.4 outlined in Chapter 7 of CAC (2016), for which the maximum number of $25M$ rebars for a cross-section of size $350mm \times 350mm$ was selected. The cross-sectional view of the column is outlined in Figure 5.1:

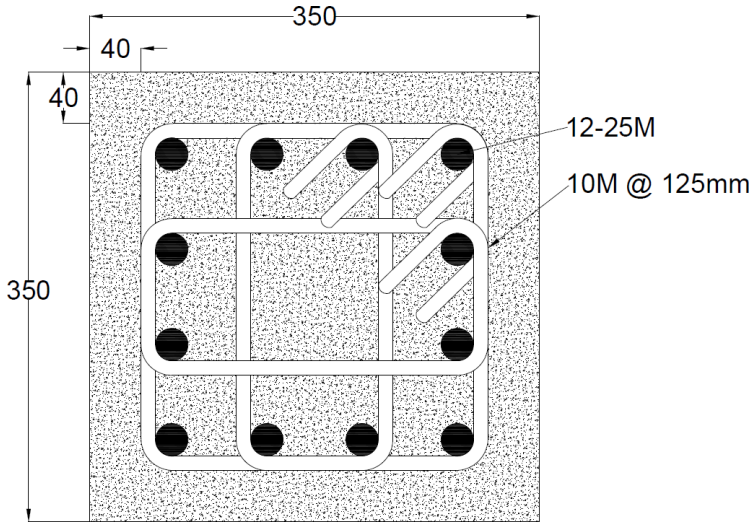


Figure 5.1: Reinforced Concrete Cross-Section

5.3 Development of Impact Force Histories

The impact force histories were developed by following Clauses 6.11.6 and 6.11.8 of ASCE 7 (2016). Clause 6.11.6 of ASCE 7 (2016) defines the debris impact magnitude and duration for shipping container impacts. The nominal impact magnitude is a function of the maximum flow velocity, debris mass, and the lesser of the effective stiffness of the debris or the lateral stiffness of the impacted structural element as shown in Eq. 5.1. Furthermore, Clause 6.11.6 of ASCE 7 (2016) specifies that the nominal design impact force for shipping

containers does not need to be taken as greater than $980kN$.

$$F_{ni} = u_{max}\sqrt{km_d} \tag{5.1}$$

The impact duration is calculated as per Eq. 5.2, as it was assumed that the shipping container is empty (Clause 6.11.6 of ASCE 7 (2016)).

$$t_d = \frac{2m_d u_{max}}{F_{ni}} \tag{5.2}$$

The design impact force is calculated as per Eq. 5.3, it was assumed that the importance factor of the structure is equal to one and that the orientation coefficient for shipping containers is equal to 0.65 (Clause 6.11.6 of ASCE 7 (2016)).

$$F_i = I_{tsu} C_0 F_{ni} \tag{5.3}$$

For this analysis the debris was assumed to be an empty 20-ft shipping container. The mass and stiffness of the shipping container were assumed to be equal to $2,270kg$ and $42,900\frac{kN}{m}$ respectively (Table 6.11-2 of ASCE 7 (2016)). Additionally, the maximum flow velocity was assumed to be equal to $5\frac{m}{s}$, which is not unrealistic based on post-tsunami field surveys (Naito et al., 2014).

To calculate the design debris impact force, the stiffness of the structure needs to be defined. For this study, the structure stiffness was assumed to be equal to the elastic bending stiffness for a fixed-fixed beam with a concentrated load located at the center of the beam. The elastic bending stiffness is defined as the load required to produce one unit of deflection. For the static analysis of a fixed-fixed beam with a concentrated load at the center, the deflection at the center of the beam is equal to the equation below:

$$\delta_c = \frac{PL^3}{192EI} \tag{5.4}$$

Where:

- δ_c = Deflection at the center of the beam
- P = Concentrated load
- L = Length of the beam
- EI = Effective stiffness of the cross-section

Hence, for a concentrated load of P, the elastic bending stiffness can be estimated by Eq. 5.5 and further simplified in Eq. 5.6 by substituting in the definition of δ_c:

$$k_s = \frac{P}{\delta_c} \tag{5.5}$$

$$k_s = \frac{192EI}{L^3} \tag{5.6}$$

The effective stiffness of the reinforced concrete cross-section outlined in Figure 5.1 was calculated as per Clause 10.14.1.2 in CSA A23.3-14 (2014). Clause 10.14.1.2 of CSA A23.3-14 (2014) provides scaling factors to apply to the gross moment of inertia based on the type of member (i.e. beams, columns, walls, and slabs). As the column supports are free in the axial DOF and the only load being applied is a purely shear load, the choice was made to select the scaling factor associated to beams. Hence, the effective stiffness of the reinforced concrete section was assumed to be equal to:

$$EI = 0.35E_cI_g \tag{5.7}$$

Where:

- E_c = Modulus of elasticity of concrete
- I_g = Gross moment of inertia

The modulus of elasticity for the concrete section was calculated as per Eq. 8.1 in Clause 8.6.2.2 of CSA A23.3-14 (2014), which is outlined below in Eq. 5.8. The density of the concrete was assumed to be equal to $2300\frac{kg}{m^3}$.

$$E_c = \left(3300\sqrt{f'_c} + 6900\right)\left(\frac{\gamma_c}{2300}\right)^{1.5} \tag{5.8}$$

Where:

- f'_c = Concrete cylinder strength
- γ_c = Density of the concrete

Based on these formulas and assumptions the effective stiffness of the reinforced concrete section can be calculated, along with the elastic bending stiffness for each concrete cylinder strength analysed. Furthermore, with the elastic bending stiffness of the structure defined, the design debris impact force and duration can be calculated. Table 5.1 defines the effective stiffness, elastic bending stiffness, impact force, and impact duration for every concrete cylinder strength analysed in this study. As can be seen from Table 5.1, the debris impact force and duration is the same regardless of the concrete cylinder strength chosen. This is because the elastic bending stiffness of the structure and the debris stiffness all resulted in impact magnitudes that were larger than $980kN$ and hence, the nominal debris impact magnitude was selected to be $980kN$ as per Clause 6.11.6 of ASCE 7 (2016). Figure 5.2 defines the impact force history that was applied to the reinforced concrete model.

f'_c (MPa)	E_c (MPa)	EI (Nmm^2)	k_s (kN/m)	k_s/k_d	F_{ni} (kN)	F_i (kN)	t_d (s)
5	$1.43e^4$	$6.25e^{12}$	$1.87e^4$	0.44	980	637	0.023
10	$1.73e^4$	$7.59e^{12}$	$2.28e^4$	0.53	980	637	0.023
15	$1.97e^4$	$8.61e^{12}$	$2.58e^4$	0.60	980	637	0.023
20	$2.17e^4$	$9.48e^{12}$	$2.84e^4$	0.66	980	637	0.023
30	$2.50e^4$	$1.09e^{13}$	$3.28e^4$	0.76	980	637	0.023
40	$2.78e^4$	$1.22e^{13}$	$3.65e^4$	0.85	980	637	0.023
60	$3.25e^4$	$1.42e^{13}$	$4.26e^4$	0.99	980	637	0.023
80	$3.64e^4$	$1.59e^{13}$	$4.78e^4$	1.11	980	637	0.023

Table 5.1: Debris Impact Force Parameters

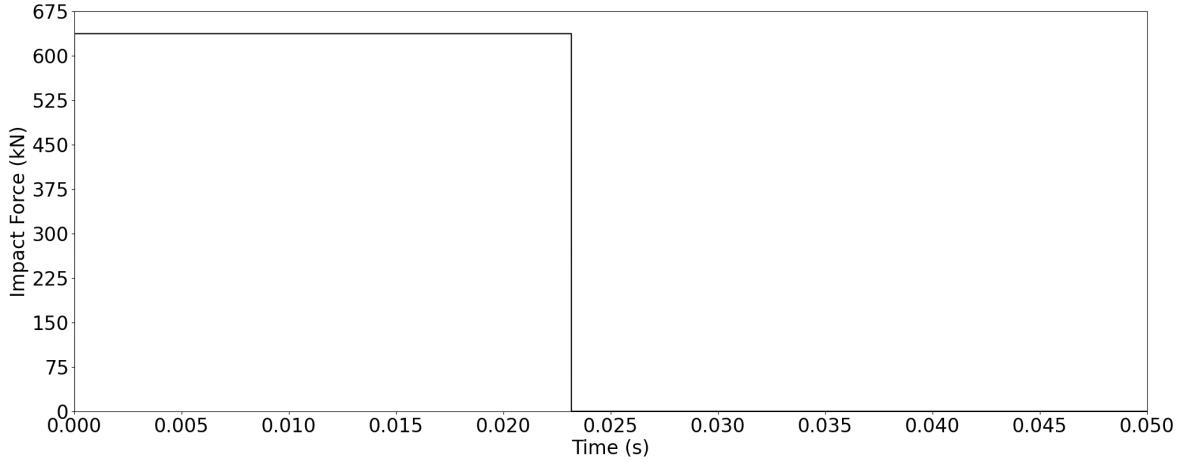


Figure 5.2: Design Debris Impact Force History

5.4 Modelling Parameters

5.4.1 Load Location and Analysis Type

The debris impact load was applied as a point load at the midspan of the column (i.e. $2.0m$). The point load was applied at the midspan of the column, as the midspan represents the critical location for flexure as this is where the deflection is maximum for a static analysis of a fixed-fixed beam. Furthermore, a $2.0m$ impact location is not unreasonable for a debris impact location based on field surveys of the 2004 Sumatra Earthquake and Tsunami (Saatcioglu et al., 2005).

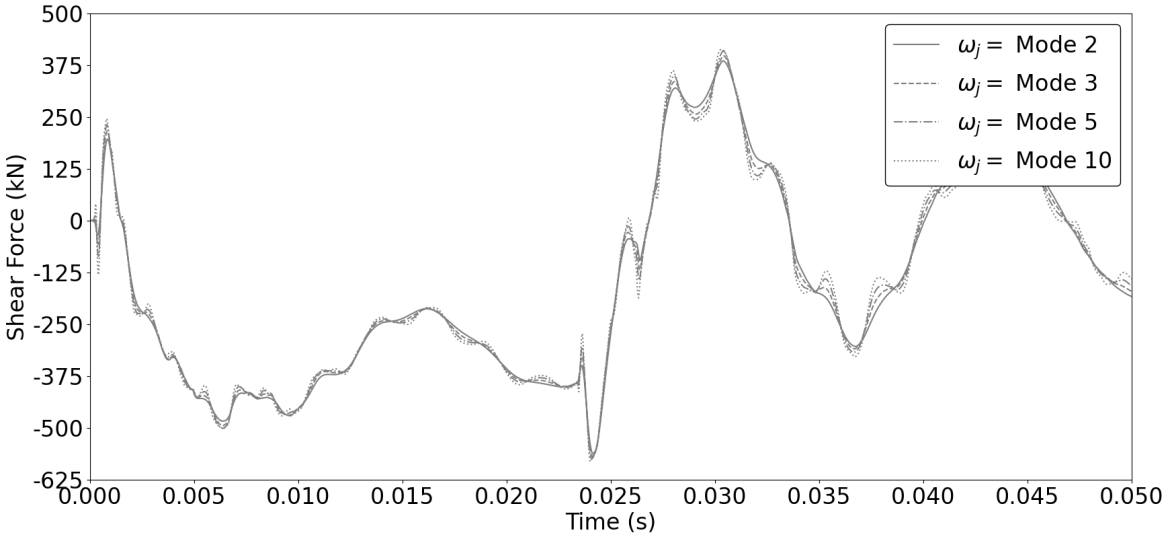
Following Clause 6.11.8 of ASCE 7 (2016), the debris impact load is defined as a time dependant load. As such, a *Transient* structural analysis was conducted for this column to fully capture the response of the column due to the dynamic loading. Additionally, the

column was chosen to be modelled in two-dimensional space with three DOFs per node. A two-dimensional analysis was conducted as Stolle et al. (2018a) showed that the force response during experimental debris impacts was governed by shear loading. Furthermore, the point load is applied as a lateral load in one direction with no eccentricity, suggesting the response of the column will be governed by the shear forces in the direction of the load.

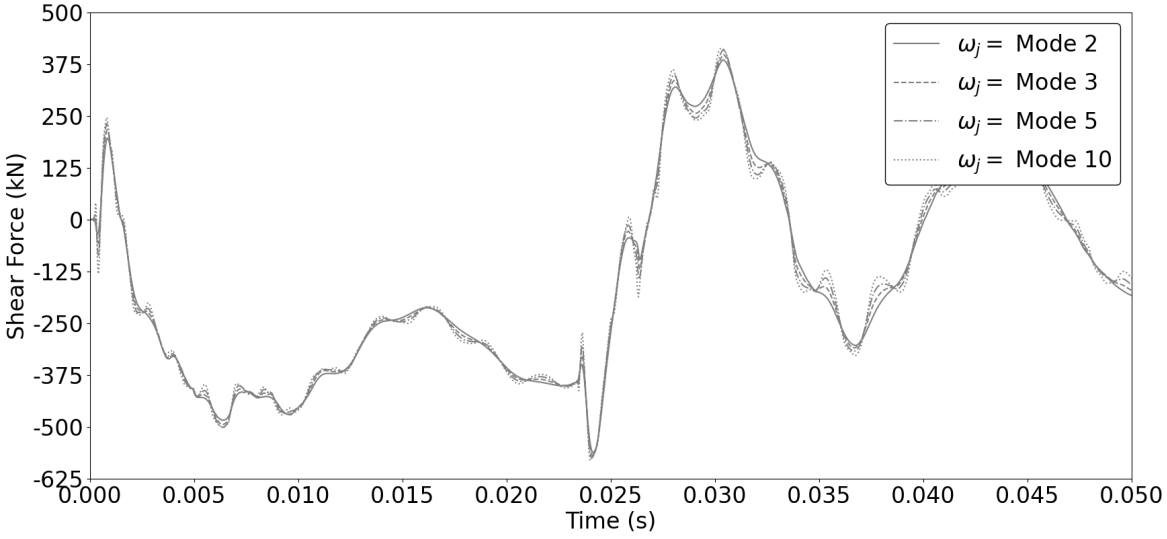
5.4.2 Damping Model

The damping model defines how inherent damping is included into the system, the inclusion of damping in the model is necessary as to ignore damping would give unrealistically high responses. Similar to the damping model outlined in Section 3.5.3, the damping in this model was defined by Rayleigh damping using the *Rayleigh* command in *OpenSees*. The damping in this model was assumed to be 5% and the first of the two frequencies selected to derive the Rayleigh damping coefficients was defined to be the first natural frequency of the column. The second frequency (ω_j) selected varied from the second natural frequency of the column to the tenth, this was done to investigate the influence that increasing the second frequency has on the response of the column. Unlike Section 3.5.3, a modal time history analysis of this column cannot be completed to compare which second natural frequency provides approximately 5% damping in the structure, as modal time history analysis is only valid for linear structures (Chopra, 2017).

Figure 5.3 outlines the top and bottom shear force time histories of the column for each ω_j investigated. Based on Figure 5.3, it is apparent that as ω_j increases from the second natural frequency to the tenth, the influence of higher mode effects increases. The higher modes effects that are not damped out cause the peaks in the model to increase.



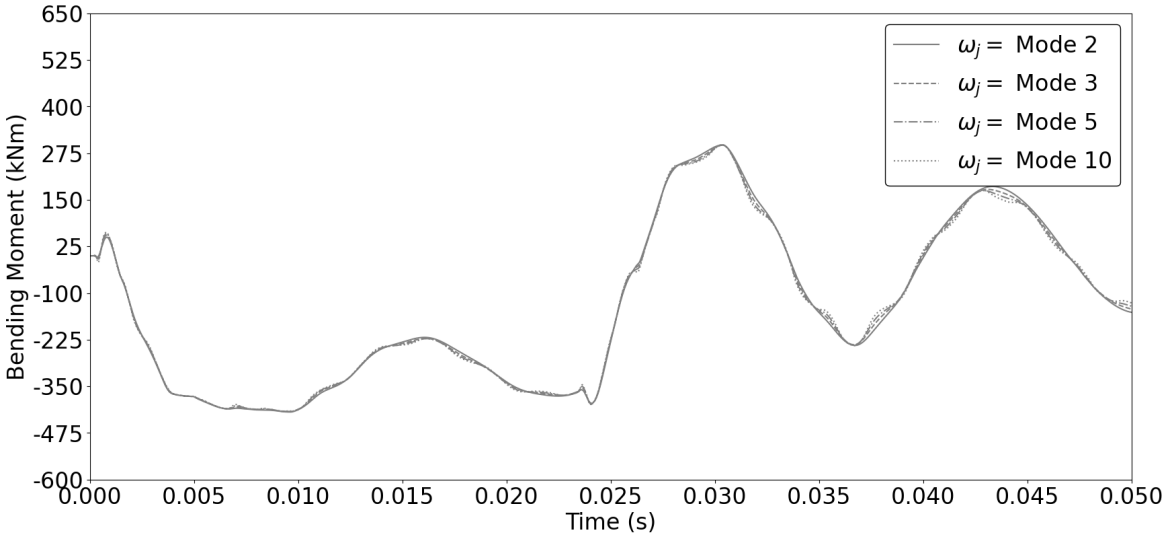
(a) Top Shear Forces



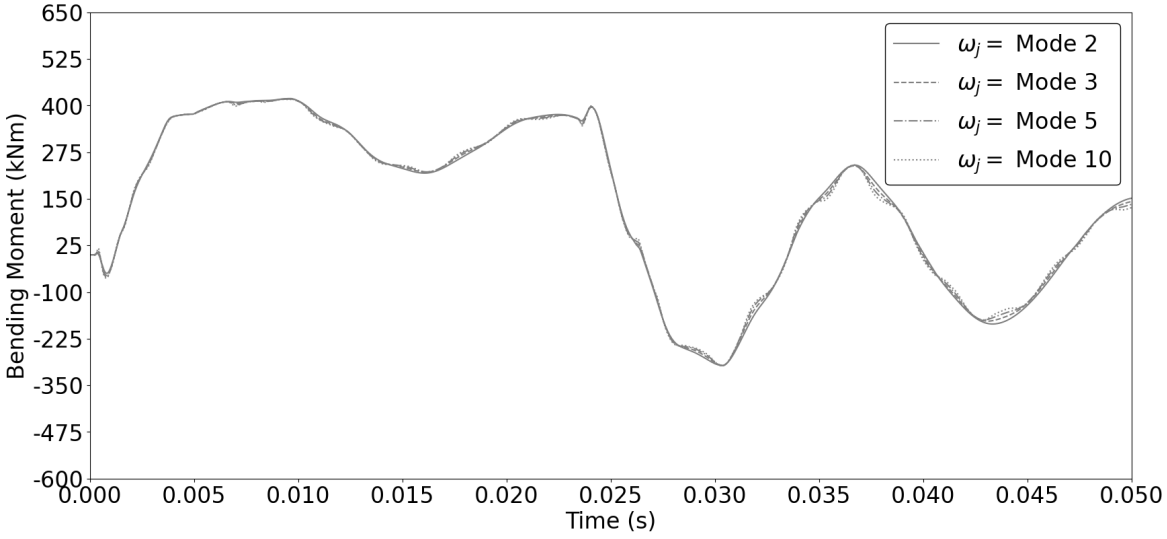
(b) Bottom Shear Forces

Figure 5.3: Damping Study - Shear Forces

Figure 5.4 outlines the top and bottom bending moment time histories of the column for each ω_j investigated. Based on Figure 5.4, it is apparent that as ω_j increases from the second natural frequency to the tenth, the influence of higher mode effects increases. The higher modes effects that are not damped out cause the peaks in the model to increase, however, the increase is not as significant as the shear forces.



(a) Top Bending Moments



(b) Bottom Bending Moments

Figure 5.4: Damping Study - Bending Moment

Figure 5.5 outlines the midspan deflection time history of the column for each ω_j investigated. Based on Figure 5.5, it is apparent that as ω_j increases the magnitude of midspan deflection increases but overall shape does not. This suggests that the midspan deflection responds mainly in the first two modes of vibration, as when ω_j increases, the damping in the lower modes decreases below 5% when using Rayleigh damping, an example of this phenomenon is presented in Figure 3.19. Due to the amount of damping decreasing in the lower modes, the midspan deflection increases as the lower mode effects are not being damped out as quickly.

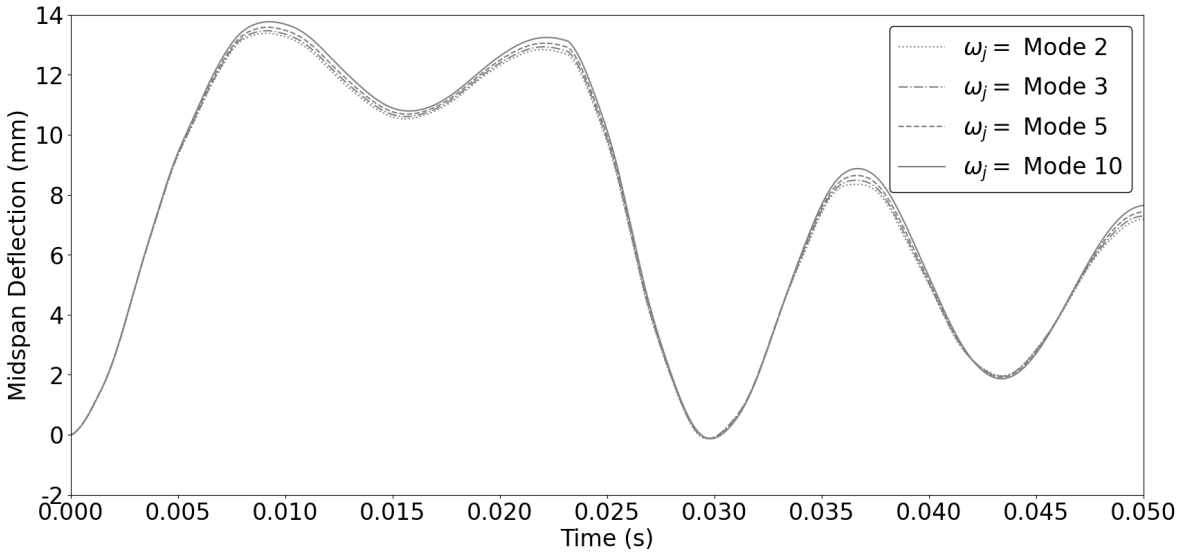


Figure 5.5: Damping Study - Midspan Deflection

As a modal time history analysis cannot be completed for this model, an ω_j equal to fifth natural frequency of the column was selected. This value was selected as it provides a balance between a smoothed solution due to ω_j being equal to the second natural frequency of the structure and a more peaky solution due to ω_j being equal to the tenth natural frequency of the structure.

5.4.3 Mass Definition

For transient structural simulations the inclusion of mass in the model is crucial to the response of the structure. This is because the product of the mass and acceleration of the structure induces additional forces into the structure, termed inertial forces as shown in Eq. 3.5. The mass of the column was estimated by multiplying the density of concrete, which was assumed to be $2300\frac{kg}{m^3}$, by the volume of the column, which is equal to $0.49m^3$. This total mass was then evenly distributed to the nodes of each element using the *mass* command in *OpenSees*, which allows the user to define the mass in each DOF and at each node. The mass was evenly distributed to the shear and moment DOFs, no mass was added to the axial DOF to prevent inertial forces from developing in the axial DOF.

5.4.4 Concrete Model

The concrete model is used to define the stress-strain relationship of the unconfined and confined concrete. In *OpenSees* there are ten different concrete models, however, only two concrete models were used in this analysis. The two concrete models used in this analysis were the *Concrete01* and *Concrete04* material models. The *Concrete01* material model is

based on the Kent-Scott-Park model (Kent and Park, 1971) and uses the following input parameters to define the stress-strain relationship:

- Concrete compressive strength, f'_c
- Concrete strain at maximum strength, ϵ_0
- Concrete crushing strength, f'_{cu}
- Concrete strain at crushing strength, ϵ_u

The *Concrete04* material model is based on Popovics model (Popovics, 1973) and uses the following input parameters to define the stress-strain relationship:

- Concrete compressive strength, f'_c
- Concrete strain at maximum strength, ϵ_0
- Concrete strain at crushing strength, ϵ_u
- Initial stiffness, E_c
- Maximum tensile strength of concrete, f_t
- Ultimate tensile strain of concrete, ϵ_t
- Exponential curve parameter to define the residual stress, $\beta = 0.1$ (recommended)

Two concrete models were used in this analysis as it was found that when the unconfined concrete was modelled with *Concrete04*, the model was highly unstable for the larger concrete cylinder strengths. However, when the unconfined concrete modelled was changed from *Concrete04* to *Concrete01*, the model instabilities for the larger concrete cylinder strengths were resolved. The confined concrete was modelled with the *Concrete04* model and no model instabilities were experienced for the full range of cylinder strengths investigated. The input parameters for the unconfined concrete using the *Concrete01* material model were derived from the following assumptions:

- The unconfined concrete compressive strength is equal to 90% of the concrete cylinder strength.
- The unconfined concrete strain at the maximum compressive strength is 0.002.
- The unconfined concrete crushing strength is equal to 85% of the unconfined concrete compressive strength.
- The unconfined concrete strain at the crushing strength of concrete is 0.0038.

The input parameters for the confined concrete using the *Concrete04* material model were derived from procedures outlined in Saatcioglu and Razvi (1992). The method outlined in Saatcioglu and Razvi (1992) estimates the confined concrete strength by considering the influence that the confining pressure due to the reinforcement has on the concrete. The stress-strain relationship for both concrete material models is presented below in Figure 5.6 for a concrete cylinder strength of $40MPa$. It should be noted that these curves change based on the concrete cylinder strength being used in the analysis and that the tensile concrete strength branch is not shown for the confined concrete model.

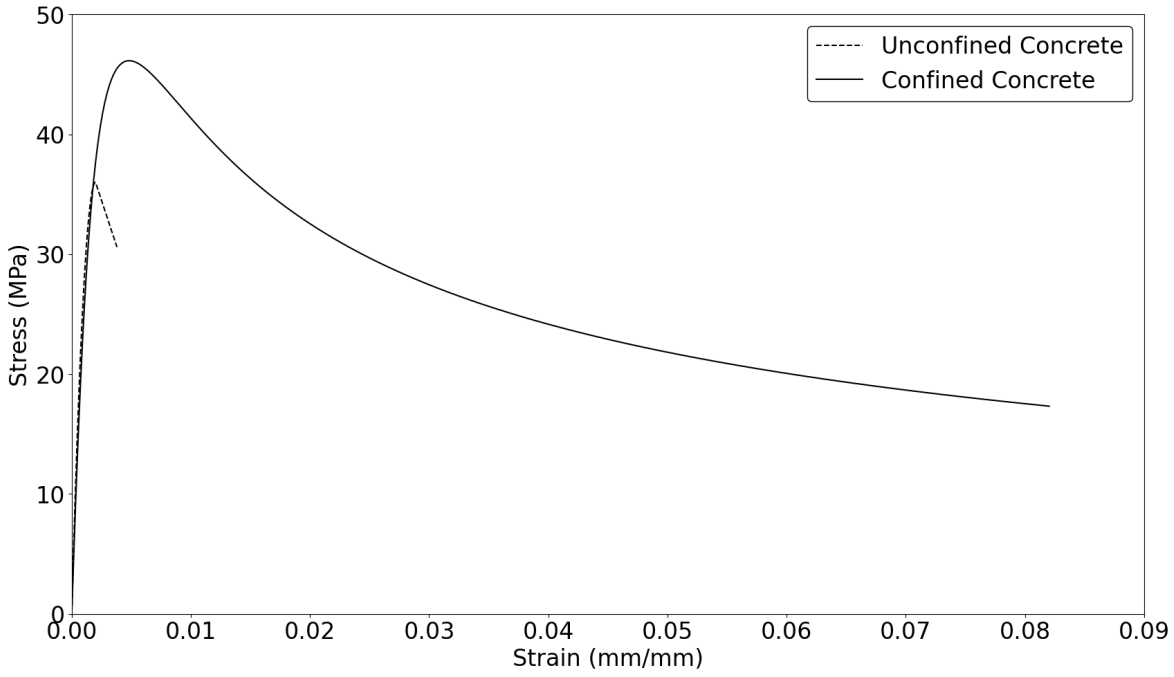


Figure 5.6: Concrete Material Models

5.4.5 Reinforcing Steel Model

The steel model is used to define the stress-strain relationship of the longitudinal reinforcement bars. In *OpenSees* there is a reinforcing steel material model that is intended for use in reinforced concrete fiber sections, entitled the *ReinforcingSteel* material model. The *ReinforcingSteel* material model is based on the uniaxial steel model outlined in Chang and Mander (1994), which implies that there are three regions to the stress-strain relationship. The first region is defined as the elastic branch, the second region is defined as the yield plateau branch, and the third is defined as the strain hardening branch. The *ReinforcingSteel* material model requires six input parameters and the assumed values for each parameter is illustrated below:

- Yield stress in tension, $f_y = 450MPa$

- Ultimate stress in tension, $f_u = 650MPa$
- Initial elastic tangent, $E_s = 200GPa$
- Elastic modulus at initial strain hardening, $E_{sh} = 7250MPa$
- Strain at initial strain hardening, $\epsilon_{sh} = 0.01$
- Strain at peak stress, $\epsilon_{ult} = 0.09$

The stress-strain relationship for the longitudinal reinforcement bars following the Chang and Mander (1994) model and used as input into *OpenSees*, is plotted below in Figure 5.7:

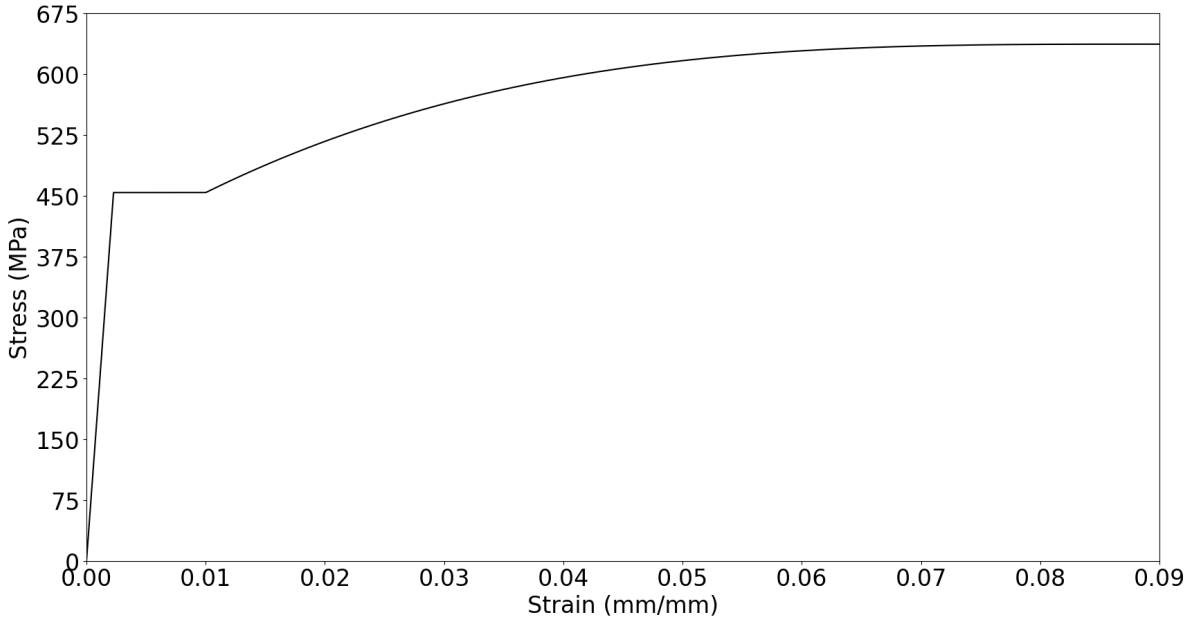


Figure 5.7: Longitudinal Reinforcement Material Model

5.4.6 Section Model

The section model is used to define the force-deformation relationships for beam-column elements. The section model selected for this analysis was the *Fiber* section model, which defines geometry and materials through a cross-section by the use of small finite fibers distributed across the section. A fiber section was selected for this analysis as it allows for the unconfined and confined regions of concrete to be explicitly modelled with the *Patch* command, which generates fibers over a cross-sectional area. Furthermore, the longitudinal reinforcement can also be explicitly modelled with the *Layer* command, which generates fibers along a line. The transverse reinforcement is not explicitly modelled but the effects of the transverse reinforcement are included in the confinement model. An example of how

the fiber models splits the cross-section is defined in Figure 5.8. The fiber model generates a user defined number of fibers along both the unconfined and confined concrete regions. Hence, the number of fibers defined by the user has an influence on the model accuracy, a larger number of fibers results in a more accurate representation of the cross-section. Section 5.4.6.1 outlines how the response changes based on the number of fibers defined in the cross-section.

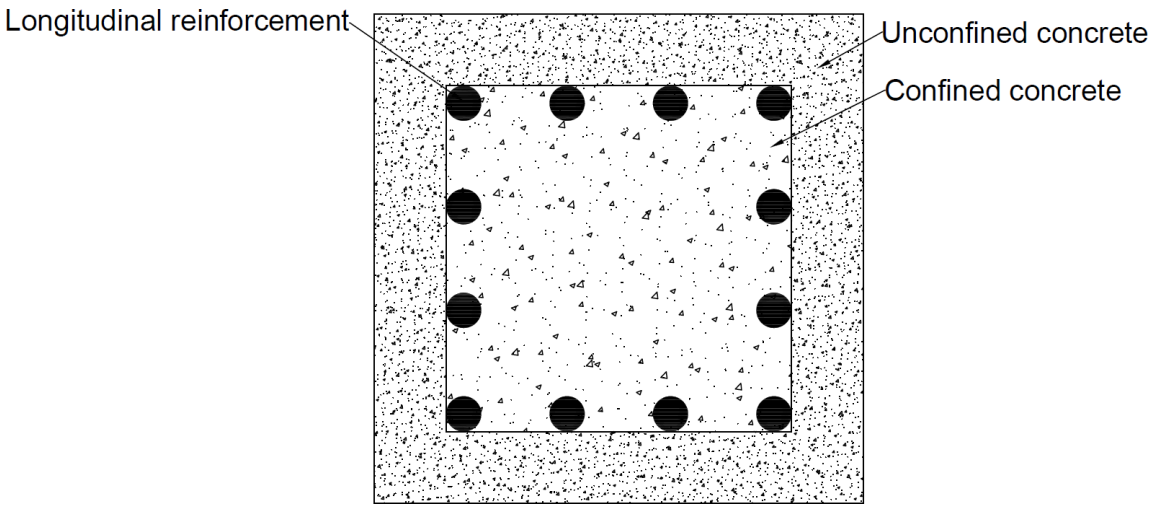


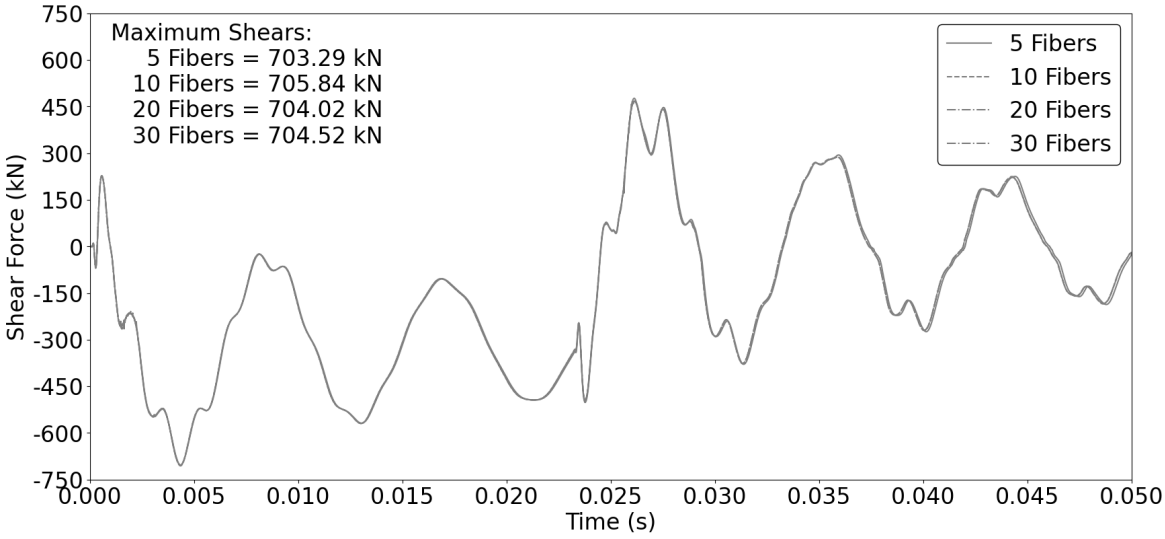
Figure 5.8: Fiber Model Cross-Section

5.4.6.1 Mesh Refinement Study - Section Fibers

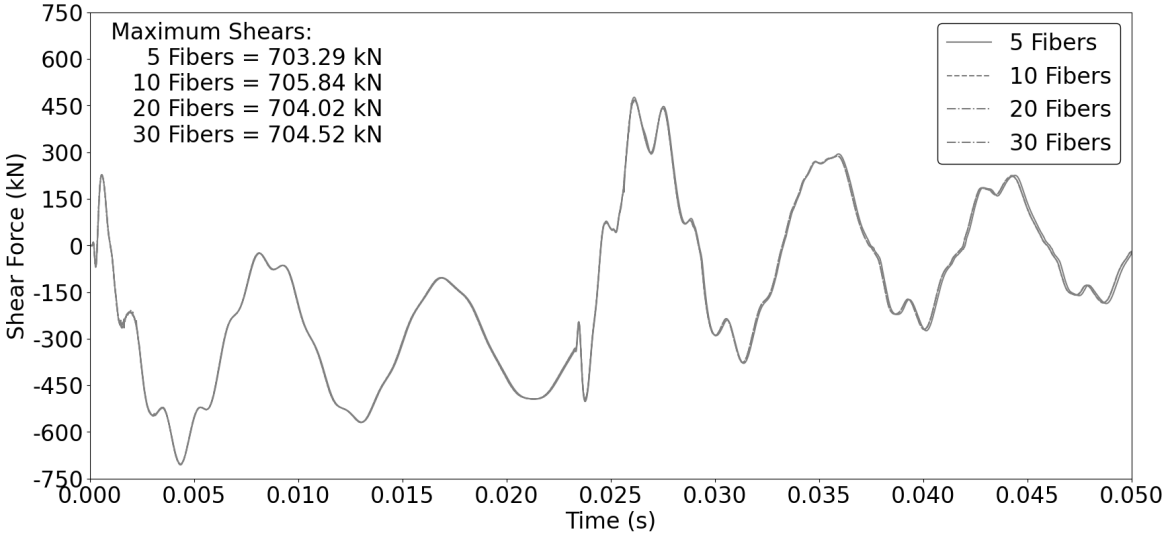
The number of fibers defined in the cross-section has an influence on the response of the column and hence, a mesh study was completed to analyse this influence. The mesh study consists of increasing the number of fibers in both the unconfined and confined concrete regions from 5 to 30 fibers in each direction.

Figure 5.9 presents how the shear force time histories for the top and bottom supports change as the fiber mesh refinement increases. From the figure, it is clear that with mesh refinement the maximum shear forces increase slightly but not significantly. The percentage change in the maximum shear forces for both the top and bottom supports as the fiber refinement increases is outlined below:

- 5 fibers to 10 = 0.36%
- 10 fibers to 20 = −0.26%
- 20 fibers to 30 = 0.07%



(a) Top Shear Forces

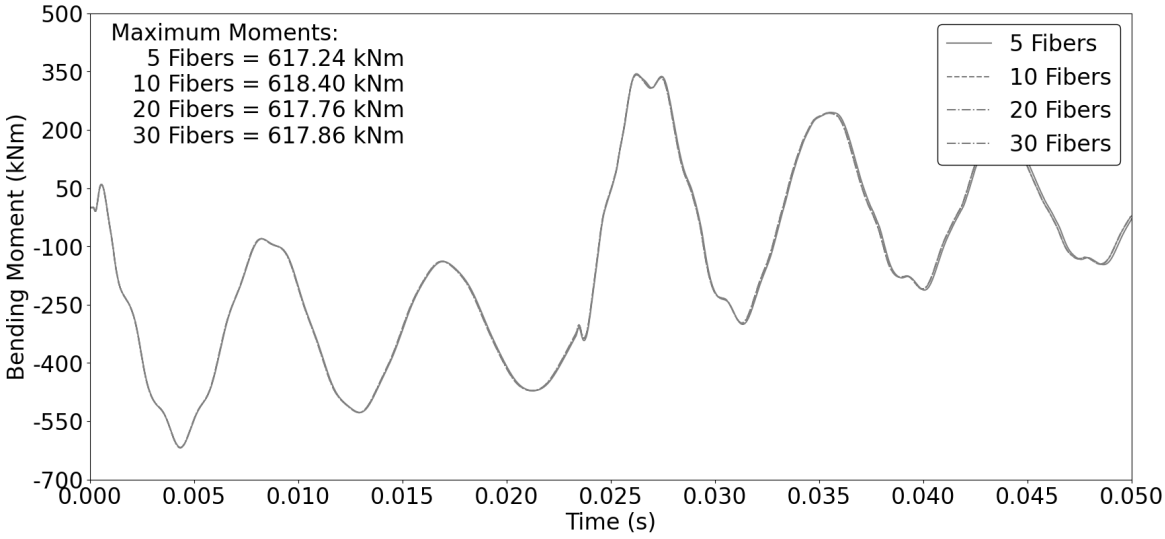


(b) Bottom Shear Forces

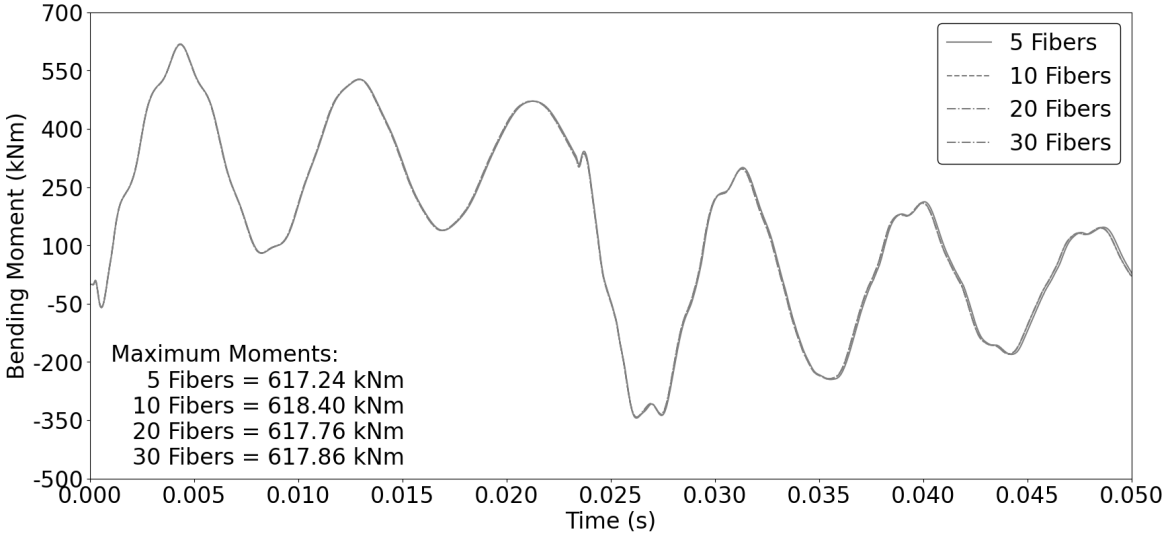
Figure 5.9: Fiber Study - Shear Forces

Figure 5.10 presents how the bending moment time histories for the top and bottom supports change as the fiber mesh refinement increases. From the figure, it is clear that with mesh refinement the maximum bending moments increase slightly but not significantly. The percentage change in the maximum bending moments for both the top and bottom supports as the fiber refinement increases is outlined below:

- 5 fibers to 10 = 0.19%
- 10 fibers to 20 = −0.10%
- 20 fibers to 30 = 0.02%



(a) Top Bending Moments



(b) Bottom Bending Moments

Figure 5.10: Fiber Study - Bending Moments

Figure 5.11 presents how the midspan deflection time histories change as the fiber mesh refinement increases. From the figure, it is clear that with mesh refinement the maximum midspan deflections decrease slightly but not significantly. The percentage change in the maximum midspan deflections as the fiber refinement increases is outlined below:

- 5 fibers to 10 = -0.44%
- 10 fibers to 20 = -0.10%
- 20 fibers to 30 = -0.02%

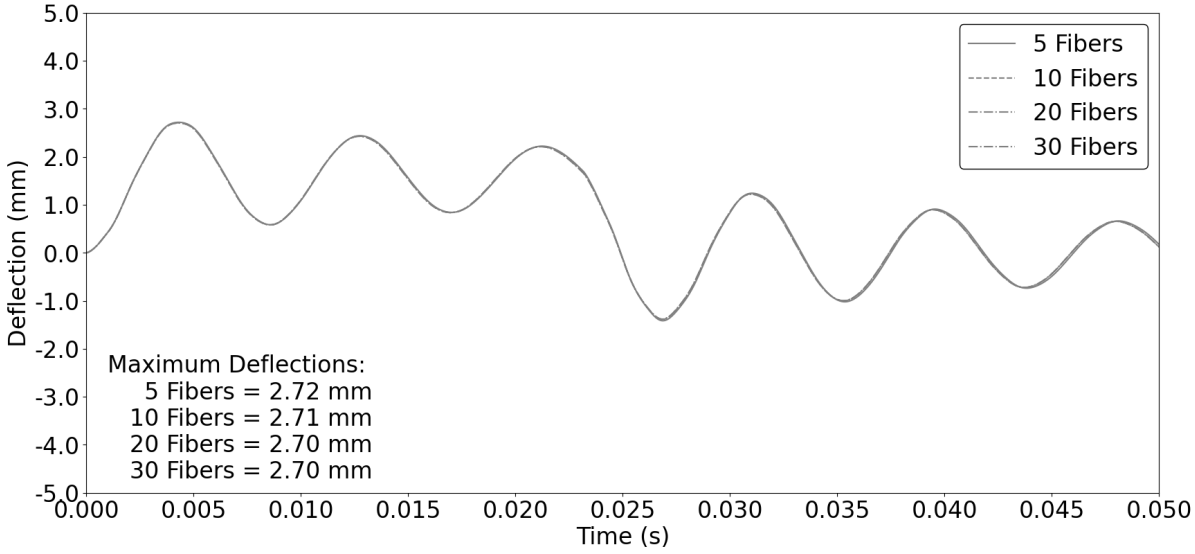


Figure 5.11: Fiber Study - Midspan Deflection

Based on these results, the conclusion can be made that the shear and bending moments at the support location are not sensitive to the fiber refinement. Whereas, the midspan deflections experienced the largest percentage change with refinement. Hence, a fiber model with 20 fibers in each direction for both the unconfined and confined concrete was selected as the deflection governed the refinement study.

5.4.7 Element Type

The column in this study was chosen to be modelled with beam-column elements and in *OpenSees*, there are two main options for these elements that can model nonlinear behavior. The two main options for beam-column elements in *OpenSees* are:

- *Displacement-Based* Beam-Column Elements
- *Force-Based* Beam-Column Elements

Both of these element formulations are distributed plasticity models as opposed to lumped plasticity models. A lumped plasticity model defines regions in the beam-column element where a plastic hinge can be formed, these regions are typically located at a certain distance away from the support locations, entitled the plastic hinge length. The region defined by the support and plastic hinge locations at either end of the beam-column can consider nonlinearity in the model and the region of the beam-column defined between the plastic hinge locations does not consider nonlinearity in the model. A distributed plasticity model differs from a lumped plasticity model by defining integration points along the length of the beam-column and it is at these integration points that a plastic hinge can be formed.

This means that nonlinearity is considered along the full length of the beam-column instead of only at the locations defined by the plastic hinge length.

The two beam-column element formulations differ in how they calculate forces due to applied nodal deformations. To calculate the forces due to the applied nodal deformations, the two beam-column formulations start with the same procedure. The two beam-column formulations start with element properties and applied nodal deformations, which are transformed from global deformations to local deformations. A *Displacement-Based* beam-column element then assumes a constant axial strain and a linear curvature along the element. Based on this assumption, the sectional stresses are calculated and integrated over the depth of the section to get overall sectional forces along the element. Finally, virtual work is used to calculate the resulting forces at the ends of each element. As stated, the *Displacement-Based* beam-column element assumes a constant axial strain and linear curvature distribution along the element, which provides exact equilibrium for linear elements but is not a valid assumption for nonlinear elements.

The *Force-Based* beam-column element differs from the *Displacement-Based* beam-column element by instead of assuming a constant axial strain and linear curvature distribution, a constant axial load and linear distribution of moment is assumed. Assuming a constant axial load and linear distribution of moment along the element allows the *Force-Based* beam-column element to provide exact equilibrium for nonlinear elements. However, this assumption further complicates the procedure for solving the resulting forces at the ends of each element. The procedure starts with forces and moments and uses an iterative procedure for which a guess of the nodal forces is made, the section curvatures are calculated, and then the resulting nodal deformations are calculated using virtual work and validated with in the known local deformations. If these resulting nodal deformations are equal to the known local deformations, then the nodal forces are transformed to global member element forces and the analysis continues to the next step. If the nodal deformations are not equal to the known local deformations, then another guess is made for the nodal forces and the procedure repeats. This iteration results in the *Force-Based* beam-column elements being more computationally expensive when compared to the *Displacement-Based* elements. As the *Force-Based* beam-column elements use exact equilibrium, they result in better accuracy using a single element when compared to the *Displacement-Based* beam-column elements. Hence, the *Force-Based* beam-column elements were used for this analysis.

5.4.8 Geometric Transformation Method

Geometric transformations describe how the beam stiffness and resisting forces are transformed from the local system to the global system. Three options are available in *OpenSees*:

- *Linear* Transformation
- *P*-Δ Transformation
- *Corotational* Transformation

The *linear* transformation method does not consider large deformation effects and hence, was not considered for this analysis. The P-Δ transformation method is capable of considering large deformations by considering second-order P-Δ effects and hence, was considered for this analysis. The *Corotational* transformation method can consider both large deformations and small strain problems and hence was also a candidate for this analysis. Comparing the two methods proved that using the *Corotational* transformation method provided more stability in the model for the smaller concrete cylinder strengths, when compared to the P-Δ transformation method. Therefore, based on the stability of the *Corotational* transformation method and the fact that it can consider both large deformations and small strains, the *Corotational* method was selected as the geometric transformation method for this analysis.

5.4.9 System of Equations Solver and Convergence Test

5.4.9.1 System of Equations Solver

The system of equations solver is the method for which the equations of equilibrium in the solution algorithm are solved at each time step. For example the system of equations solver is used to solve the following problem:

$$\left[\bar{k_t}\right]\{\Delta x\} = \{\Delta \bar{P}\} \tag{5.9}$$

Where:

- $[\bar{k_t}]$ = The tangent stiffness matrix
- $\{\Delta x\}$ = The displacements
- $\{\Delta \bar{P}\}$ = The forces

Solving this system of equations by direct inversion is ineffective as the determinate of the tangent stiffness matrix could be singular, which can lead to instabilities in the model. Furthermore, direct inversion does not take advantage of memory saving techniques for solving the system of equations. This means that a matrix of size $n \times n$ is stored in an array of size $n \times n$. This is not efficient for banded, symmetric, and positive definite matrices which are commonly seen in structural problems. Some of the options for solving the system of equations in *OpenSees* are as follows:

- *BandGeneral* - Is a direct solver for banded matrices and does not require the matrix to be positive definite or symmetric, which is beneficial for complex models with large deformations.
- *BandSPD* - Is similar to *BandGeneral* but requires the matrix to be positive definite.
- *UmfPack* - Is a general solution solver that does not require the matrix to be positive definite or symmetric.

As the cylinder strength of the concrete varies from $5MPa$ to $80MPa$, large deformations were expected in the model and hence, the *BandSPD* solver was not considered for this analysis. Comparing the *BandGeneral* and *UmfPack* solvers for the dynamic analysis of this column, it was found that the *UmfPack* solver provided a more stable solution for the smaller cylinder strength analyses. Furthermore, it was found that both system of equation solvers provided the same solution for the higher cylinder strength analyses. Hence, based on these results the *UmfPack* solver was selected for this analysis as it provided a more stable solution.

5.4.9.2 Convergence Test

The convergence test is required to determine if convergence has been achieved at each iteration step in the solution algorithm for the nonlinear problem. Some of the options available in *OpenSees* are as follows:

- *Norm Unbalance Test* - Defines a convergence test which uses the right-hand side of the matrix equation to determine if convergence has been reached. This typically can be interpreted as the unbalanced forces in the system.
- *Norm Displacement Increment Test* - Defines the convergence test which uses the left-hand side solution vector of the matrix equation to determine if convergence has been reached. This typically can be interpreted as the displacement increments that are being applied to the model.
- *Energy Increment Test* - Defines the convergence test as the dot product between the left-hand side solution vector and the right-hand side of the matrix equation to determine if convergence has been reached. This typically can be interpreted as the energy imbalance in the system.

The *Energy Increment Test* was selected as the convergence test for this analysis as it takes into consideration both the unbalanced forces and displacement increments when performing the convergence test. Whereas, the other convergence tests consider either the unbalanced load or displacement increment.

5.4.10 Time Integration Method and Solution Algorithm

5.4.10.1 Time Integration Method

The time integration method defines how the equation of motion is solved. For a transient analysis some of the time integrators available in *OpenSees* are as follows:

- *Newmark* Method (Newmark, 1959)
- *Hilber-Hughes-Taylor (HHT)* Method (Hilber et al., 1977)

- *Generalized-α* Method (Chung and Hulbert, 1993)
- *TRBDF2* Method (Bathe, 2007)

The integrator used for this analysis was the constant average acceleration *Newmark* method. Alternative integrators are the *HTT* integrator and the *Generalized-α* integrator, however, both of these methods can introduce an unknown amount of numerical damping into the solution and hence were not considered. Another integrator for consideration is the *TRBDF2* integrator, which is a composite scheme that alternates between the trapezoidal scheme and 3-point backward Euler scheme. The *TRBDF2* integrator does this in an attempt to conserve energy and momentum, which the *Newmark* method does not always do (Bathe, 2007). However, even though the *TRBDF2* integrator can conserve energy and momentum, the *Newmark* integrator was selected as it is the most commonly used method for solving dynamic analysis problems.

5.4.10.2 Solution Algorithm

The solution algorithm determines the sequences of steps that are taken to solve the non-linear equation within the integrator at each time step. The algorithm used for this analysis was selected based off of an adaptive algorithm scheme, in which the analysis runs for one type of algorithm and if it fails the script skips to the next algorithm and performs the analysis. The algorithms considered in the adaptive scheme are as follows:

- *Modified Newton* Algorithm
- *Krylov-Newton* Algorithm
- *Broyden* Algorithm

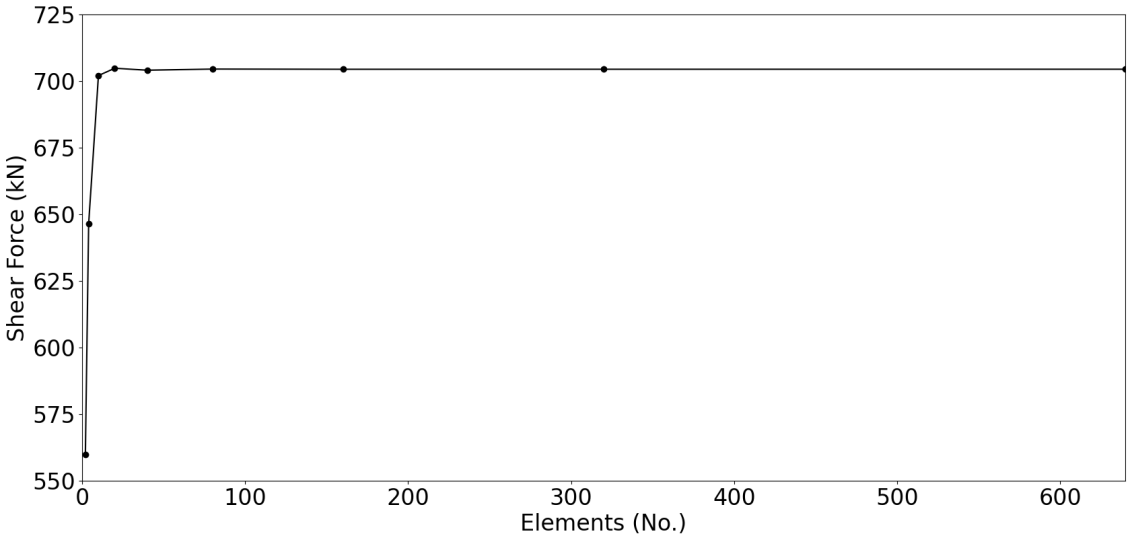
Initially, the adaptive algorithm started with using the *Modified Newton* algorithm, then moved to the *Krylov-Newton* algorithm if the analysis failed, and finally if both of these methods failed the *Broyden* algorithm was used. Based on the adaptive algorithm scheme, it was determined that both of the *Newton* methods failed for the smaller concrete cylinder strength analyses. Whereas, the *Broyden* algorithm was stable for the full range of concrete cylinder strengths and hence, the *Broyden* algorithm was selected for this analysis.

5.4.11 Mesh Refinement Study - Elements

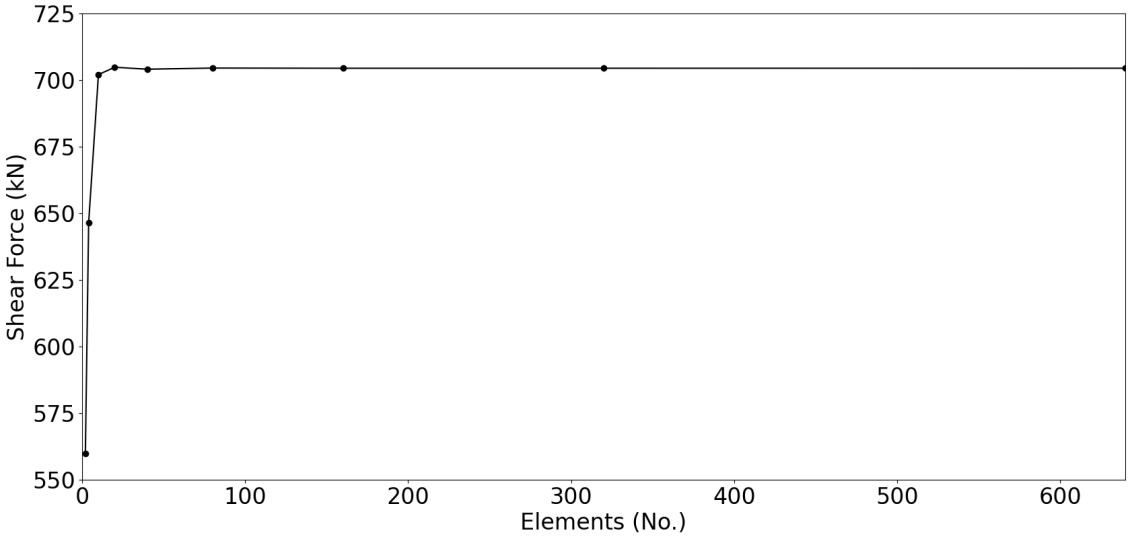
This section outlines how sensitive the structural response is to the refinement of the mesh for a concrete cylinder strength of $40MPa$. The mesh refinement consisted of increasing the number of elements in the model from 2 elements to 640 elements and analysing how the maximum base shear, top shear, base bending moment, top bending moment, and midspan deflection changed as a result of the mesh refinement. The influence of the mesh refinement on each response parameter was determined by calculating the percentage change between

each mesh refinements. A converged mesh was defined as the number of elements at which the percentage change between mesh refinements was less than 0.25%.

Observing Figure 5.12, it is clear that both the top and base shear forces produced the same results for all mesh refinements. Furthermore, Table 5.2 outlines the percentage change in shear forces with each mesh refinement and it is evident from the table that both the top and base shear forces converge at a mesh size of 40 elements.



(a) Top Shear Forces



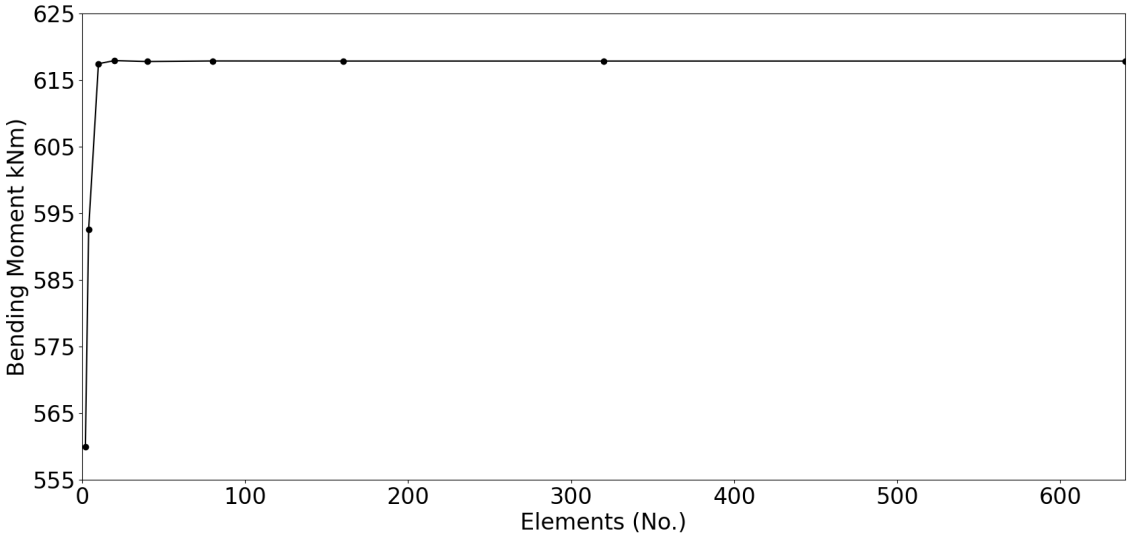
(b) Bottom Shear Forces

Figure 5.12: Mesh Study - Shear Forces

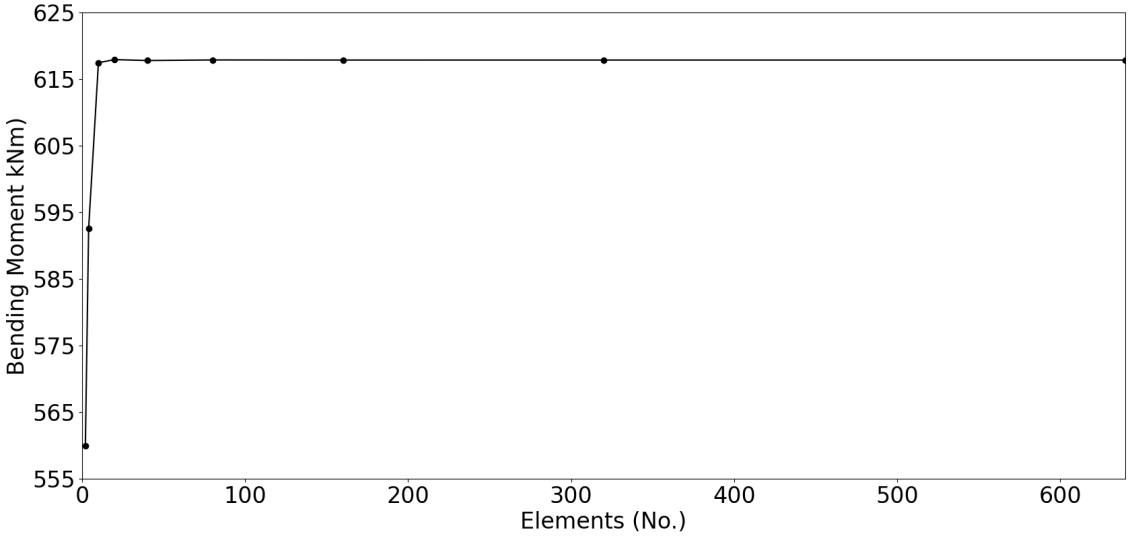
Elements (No.)	Top Shear (kN)		Base Shear (kN)	
	Value	% Change	Value	% Change
2	559.85	N/A	559.85	N/A
4	646.39	15.46%	646.39	15.46%
10	702.00	8.60%	702.00	8.60%
20	704.75	0.39%	704.75	0.39%
40	704.02	−0.10%	704.02	−0.10%
80	704.45	0.06%	704.45	0.06%
160	704.38	−0.01%	704.38	−0.01%
320	704.38	0.00%	704.38	0.00%
640	704.39	0.00%	704.39	0.00%

Table 5.2: Mesh Refinement Study Summary Table - Shear Forces

Observing Figure 5.13, it is clear that both the top and base bending moments produced the same results for all mesh refinements. Furthermore, Table 5.3 outlines the percentage change in bending moments with each mesh refinement and it is evident from the table that both the top and base bending moments converge at a mesh size of 20 elements.



(a) Top Bending Moments



(b) Bottom Bending Moments

Figure 5.13: Mesh Study - Bending Moments

Elements (No.)	Top Bending Moment (kNm)		Base Bending Moment (kNm)	
	Value	% Change	Value	% Change
2	559.92	N/A	559.92	N/A
4	592.59	5.84%	592.59	5.84%
10	617.44	4.19%	617.44	4.19%
20	617.90	0.07%	617.90	0.07%
40	617.76	−0.02%	617.76	−0.02%
80	617.84	0.01%	617.84	0.01%
160	617.83	0.00%	617.83	0.00%
320	617.83	0.00%	617.83	0.00%
640	617.83	0.00%	617.83	0.00%

Table 5.3: Mesh Refinement Study Summary Table - Bending Moments

Observing Figure 5.13 and Table 5.4, it is apparent that the midspan deflection converges at a mesh size of 20 elements.

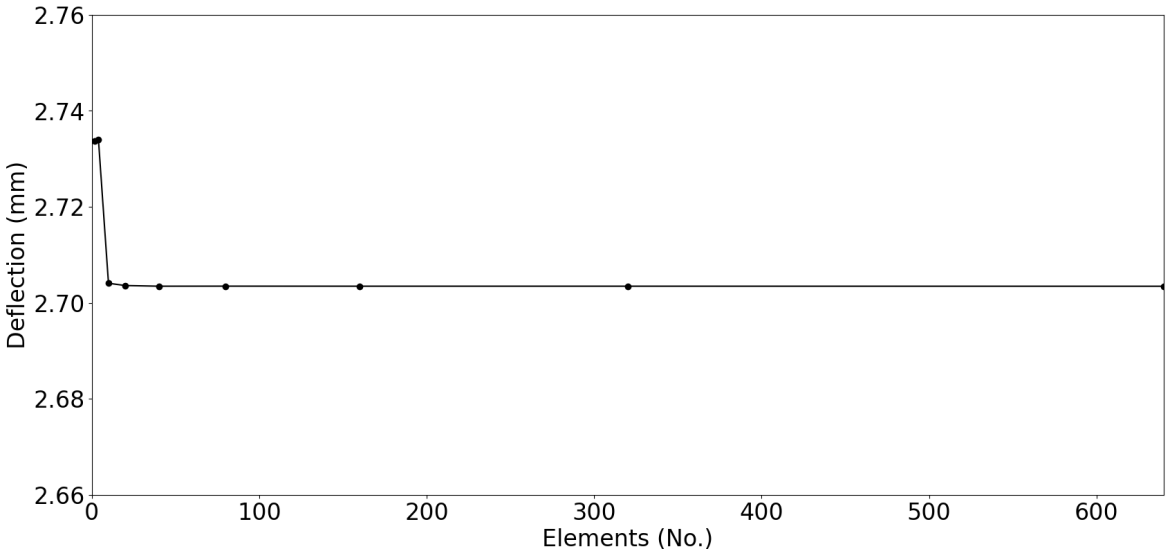


Figure 5.14: Mesh Study - Midspan Deflection

Elements (No.)	Midspan Deflection (mm)	
	Value	% Change
2	2.73	N/A
4	2.73	0.01%
10	2.70	−1.10%
20	2.70	−0.02%
40	2.70	−0.01%
80	2.70	0.00%
160	2.70	0.00%
320	2.70	0.00%
640	2.70	0.00%

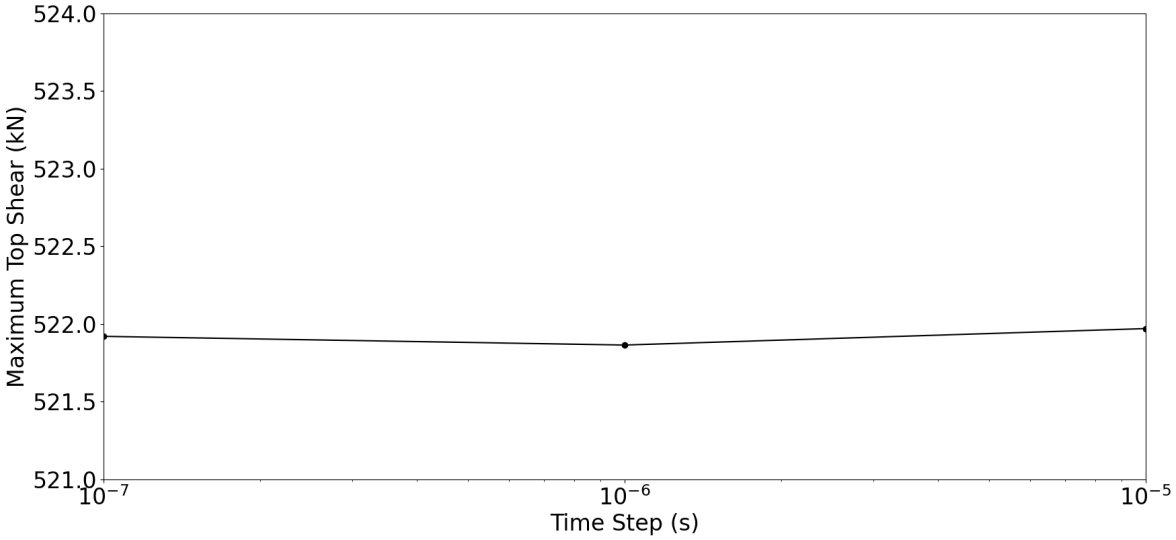
Table 5.4: Mesh Refinement Study Summary Table - Midspan Deflection

Based on these results the conclusion can be made that for the midspan deflection and top and bottom bending moments, a minimum mesh size of 20 elements is required for a converged solution. While, for the top and base shear forces a minimum mesh size of 40 elements is required for a converged solution. Hence, a mesh size of 40 elements was selected for this analysis.

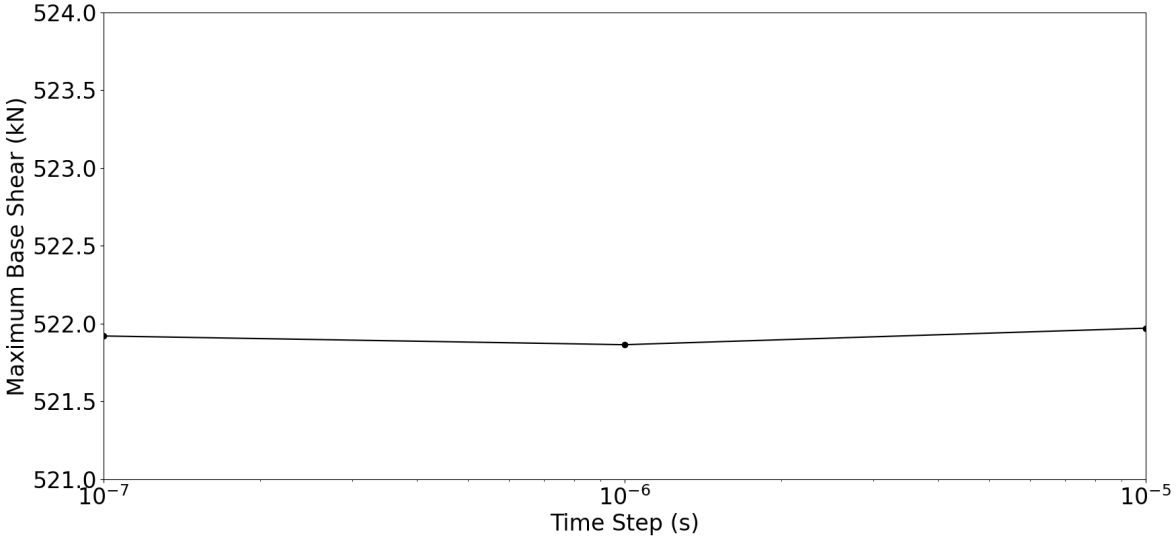
5.4.12 Time Step Study

This section outlines how sensitive the structural response is to the refinement of the time step for a concrete cylinder strength of $40MPa$. The time step refinement consisted of decreasing the time step from $1e^{-5}s$ to $1e^{-7}s$ and analysing how the maximum base shear, top shear, base bending moment, top bending moment, and midspan deflection changed as a result of the time step refinement. The influence of the time step refinement on each response parameter was determined by calculating the percentage change between each time step refinements. A converged mesh was defined as the number of elements at which the percentage change between time step refinements was less than 0.25%.

Observing Figures 5.15, 5.16, and 5.17, it is clear that decreasing the time step did not have an influence on shear, moment, or deflection responses. The percentage change for each response parameter was less than 0.01% and hence, a time step of $1e^{-5}s$ could be used for this analysis. However, the model was more stable with a time step of $1e^{-6}s$ for the higher concrete cylinder strengths investigated and as such a time step of $1e^{-6}s$ was used for this analysis.

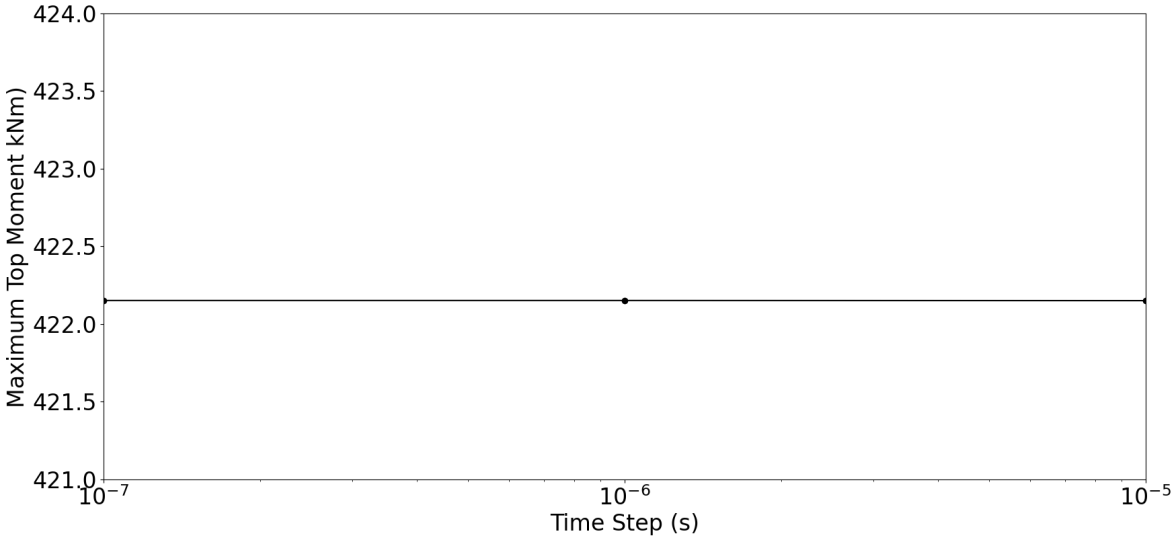


(a) Top Shear Forces

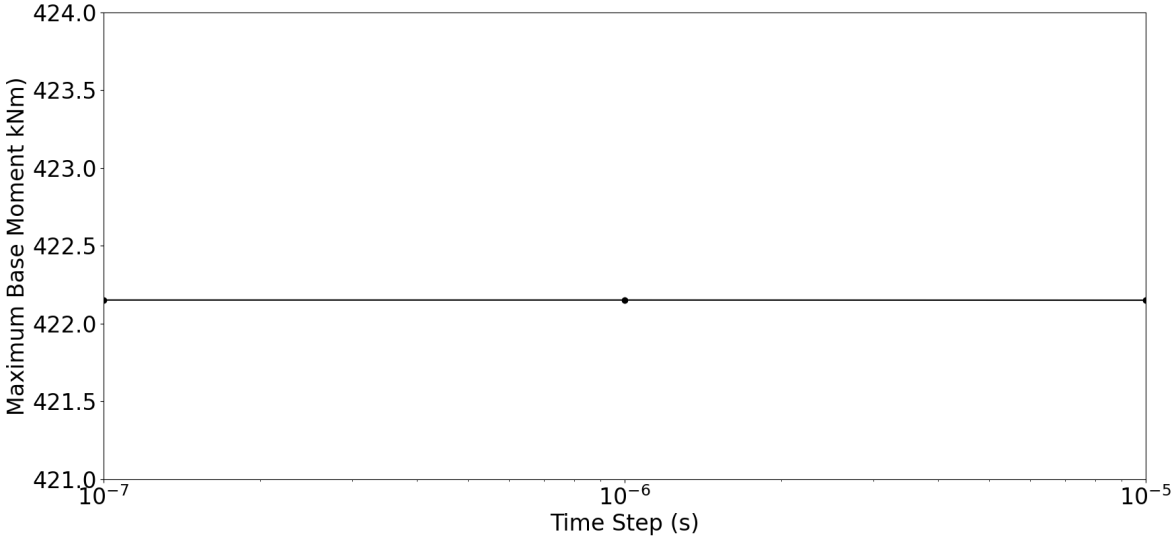


(b) Bottom Shear Forces

Figure 5.15: Time Step Study - Shear Forces



(a) Top Bending Moment



(b) Bottom Bending Moment

Figure 5.16: Time Step Study - Bending Moments

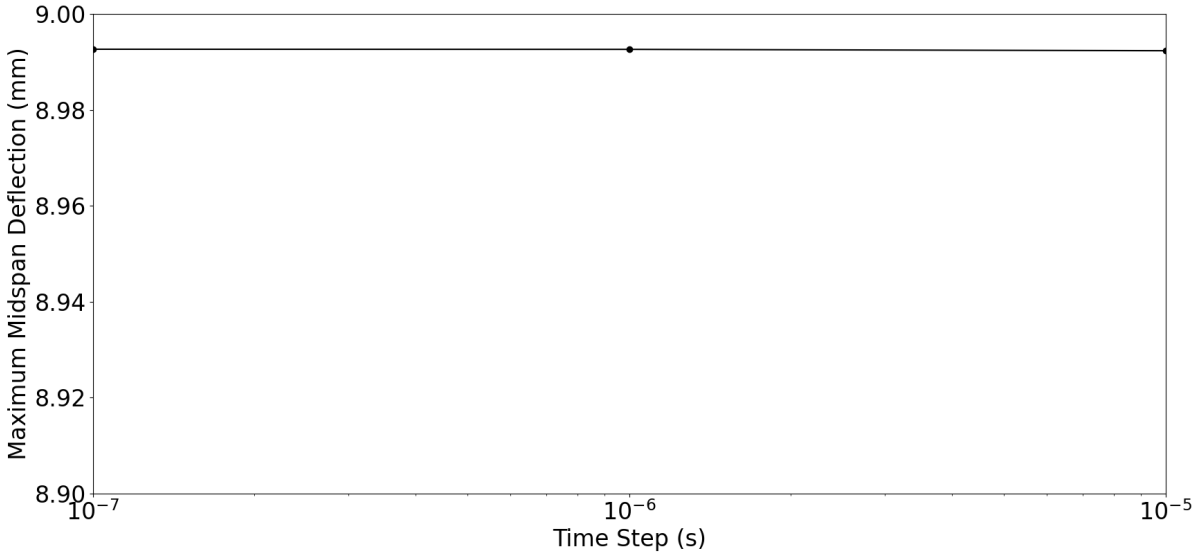


Figure 5.17: Time Step Study - Midspan Deflection

5.4.13 Yield Deflection Study

This section will present how the yield displacement in the column was determined for all concrete cylinder strengths investigated. The yield displacement is an important parameter as it will bound the analysis of the results in this parametric study. The yield displacements will bound the analysis of this parametric study as the structural stiffness value used in this study is only valid within the elastic response of the column and does not necessarily give insight into the nonlinear response of the column. Hence, while the nonlinear response of the column is being modelled, only the response within the elastic range will be analysed.

The yield displacement will be determined by applying a quasi-static *single point constraint* to the midspan node of the column. The *single point constraint* will apply a displacement pattern at the midspan node to determine the associated force displacement curve and yielding displacement of the column. The displacement pattern applied at the midspan node of the column is shown in Figure 5.18, where it can be seen that the displacement increases from $0mm$ to $200mm$ at a rate of $0.02\frac{mm}{s}$.

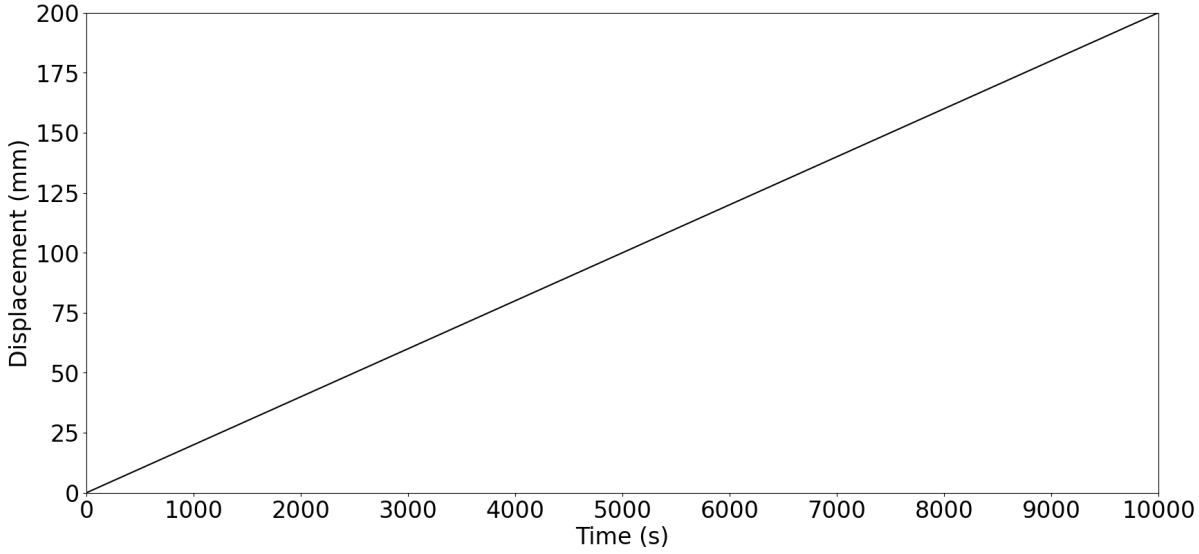


Figure 5.18: Imposed Displacement History

Figure 5.19 outlines the resulting force displacement curves due to the imposed displacement pattern for all concrete cylinder strengths investigated. From Figure 5.19, the yield displacement can be defined as the start location of the yield plateau in the force displacement curve, which varies from approximately $6mm$ to $8mm$. Table 5.5 defines the yield displacements (δ_y) and the yield forces (F_y) for each concrete cylinder strength analysed. From the table and figure, it is apparent that as the concrete cylinder strength increased, the yield displacement decreased, and the yield force increased. This is expected behavior as a stiffer column will both deflect less and require a larger force to cause deflection in the member when compared to a more flexible column.

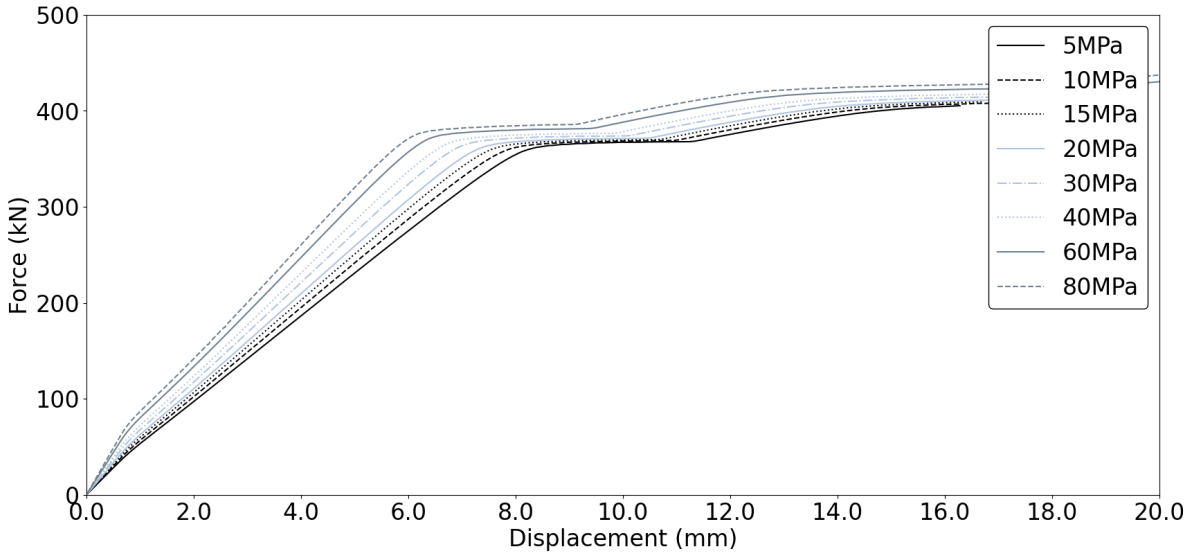


Figure 5.19: Midspan Force Displacement Curve

$f'_c\ (MPa)$	$\delta_y\ (mm)$	$F_y\ (kN)$
5	7.95	352.95
10	7.61	353.31
15	7.40	355.82
20	7.17	356.62
30	6.87	360.24
40	6.60	362.07
60	6.14	362.92
80	5.91	367.62

Table 5.5: Yield Displacements and Forces

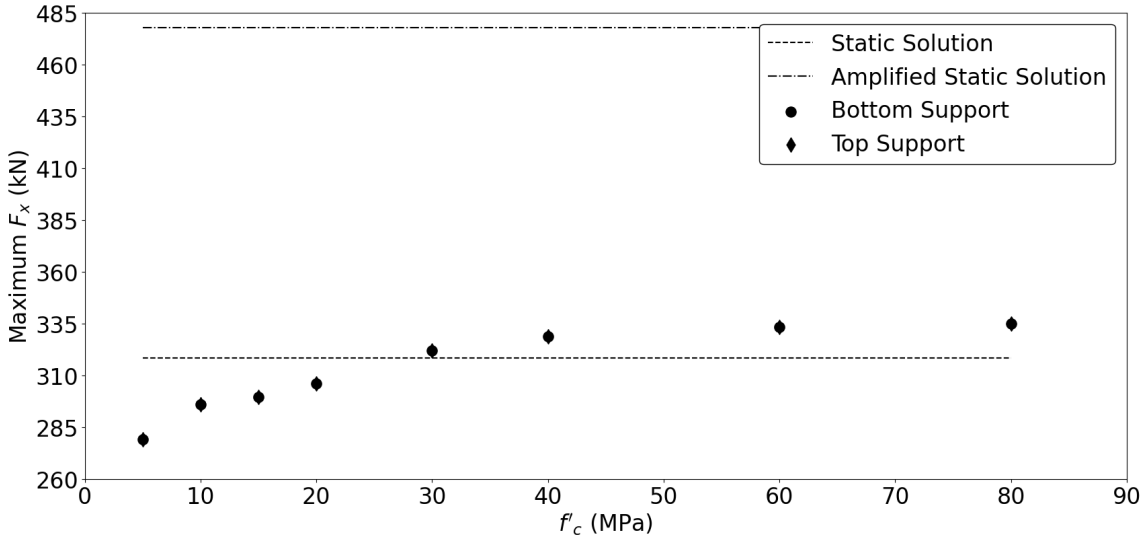
5.5 Results and Discussion

This section presents and discusses how the structural stiffness influences the elastic response of the column outlined in this study by investigating the shear, bending moment, and deflection responses of the column. Only the elastic response of the column is analysed as the structural stiffness used to define this column is only valid within its elastic range. Furthermore, the dynamic analysis results will be compared to the static analysis of a fixed-fixed beam with a concentrated load at the midspan. Additionally, the dynamic results will be compared to the amplified static results, which are amplified using the response ratios defined in Table 6.11-1 of ASCE 7 (2016). For this particular column, the first natural period is $0.009s$ and the ratio of the impact duration to the first natural period is 2.51, which corresponds to a dynamic response ratio of 1.50. The impact magnitude will

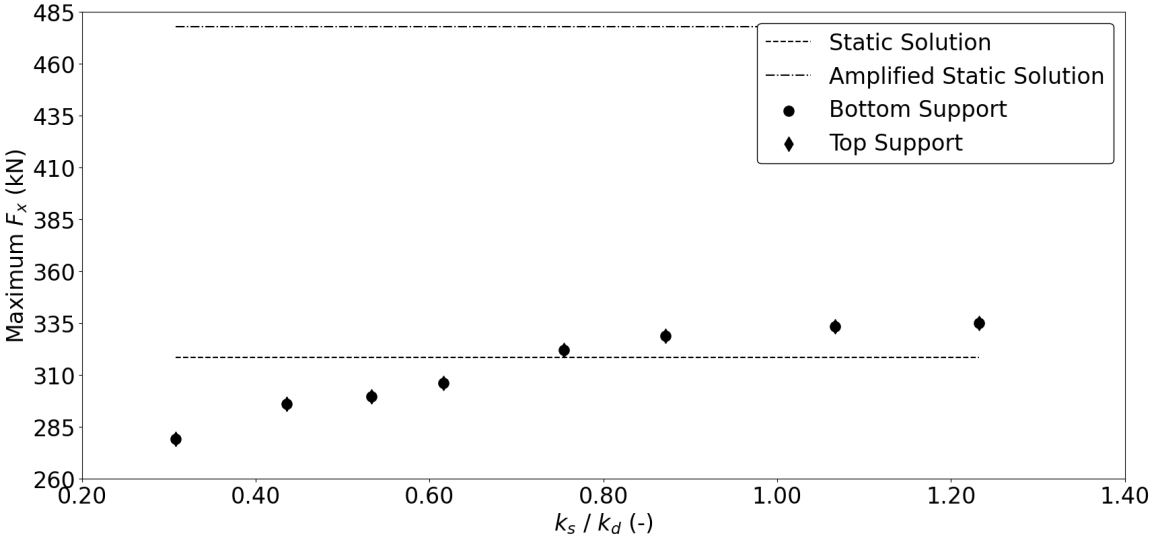
be amplified by the dynamic response ratio, which will provide the results for the amplified static analysis.

5.5.1 Shear Response

Using the impact force history shown in Figure 5.2 and applying it to the column over the entire range of concrete cylinder strengths analysed, the influence of the structural stiffness on the shear response can be determined. Figure 5.20 outlines how the reaction shear forces are influenced as the concrete cylinder strength and structural stiffness are increased. As can be seen in Figure 5.20, both the bottom and top supports provide the same reaction forces. This is expected as the boundary conditions of the column are symmetric, and the load is applied directly at the midspan. From Figure 5.20, the conclusion can be made that as the concrete cylinder strength and structural stiffness increased, the shear reaction forces also increased. This coincides with the force displacement curves presented in Section 5.4.13, where it can be seen that the forces required to reach yielding in the column increased as the cylinder strength increased. Furthermore, as the concrete cylinder strength increases, there is a clear point where the maximum shear reaction forces are larger than those generated from the static analysis. The point at which the dynamic analysis provides larger shear forces than the static analysis occurs around a cylinder strength of $27MPa$ and a k_s/k_d ratio of 0.73. Conversely, below this point the dynamic analysis provides smaller shear forces than the static analysis. Comparing the dynamic results to the amplified static solution, it is apparent that the dynamic analysis results in smaller reaction shear forces than the amplified static solution. The amplified static solution results in shear reaction forces that ranged from 1.43 to 1.71 times larger than the dynamic analysis results.



(a) Reaction Shear Forces (F_x) vs $f_c^{'}$



(b) Reaction Shear Forces (F_x) vs $\frac{k_s}{k_d}$

Figure 5.20: Comparison of Shear Reaction Forces to $f_c^{'}$ and $\frac{k_s}{k_d}$

Figure 5.21 normalizes the shear force by the impact magnitude. The static solution for a fixed-fixed beam with a concentrated load at the center will always provide the same shear force irrespective of the structural stiffness, as the material properties do not influence the reaction forces. For the static analysis of a fixed-fixed beam with a concentrated load at the center, the shear reaction forces will always be equal to half of the impact magnitude, which explains why the static and amplified static solutions always results in a ratio of 0.50. As can be seen in Figure 5.21, when a dynamic analysis was used, the ratio of the maximum shear reaction forces to the impact magnitude ranged from 0.44 to 0.53. This implies that in the elastic range, as the concrete cylinder strength and structural stiffness increase, the design shear reaction forces also increase.

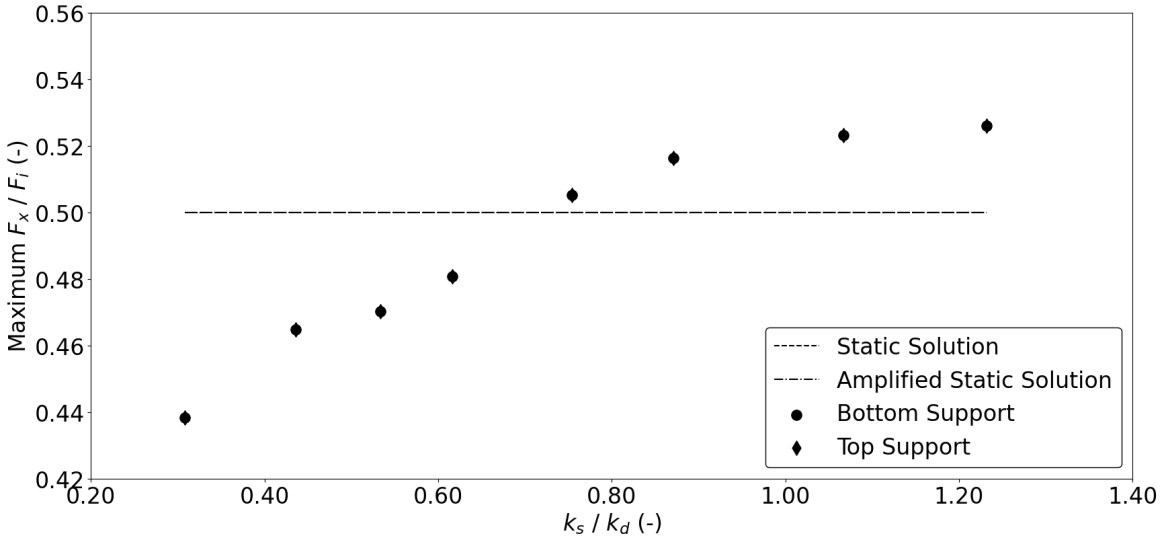
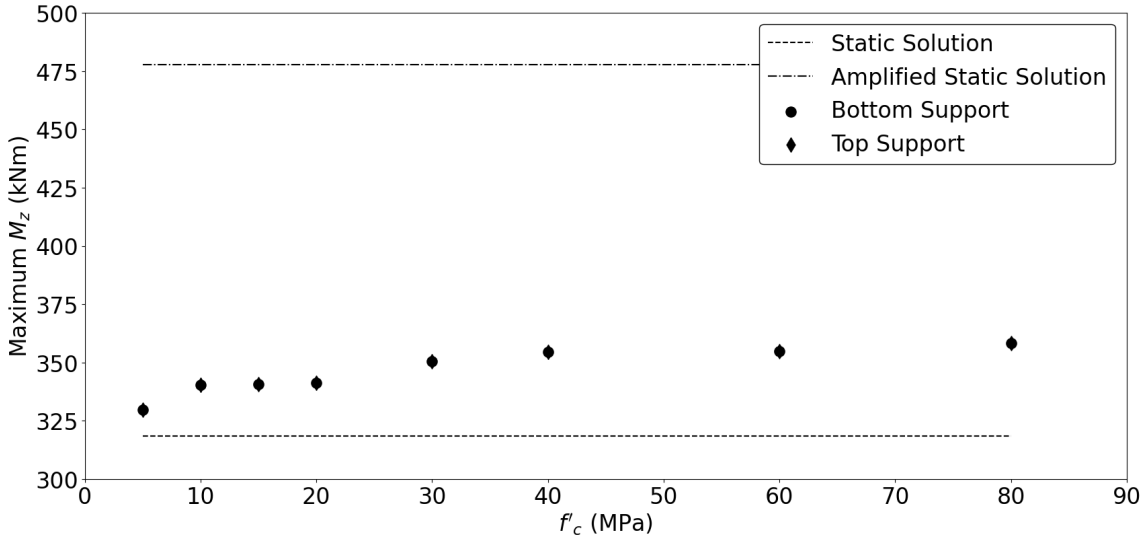


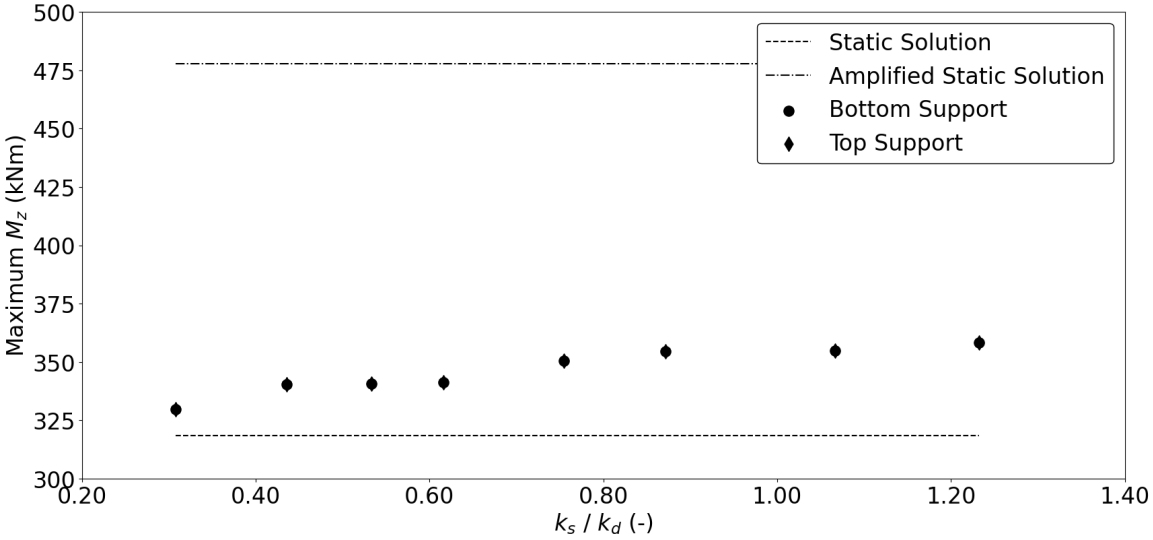
Figure 5.21: Normalized Shear Reaction Forces ($\frac{F_x}{F_i}$) vs $\frac{k_s}{k_d}$

5.5.2 Bending Moment Response

Using the impact force history shown in Figure 5.2 and applying it to the column over the entire range of concrete cylinder strengths analysed, the influence of the structural stiffness on the bending moment response can be determined. Figure 5.22 outlines how the reaction bending moments are influenced as the concrete cylinder strength and structural stiffness are increased. As can be seen in Figure 5.22, both the bottom and top supports provide the same bending moment reaction forces. This is expected as the boundary conditions of the column are symmetric, and the load is applied directly at the midspan. From Figure 5.22, the conclusion can be made that as the concrete cylinder strength and structural stiffness increased, the reaction bending moments also increased. This coincides with the force displacement curves presented in Section 5.4.13, where it can be seen that the forces and consequently the bending moments required to reach yielding in the column increase as the cylinder strength increases. However, unlike the shear reaction forces presented in Section 5.5.1, the reaction bending moments from the dynamic analysis are larger than those resulting from the static analysis. The dynamic analysis results are bounded by the two static analysis solutions, with the amplified static solution resulting in bending moments that ranged from 1.33 to 1.45 times larger than the dynamic results.



(a) Reaction Bending Moments (M_z) vs $f_c^{'}$



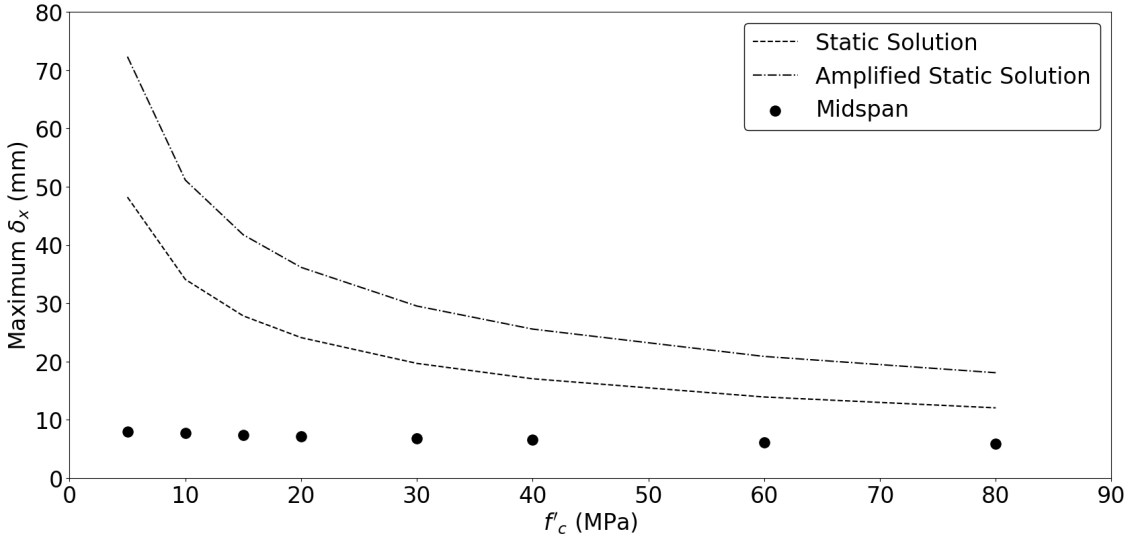
(b) Reaction Bending Moments (M_z) vs $\frac{k_s}{k_d}$

Figure 5.22: Comparison of Reaction Bending Moments to $f_c^{'}$ and $\frac{k_s}{k_d}$

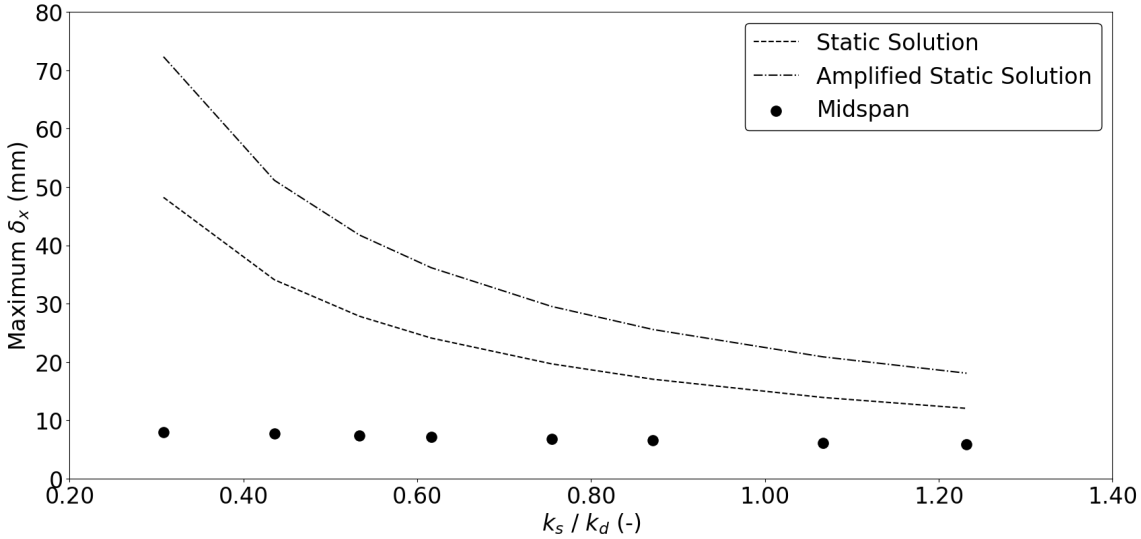
5.5.3 Midspan Deflection Response

Using the impact force history shown in Figure 5.2 and applying it to the column over the entire range of concrete cylinder strengths analysed, the influence of the structural stiffness on the midspan deflection response can be determined. Figure 5.23 outlines how the midspan deflection is influenced as the concrete cylinder strength and structural stiffness are increased. From Figure 5.23, the conclusion can be made that as the concrete cylinder strength and structural stiffness increased, the midspan deflection decreased. This result is expected as the analysis of this column is bounded by the yield displacements of the column and as shown in Section 5.4.13, the yield displacement decreased as the concrete

cylinder strength increased. Furthermore, conceptually this result is expected as a stiffer column will not deflect as much when compared to a more flexible column. However, unlike the shear and bending moment support reactions, the midspan deflections resulting from the dynamic analysis are all smaller than both of the static analysis solutions. The static solution resulted in midspan deflections that ranged from 2.04 to 6.01 times larger than the dynamic results. Whereas, the amplified static solution resulted in midspan deflections that ranged from 3.07 to 9.01 times larger than the dynamic results.



(a) Midspan Deflection (δ_x) vs $f_c^{'}$

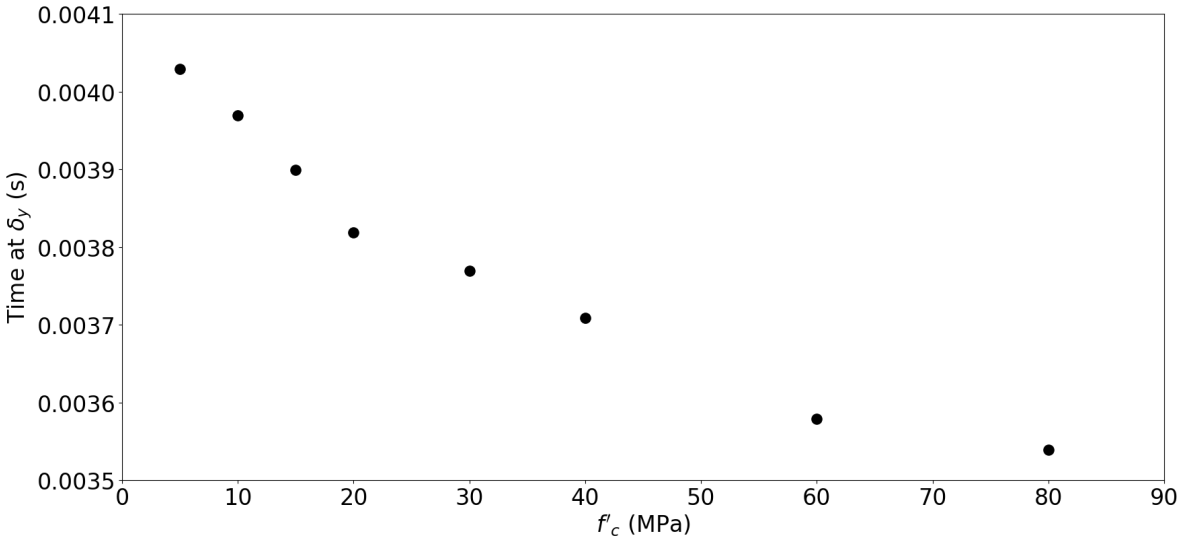


(b) Midspan Deflection (δ_x) vs $\frac{k_s}{k_d}$

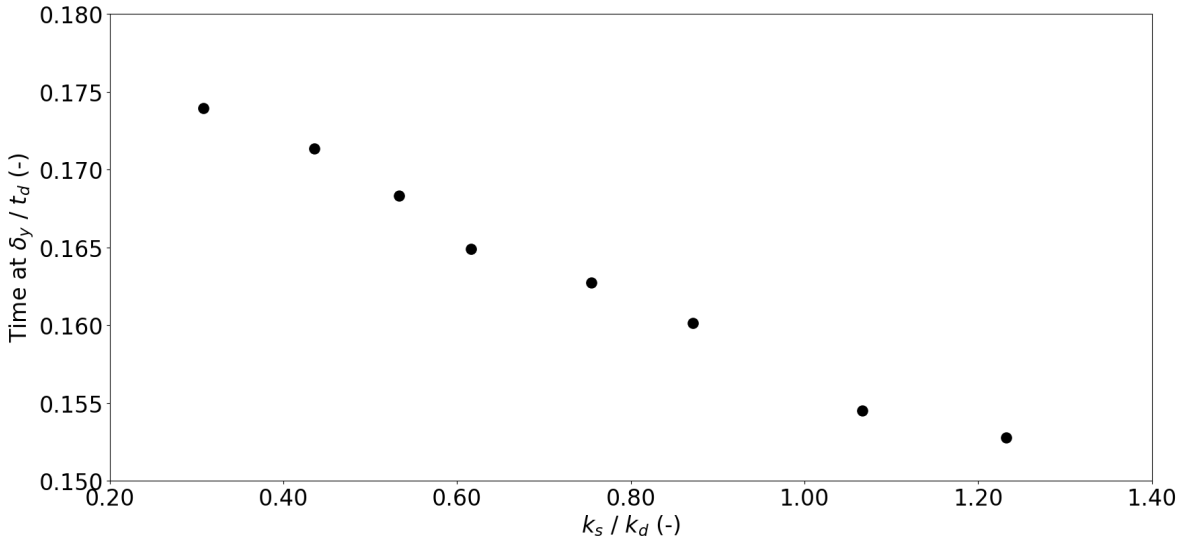
Figure 5.23: Comparison of Midspan Deflections to $f_c^{'}$ and $\frac{k_s}{k_d}$

Figure 5.24a compares the concrete cylinder strength to the analysis time associated with the column reaching its yield displacement. From Figure 5.24a, it is clear that as the

concrete cylinder strength increased, the analysis time at which the yield displacement is reached decreased. Figure 5.24b, normalizes the analysis time associated with the column reaching its yield displacement by the impact duration outlined in Table 5.1. From Figure 5.24b, it is apparent that the normalized time appears to decrease linearly as the k_s/k_d ratio increases.



(a) Time at Yield Displacement (δ_y) vs $f_c^{'}$



(b) Normalized Time at Yield Displacement ($\frac{\delta_y}{t_d}$) vs $\frac{k_s}{k_d}$

Figure 5.24: Comparison of Time at Yield Displacement (δ_y) to $f_c^{'}$ and $\frac{k_s}{k_d}$

5.6 Conclusions

This study outlined how the shear reaction forces, bending moment reaction forces, and midspan deflections are influenced by the strength of the concrete used in the analysis. The

strength of the concrete was varied from $5MPa$ to $80MPa$ and the structural stiffness was calculated for each concrete strength. As the concrete strength increased, the structural stiffness also increased, this resulted in a ratio of the structural stiffness to the debris stiffness that ranged from 0.44 to 1.11.

This analysis consisted of applying a point load at the midspan of the column and bounding the results to the elastic response of the column. The results are bounded by the elastic response of the column as the stiffness used to define the column is the elastic stiffness. Hence, the stiffness is only relevant within the columns elastic range and does not necessarily give insight into the columns nonlinear response. Observing how the shear, bending moment, and midspan deflection responses changed as the concrete cylinder strength and structural stiffness increased, the following conclusions can be made:

1. As the concrete cylinder strength and structural stiffness increased, the shear reaction forces also increased.

2. The dynamic analysis shear reaction forces were larger than the static analysis shear reaction forces when the k_s/k_d ratio and concrete cylinder strength were greater than 0.73 and $27MPa$, respectively.

3. The amplified static analysis resulted in shear reaction forces that overestimated the dynamic analysis results by a minimum factor of 1.43 and a maximum factor of 1.71.

4. Normalizing the shear reaction forces by the impact magnitude showed that the shear reaction forces varied from a minimum of 44% of the impact magnitude to a maximum of 53%. Whereas, a static solution will always result in shear reaction forces equal to 50% of the impact magnitude for a fixed-fixed beam.

5. Observing Figure 5.21, the shear reaction forces appear to follow an approximately increasing linear trend from a k_s/k_d ratio of 0.31 to 0.75. After which the shear reaction forces increase at a slower rate.

6. As the concrete cylinder strength and structural stiffness increased, the reaction bending moments also increased.

7. The dynamic analysis results for the reaction bending moments are bounded by the two static analysis results.

8. The amplified static analysis resulted in reaction bending moments that overestimated the dynamic analysis results by a minimum factor of 1.33 and a maximum factor of 1.45.

9. Observing Figure 5.22, the reaction bending moments appear to follow an approximately increasing linear trend from a k_s/k_d ratio of 0.31 to 0.75. After which the reaction bending moments increase at a slower rate.

10. Fitting a linear trend to both the shear and bending moment reaction forces indicates that the shear reaction forces increased at approximately twice the rate of the bending

moments. This suggests that the shear reaction forces are more sensitive to the structural stiffness when compared to the reaction bending moments.

11. As the concrete cylinder strength and structural stiffness increased, the midspan deflections decreased. This is expected behavior as the analysis is bounded by the yield displacements, which decreased as the concrete cylinder strength increased.

12. Unlike the shear and bending moment reactions, the midspan deflections resulting from the dynamic analysis are all smaller than the static analysis solutions.

13. The static analysis resulted in midspan deflections that overestimated the dynamic analysis results by a minimum factor of 2.04 and a maximum factor of 6.01.

14. The amplified static analysis resulted in midspan deflections that overestimated the dynamic analysis results by a minimum factor of 3.07 and a maximum factor of 9.01.

15. The time at which the column reached its yield displacement decreased as the concrete cylinder strength increased.

16. Normalizing the analysis time at the columns yield displacement by the impact duration demonstrated that as the structural stiffness increased, the normalized time appeared to follow a decreasing linear trend.

17. As the yield displacements are reached quicker as the concrete cylinder strength increased, this implies that the forces developed in the column are also developed quicker. This indicates that both the rate and magnitude of the forces developed in the column increased as the concrete cylinder strength and structural stiffness increased.

While the analysis of this column did include the nonlinear response, the analysis was bounded within the elastic response of the column. Hence, the results presented can only provide insight into the elastic response of this column. Further analysis would have to be completed to quantify how the nonlinear response of the column changes based on the concrete cylinder strength and structural stiffness. Furthermore, a different definition of the structural stiffness would need to be defined to include the influence of the nonlinear response of the column. Potentially, the effective secant stiffness as defined in Commentary C6.11.8 of ASCE 7 (2016) could be used to define the stiffness of the structure when nonlinearity is considered in the design. However, a more in-depth study would need to be completed to investigate how the nonlinear response of a column is influenced as the structural stiffness is increased, as there are several failure mechanisms for columns / beams subjected to lateral loads that complicate the analysis (Zhang et al., 2020). Furthermore, this study only analysed the response using a fiber model in two-dimensional space, a future study could extend this analysis to a full finite element model in three-dimensional space to see if the same conclusions can be drawn. Additionally, a full finite element model would allow the user to view crack patterns that develop within the column, which would provide further understanding into how the columns fail under lateral loads.

Chapter 6

Numerical Modelling of Dam-Break Wave Generated Debris Impacts[1]

6.1 Introduction and Objective

Based on post-tsunami field studies such as those completed by Saatcioglu et al. (2005), Naito et al. (2014), and Stolle et al. (2020a), it is apparent that tsunami generated debris impacts are an important design consideration for structures. Previous literature has focused on quantifying tsunami generated debris impact loads through scaled-down experimental studies (see Matsutomi (2009); Ko et al. (2015); Stolle et al. (2018a, 2019)) or full-scale experimental and numerical studies that do not include the hydrodynamics associated with tsunami generated debris impacts (see Aghl et al. (2014, 2015)). The inclusion of hydrodynamics in a numerical model further complicates the simulation due to the complex interaction between a fluid and a solid. However, the inclusion of hydrodynamics should be considered as it can influence the debris impact force (Haehnel and Daly, 2004; Matsutomi, 2009; Riggs et al., 2013; Ikeno et al., 2016).

The objective of this study is to numerically simulate dam-break wave generated debris impact events using the general-purpose finite element program LS-DYNA (LST, 2020). The numerical model is based off of the experimental program outlined in Stolle et al. (2019, 2020b), who used a dam-break wave to generate debris impact events, more details on the physical model can be found in Section 6.3. A dam-break wave was used to approximate a tsunami bore, as Chanson (2006) determined that a tsunami bore front propagating over a coastal plain resembles that of a dam-break wave front.

6.2 Numerical Modelling Methods in LS-DYNA

LS-DYNA is a general-purpose finite element program that is capable of simulating highly nonlinear transient dynamic problems using explicit time integration or implicit time in-

[1]This Chapter forms a portion of a manuscript being prepared for submission to the Coastal Engineering Journal.

tegration in some specific use cases. Generically, there are three available methods for solving finite element problems in LS-DYNA:

1. The Lagrangian method
2. The Eulerian method
3. The Arbitrary Lagrangian-Eulerian (ALE) method

A brief description of each method, potential use cases, and the capability of each method to simulate dam-break wave generated debris impact events is outlined in the following sections.

6.2.1 Lagrangian Method

The Lagrangian method can be broken down into two categories: (1) a mesh-based approach and (2) a mesh-free approach. Within the mesh-based approach, the Lagrangian method is typically described by the Finite Element Method (FEM). The FEM approach is a method for which mesh nodes are fixed to the material for the entire numerical simulation. The mesh nodes are always attached to the material and as such, if the material deforms then the computational mesh also deforms. Hence, large deformations of the material will lead to large distortions of the mesh, which can lead to numerical inaccuracies and instabilities. Based on this reasoning, the Lagrangian mesh-based approach is typically reserved for simulations where large deformations are not expected, such as linear dynamic simulations.

The mesh-free Lagrangian approach can solve the problem of large mesh distortions by representing the numerical simulation by a finite number of discrete particles instead of a mesh. Each particle can represent either a single discrete object in the simulation, such as sand particles in an injection analysis, or it can represent a portion of a continuum, such as fluid particles in a wave. Simulating single discrete objects is typically done using the Discreet Element Method (DEM), whereas, the simulation of particles defining a continuum is typically done using the Smoothed Particle Hydrodynamics (SPH) method.

Using a purely Lagrangian approach for the simulation of dam-break wave generated debris impact events was investigated. The structure and debris in the simulation were modelled using the FEM approach and the fluid was modelled using the SPH method. However, it was determined that using the SPH approach for this type of simulation is not optimal. This was concluded as the SPH particles physically block the debris from impacting the structure, instead of acting like a continuum and allowing the debris to be transported through the particles and impact the structure.

6.2.2 Eulerian Method

The Eulerian method is a mesh-based approach for numerical simulations that is typically described by the Finite Volume Method (FVM). The FVM approach is a method for

which a mesh is fixed in both space and time and the materials move through the mesh. As the mesh is fixed in space and time, the issue of mesh distortion due to large material deformations is not a concern. As the issue of mesh distortion is not a concern, the Eulerian mesh-based approach is typically reserved for simulations where large material deformations are expected, such as free-surface flow simulations. Using a purely Eulerian approach for the simulation of dam-break wave generated debris impact events was not investigated as a very fine mesh would be needed to capture the structure and debris geometry and responses.

6.2.3 Arbitrary Lagrangian-Eulerian Method

The Arbitrary Lagrangian-Eulerian (ALE) method can be described as a method that combines the Lagrangian and Eulerian approaches for numerical simulations. The ALE method aims to solve the issue of large mesh distortions in the Lagrangian method by allowing both the material and mesh to deform in space and time. An ALE time step as described in Hallquist (2006) can be defined by the following steps:

1. Perform a Lagrangian time step:
   (a) The mesh follows the material deformation
2. Perform an advection step:
   (a) Decide which nodes to move
   (b) Move the boundary nodes
   (c) Move the interior nodes
   (d) Calculate the transport of element-centered variables
   (e) Calculate the momentum transport and update the velocity

Using an ALE approach for the simulation of dam-break wave generated debris impact events was investigated and ultimately, it was decided to use this approach for the numerical model as the purely Lagrangian approach was not feasible. The structure and debris were simulated using the FEM approach and the fluid was modelled using the FVM approach. Using the ALE method to model the fluid, debris, and structure allowed for direct fluid-structure interactions to be modelled between the Lagrangian and Eulerian meshes by the use of coupling points at the interface between the two meshes. These coupling points allow for the contact to occur between dissimilar meshes by adding contact points along the Lagrangian surface. This method is ideal for the simulation of dam-break wave generated debris impact events based on the following conclusions:

1. The debris and structure will not deform significantly as shown in the experimental results of Stolle et al. (2019), meaning a typical FEM mesh for these parts is suitable.
2. The water will deform significantly and as such a FVM mesh was used for this part.

3. The ALE solver in LS-DYNA allows for direct coupling between the Lagrangian and Eulerian meshes.

4. Modelling the water using the FVM approach allows for the debris to be transported through the water and impact the structure, unlike the SPH approach which physically blocked the debris from impacting the structure.

6.3 Physical Model Reference

The numerical model for this study is based off of the experimental work by Stolle et al. (2019, 2020b). Stolle et al. (2019, 2020b) performed the experimental program in the Hydraulics Laboratory at the University of Ottawa. The facility houses a dam-break wave flume with a length of $30m$, a width of $1.5m$, and a maximum impoundment depth of $0.7m$. The reservoir of water has a length of $21.55m$, which was impounded behind a swing-gate at various inundation depths for the experimental studies of Stolle et al. (2019, 2020b). However, for the numerical model presented in this chapter only the results associated with an impoundment depth of $0.40m$ are used.

The experimental program consisted of a structural column subjected to dam-break wave generated debris impact events. The debris used in the study were $1:40$ geometrically scaled $20-ft$ shipping containers constructed of positively buoyant polyethylene with dimensions of $0.06 \times 0.06 \times 0.15m$, a wall thickness of $0.005m$, and a mass of $0.236kg$. The structure used in the experimental study had a square hollow cross-section, which was constructed from acrylic and had dimensions of $0.20 \times 0.20 \times 0.80m$ with a wall thickness of $0.005m$. Figure 6.1 outlines the dam-break wave flume at the University of Ottawa.

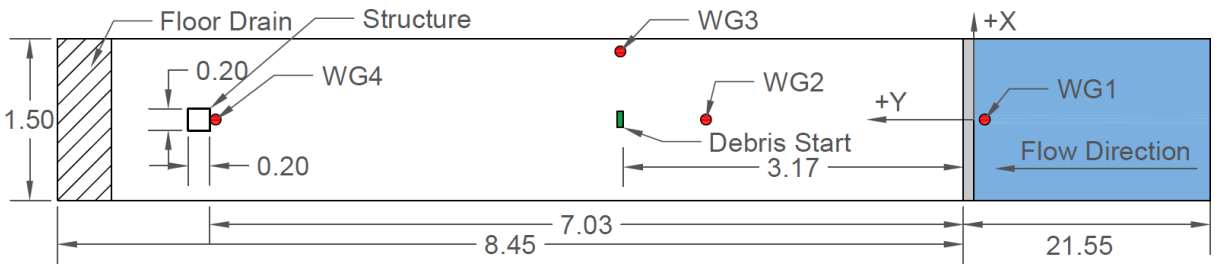


Figure 6.1: University of Ottawa Dam-Break Wave Flume (Units in Meters)

The material properties of the debris and structure outlined in Stolle et al. (2019) were used as input into the numerical model and are outlined as follows:

- Modulus of Elasticity (E):
  - Debris $= 1.5GPa$
  - Structure $= 2.5GPa$

- Density (ρ):
  - Debris = $920\frac{kg}{m^3}$
  - Structure = $1200\frac{kg}{m^3}$ (density for acrylic as per ANSYS® (2018))

The key parameters that were recorded during the experimental program and were used for quantitative comparisons to the numerical model included the following:

- Water surface elevation of the dam-break wave at four different (x, y) locations along the flume, note that the origin was assumed to be at the center of the flume and the swing gate as shown in Figure 6.1.
  - WG1 = $(0.00,\ -0.10)$
  - WG2 = $(0.00,\ 2.40)$
  - WG3 = $(0.50,\ 3.20)$
  - WG4 = $(0.00,\ 7.03)$
- The force response of the structure due to the combined wave and debris impact.
- The debris transport paths.
- The debris impact velocity.

6.4 Computational Domain

The computational domain is split into four components: (1) The structure; (2) The debris; (3) The water; and (4) The air. The water is further split into two components, the first being the reservoir of water and the second being downstream of the swing gate. The downstream portion of the computational domain reproduced the downstream dimensions of the wave flume in the experimental setup as shown in Figure 6.2. The downstream computational domain was cut-off at a length of $7.25m$, which is $0.02m$ past the downstream face of the structure in the experimental setup. The downstream computational domain did not model the full length of the downstream experimental setup, as in the experimental setup there are no points of interest past the structure except the floor drain. Hence, the decision was made to reduce the downstream computational domain from $8.45m$ to $7.25m$, to reduce the domain size and computational time. Additionally, a wet-bed condition was modelled by including $15mm$ of water along the downstream portion of the flume.

The reservoir of water in the computational domain does not reproduce exactly the size of the reservoir in the experimental setup, which has a length of $21.55m$. The length of the reservoir (L) in the computational domain was increased such that the water surface elevation at WG1 was constant after a simulation time of $6.0s$. This criterion indicates that a quasi-steady state has been reached behind the swing gate. A simulation time of $6.0s$ was chosen, as this length of time allows for the debris to be fully transported down

the flume and the hydrodynamic force of the dam-break wave to reach a quasi-steady state value.

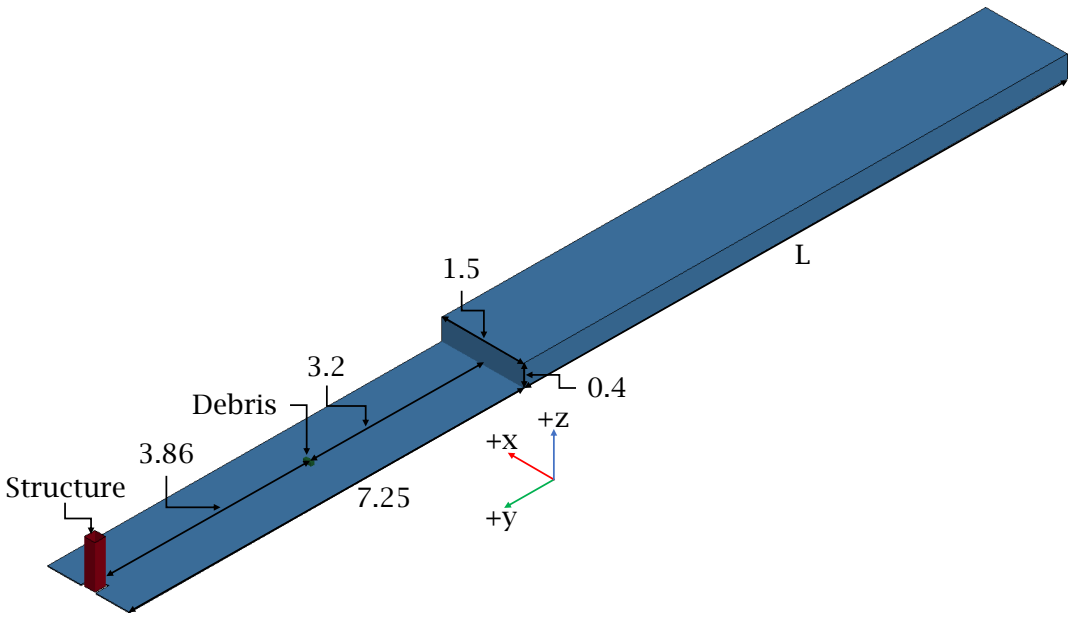


Figure 6.2: University of Ottawa Dam-Break Wave Flume in LS-DYNA (Units in Meters)

The length of the reservoir was increased from $5.0m$ to $10.0m$ and the influence of the reservoir length on the water surface elevation time history at WG1 is plotted in Figure 6.3. From Figure 6.3, it is clear that a $5m$ reservoir is not adequate to reach a constant water surface elevation at WG1 after $6.0s$. The $7m$ reservoir provided a constant water surface elevation at WG1 until approximately $5.5s$, at which point there is a slight decrease in water surface elevation. From Figure 6.3, it is apparent that a $10m$ reservoir achieved a constant water surface elevation after $6.0s$. Furthermore, Table 6.1 outlines the computational time associated with each reservoir length. The simulated time (T_{sim}) is the same for all reservoir lengths and as can be seen in the table, the computational time (T_{comp}) increases as the reservoir size increases. This is due to more elements being modelled as the computational domain increases in size. The relative increase in computational time (T_{rel}) is also presented in Table 6.1. From Table 6.1, it can be seen that increasing the reservoir length from $5m$ to $7m$ resulted in a 7.1% or $30min$ increase in computational time and increasing from $7m$ to $10m$ resulted in a 9.5% or $43min$ increase in computational time. Hence, as the water surface elevation at WG1 is constant after $6s$ and the increase computational time is not significant, a $10m$ reservoir was chosen to be modelled.

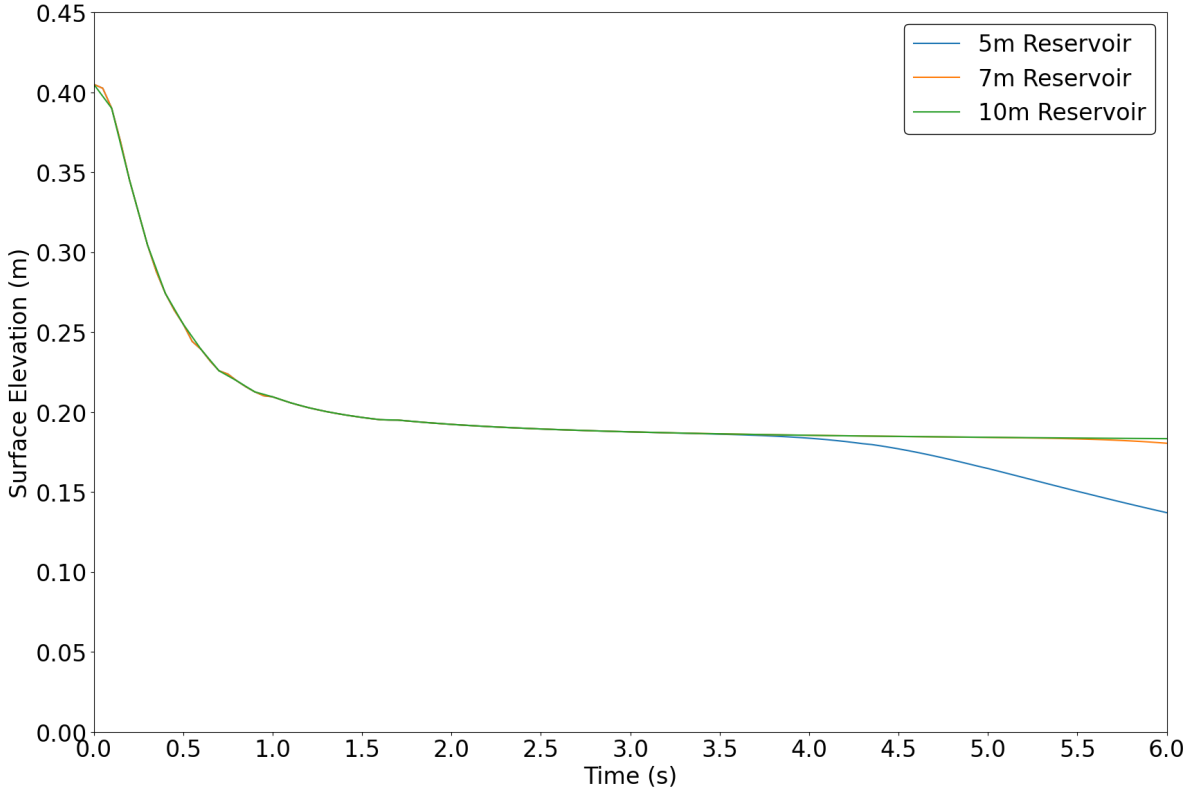


Figure 6.3: Water Surface Elevation Time Series at WG1 $(0.00, -0.10)$

Reservoir Length (m)	CPUs $(No.)$	T_{sim} (s)	T_{comp} (hrs)	T_{rel} $(\%)$
5	64	6	6.99	N/A
7	64	6	7.49	7.1%
10	64	6	8.20	9.5%

Table 6.1: Reservoir Length Study

6.5 General ALE Description of Navier-Stokes Equations

Using the ALE description of motion the total time derivative of a variable h can be described as follows (Aquelet et al., 2006):

$$\frac{\mathrm{d}h(\overrightarrow{X},t)}{\mathrm{d}x} = \frac{\partial h(\overrightarrow{x},t)}{\partial t} + (\overrightarrow{v} - \overrightarrow{w}) \cdot \overrightarrow{\boldsymbol{\nabla}} h(\overrightarrow{x},t) \tag{6.1}$$

Where:

- t = Time

- $\overrightarrow{X}$ = Lagrangian coordinate
- $\overrightarrow{x}$ = ALE coordinate
- $\overrightarrow{v}$ = Material velocity vector
- $\overrightarrow{w}$ = Mesh velocity vector

The conservation equations for mass, momentum, and energy in the general ALE formulation are outlined as follows (Aquelet et al., 2006):

$$\frac{\partial \rho}{\partial t} + \rho \boldsymbol{\nabla} \cdot \overrightarrow{v} + (\overrightarrow{v} - \overrightarrow{w}) \boldsymbol{\nabla} \rho = 0 \tag{6.2}$$

$$\rho \frac{\partial \overrightarrow{v}}{\partial t} + \rho (\overrightarrow{v} - \overrightarrow{w}) \cdot \overrightarrow{\overline{\boldsymbol{\nabla}}} \overrightarrow{v} = \overrightarrow{\boldsymbol{\nabla}} \cdot \overline{\overline{\sigma}} + \overrightarrow{f} \tag{6.3}$$

$$\rho \frac{\partial e}{\partial t} + \rho (\overrightarrow{v} - \overrightarrow{w}) \cdot \overrightarrow{\boldsymbol{\nabla}} e = \overline{\overline{\sigma}} : \overrightarrow{\overline{\boldsymbol{\nabla}}} \overrightarrow{v} + \overrightarrow{f} \cdot \overrightarrow{v} \tag{6.4}$$

Where:

- ρ = Mass density
- e = Energy
- $\overline{\overline{\sigma}}$ = Cauchy stress tensor
- $\overrightarrow{f}$ = Force vector which includes the components associated with pressure

If a Lagrangian formulation is being used by LS-DYNA, the velocity components ($\overrightarrow{v}$, $\overrightarrow{w}$) are set equal to each other and if the Eulerian formulation is being used, the mesh velocity component ($\overrightarrow{w}$) is set equal to zero. LS-DYNA solves the conservation equations in the ALE method by using the split operator technique outlined in Benson (1992a). The split operator technique splits each time step into two phases, a Lagrangian phase and a Eulerian phase. The first phase of the split operator technique is the Lagrangian phase, where the material and mesh velocities are equal, this phase can also be referred to as a linear Stokes problem (Aquelet et al., 2006). In the Lagrangian phase the momentum and energy conservation equations are reduced to the following (Aquelet et al., 2006):

$$\rho \frac{\mathrm{d} \overrightarrow{v}}{\mathrm{d} t} = \overrightarrow{\boldsymbol{\nabla}} \cdot \overline{\overline{\sigma}} + \overrightarrow{f} \tag{6.5}$$

$$\rho \frac{\mathrm{d} e}{\mathrm{d} t} = \overline{\overline{\sigma}} : \overrightarrow{\overline{\boldsymbol{\nabla}}} \overrightarrow{v} + \overrightarrow{f} \cdot \overrightarrow{v} \tag{6.6}$$

For the Lagrangian formulation, the mass conservation is used in its integrated form, as it is simpler and more accurate to use in this form to calculate the current density (ρ).

The current density is a function of the initial density (ρ_0) and the volumetric strain (J) (Aquelet et al., 2006):

$$\rho J = \rho_0 \tag{6.7}$$

Where the volumetric strain is given by the Jacobian (Aquelet et al., 2006):

$$J = \det\left(\frac{\partial x_i}{\partial X_j}\right) \tag{6.8}$$

During the Lagrangian phase the mesh will move with the material exactly and a drop in the time step will signifying that the mesh is distorted, which triggers the second phase of the split operator technique. The second phase is the Eulerian phase where the mesh velocity is set to zero and mesh rezoning algorithms are used to place the mesh back into its original location. In LS-DYNA mesh rezoning is done using the equipotential method developed by Winslow (1963). The method is used to construct a structured mesh for finite difference or finite element calculations by using the solution of Laplace equations (and later Poisson equations) as the mesh lines (Hallquist, 2006). The transport equations for the Eulerian phase are defined as follows (Aquelet et al., 2006):

$$\frac{\partial \phi}{\partial t} + (\overrightarrow{v} - \overrightarrow{w}) \cdot \boldsymbol{\nabla} \phi = 0 \tag{6.9}$$

$$\phi(\overrightarrow{x}, 0) = \phi_0(x) \tag{6.10}$$

Where:

- ϕ = Conservative variable
- $\phi_0(x)$ = Initial condition of the conservative variable at coordinate x

The hyperbolic equation system defining the transport equations are then solved for mass, momentum, and energy in the Eulerian phase by using a finite volume method. In LS-DYNA there is the option between a first-order upwind scheme or a second-order Van Leer algorithm to solve the transport equations (Aquelet et al., 2006), these options are defined Section 6.7.

6.6 Time Integration Method

In LS-DYNA there is the option between using an explicit or implicit time integration solver. However, the implicit time integration solver is restricted to specific use cases and the ALE method does not fall within these use cases. Hence, the explicit solver in LS-DYNA was used. LS-DYNA uses the central difference time integration method, which is a second order accurate method. LS-DYNA defines the semi-discrete equation of motion at time i as follows (Hallquist, 2006):

$$Ma_i = P_i - F_i + H_i \tag{6.11}$$

Where M is the diagonal mass matrix, a_i is the acceleration vector, P_i accounts for the external and body force loads, F_i is the stress divergence vector, and H_i is the hourglass resistance. To advance the time to t_{i+1}, LS-DYNA uses the central difference time integration scheme where the acceleration at time i is estimated as:

$$a_i = M^{-1}\left(P_i - F_i + H_i\right) \tag{6.12}$$

Next the global nodal velocity vector (v) at time $t_{i+1/2}$ is estimated as:

$$v_{i+1/2} = v_{i-1/2} + a_i \Delta t_i \tag{6.13}$$

The displacement vector (u) is then calculated at time t_{i+1} as:

$$u_{i+1} = u_i + v_{i+1/2} \Delta t_{i+1/2} \tag{6.14}$$

Where:

$$\Delta t_{i+1/2} = \frac{\Delta t_i + \Delta t_{i+1}}{2} \tag{6.15}$$

Finally, LS-DYNA updates the model geometry (x_{i+1}) by adding the displacement increments to the initial geometry (x_0), which is done to reduce the sensitivity of the results to round-off errors (Hallquist, 2006).

$$x_{i+1} = x_0 + u_{i+1} \tag{6.16}$$

Additionally, it should be noted that LS-DYNA does not use a constant time step for the entire simulation, the time step is always limited by a single element in the mesh. How the time step is controlled is outlined in Section 6.6.1. The general time integration loop that LS-DYNA follows, as outlined in Hallquist (2006), is defined below:

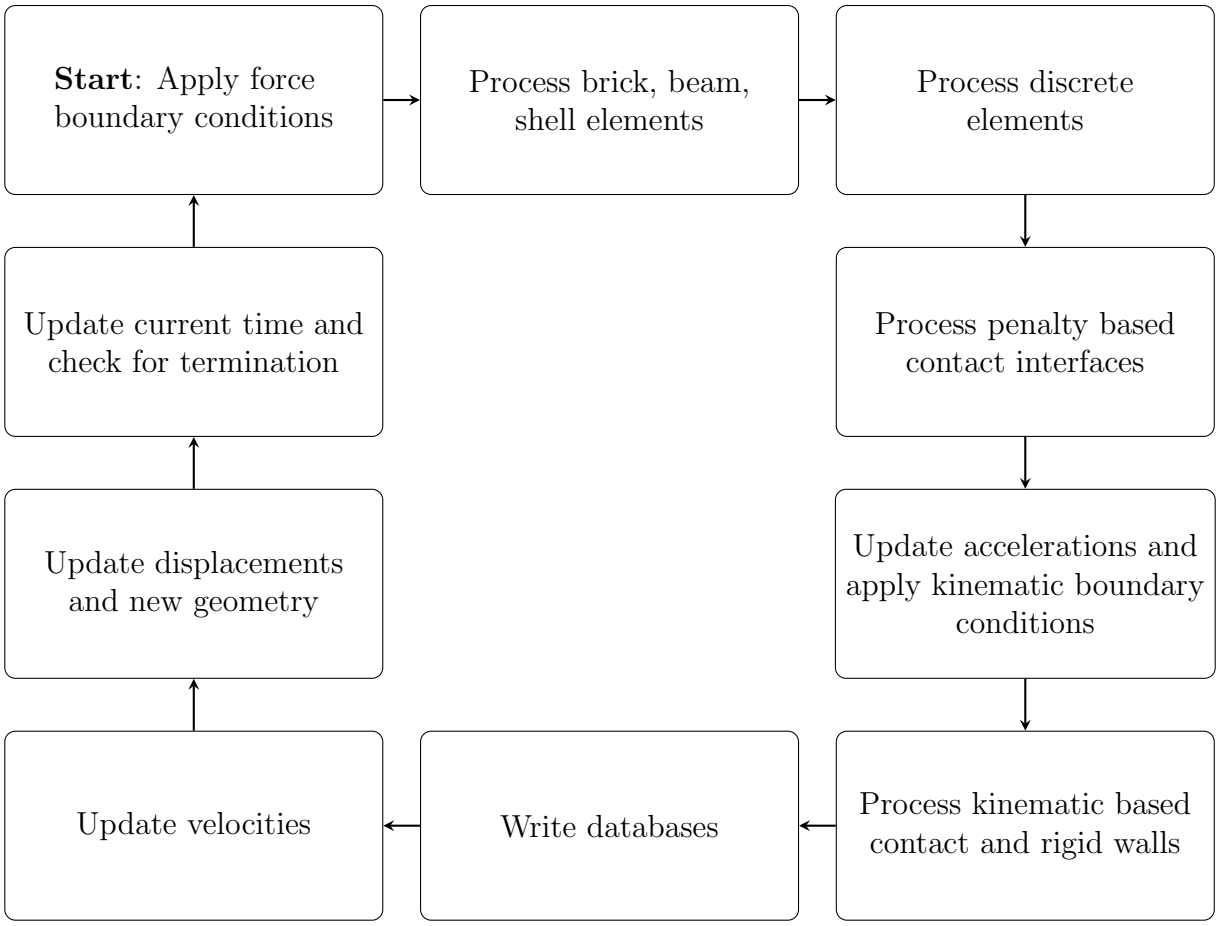


Figure 6.4: LS-DYNA Time Integration Loop

6.6.1 Time Step Control

During the time integration loop, LS-DYNA determines the new time step size (Δt_{i+1}) as the minimum value over all elements (N) multiplied by a scaling factor (a):

$$\Delta t_{i+1} = a \cdot \min\{\Delta t_1, \Delta t_2, \ldots, \Delta t_N\} \tag{6.17}$$

The scaling factor is used for stability reasons as the explicit time integration scheme is conditionally stable based on the minimum required time step for all elements in the simulation. The dam-break wave generated debris impact simulation uses solids elements for the fluid parts and shell elements for the structure and debris. Hence, the critical time step for each element is dependent on the type of element used.

For solid elements, Hallquist (2006) defines the critical time step size (Δt_e) as a function of the characteristic length (L_e), the bulk viscosity function (Q), and the sound speed (c):

$$\Delta t_e = \frac{L_e}{\left[Q + (Q^2 + c^2)^{1/2}\right]} \tag{6.18}$$

For shell elements, Hallquist (2006) defines the critical time step size as a function of the shell characteristic length (L_s) and the sound speed:

$$\Delta t_e = \frac{L_s}{c} \tag{6.19}$$

When using the explicit solver in LS-DYNA the user has control over the time step size through the use of the scaling factor a, which defaults to a value of 0.90. For blast or other high velocity simulations a time step scale factor of 0.67 is recommended (LST, 2020). The influence of the time step scale factor on the dam-break wave simulation was investigated by reducing the factor from 0.90 to 0.45 and seeing how the hydrodynamic forces on the structure change.

Figure 6.5 outlines the hydrodynamic forces on the structure in the positive Y direction. As can be seen in the figure, with a smaller time step scale factor the hydrodynamic forces in the positive Y direction become more noisy. However, as the time step scale factor decreases, the hydrodynamic forces do not change significantly, which suggests that the hydrodynamic forces are not significantly sensitive to the time step scale factor. Figure 6.6 outlines the time step size history, where it can be seen that as the scale factor decreases, the time step time also decreases as expected. The total run time using eight cores and a time step scale factor equal to 0.90 was $5.95hrs$ with an average time step of $2.69e^{-4}s$, the run time increased to $7.77hrs$ for a scale factor of 0.67, resulting in an average time step of $2.11e^{-4}s$. Furthermore, the run time increased to $12.47hrs$ for a scale factor of 0.45, resulting in an average time step of $1.39e^{-4}s$. It should be noted that these three simulations did not include the debris and that with the debris in the simulation the minimum required time step decreased further to approximately $9.6e^{-6}s$, as the debris governs the time step size. Based on these results a time step scale factor of 0.45 was chosen to ensure stability issues did not arise when the debris was introduced into the model.

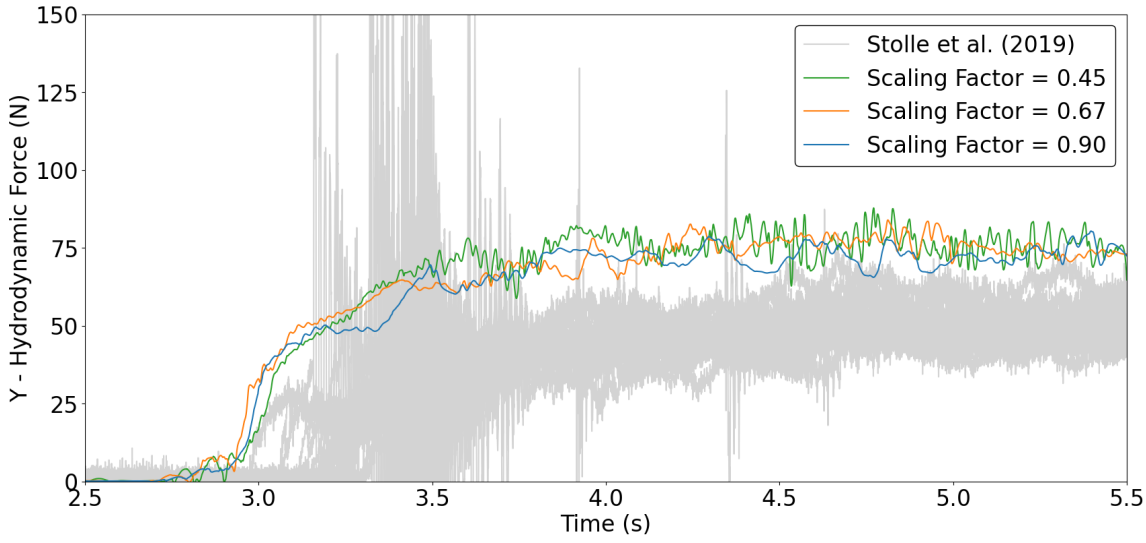


Figure 6.5: Influence of Time Step Scale Factor on Hydrodynamic Force in Y-Direction

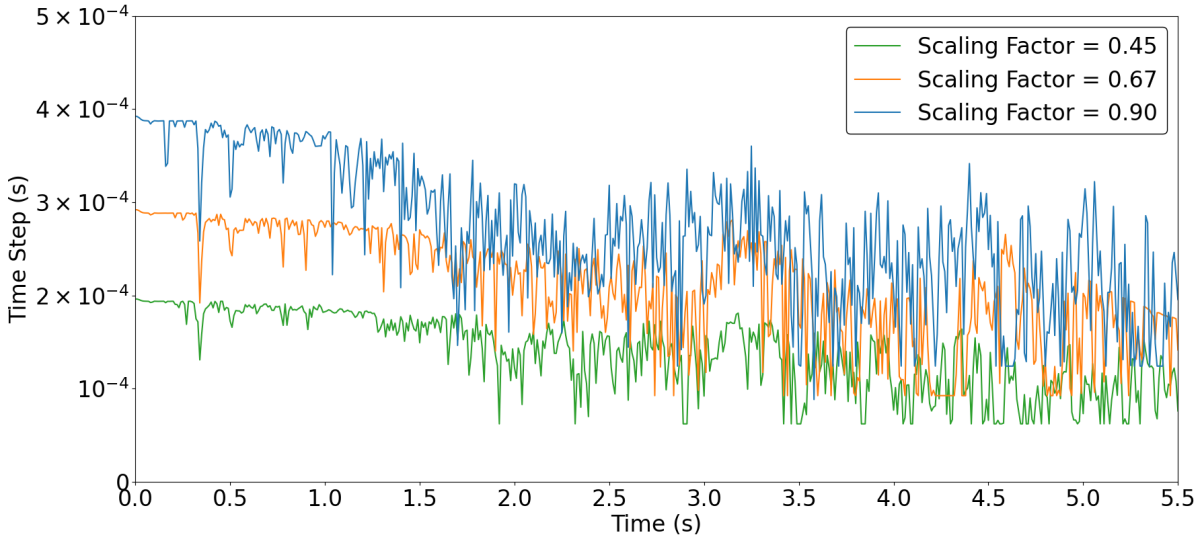


Figure 6.6: Influence of Time Step Scale Factor on Time Step

6.7 ALE Advection Schemes

The advection algorithms in LS-DYNA are used to facilitate the movement of material flux through the mesh. The number of variables that are advected depend on the type of material and elements being used. However, density, internal energy, the stress tensor, and the history variables are always advected.

LS-DYNA allows the user to choose between two advection methods to calculate the values of the solution variables in the transport fluxes (Hallquist, 2006). The first method is the Donor cell algorithm which is first order accurate. The second method is the Van Leer algorithm (Van Leer, 1977), specifically the monotone upwind schemes for conservation laws (MUSCL), which is a second order accurate scheme. One of the differences between the Donor cell and Van Leer algorithms is that Donor cell algorithm assumes that the distribution of a solution variable is constant over an element. Whereas, the Van Leer algorithm replaces the piecewise constant distribution with a higher order interpolation function that is subject to an element level conservation constraint (Hallquist, 2006). Due to the Donor cell algorithm assuming that the distribution of a solution variable is constant over an element, it tends to diffuse sharp gradients over time. This is not experienced for the Van Leer algorithm due to it assuming a higher order interpolation function between elements. An example of how a solution variable (ϕ) is advected between elements using both the Donor cell and Van Leer algorithms is presented in Figure 6.7.

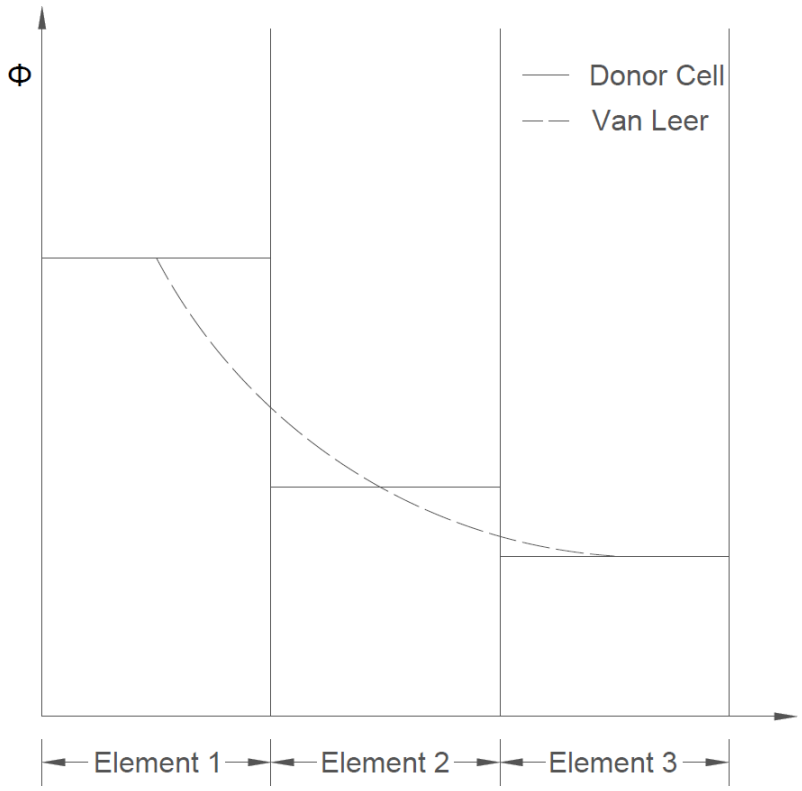


Figure 6.7: Advection Methods in LS-DYNA

The Donor Cell and Van Leer algorithms are used to calculate the values of the solution variables in the transport fluxes. To calculate the momentum transport, LS-DYNA allows the user to choose between two different algorithms. The first algorithm is the SALE algorithm (Amsden et al., 1980) and the second algorithm is the Half Index Shift (HIS) algorithm (Benson, 1992b). The SALE algorithm is computationally less expensive than the HIS algorithm, however, it suffers from known dispersion problems and may violate monotonocity by introducing spurious oscillations (Benson, 1992b). As such LS-DYNA uses by default the HIS algorithm, as it can be shown analytically to not have either problem on a regular mesh (Hallquist, 2006). For this analysis the Van Leer with HIS advection scheme was chosen as it is second order accurate, does not diffuse sharp gradients over time, and does not violate monotonicity.

6.8 Turbulence Modelling

Turbulence in LS-DYNA is typically modelled when using the Incompressible Computational Fluid Dynamics (ICFD) solver, which is an implicit time integration solver. The ICFD solver supports the RANS $\kappa-\epsilon$, LES Smagorinsky, WALE, RANS $\kappa-\omega$, and RANS Spalart-Allmaras turbulence models (LST, 2020). However, the only available option to account for turbulence when using the ALE solver in LS-DYNA is through a one-parameter

mixing-length turbulence model based on Prandtl's Mixing Length Model (Prandtl, 1926). The Prandtl's Mixing Length Model is termed a zero-equation model that is based on empirical data for the mixing length. It is also based on local equilibrium of turbulence production and dissipation and hence, it cannot account for transport and history effects of turbulence (Mohammadian, 2019). However, using this turbulence model for this simulation was not investigated as the fluid-structure interaction algorithm requires the use of a multi-material ALE formulation, which does not support the one-parameter mixing-length turbulence model. It should be noted that as no turbulence is being modelled, if two of the exact same simulations are being run, they will produce exactly the same results.

6.9 ALE Model

This section will discuss the sections, materials, equation of state, boundary conditions, and contact modelling used for this study.

6.9.1 Section Types

In LS-DYNA the section model is used to define the element formulation and integration rule used for each element type (LST, 2020). Two different sections types were defined for the dam-break wave generated debris impact simulation. A solid section was defined for the ALE part and a shell section was defined for the structure and debris.

For solid elements that define the ALE part, a one-point integration ALE multi-material element was used. This element type was used to define the ALE parts, as it is the only element type that allows for both the water and air to occupy the same element.

For the structure and debris, the fully integrated shell elements in LS-DYNA were used to model the parts. The fully integrated shell elements use four in-plane integration points except when calculating transverse shear, in which case one in-plane integration point is used to eliminate transverse shear locking (Hallquist, 2006). The element formulation also uses a local element coordinate system that rotates with the material to account for rigid body motion and automatically satisfies frame invariance of the constitutive relations (Hallquist, 2006). This element formulation was used to model the structure and debris as it is considered to be the most accurate shell element formulation in LS-DYNA.

6.9.2 Material Modelling

Material models are used in LS-DYNA to define the material properties of the different parts that are being simulated, for this study four different material models were used. The debris was modelled with the elastic material model and the structure was modelled with the rigid or elastic material model, the details of both of these material models can be found in Section 6.9.2.1. The water was modelled with the null material model in LS-DYNA and the details of that material model can be found in Section 6.9.2.2. The air was

modelled with the vacuum material model in LS-DYNA and the details of that material model can be found in Section 6.9.2.3.

6.9.2.1 Rigid and Elastic Material Models

The rigid material model in LS-DYNA is used to define a part as rigid. A part that is defined as rigid does not influence the critical time step of the simulation, as LS-DYNA bypasses rigid elements in the element processing state (Hallquist, 2006), this leads to very cost-efficient elements. The rigid material model requires the user to define the mass density, modulus of elasticity, and Poisson's ratio of the material. The properties used for the rigid material must be reasonable values as they do have an influence on contact analysis in penalty-based contacts. Hence, the rigid structure was modelled with the following properties:

- Mass density = $1200\frac{kg}{m^3}$ (ANSYS®, 2018)
- Modulus of elasticity = $2.5GPa$ (Stolle et al., 2020b)
- Poisson's ratio = 0.375 (ANSYS®, 2018)

The elastic material model in LS-DYNA is an isotropic hypoelastic material model. This means that the material exhibits the same material properties in all directions and that deformations of the material are considered small (Hallquist, 2006). The material model requires the user to define the mass density, modulus of elasticity, and Poisson's ratio of the material. Hence, the debris was modelled with the following properties:

- Mass density = $920\frac{kg}{m^3}$ (Stolle et al., 2020b)
- Modulus of elasticity = $1.5GPa$ (Stolle et al., 2020b)
- Poisson's ratio = 0.42 (ANSYS®, 2018)

By using the elastic material model, LS-DYNA calculates the co-rotational rate of the deviatoric Cauchy stress tensor ($s_{ij}^{\nabla^{i+1/2}}$) as a function of the elastic shear modulus (G) and the deviatoric strain rate ($\dot{\epsilon'}_{ij}^{n+1/2}$) as per Hallquist (2006):

$$s_{ij}^{\nabla^{i+1/2}} = 2G\dot{\epsilon'}_{ij}^{n+1/2} \tag{6.20}$$

The pressure (p^{n+1}) is then calculated as a function of the bulk modulus (K) and the relative volume (V) as per Hallquist (2006):

$$p^{n+1} = -K \ln V^{n+1} \tag{6.21}$$

6.9.2.2 Null Material Model

The null material model allows for equations of state (EOS) to be considered with the option of not computing deviatoric stresses. The null material model can be used for fluid modelling, as the model does not have a yield-strength and as such it behaves in a fluid-like manner (LST, 2020). The material model requires the user to define the mass density, pressure cut-off value, and optionally the dynamic viscosity of the material (LST, 2020). If a dynamic viscosity is specified then the null material model calculates the viscous stress (σ_{ij}) as a function of the dynamic viscosity (μ) and the deviatoric strain rate ($\dot{\epsilon'}_{ij}$) as per Hallquist (2006):

$$\sigma_{ij} = \mu \dot{\epsilon'}_{ij} \tag{6.22}$$

The pressure cut-off value is required for this material model as it defines when the material should numerically cavitate. The parameter specifies the magnitude of dilatation allowed before the material can no longer resist the dilatation. A pressure cut-off value $-5e^4$ Pa was selected for this analysis, as larger pressure cut-off values led to instabilities in the reservoir. The instabilities in the reservoir can be described as swelling at the water surface at random locations in the reservoir, an example of how the swelling appears for a SPH dam-break wave model is shown in Figure 6.8.

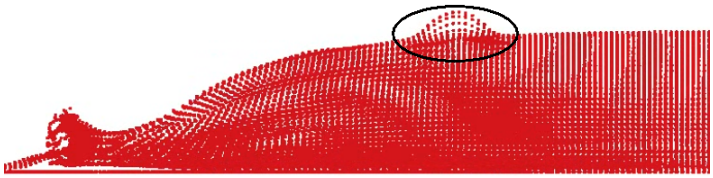


Figure 6.8: Fluid Material Swelling

Furthermore, the null material model requires an hourglass control parameter to be specified. This is because the zero energy modes need to be controlled as the ALE solid elements only use one-point integration (Hallquist, 2006). LS-DYNA suggests for fluids to use the standard viscous form of hourglass control with an hourglass coefficient equal to 10^{-6} (LST, 2020). Hence, the fluid material was modelled with the following parameters:

- Mass density = $1000 \frac{kg}{m^3}$
- Pressure cut-off = $-5e^4 Pa$
- Dynamic viscosity = $0.001 Pa\ s$
- Hourglass type = Standard LS-DYNA viscous form
- Hourglass coefficient = 10^{-6}
- EOS as defined in Section 6.9.3

6.9.2.3 Vacuum Material Model

The vacuum material model in LS-DYNA is a dummy material which represents a vacuum in an ALE simulation (LST, 2020). This material model does not increase computation time but rather it defines elements for which the null material model can be advected through. The air in the domain was modelled with the vacuum material model in LS-DYNA. The only property that is input into the material model is the estimated material density, which is only used for a stability check. For the air material an estimated density of $1.225\frac{kg}{m^3}$ was assumed.

6.9.3 Equation of State Model

As the fluid is being modelled using the null material model in LS-DYNA, an equation of state (EOS) is required to relate the fluid material to its associated pressure. LS-DYNA follows Monaghan and Kos (1999) and uses the Murnaghan EOS (Murnaghan, 1944), which can be used to enforce quasi-incompressibility while allowing for a reasonable time step in explicit simulations. The EOS defines pressure (p) at any point in the fluid as a function of the density of the fluid at rest (ρ_0), the current density (ρ), and two coefficients ($k_0,\ \gamma$) as shown below (LST, 2020):

$$p = k_0 \left[\left(\frac{\rho}{\rho_0} \right)^{\gamma} - 1 \right] \tag{6.23}$$

Typically, γ is assumed to be equal to 7 for fluid flows (Monaghan and Kos, 1999) and k_0 is chosen such that the sound speed (c_0) is greater than or equal to ten times the maximum expected fluid flow velocity (v_{max}) (LST, 2020):

$$c_0 = \sqrt{\frac{\gamma k_0}{\rho_0}} \geq 10 v_{max} \tag{6.24}$$

To determine the maximum fluid flow velocity a simulation of just the dam-break wave was completed and the maximum value over the entire domain was extracted, which was determined to be $3.5\frac{m}{s}$. Hence, the parameter k_0 was solved by assuming that c_0 is equal to ten times the maximum fluid flow velocity, which resulted in k_0 being equal to $1.8e^5$. Therefore, the values used as input into the EOS model in LS-DYNA were:

- $\gamma = 7$
- $k_0 = 1.8e^5$

6.9.4 Boundary and Loading Conditions

The boundary of the computational domain was defined by rigid walls, which is a way for LS-DYNA to define contact between a rigid surface and all nodes in the domain (LST,

2020). Figure 6.9 outlines the rigid walls that were defined for this model. There are two rigid walls that define the sides of the flume, a rigid wall that defines the floor of the flume, and a rigid wall at the back of the reservoir to ensure the fluid flows downstream. At the downstream end of the flume there is no rigid wall, meaning the fluid and debris can be transported out of the computational domain. Having no rigid wall at the downstream end of the flume simulates the floor drain in the experimental setup of Stolle et al. (2020b). The swing gate in the experimental setup of Stolle et al. (2020b) was not explicitly simulated as in an ideal experimental setup, the swing gate would not influence the dam-break wave propagation. Furthermore, Stolle et al. (2018b) concluded that the swing-gate opening time of the dam-break wave flume at the University of Ottawa did not have a significant influence on the wave propagation.

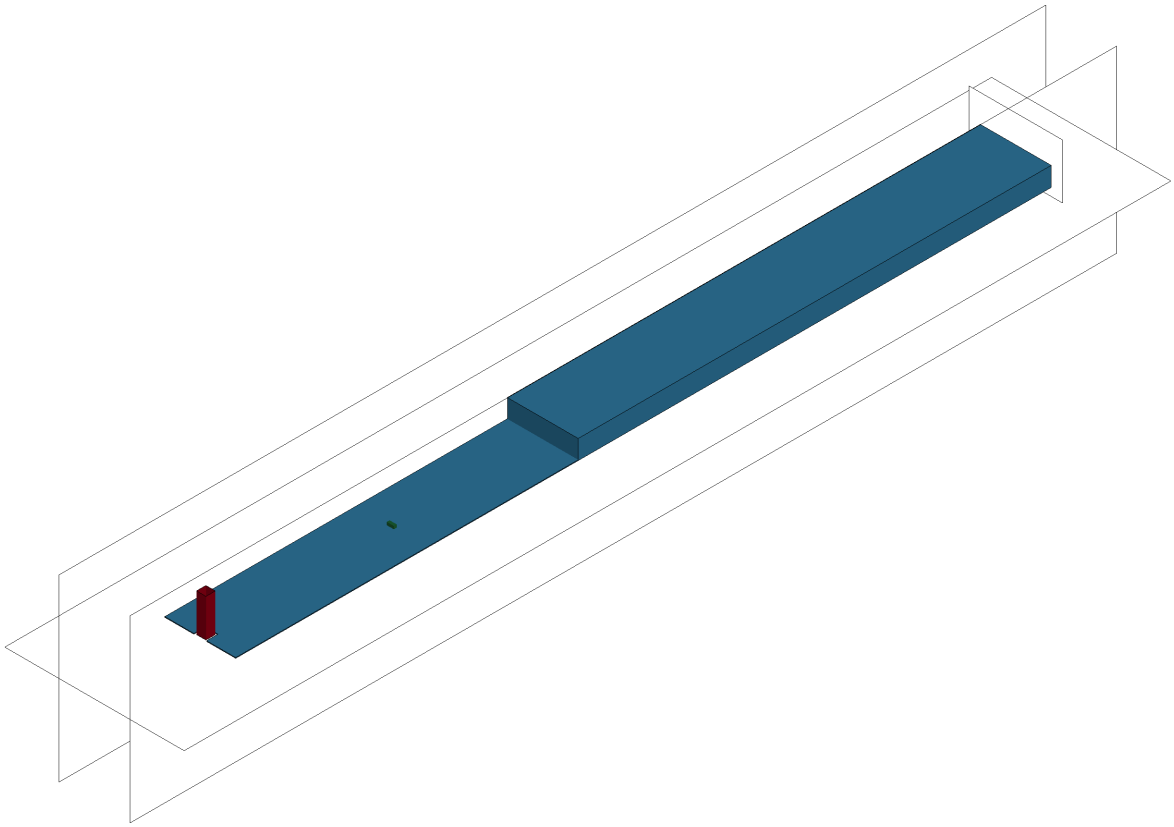


Figure 6.9: Rigid Walls in Computational Domain

The dam-break wave is generated through the force of gravity, which was applied with a body load in LS-DYNA to all parts in the model. LS-DYNA applies gravity loads to the model by fixing the base and applying the loading as part of the body force loads as per Hallquist (2006). Following Hallquist (2006), the body force ($f_{e_{body}}$) can be calculated as a function of the base acceleration (a_{base}) and the element lumped mass matrix (m_e):

$$f_{e_{body}} = m_e a_{base} \tag{6.25}$$

The gravity was applied to the numerical model using a load curve that slowly increased the gravitational acceleration up to a of constant of $9.81\frac{m}{s^2}$. The load curve defined for this simulation starts by assuming that the gravitational acceleration is zero at a time of zero. The acceleration was then increased linearly to a value of $9.81\frac{m}{s^2}$ at a time of $0.05s$, after which it remained constant for the entire simulation. This approach for applying gravity was done as it was found that applying the full acceleration at time zero resulted in splash up at the interface between the fluid and rigid walls.

6.9.5 Contact Modelling

Contact modelling for the dam-break wave generated debris impacts can be broken down into two general categories. The first category is the contact between the debris and structure. The second category is the fluid-structure interaction (FSI) between the water and the FEM parts (i.e. debris and structure). This section will review the contact algorithms used to define the contacts in the numerical simulation.

6.9.5.1 Debris-Structure Contact

The contact between the debris and structure was defined by the automatic single surface contact type (LST, 2020). This contact type is the most widely used contact option in LS-DYNA, as it allows the user to define a list of parts in the model for which contact is considered. Contact is then considered between all parts in the list and also includes self-contact for each part. Automatic contacts are the recommended contact options in LS-DYNA as these contacts are non-oriented, meaning they can detect penetrations coming from either side of an element.

Contacts in LS-DYNA are internally represented by linear springs that connect the slave node to the master segment. These springs are then used to ensure that the slave node does not penetrate through a master segment by applying a force to both the slave and master. The force (F) is calculated as a function of the spring stiffness (k) and the penetration depth (d) (Hallquist, 2006):

$$F = kd \tag{6.26}$$

How LS-DYNA calculates the spring stiffness is based on the contact formulation that the user specifies. LS-DYNA offers three methods for calculating the contact stiffness, these three methods can be grouped into two general categories. The first category is the penalty-based approach, where the contact is activated through nodes penetrating segments and the stiffness is calculated from material constants and the element segment size. This approach works best when the contacting materials have similar material properties and similar mesh densities (Contact Modeling in LS-DYNA, 2010). The contact stiffness is calculated as a function of the bulk modulus of the contacted element (K), the penalty scale factor (f_s), the area of the element (A), and the maximum diagonal for shell elements

(d_{max}) (Contact Modeling in LS-DYNA, 2010):

$$k = \frac{f_s A K}{d_{max}} \tag{6.27}$$

The second category is the constraint-based approach, which calculates the contact stiffness based on the nodal masses that come into contact and the global time step size. The constraint-based approach can be broken down into two more categories that differ in how the contact is activated. In the first constraint-based approach, the contact is activated in the same way as the penalty-based approach, through nodes penetrating segments. This method is similar to the penalty-based approach, however, it handles contacts between dissimilar materials and mesh densities better than the penalty-based approach (Contact Modeling in LS-DYNA, 2010). In the second constraint-based approach, the contact is activated through segments penetrating segments and has its origins in Pinball contact algorithms (Contact Modeling in LS-DYNA, 2010). This method is different than the two other approaches in that it handles sharp corners in geometry well. The contact stiffness for the constraint-based approaches can be calculated as a function of the scale factor (f_s), the nodal mass (m), and the global time step size (Δt) (Contact Modeling in LS-DYNA, 2010):

$$k = f_s \frac{m}{\Delta t^2} \tag{6.28}$$

For the contact between the debris and structure, the second constraint-based approach was used, this approach is entitled $SOFT = 2$ in LS-DYNA (LST, 2020). This approach was used because the mesh between the debris and structure were significantly different ($30mm$ vs $5mm$ square elements) and both parts have sharp corner geometries (i.e. rectangles). Furthermore, this contact formulation is typically regarded as the more realistic method for distributing contact forces (Contact Modeling in LS-DYNA, 2010). This is because the method treats segment to segment contacts instead of node to segment contacts. Segment to segment contact implies that when contact between two 4-noded segments occurs, the contact force is distributed to eight nodes to resist the segment penetration instead of being distributed to just the slave nodes and master segment.

6.9.5.2 Fluid-Structure Interaction

The fluid-structure interaction (FSI) between the Eulerian and Lagrangian meshes is handled through a penalty-based coupling approach. For FSI, the master surface is always assumed to be the Eulerian part and the slave surface is always assumed to be the Lagrangian part (Aquelet et al., 2006). The penalty-based approach is similar to the one described in Section 6.9.5.1, where a linear spring is attached to a slave and master node, and a coupling force is calculated to prevent penetration. The computed coupling force is then only applied to the nodes that are on the fluid structure interface. The coupling force is equal to the spring stiffness and the penetration depth as outlined in Section 6.9.5.1. Furthermore, the coupling force is applied to both the slave and master nodes to satisfy force equilibrium at the coupling interface (Aquelet et al., 2006). At the structure node, the

coupling force (F_s) is a function of the spring stiffness and the penetration depth (Aquelet et al., 2006):

$$F_s = -kd \tag{6.29}$$

The fluid coupling force is distributed to the fluid element nodes based on the shape functions at each node i (N_i). The fluid coupling force (F_f^i) at each node i is then scaled by the associated shape function (Aquelet et al., 2006):

$$F_f^i = N_i kd \tag{6.30}$$

The force equilibrium is then satisfied as the sum of the fluid coupling forces for all nodes in the element (n) are equal to the structure coupling force (Aquelet et al., 2006):

$$\sum_{i=1}^{n} F_f^i = F_s \tag{6.31}$$

To determine the spring stiffness required to calculate the coupling force for FSI, the stiffness is calculated based on the stiffness used in explicit contact algorithms (Zhong, 1993). The stiffness is a function of a scaling factor (p_f) which is used to reduce numerical instabilities, the bulk modulus (k) of the fluid element, the volume of the fluid element (V), and the average area (A) of the structure the fluid element is connected to (Aquelet et al., 2006):

$$k = p_f \frac{KA^2}{V} \tag{6.32}$$

With any FSI simulation, consideration has to be given on how to prevent the fluid from leaking into the structure. Fluid leakage typically occurs for high velocity impact problems where the penetration is deep enough into the structure such that the coupling force is not capable of returning it to the coupling interface (Aquelet et al., 2006). This problem is solved by modifying the coupling force such that the stiffness is nonlinear and a function of the penetration depth (Aquelet et al., 2006):

$$F = k(d) \cdot d \tag{6.33}$$

For FSI in this study, the ALE structured FSI method was employed in LS-DYNA (LST, 2020). This option in LS-DYNA performs FSI between Lagrangian structures modelled by shells or solids and ALE fluids that use a structured mesh. Furthermore, this option reduces the amount of user input required to setup the FSI when compared to alternative ALE FSI coupling methods in LS-DYNA. The user is required to input a list of parts that will define the Lagrangian structures and a part that defines the ALE fluid. Additionally, the user is required to outline which material the Lagrangian parts will be coupled to and the penalty scale factor (p_f) (LST, 2020). The ALE structured FSI option autonomously handles the number of coupling points required to couple the Lagrangian structures to the fluid ALE. Additionally the algorithm autonomously handles leakage control and how to couple the fluid ALE to the shell edges of the Lagrangian structure. Hence, for this study the Lagrangian parts were coupled to the water material and the penalty scale factor was kept at the default value of 0.1.

6.10 Mesh Sensitivity Analyses

Mesh sensitivity analysis is completed to determine how fine a mesh is required to obtain mesh insensitive results. The mesh sensitivity analysis was completed for the ALE mesh simulating the fluid and the FEM mesh simulating the debris.

6.10.1 ALE Mesh Sensitivity Analysis

The ALE mesh sensitivity analysis was completed to investigate how sensitive the hydrodynamics of the simulation are to mesh refinement. As such, the debris was not modelled during this mesh sensitivity analysis. The parameters that are investigated during this mesh sensitivity analysis are the water surface elevations at the four wave gauge locations outlined in Section 6.3 and the hydrodynamic force onto the structure. The results from the numerical model will be compared to the diffusion wave solution of a dam-break wave as outlined in Chanson (2006) and the experimental data from Stolle et al. (2019). Table 6.2 outlines the simulation details and run parameters required for the mesh sensitivity analysis. As can be seen in Table 6.2, as the mesh is refined, the number of elements increased significantly. From Table 6.2, it is clear that as the number of elements increased, the run time, the number of cores, and the amount of memory required to complete the simulation also increased, while the average time step decreased.

ALE Element Size (mm)	Elements $(No.)$	T_{sim} (s)	CPUs $(No.)$	Memory Req. (GB)	T_{comp} (hrs)	Average T_{step} (s)
30	$431,250$	5.5	8	3.2	0.7	$3.19e^{-4}$
20	$1,488,675$	5.5	8	9.5	3.3	$1.95e^{-4}$
15	$3,450,000$	5.5	8	20.9	12.5	$1.39e^{-4}$
10	$11,643,750$	5.5	16	64.0	38.9	$7.56e^{-5}$

Table 6.2: ALE Mesh Sensitivity - Simulation Details

6.10.1.1 Water Surface Elevation

Figure 6.10 outlines how the element size influences the water surface elevation at WG1, which has a coordinate of $(0.00,\ -0.10)$ and is located directly behind the swing gate in the experimental program outlined in Stolle et al. (2019). As can be seen in Figure 6.10, the element size does not influence the water surface elevation at this wave gauge location. Furthermore, it is apparent that the numerical model converges to the Chanson (2006) solution as the flow progresses into the quasi-steady state. However, both the numerical and experimental data show that the drop in the reservoir occurred slower when compared to the Chanson (2006) solution. Additionally, it is apparent that the experimental data provided a larger water surface elevation when compared to the two other solutions. Derschum et al. (2018) explain that for the dam-break wave flume at the University of Ottawa, there is a false floor fitted on top of the flume floor which acts like a bottom sill

and constricts the flow. Furthermore, there are two support columns for the swing-gate that protrude into the flume, which also constrict the flow. Stolle et al. (2018b), suggest that the observed wave profile is a result of the flow constriction. The sill and support columns were not implemented in the numerical model as the points of interest for this study are located further down the flume.

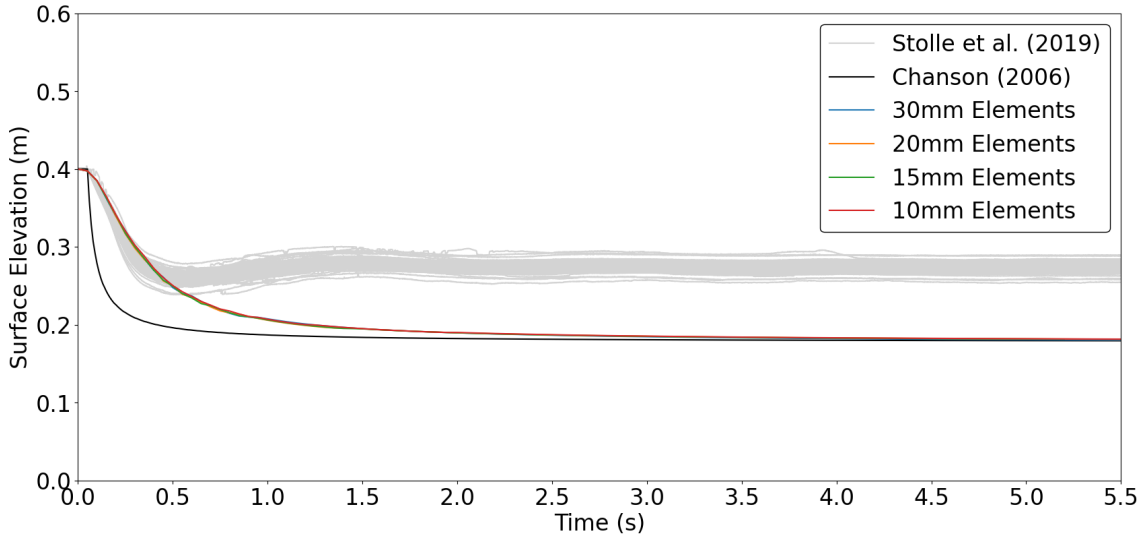


Figure 6.10: ALE Mesh Sensitivity - Water Surface Elevation at WG1

Figure 6.11 outlines how the element size influences the water surface elevation at WG2, which has a coordinate of (0.00, 2.40) and is located $0.80m$ upstream from the initial location of the debris. From this figure, there is a clear relationship between the amount of downstream water and the size of the bore front, the bore front size increased as the amount of downstream water increased. Additionally, there are clearly two stages to the flow, the first stage is associated with the leading front of the bore, while the second stage is associated with the quasi-steady flow state which resulted in a constant water surface elevation at the wave gauge. One of the limitations to the method used to fill the ALE mesh in LS-DYNA is that the amount of downstream water is always equal to the size of one element length. Hence, for a $30mm$ element size, there is $30mm$ of downstream water. However, it is apparent that as the element size decreases, the initial bore front approaches the Chanson (2006) solution. In the quasi-steady flow state, all of the numerical models converged to the Chanson (2006) solution. However, as the mesh refinement increased the numerical solution converged faster to the Chanson (2006) solution. Both the numerical model and the Chanson (2006) solution resulted in a water surface elevation that is within the bounds of the experimental data of Stolle et al. (2019). Furthermore, the numerical model and Chanson (2006) solution resulted in a bore arrival time that is very similar to the experimental data of Stolle et al. (2019). The bore arrival time for the numerical model and the Chanson (2006) solution is approximately $0.88s$, while the bore front for the experimental data arrived at approximately $0.91s$, implying that the bore front is traveling faster in the numerical model. The step profile of the dam-break wave for the

experimental data of Stolle et al. (2019) is due to cross-waves that were generated from the support columns of the swing gate (Stolle et al., 2018b). These support columns were not modelled as the interest of this simulation is in the debris transport and impact, which occurs within the initial phase of the bore and hence the influence of cross-waves is negligible (Stolle, 2019).

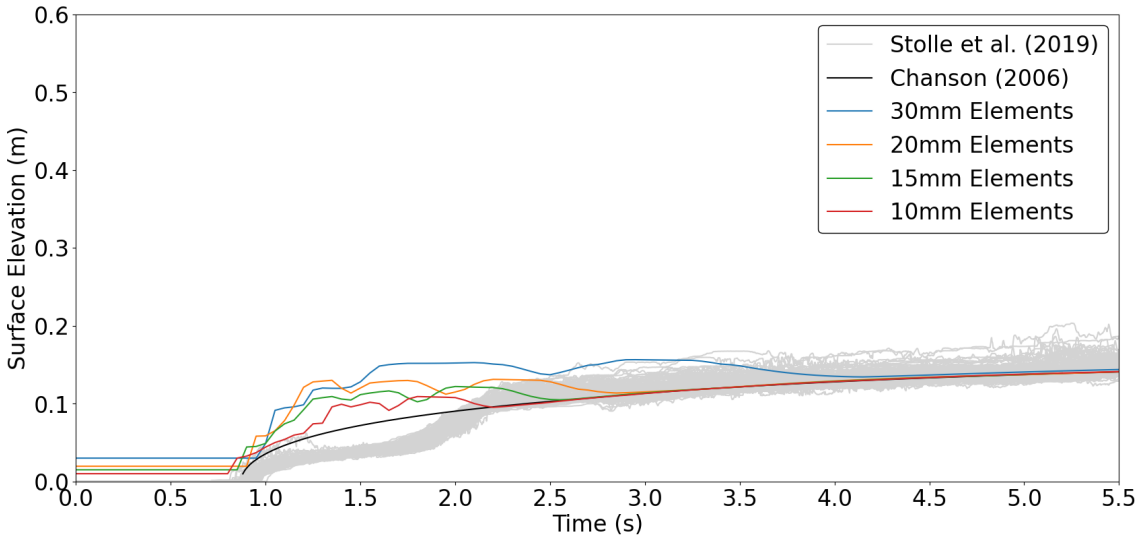


Figure 6.11: ALE Mesh Sensitivity - Water Surface Elevation at WG2

Figure 6.12 outlines how the element size influences the water surface elevation at WG3, which has a coordinate of (0.50, 3.20) and is located $0.50m$ in the positive x-direction away from the debris starting location. As described for WG2, the bore front size increased as the amount of downstream water increased. Also described for WG2, it is apparent that as the element size decreased, the initial bore front approaches the Chanson (2006) solution and that in the quasi-steady flow state, all of the numerical models except the $30mm$ mesh converged to the Chanson (2006) solution. Once again, as the mesh refinement increased, the solution converged faster to the Chanson (2006) solution. Both the numerical model and the Chanson (2006) solution resulted in a water surface elevation that falls slightly below the bounds of the experimental data. Additionally, both the numerical model and the Chanson (2006) solution resulted in a faster bore arrival time when compared to the experimental data. The bore arrival time for the numerical model is approximately $1.18s$, the Chanson (2006) solution resulted in a bore arrival time of approximately $1.20s$, while the bore front for the experimental data arrived at approximately $1.39s$, implying that the bore front is traveling faster in the numerical model.

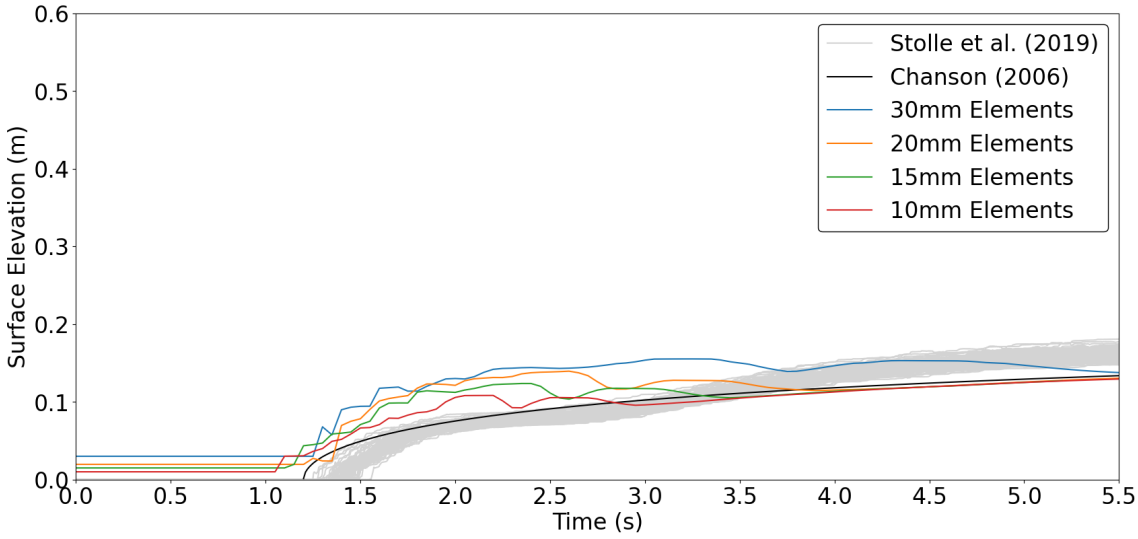


Figure 6.12: ALE Mesh Sensitivity - Water Surface Elevation at WG3

Figure 6.13 outlines how the element size influences the water surface elevation at WG4, which has a coordinate of (0.00, 7.03) and is located directly in front of the structure. As can be seen in the figure, as the element size decreased, the bore arrival time and magnitude of the splash up increased. The bore arrival time changes from approximately $3.0s$ for a $30mm$ element size to approximately $2.75s$ for a $10mm$ element size, while the bore arrival time for the experimental data is approximately $3.27s$. This further implies that the bore front in the numerical model is traveling faster than the bore front from the experimental data. The magnitude of the splash up for all of the numerical models falls within the bounds of the experimental data. Furthermore, the quasi-steady state water surface elevation from the numerical model falls within the upper boundary of the experimental data.

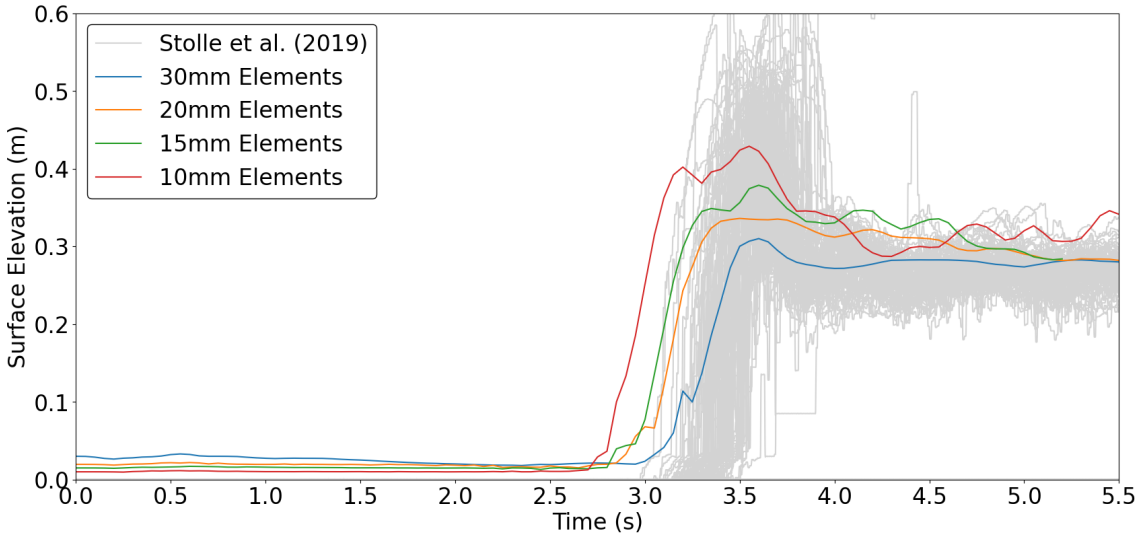


Figure 6.13: ALE Mesh Sensitivity - Water Surface Elevation at WG4

6.10.1.2 Hydrodynamic Force

Figure 6.14 outlines the how the element size influences the hydrodynamic force on the structure. Presented on the figure is the raw data from the numerical model (solid lines), along with the rolling mean of the data points (dashed lines). The rolling mean of the data points was calculated using a window length of 1000 points, which correlates to a data point every $0.01s$, as the raw output from the model is at intervals of $1e^{-5}s$. Examining Figure 6.14, it is apparent that the numerical model overestimates the experimental data, both at the initial hydrodynamic force and the quasi-steady state force. This result can be expected as the bore front arrives at the structure quicker in the numerical model, meaning the bore front is travelling at a faster velocity than in the experimental data. Furthermore, as shown in Figure 6.13, the bore velocity increased as the element size decreased, this correlates to larger initial hydrodynamic forces being generated as the element size decreased, which is exactly what is seen in Figure 6.14. The quasi-steady state hydrodynamic force from the numerical model decreased as the element size decreased, with the $10mm$ element size providing the closest results to the experimental data. It should be noted that the experimental data presented on Figure 6.14 included the force data from the debris impact events, which present themselves as large spikes around the $3.5s$ time stamp.

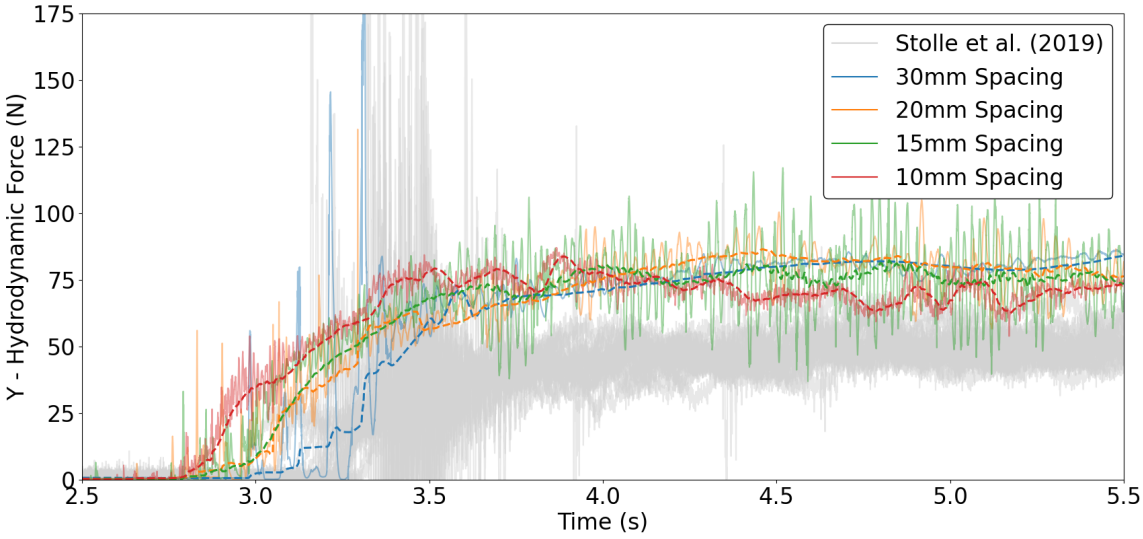


Figure 6.14: ALE Mesh Sensitivity - Hydrodynamic Force

6.10.1.3 Conclusions

Based on the results from the mesh sensitivity analysis the following conclusions can be made:

1. The number of elements in the simulation increased significantly as the element size decreased. This resulted in large increases in the amount of memory required to run the simulation, along with significant increases in computation time, which ultimately limited the mesh sensitivity analysis to an element size of $10mm$.

2. The numerical model provided water surface elevations that approximated the experimental data and Chanson (2006) solution for the propagation of a dam-break wave.

3. The numerical model typically overestimated the size of the bore front, while capturing the quasi-steady state water surface elevation within the bounds of the experimental data. The overestimation of the bore front size in the numerical model is likely a result of the amount of downstream water present in the model, which was limited to one element size by filling method used. The bore front size increased as the amount of downstream water increased.

4. As the element size decreased, the bore front velocity increased, causing the bore front to reach the structure at a sooner time when compared to the experimental data. This can be attributed to reduced flow resistance due to a smaller amount of downstream water being modelled with smaller element sizes. Furthermore, a constant frictional factor of 0.0293 was applied to the flume bed over the entire computational domain, which is based on the mean frictional factor from Stolle et al.

(2019). Applying a constant frictional factor may not be sufficient to capture the frictional effects of a rough flume bed. Alternatively the frictional factor could have been increased beyond the value determined from the physical experiments such that bore front arrival time better fit the experimental data.

5. The initial hydrodynamic forces increased as the element size decreased. This can be attributed to the bore front velocity travelling faster as the element size decreased. However, as the flow state transitioned into the quasi-steady state, the hydrodynamic forces decreased as the element size decreased. All of the element sizes investigated resulted in an overestimation of the experimental data.

6. Mesh insensitivity was not reached for the water surface elevations or the hydrodynamic forces for the element sizes investigated in this study. A smaller element size would need to be investigated to determine at which element size the results become mesh insensitive. For example, if a mesh of $5mm$ was to be simulated, this would result in $93,150,000$ ALE elements being generated, which would require a significant amount of memory to simulate. Testing showed that more than $256GB$ of memory is required to simulate a $5mm$ element size, an adaptive mesh algorithm would be better suited for finer mesh simulations but this option in LS-DYNA was not investigated.

7. Ultimately, an element size of $15mm$ was chosen to simulate the hydrodynamics of this numerical model. This was decided as the $10mm$ solution provided a bore front that arrived significantly sooner than the experimental data, which resulted in larger initial hydrodynamic forces. However, the quasi-steady state hydrodynamic forces between the $10mm$ and $15mm$ element size solutions did not differ significantly. Furthermore, the $10mm$ solution required significantly more memory and computational power when compared to the $15mm$ solution. The difference between the $20mm$ and $15mm$ simulation is that the $20mm$ solution resulted in larger bore fronts due to the increased depth of the downstream water. Hence the $15mm$ solution better fit the experimental data and the Chanson (2006) solution, while still only requiring the use of eight cores. The $30mm$ solution was not considered as it poorly fits both the experimental data and Chanson (2006) solution at WG3.

6.10.2 Debris FEM Mesh Sensitivity Analysis

The debris FEM mesh sensitivity analysis was completed to investigate how sensitive the debris transport and impact force are to mesh refinement. The debris transport will be compared to the experimental data of Stolle et al. (2019) and the analytical debris spreading area as defined by Naito et al. (2014) and Nistor et al. (2017b). Naito et al. (2014) examined the debris transport from shipping containers in a post-tsunami survey of the 2011 Tohoku Tsunami. The authors conservatively estimated the debris spreading area to be defined by a triangle starting at the debris centroid with a spreading angle (θ) of $\pm 22.5^{\circ}$. Nistor et al. (2017b) examined debris transport in an ideal experimental setting and found the debris spreading area to be a defined by a triangle starting at the debris centroid. However, the

spreading angle is defined as a function of the number of debris (N) as shown below (Nistor et al., 2017b):

$$\pm\,\theta = \pm 3.69 \pm 0.80N \tag{6.34}$$

The debris impact forces generated from the numerical model will be compared to the MDOF fitting results from the experimental data of Stolle et al. (2019), as presented in Section 3.5. Table 6.3 outlines the simulation details and run parameters required for the mesh sensitivity analysis. From Table 6.3, it is clear that as the number of elements increased the time to complete the simulation increased significantly. This is because the time step is tied to the characteristic length of the element as shown in Section 6.6.1, which decreases as the element size decreases. Only two element sizes were investigated as the computational time required to simulate a $15mm$ element size is significantly larger than the $30mm$ element size simulation. The $15mm$ element size solution only simulated $4.0s$ of model time, while requiring four days of computational time. Whereas, the $30mm$ element size solution was capable of simulating the full $5.5s$ of model time, while requiring only 2.75 days of computational time.

Debris Element Size (mm)	Elements ($No.$)	T_{sim} (s)	CPUs ($No.$)	Memory Req. (GB)	T_{comp} (hrs)	Average T_{step} (s)
30	48	5.5	64	256	65.9	$9.6e^{-6}$
15	192	4.0	64	256	96.0	$4.8e^{-6}$

Table 6.3: Debris FEM Mesh Sensitivity - Simulation Details

6.10.2.1 Debris Transport

Figure 6.15 outlines the transport paths (traces) that the center of gravity of the debris followed for both simulations. Furthermore, the potential spreading areas of the debris are also shown on the figure, along with the debris traces from the experimental studies of Stolle et al. (2019). Comparing the numerical modelling results to the potential spreading areas, it is apparent that the numerical models fall within the spreading area of both Naito et al. (2014) and Nistor et al. (2017b). Furthermore, the numerical model resulted in debris traces that fit within the bounds of the experimental data of Stolle et al. (2019). On Figure 6.15 the structure is represented as a black box and the rebound of the debris due to the contact with the structure is shown. As can be seen in Figure 6.15, the magnitude of the debris rebound is similar for both element sizes investigated, suggesting that the impact magnitude is similar. However, it is apparent that the debris trace changed based on the element size. Why the debris traces are different can be attributed to how FSI is handled in LS-DYNA. As described in Section 6.9.5.2, the FSI is handled through coupling points between the ALE and FEM meshes. These coupling points apply a coupling force to the nodes of the ALE and FEM meshes to prevent penetration. As the number of coupling points changes based on the number of nodes used to model the debris, the forces being applied onto the debris also change. This is shown in Figure 6.16, where the pressure on the debris resulting from the FSI is presented. Clearly, the pressure time histories are different, which will influence how the debris is transported down the flume.

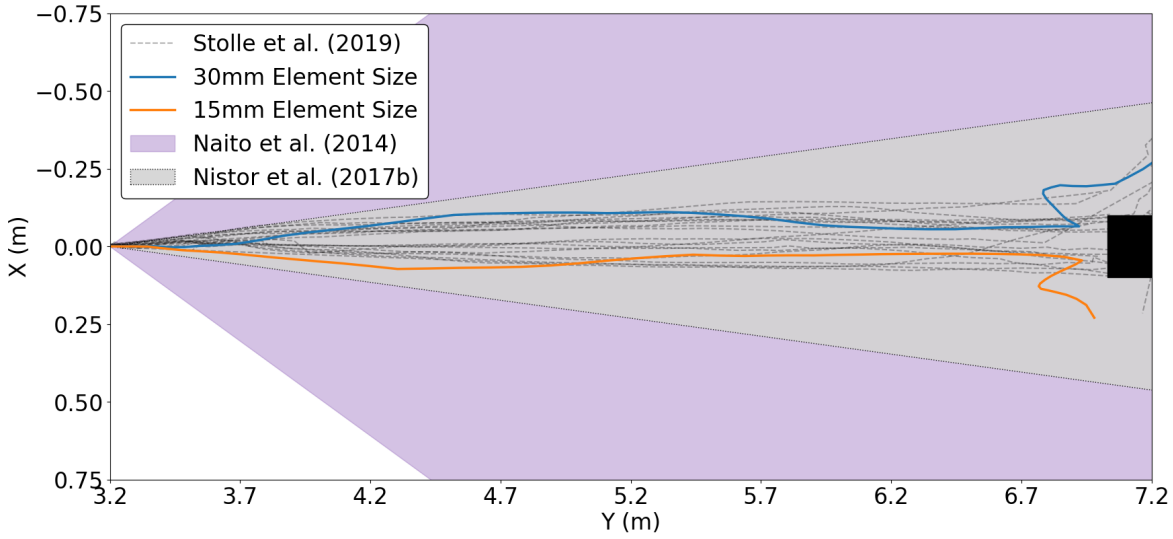


Figure 6.15: Debris FEM Mesh Sensitivity - Debris Transport

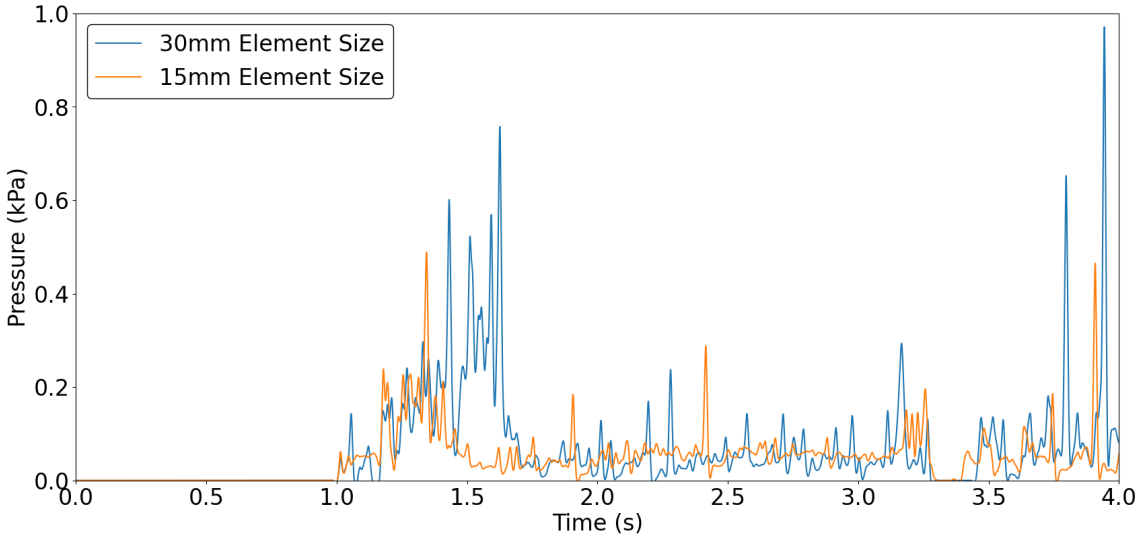


Figure 6.16: Debris FEM Mesh Sensitivity - Pressure on Debris

6.10.2.2 Debris Impact Force

Figure 6.17 outlines how the debris impact force history changes based on the element size. Furthermore, how the numerical model compared to debris impact force histories generated from the MDOF fitting results is also presented. From Figure 6.17, it is clear that the debris impact force history differs as the element size reduces. However, both debris impact force histories have reasonable impact magnitudes and durations when compared to the MDOF fitting results. The impact magnitude is slightly larger when a $15mm$ element size is

used but the impact duration is smaller when compared to the $30mm$ element size results. Overall, the $15mm$ element size resulted in a debris impact force history that better fit the MDOF fitting results. However, the $30mm$ element size solution did not result in a debris impact force history that appears unrealistic when compared to the MDOF fitting results. The reason the debris impact force histories are different can be attributed to a few factors. The first factor is that the pressure force histories on the debris are different which resulted in different debris traces. As the debris trace is different, there is no reason to assume that the debris impact forces would be the same. The second factor is that the time step size changes as the element size decreases, which has a direct influence on the contact between the debris and structure as outlined in Section 6.9.5.1. Furthermore, the debris impact velocity is different for both element sizes investigated as shown in Figure 6.18, this implies that the debris impact force will also be different. The debris impact velocity is slightly larger when a $15mm$ element size is used, which correlates to a larger debris impact force. However, both of the simulations resulted in debris impact forces and velocities that fell within the bounds of the experimentally determined debris impact velocities (Stolle et al., 2019) and the associated debris impact magnitudes determined from the MDOF fitting method.

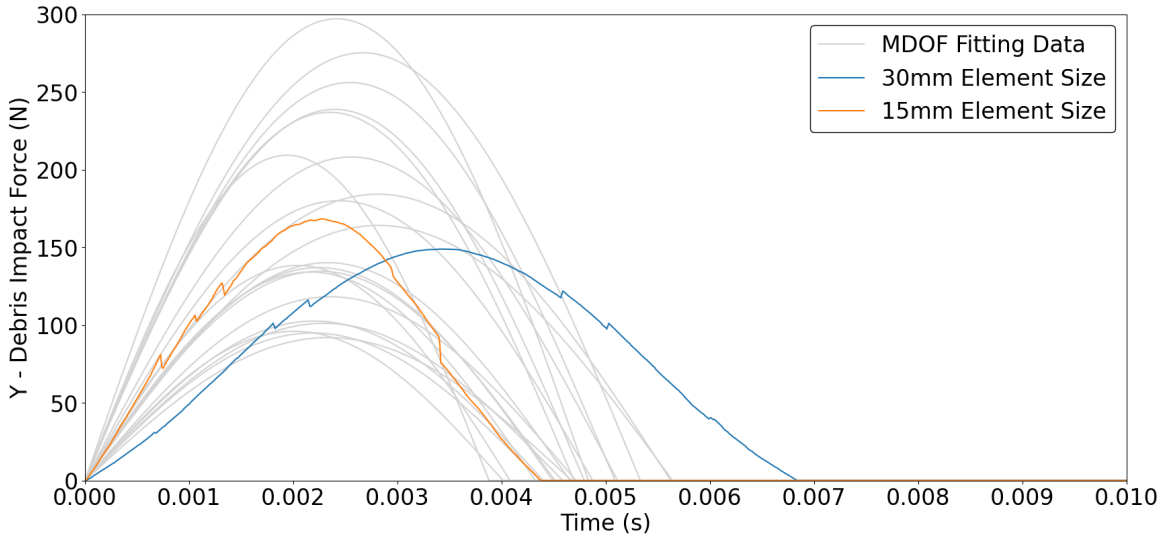


Figure 6.17: Debris FEM Mesh Sensitivity - Debris Impact Force

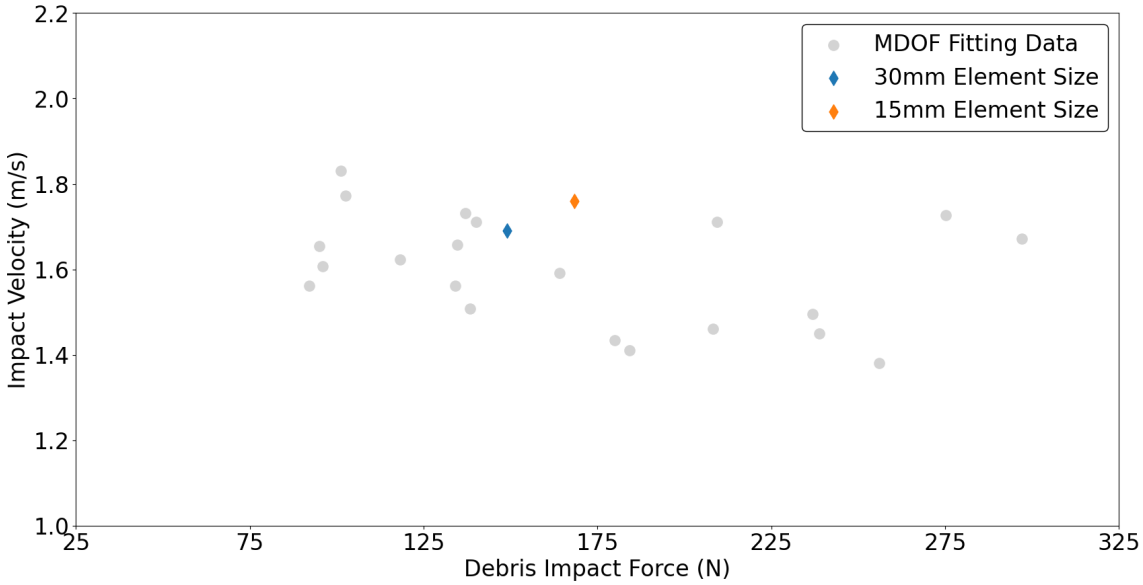


Figure 6.18: Debris FEM Mesh Sensitivity - Debris Impact Velocity

6.10.2.3 Conclusions

Based on the results from the mesh sensitivity analysis the following conclusions can be made:

1. As the element size decreased, the time step size also decreased, which significantly increased the computational time. The significant computation time associated with using a smaller element size than $15mm$ ultimately limited the mesh sensitivity analysis to an element size of $15mm$.

2. The numerical model resulted in debris traces that fit within the spreading area defined by Nistor et al. (2017b) and within the experimental data of Stolle et al. (2019).

3. The debris trace changed as the element size changed. This is likely due to how LS-DYNA handles FSI, which ultimately led to the debris experiencing different pressures as the element size decreased. The different pressures on debris resulted in the debris traces not being the same for the $30mm$ and $15mm$ element size solutions.

4. The debris impact force changed as the element size changed. The $15mm$ element size simulation resulted in an impact force history that had a larger magnitude but smaller duration when compared to the $30mm$ element size solution.

5. The $15mm$ element size simulation resulted in a debris impact force history that better fit the impact force histories developed from the MDOF fitting method outlined in Section 3.5. However, the $30mm$ element size simulation did not result in a debris

impact force history that appears unrealistic when compared to the MDOF fitting results.

6. The $15mm$ element size simulation resulted in a debris impact velocity that is slightly larger than the impact velocity developed from the $30mm$ element size simulation. Both of the impact magnitudes and velocities fell within the bounds of the experimentally determined impact velocities and the impact magnitudes developed from the MDOF fitting method.

7. Mesh insensitivity was not reached for the debris trace or the debris impact force. A smaller element size would need to be investigated to determine at which element size the results become mesh insensitive. However, the significant increase in computational time associated with using a smaller element size limited the study to an element size of $15mm$. Alternative methods for increasing the computational time step would need to be investigated, such as mass scaling, or a larger number of cores would need to be used to simulate a smaller element size.

8. Ultimately, an element size of $30mm$ was chosen to simulate the debris of this numerical model. This was decided as both of the simulations resulted in debris traces and debris impact force histories that fit within the expected values and the computational time increased significantly while using an element size of $15mm$.

6.11 Rigid vs Elastic Structure

This study analyses the influence that changing the material of the structure from rigid to elastic has on the water surface elevation, hydrodynamic force, debris transport, and debris impact. Furthermore, the top deflection of the structure due to the impact and hydrodynamic force is also presented. All of these numerical results will be compared to the experimental data of Stolle et al. (2019). The rigid structure is completely fixed, while the elastic structure is fixed at the base of the structure, similar to the structure in Stolle et al. (2019).

Table 6.4 outlines the simulation details for both runs. The parameters that changed during this study were the material definitions of the structure and the element size of the structure. The element size for a rigid material does not influence the time step size of the simulation and hence a fine mesh with an element size of $5mm$ was used. As the material changes from rigid to elastic, the element size will influence the time step size. Hence, when the structure material was elastic, an element size $30mm$ was used. This element size was investigated as it is the same size as the elements used for the debris and as such, the critical time step size will not change significantly between the two simulations as the debris will govern the time step. The computational time associated with the rigid structure is slightly larger than the computational time associated with the elastic structure, even though the average time step is the same. This is likely because the rigid structure has a larger number of elements that need to be processed during the contact algorithms.

Structure Type	Elements Size (mm)	Elements $(No.)$	T_{sim} (s)	CPUs $(No.)$	Memory Req. (GB)	T_{comp} (hrs)	Average T_{step} (s)
Rigid	5	576	5.5	64	256	65.9	$9.6e^{-6}$
Elastic	30	48	5.5	64	256	59.3	$9.6e^{-6}$

Table 6.4: Elastic vs Rigid Structure - Simulation Details

6.11.1 Water Surface Elevation

Figures 6.19, 6.20, 6.21, and 6.22 outline the water surface elevations at wave gauges one, two, three, and four. As can be seen in Figures 6.19, 6.20, and 6.21, the water surface elevation for a rigid structure is the same as the water surface elevation for an elastic structure. This is expected behavior as these wave gauges are located away from the structure. However, the water surface elevation at wave gauge four is different for a rigid and elastic structure as shown in Figure 6.22. Comparing the water surface elevations at wave gauge four, it can be seen that the elastic structure resulted in a bore front that reached the wave gauge at a slightly later time stamp when compared to the rigid structure results. This is likely a result of the FSIs behaving differently when the structure material and element size changes. There is no physical explanation as to why the bore front arrival times are different for each type of structure analysed. This is because the bore front arrival time at wave gauge four is the time at which the bore reaches the structure and as such, the response of the structure should not influence the bore arrival time. The splash up for both of the structures falls within the bounds of the experimental data of Stolle et al. (2019). Furthermore, the quasi-steady state water surface elevation for both structures converge at approximately the same value, which falls within the upper bounds of the experimental data of Stolle et al. (2019).

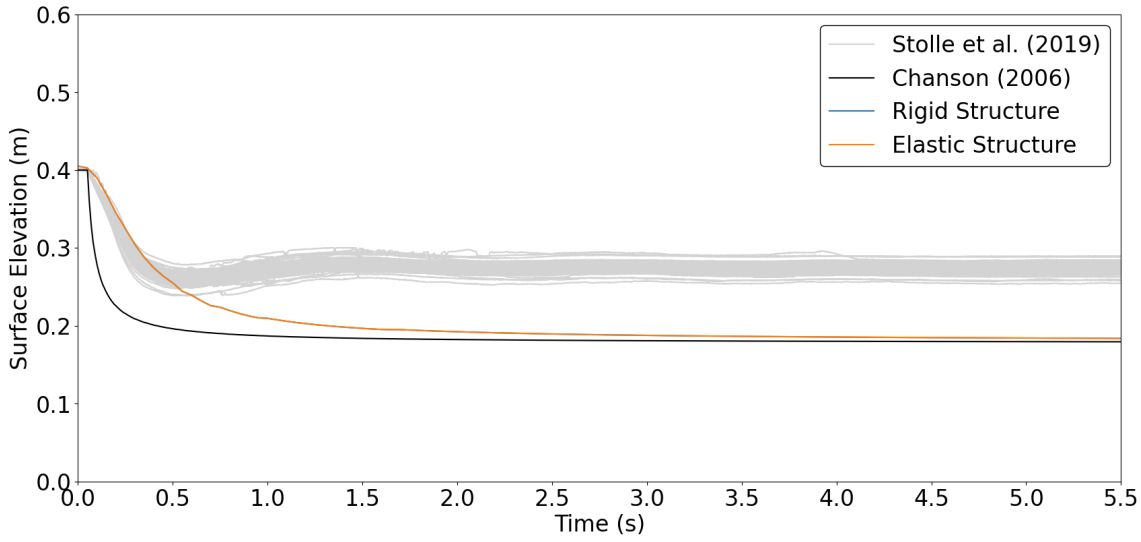


Figure 6.19: Elastic Structure Study - Water Surface Elevation at WG1

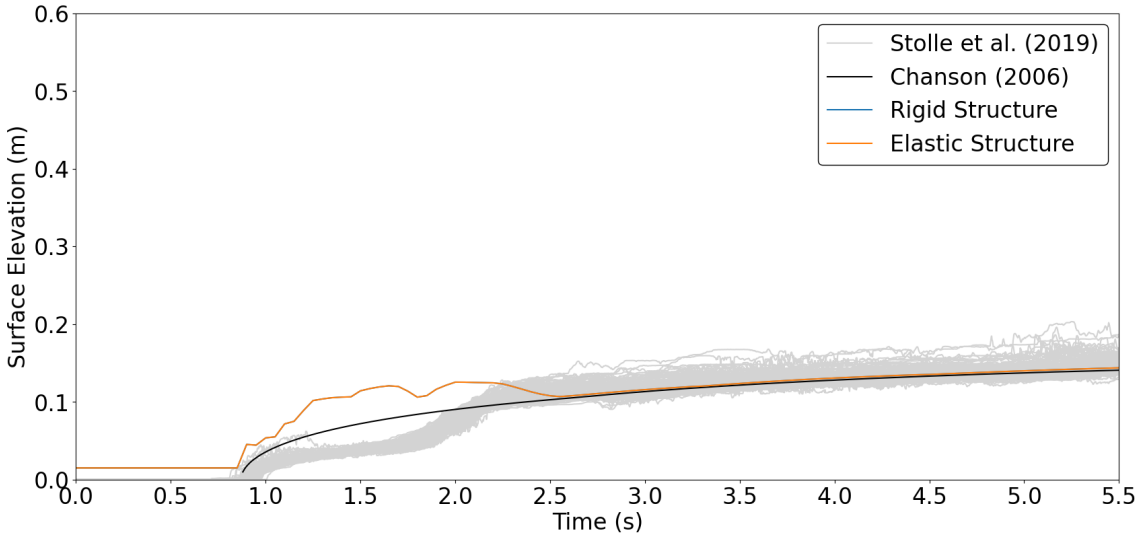


Figure 6.20: Elastic Structure Study - Water Surface Elevation at WG2

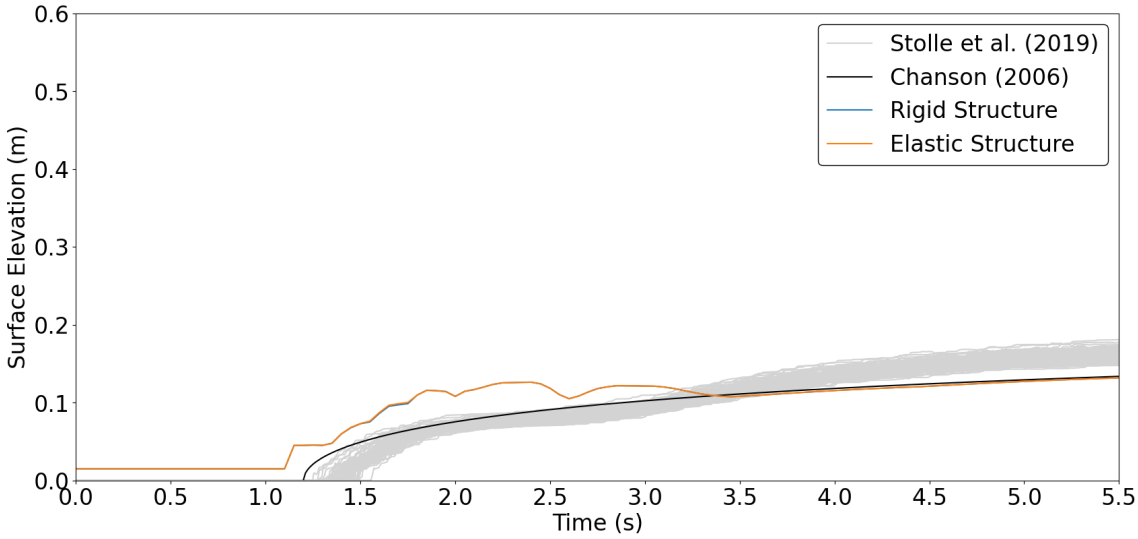


Figure 6.21: Elastic Structure Study - Water Surface Elevation at WG3

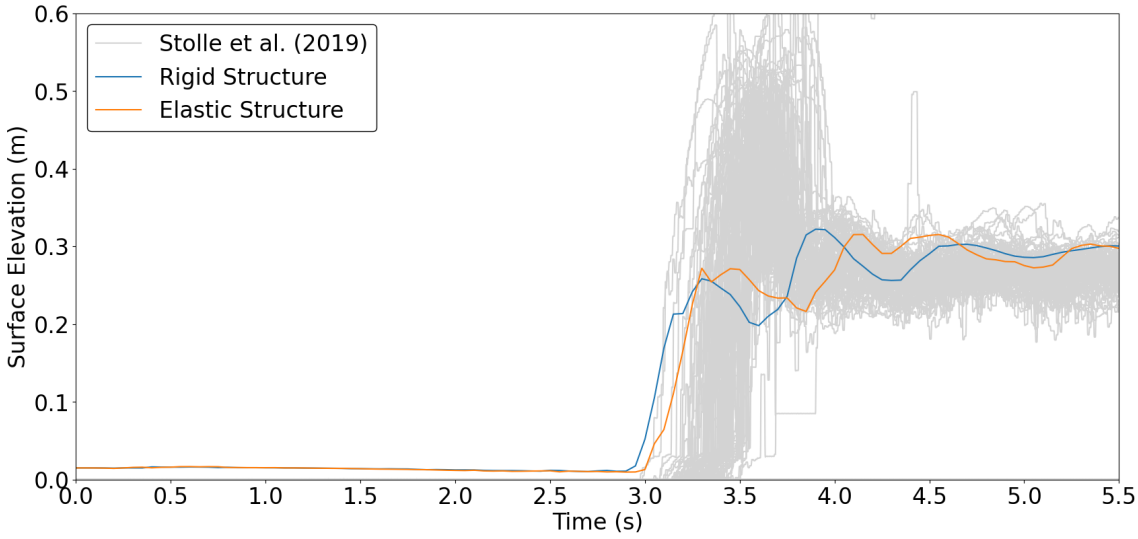


Figure 6.22: Elastic Structure Study - Water Surface Elevation at WG4

6.11.2 Hydrodynamic Force

Figure 6.23 outlines the hydrodynamic force for both simulations. As can be seen in Figure 6.23, the elastic structure resulted in a noisier solution for the hydrodynamic force when compared to the rigid structure. However, comparing the average hydrodynamic forces (dashed lines) for both simulations, the conclusion can be made that after the initial splash up of water onto the face of the structure, the elastic structure developed smaller hydrodynamic forces when compared to the rigid structure. This result is expected as the elastic structure allows deflections to develop in the model, which reduces the forces developed by the structure. The rigid structure does not allow any deflections to develop in the model and as such, the forces developed in the structure are larger when compared to the elastic structure.

Comparing the numerical modelling results to the experimental data of Stolle et al. (2019), it can be seen that both simulations resulted in initial hydrodynamic forces that fall within the bounds of the experimental data. However, the quasi-steady state hydrodynamic forces developed by the model overestimate the experimental data. The elastic structure resulted in a quasi-steady state hydrodynamic force that fits closer to the experimental data when compared to the rigid structure results.

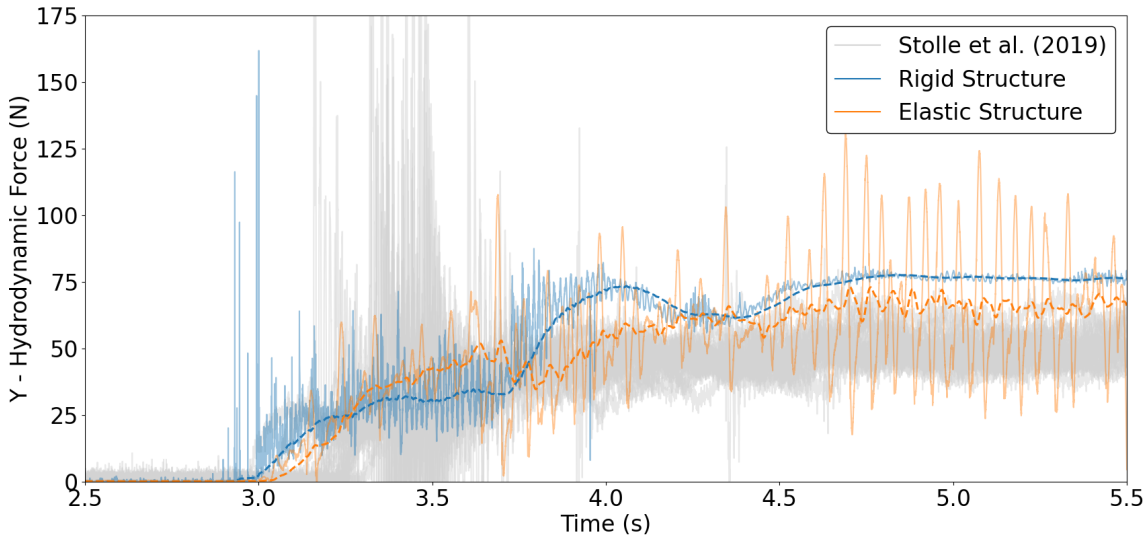


Figure 6.23: Elastic Structure Study - Hydrodynamic Force

6.11.3 Debris Transport

Figure 6.24 outlines the transport paths (traces) that the center of gravity of the debris followed for both simulations. Furthermore, the potential spreading areas of the debris are also shown on the figure, along with the debris traces from the experimental studies of Stolle et al. (2019). Comparing the numerical modelling results to the potential spreading areas, it is apparent that the numerical models fall within the spreading areas defined by both Naito et al. (2014) and Nistor et al. (2017b). Furthermore, comparing the numerical modelling results to the experimental data of Stolle et al. (2019), it is apparent that the rigid structure results fall within the bounds of the experimental data, while the elastic structure results do not.

Comparing the debris traces between both simulations, it is clear that the debris traces are not the same. This is unexpected behavior as the difference between the simulations is how the structure is being modelled, which should have no influence on how the debris is transported to the structure. Figure 6.25 compares the pressure time history exerted on the debris for both simulations and as can be seen, the pressure histories are different. This is also unexpected behavior for the same reasoning explained above. It is speculated that this result is due to how the FSI algorithm is defined in LS-DYNA. The FSI algorithm groups the contacts under one definition that combines how the fluid interacts with both the structure and debris. As such, it is speculated that there is an influence on the FSI algorithm due to the structure mesh and material properties changing for the elastic structure simulation, which may also influence the FSI for the debris as they are grouped under one definition. However, further investigation into the different options and methods for defining FSI in LS-DYNA would need to be investigated to definitively determine the cause of the different debris transport paths.

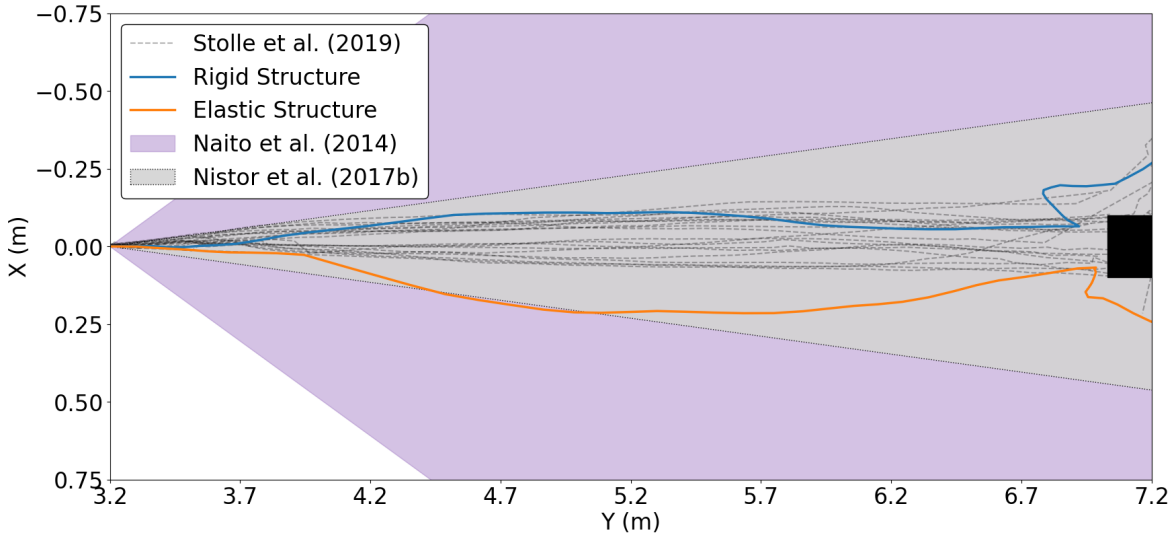


Figure 6.24: Elastic Structure Study - Debris Transport

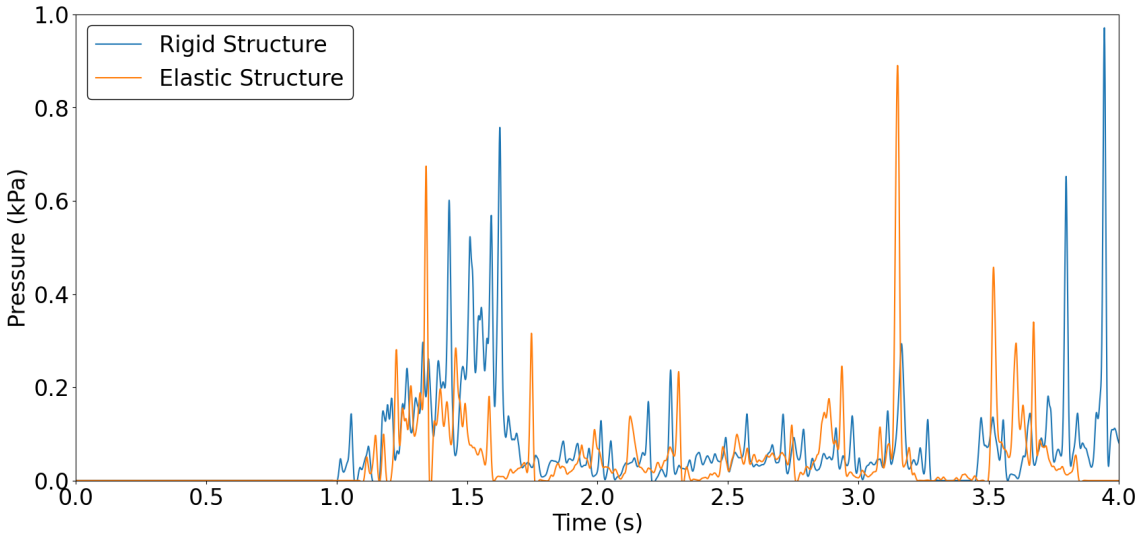


Figure 6.25: Elastic Structure Study - Pressure on Debris

6.11.4 Debris Impact Force and Top Deflection

Figure 6.26 outlines how the debris impact force history changes based on the element formulation of structured used in the simulation. Furthermore, how the numerical model compares to debris impact force histories generated from the MDOF fitting results is also presented. From Figure 6.26, it is clear that the debris impact force history differs when an elastic or rigid structure is used. The rigid structure results in a debris impact force history that has a similar magnitude and duration when compared to the impact force

histories developed from the MDOF fitting method outlined in Section 3.5. However, the debris impact force history developed from the elastic structure simulation is significantly different from both the rigid structure results and the MDOF fitting results. Comparing the debris impact velocities outlined in Figure 6.27, it is apparent that only the rigid structure resulted in a debris impact velocity that falls within the experimental data of Stolle et al. (2019).

The significance difference between the rigid and elastic structure debris impact force histories is unexpected, as the deflection developed in the structure from the experimental study of Stolle et al. (2019) was not significant as demonstrated in Figure 6.28. Additionally, the deflections developed in the structure for the numerical model were also not significant but were larger than those from the experimental study of Stolle et al. (2019). Furthermore, the frequency of the deflection response in the numerical model is significantly smaller than the frequency of the deflection response from the experimental data of Stolle et al. (2019). The reasoning for the significant difference in the debris impact force histories between the numerical simulations and the deflection response is likely due to how the contact between the debris and structure is defined in LS-DYNA. The same contact parameters used for a rigid structure were also used for the elastic structure. However, these contact parameters were not investigated to determine how they influence the contact between the debris and elastic structure. As such, the contact parameters defined may not be suitable for an elastic structure and calibration of the contact parameters for the elastic structure would need to be completed. However, this is not investigated in this study as a rigid structure is used throughout the analysis of this chapter. If future studies are being performed using an elastic structure, significant investigations into how the contact parameters influence the debris-structure contact would need to be investigated.

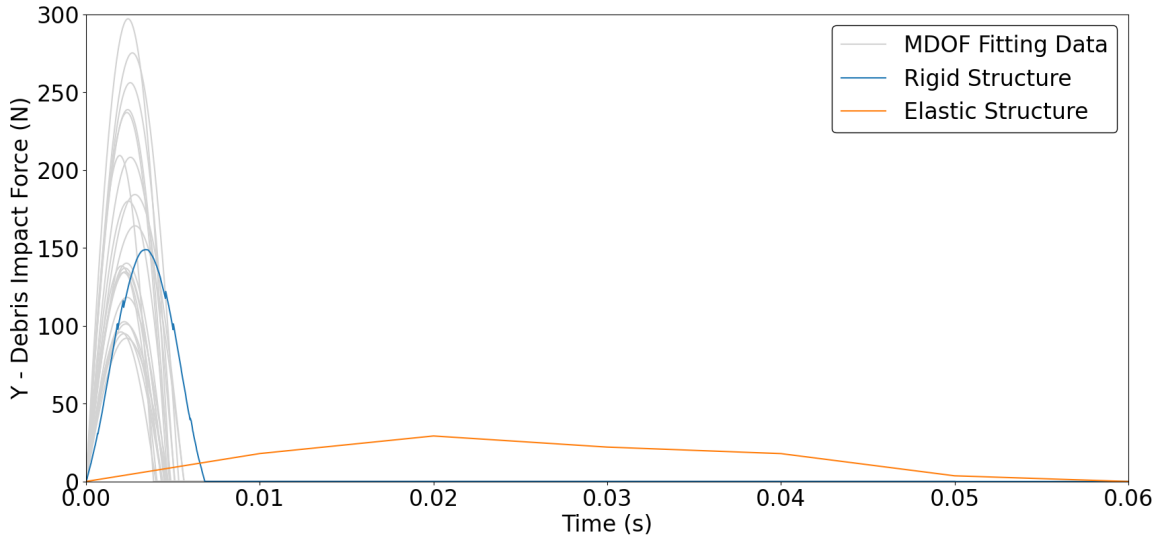


Figure 6.26: Elastic Structure Study - Debris Impact Force

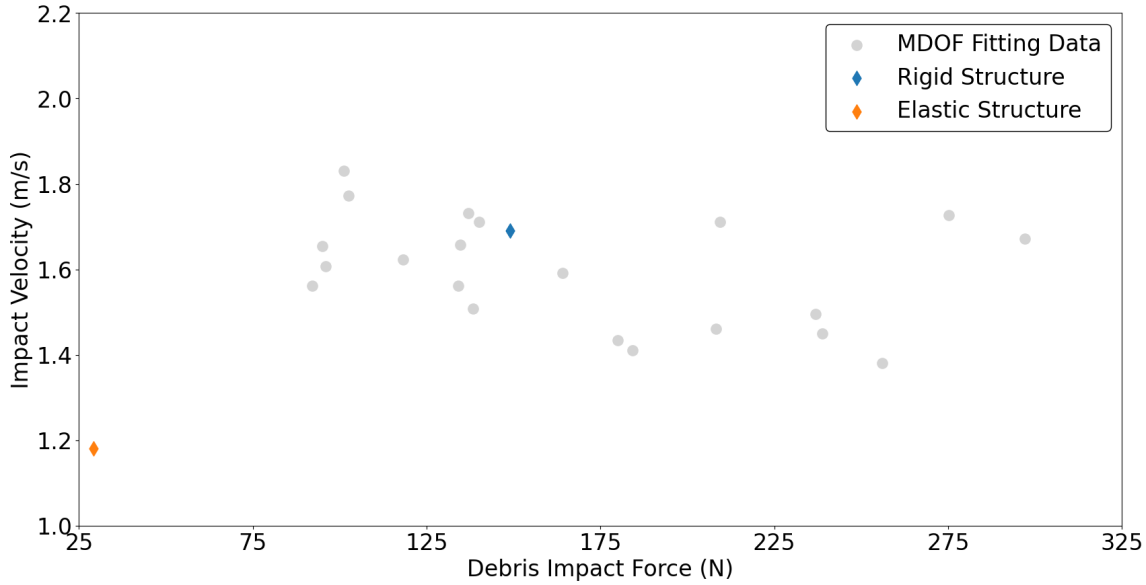


Figure 6.27: Elastic Structure Study - Debris Impact Velocity

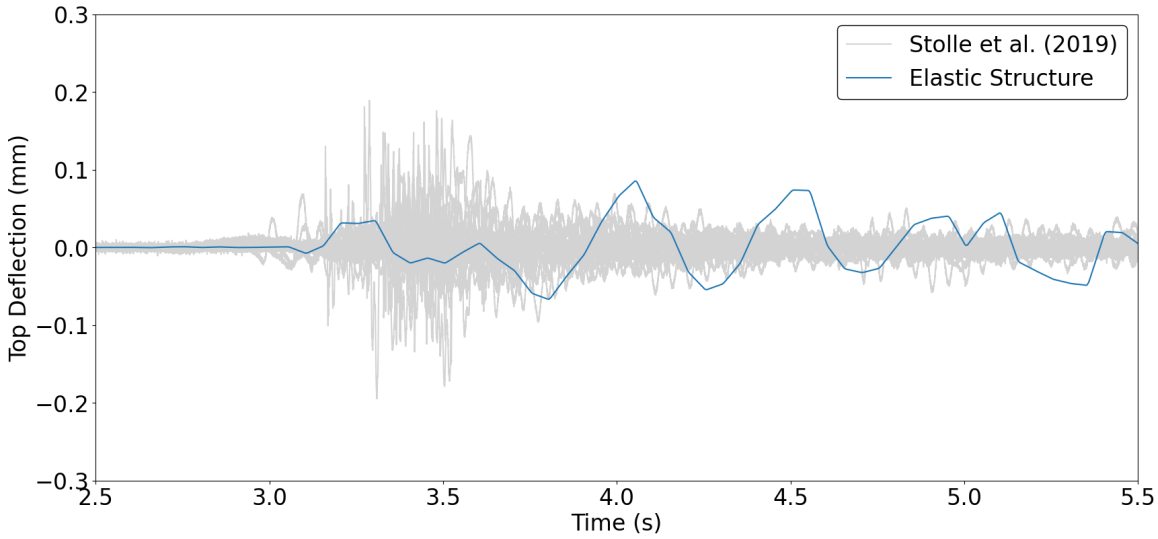


Figure 6.28: Elastic Structure Study - Top Deflection

6.11.5 Conclusions

Based on the results from the elastic structure study the following conclusions can be made:

1. The water surface elevations at wave gauges one, two, and three are not influenced by the elastic structure as the structure is located further down the flume.

2. The elastic structure resulted in a bore front that arrived at the structure later than when a rigid structure is used, which is unrealistic. This is unrealistic as the element formulation of the structure should not influence the time at which the bore front reaches the structure. It is speculated that this result is due to the FSIs behaving differently when the structure material and element size changes.

3. The splash up and quasi-steady state water surface elevations at wave gauge four fall within the experimental data of Stolle et al. (2019) for both simulations.

4. The elastic structure resulted in a hydrodynamic force solution that is significantly more noisy when compared to the rigid structure solution.

5. After the initial splash up of water, the elastic structure resulted in smaller hydrodynamic forces when compared to the rigid structure. This is expected behavior as elastic structure develops deflections, which reduce the forces developed in the structure.

6. Both simulations resulted in hydrodynamic forces that overestimated the experimental data of Stolle et al. (2019). However, the elastic structure resulted in a hydrodynamic force history that fit closer to the experimental data when compared to the rigid structure results.

7. The debris transport paths are different for a rigid structure and an elastic structure. This is unexpected behavior as the element formulation of the structure should not influence the debris transport to the structure. It is speculated that this is a result of how the FSIs are defined in LS-DYNA. The FSIs are grouped into one definition and as such, if the FSI is influenced due to the structure being elastic and the element sizes being different, there is the potential for this to influence the FSI for the debris as they are grouped under one definition. This is speculated as the pressures exerted onto the debris are different when a rigid or elastic structure is used, suggesting that the FSI is influenced by the element formulation of the structure.

8. The debris impact force histories are significantly different for an elastic structure when compared to the rigid structure results and the MDOF fitting results. Further investigation into how the contact parameters influence the debris impact force for an elastic structure would need to be investigated, as the same contact parameters used for the rigid structure were used for the elastic structure, which may not be a valid assumption.

9. The top deflections developed in the elastic structure simulation are of a similar magnitude to the experimental data of Stolle et al. (2019). However, the frequency of the response in the numerical model is significantly smaller than the experimental data.

10. In order to use an elastic structure model the following additional studies should be completed, but were not investigated for this thesis as a rigid structure was used:

(a) How the FSI is defined in the numerical model would need to be investigated to determine if grouping the contacts together is influencing the debris transport.

(b) The influence of element size on the simulation for an elastic structure would need to be investigated.

(c) How the contact parameters influence the debris-structure interaction would need to be investigated.

6.12 Multi-Debris Study

This study aims to reproduce the experimental data of Stolle et al. (2020b), where multi-debris transport and debris impacts were investigated. The water surface elevation, hydrodynamic force, debris transport, and debris impacts will all be investigated and compared to the experimental data of Stolle et al. (2019, 2020b).

Table 6.5 outlines the simulations details for all runs. The only parameter that was changed between simulations was the number or orientation of the debris being simulated. A $15mm$ element size mesh was used for the hydrodynamics, a $30mm$ element size mesh was used for the debris, and the structure was modelled with rigid elements with a size of $5mm$. As can be seen in Table 6.5, the run time between simulations are very similar, even though more debris are being added into the simulation. This is due to a couple of factors:

1. The debris all have the same material properties and element sizes. As such, the critical time step is not influenced by the number of debris.

2. No additional contact algorithms need to be modelled as more debris are added into the simulation. This is because the contact algorithms used to model the FSI and debris-structure contact allow the user to specify a list of parts that can potentially interact with each other, instead of defining a completely separate contact for each part combination.

In Table 6.5, the simulations are discretized by the number of rows and columns of debris. The definition of a row and column is shown in Figure 6.29, where a row defines the number of debris along the flume width (x) and a column defines the number of debris along the flume length (y). The centroid of the debris or group of debris is always located at an ($x,\ y$) coordinate of (0.0, 3.2) and when more than one debris is being simulated there is a $0.03m$ spacing between the debris (Stolle et al., 2020b).

No. of Debris	No. of Rows	No. of Columns	T_{sim} (s)	CPUs $(No.)$	Memory Req. (GB)	T_{comp} (hrs)
1	1	1	5.5	64	256	65.9
3	1	3	5.5	64	256	68.7
3	3	1	5.5	64	256	68.3
6	2	3	5.5	64	256	67.0

Table 6.5: Multi-Debris Study - Simulation Details

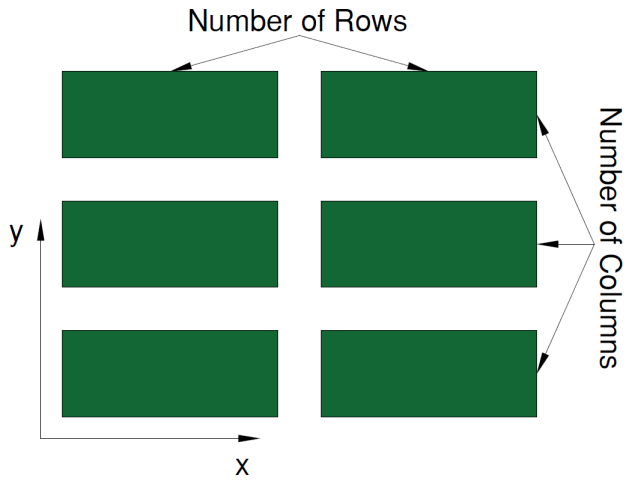


Figure 6.29: Example Debris Layout

6.12.1 Water Surface Elevation

Figure 6.30 outlines the water surface elevation at wave gauge one. Wave gauge one is located directly behind the swing gate in the experimental study of Stolle et al. (2019), as described in Section 6.3. As the debris is located $3.20m$ down the flume, there is no influence of the debris on the water surface elevation at wave gauge one. As there is no influence at wave gauge one, the same conclusions made in Section 6.10.1 for a $15mm$ element size mesh can be applied to these results. The main conclusion is that at wave gauge one, the numerical model converges to the Chanson (2006) solution, but the drop in the reservoir is slower. However, comparing the numerical model to the experimental data of Stolle et al. (2019), the conclusion can be made that the initial drop in the reservoir for both data sets occurs at approximately the same rate. After a time stamp of approximately $0.50s$, the data sets diverge from each other as explain in Section 6.10.1.

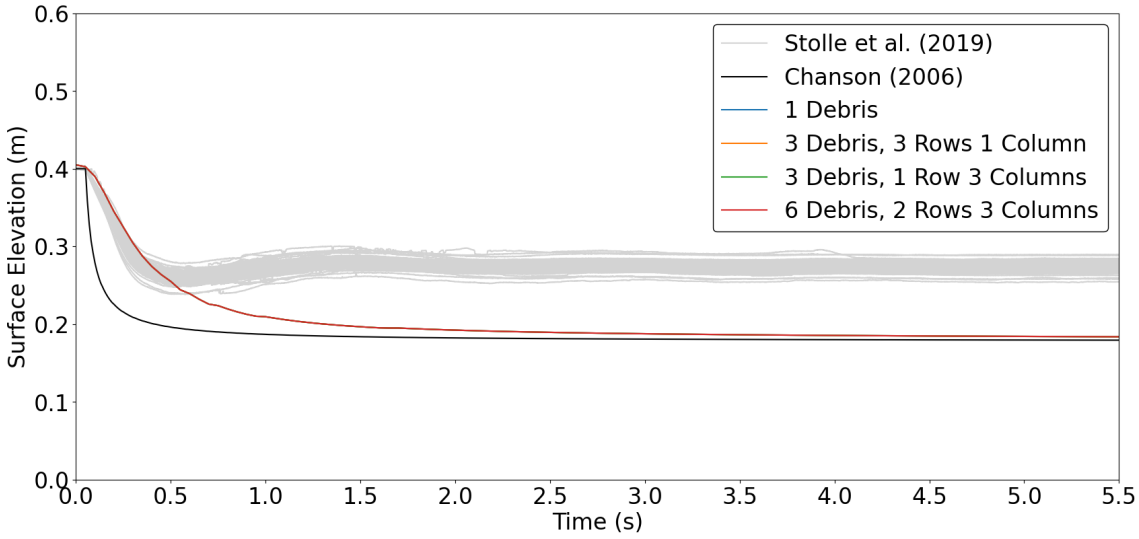


Figure 6.30: Multi-Debris Study - Water Surface Elevation at WG1

Figure 6.31 outlines the water surface elevation at wave gauge two, which is located $2.4m$ down the flume as described in Section 6.3. As the debris is located $3.20m$ down the flume, there is no influence of the debris on the water surface elevation at wave gauge two. As there is no influence at wave gauge two, the same conclusions made in Section 6.10.1 for a $15mm$ element size mesh can be applied to these results. The main conclusion is that at wave gauge two, the numerical model converges to the Chanson (2006) solution, which both fall within the bounds of the experimental data of Stolle et al. (2019). However, the numerical model resulted in a larger bore front when compared to the Chanson (2006) solution and the experimental data of Stolle et al. (2019). The larger bore front developed in the numerical model is due to the numerical model overestimating the amount of downstream water being modelled as described in Section 6.10.1.

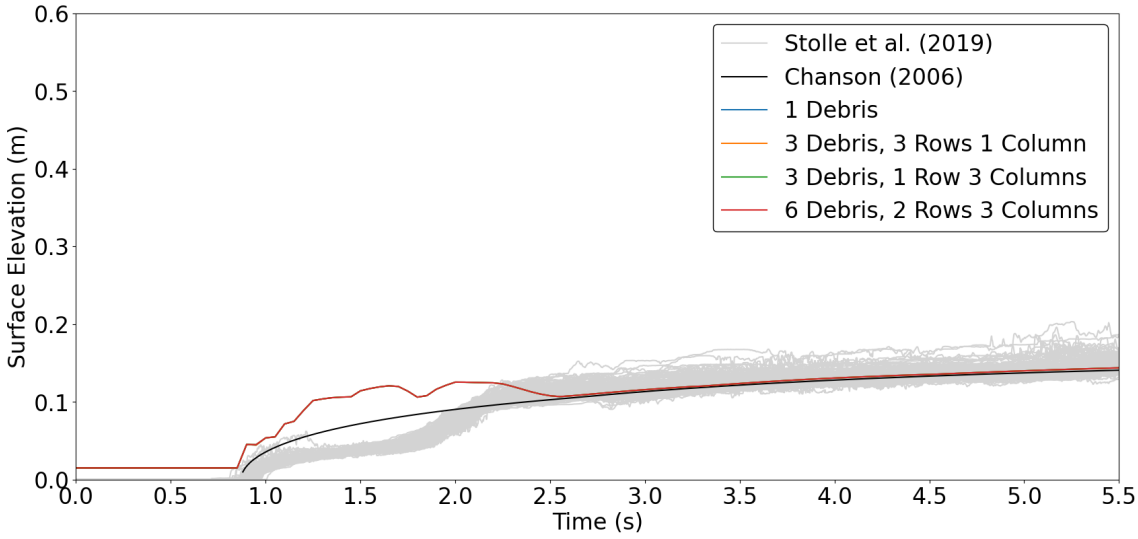


Figure 6.31: Multi-Debris Study - Water Surface Elevation at WG2

Figure 6.32 outlines the water surface elevation at wave gauge three, which is located at the debris centroid but offset in the positive x-direction by $0.50m$ as described in Section 6.3. As the debris is located in the center of the flume, there is no influence of the debris on the water surface elevation at wave gauge three. As there is no influence at wave gauge three, the same conclusions made in Section 6.10.1 for a $15mm$ element size can be applied to these results. The main conclusion is that at wave gauge three, the numerical model converges to the Chanson (2006) solution, which both fall slightly below the bounds of the experimental data of Stolle et al. (2019). Similar to wave gauge two, the numerical model resulted in a larger bore when compared to the Chanson (2006) solution and the experimental data of Stolle et al. (2019), which is due to the amount of downstream water being modelled.

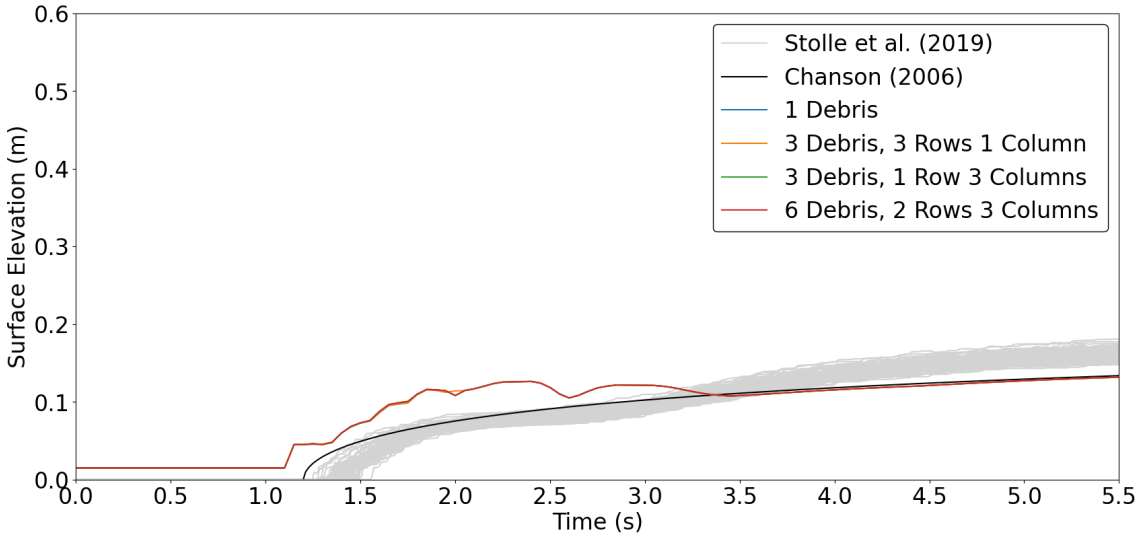


Figure 6.32: Multi-Debris Study - Water Surface Elevation at WG3

Figure 6.33 outlines the water surface elevation at wave gauge four, which is located at the face of the structure as described in Section 6.3. As the structure is located further down the flume when compared to the debris, there is the potential for the debris to influence the water surface elevation at the face of the structure. Observing Figure 6.33, there is no clear indication that the water surface elevation becomes more disrupted as the number of debris being simulated increased. This is because there are only a maximum of six debris being simulated, which is not enough to cause significant disruptions to the water surface elevation. From Figure 6.33, it is apparent that for all simulations, the numerical model resulted in a bore front that arrives at the structure sooner than the experimental data of Stolle et al. (2019), the reason for the bore front arrival being sooner is described in Section 6.10.1. However, the splash and quasi-steady state water surface elevations fall within the bounds of the experimental data of Stolle et al. (2019).

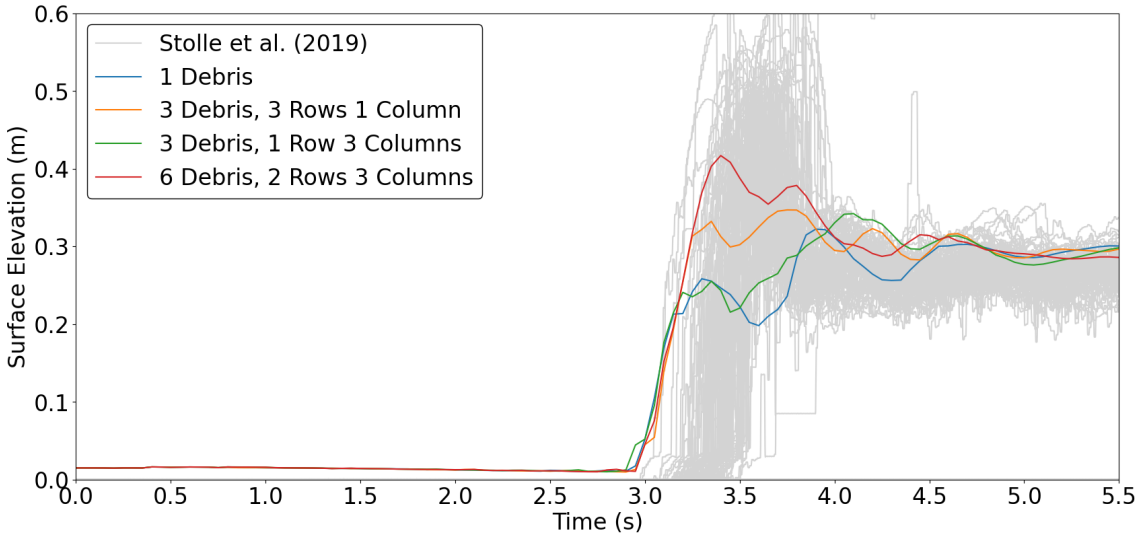


Figure 6.33: Multi-Debris Study - Water Surface Elevation at WG4

6.12.2 Hydrodynamic Force

Figure 6.34 outlines the hydrodynamic force for each simulation. The raw hydrodynamic force output from the numerical model is outlined on the figure as the solid lines, whereas, the average hydrodynamic forces are shown as the dashed lines. As described for wave gauge four, there is no clear trend associated with the hydrodynamic force and the amount of debris being modelled. The hydrodynamic force is directly related to the water surface elevation at the face of the structure which is presented in Figure 6.33. As can be seen in Figure 6.34, the hydrodynamic force increased as the water surface elevation at the face of the structure increased. Furthermore, the hydrodynamic force reached a quasi-steady value as the water-surface elevation reached the quasi-steady state.

Additionally, Figure 6.34 compares the numerical modelling results to the measured hydrodynamic force from Stolle et al. (2019). As can be seen in Figure 6.34, the numerical model results in an initial hydrodynamic force that falls within the bounds of the experimental data. However, in the quasi-steady flow state, the numerical model overestimates the hydrodynamic force. The overestimating of the hydrodynamic forces can be explained by a couple of factors. The first factor is that the numerical model resulted in a quasi-steady state water surface elevation at the face of the structure that falls within the upper bounds of the experimental data of Stolle et al. (2019). Secondly, the bore fronts in the numerical models arrive at the structure earlier than the bore front arrival time of Stolle et al. (2019). The combination of these two factors leads to the numerical model overestimating the hydrodynamic force, as the hydrodynamic force is influenced by both the water depth and flow velocity as shown in Clause 6.10.2 of ASCE 7 (2016).

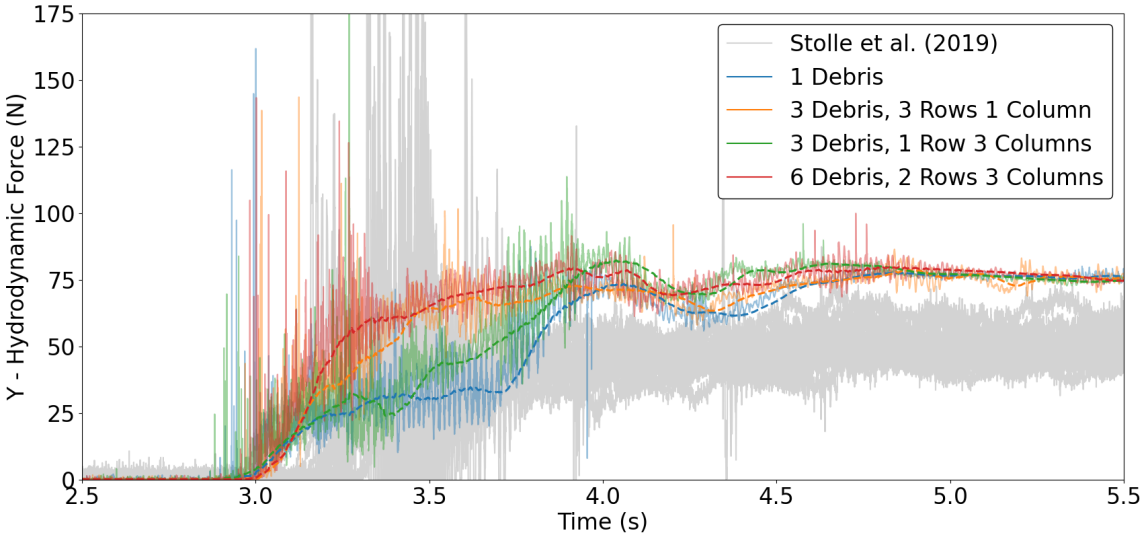


Figure 6.34: Multi-Debris Study - Hydrodynamic Force

6.12.3 Debris Transport

Figure 6.35 outlines the transport paths (traces) that the center of gravity of the debris followed for all simulations. Furthermore, the potential spreading areas of the debris are also shown on the figure, along with the debris traces from the experimental studies of Stolle et al. (2020b). The debris spreading areas outlined by Naito et al. (2014) and Nistor et al. (2017b) were modified as the current definitions start the spreading area at the debris centroid. This is problematic when there is more than one debris, as there is no clear guideline on which debris centroid or location starts the debris spreading area or if the debris spreading area is a function of the potential spreading areas for all debris. The modification to the spreading area starts the debris spreading area at a line instead of a point, this modification is currently being proposed for a change in ASCE 7 (2016). The location of the starting line is defined by a y-coordinate equal to the debris centroid that is furthest upstream from the structure and x-coordinates equal to the debris centroids that are furthest from each other. For these particular simulations, the y-coordinate was governed by the six debris simulation and the x-coordinate was governed by the three debris simulation using three rows and one column. Using the starting line, the debris spreading area is then defined by the spreading angles outlined in Naito et al. (2014) and Nistor et al. (2017b). As can be seen in Figure 6.35, this modification to the debris spreading area does capture the debris traces from the numerical simulations with only one debris falling slightly outside of the debris spreading area defined by Nistor et al. (2017b).

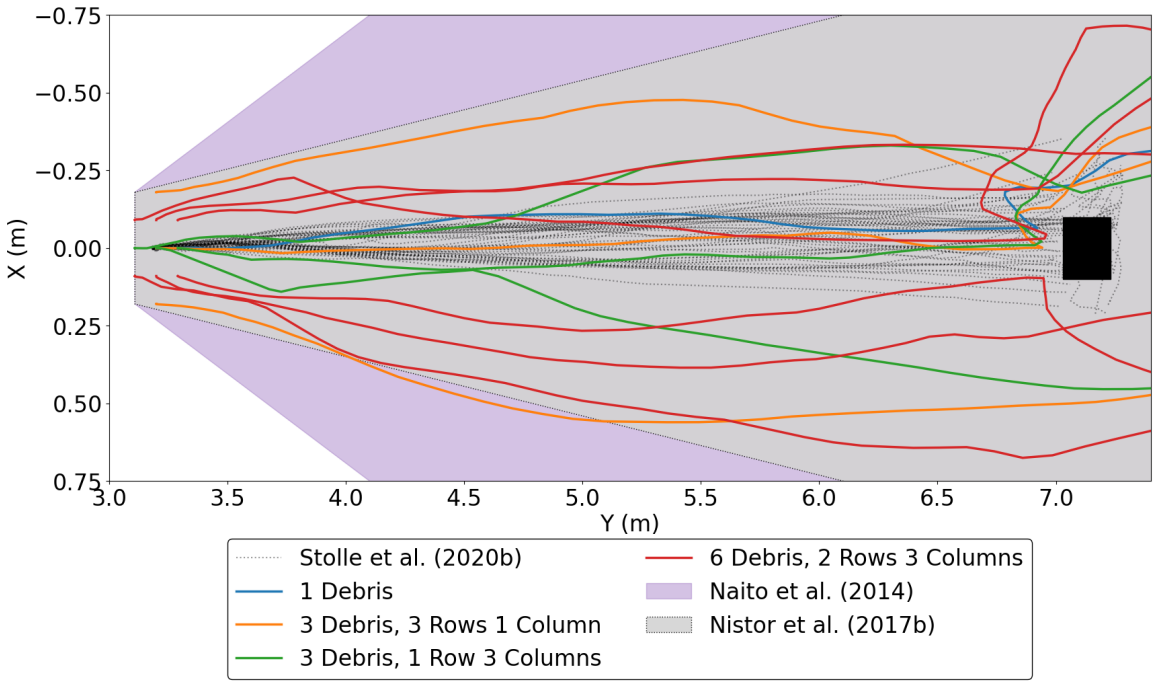


Figure 6.35: Multi-Debris Study - Debris Transport

6.12.4 Debris Impact Force

Figure 6.36 outlines the debris impact force histories from each simulation. As can be seen in Figure 6.36, not all of the debris contacted the structure. In the event that more than one debris contacts the structure, the different impact force histories will have the same color, designating them as occurring in the same simulation, however, the line styles will differ.

From Figure 6.36, the conclusions can be made that the numerical model resulted in initial debris impact force histories that are realistic when compared to the impact force histories developed by the MDOF fitting method described in Section 3.5. From Figure 6.36, the single debris simulation resulted in a debris impact force history that fits within the impact force histories developed from the MDOF fitting method. Observing Figure 6.37, the debris impact velocity and magnitude for the one debris simulation fall within the experimental values of Stolle et al. (2019). This further suggests that a one debris simulation is capable of producing realistic debris impact force histories when compared to the experimental data of Stolle et al. (2019).

From Figure 6.36, it can be seen that the three debris simulation oriented with three rows and one column resulted in two impact events. The first impact event is defined by the orange solid line in Figure 6.36, which resulted in two impacts with relatively small magnitudes and durations. The negative impact force implies that the debris was transported around to the downstream side of the structure after the initial impact and contacted the structure in the negative y-direction. The small magnitudes and durations

are due to the impact event being a glancing impact. The second impact event is defined by the dashed orange line in Figure 6.36. This impact event resulted in an impact force history that fits within the expected values developed from the MDOF fitting method. These results suggest that the numerical model is capable of simulating multi-debris impact events.

From Figure 6.36, it can be seen that the three debris simulation oriented with one row and three columns resulted in one impact event. The impact event resulted in the debris striking the structure twice, as demonstrated by the two impact force histories that were developed. The initial impact event falls within the impact force histories developed by the MDOF fitting method. While the secondary impact is developed after the debris has rebounded from the structure, which resulted in an impact with a small magnitude as the rebound velocity is relatively small when compared to the initial impact velocity ($0.16\frac{m}{s}$ vs $1.51\frac{m}{s}$). From Figure 6.37, it is apparent that the initial debris impact velocity is reasonable when compared to the experimental data of Stolle et al. (2019). These results suggest that the numerical model is capable of simulating multi-debris impact events.

From Figure 6.36, it can be seen that the six debris simulation resulted in two impact events. The first impact event is defined by a solid red line in Figure 6.36. The first debris impact force history falls within a reasonable value when compared to the results from the MDOF fitting method. However, the debris impact velocity defined by the diamond marker in Figure 6.37 is larger than the experimentally determined debris impact velocities. This is due to the impact event being a glancing impact, which results in smaller debris impact forces, as shown by the first debris impact event for the three debris simulation oriented with three rows and one column. The second impact event is defined by a dashed red line in Figure 6.36. This impact event resulted in the debris striking the structure twice. The initial debris impact history resulted in an impact magnitude that fits within the MDOF fitting results, however, the impact duration is smaller than those generated from the MDOF fitting method. The secondary impact is very similar to the secondary impact developed from the three debris simulation oriented with one row and three columns. As in the three debris simulation, the secondary debris impact event was developed from the debris rebounding off of the structure. The rebounded debris impact velocity is relatively small when compared to the initial debris impact velocity ($0.54\frac{m}{s}$ vs $1.69\frac{m}{s}$), which explains why the impact magnitude is smaller. The initial debris impact velocity is defined by the x marker in Figure 6.37, which falls within the bounds of the experimentally determined debris impact velocities. These results suggest that the numerical model is capable of simulating multi-debris impact events.

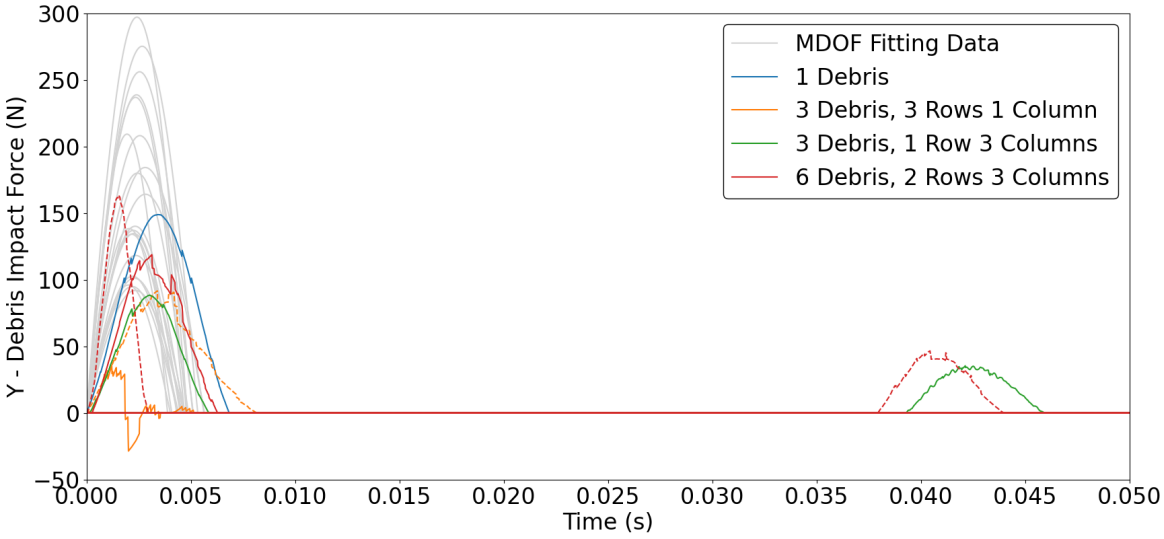


Figure 6.36: Multi-Debris Study - Debris Impact Forces

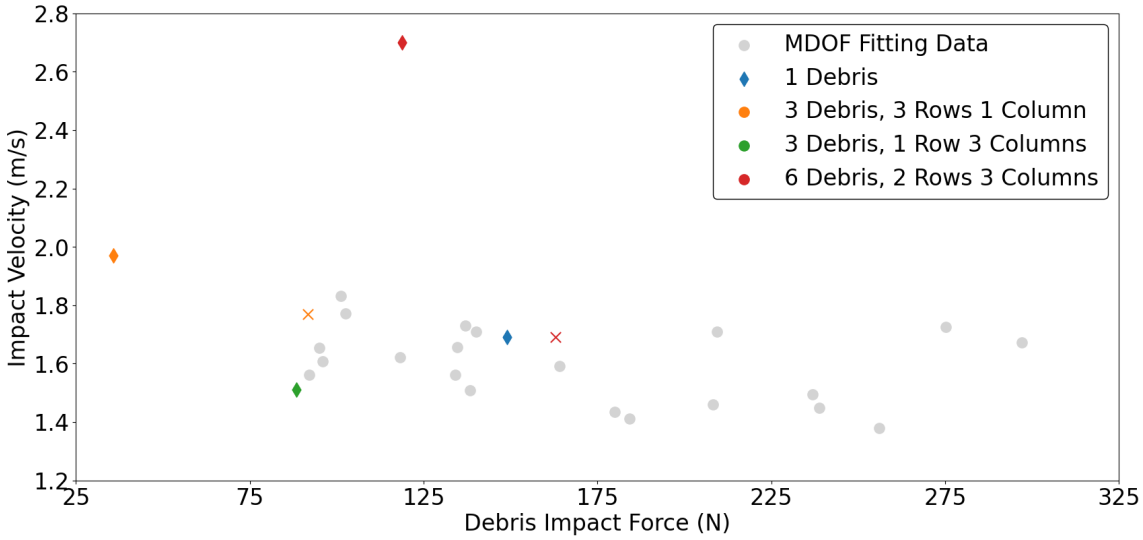
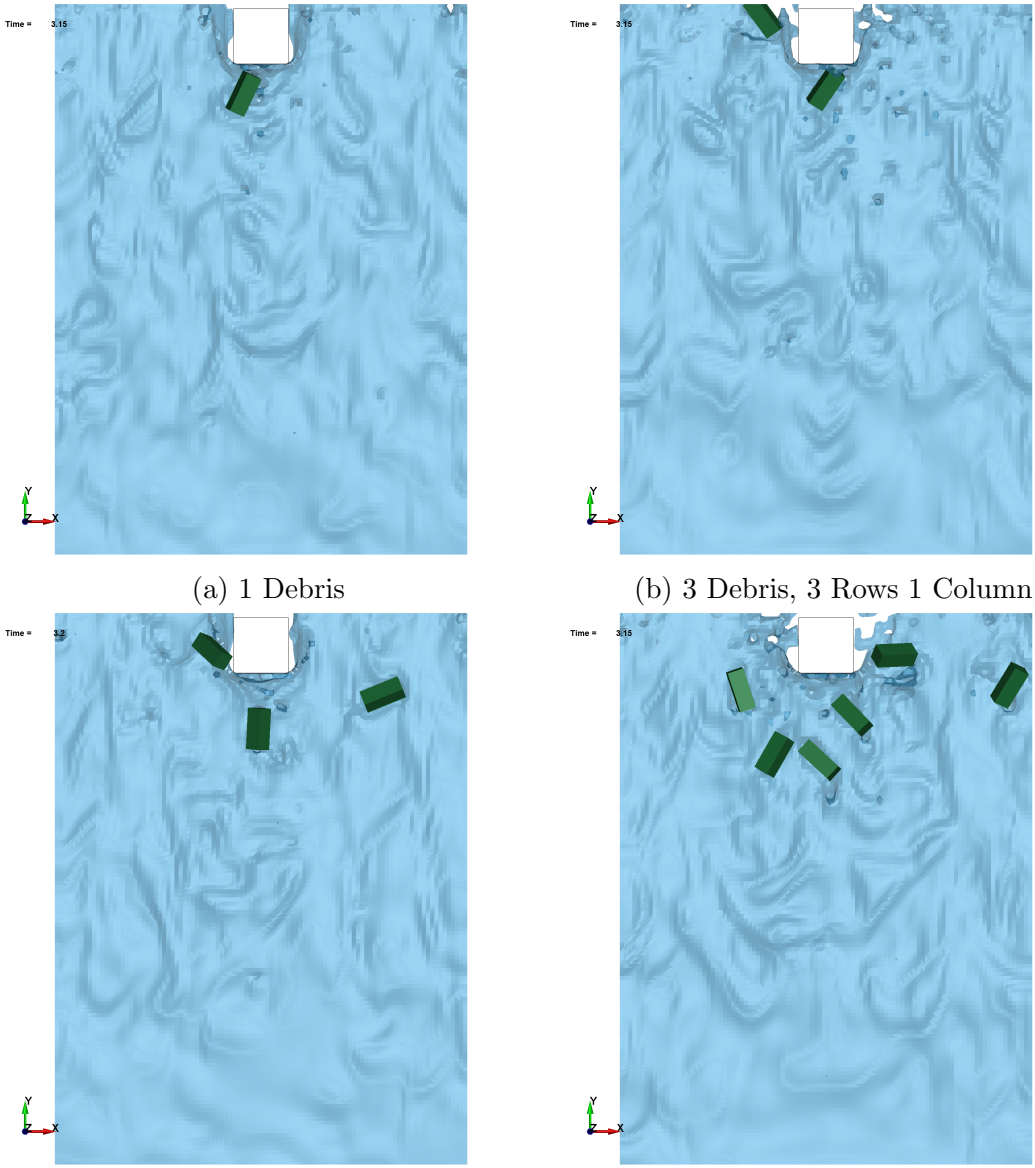


Figure 6.37: Multi-Debris Study - Initial Debris Impact Velocities

Figure 6.38 defines the impact orientations of all simulations. The one debris simulation resulted in one impact event and the impact orientation can be seen in Figure 6.38a, the debris impacts the structure longitudinally with some obliquity. For the simulation with three debris oriented in three rows and one column, two debris impacted the structure and the impact orientation is shown in Figure 6.38b. Similar to the one debris simulation, one of the debris impacts the structure longitudinally with some obliquity, while the second debris impact is a glancing impact. The three debris simulation oriented in one row and three columns resulted in one debris impacting the structure twice, the impact orientation

is shown in Figure 6.38c. Once again, similar to the one debris simulation, the debris is orientated longitudinally during the impact event. The six debris simulation resulted in two debris impact events, with one of the impact events striking the structure twice, the orientation of the debris impacts can be seen in Figure 6.38d. From Figure 6.38d, it is clear that all debris that impact the structure, contact the structure at an angle.



(a) 1 Debris

(b) 3 Debris, 3 Rows 1 Column

(c) 3 Debris, 1 Row 3 Columns

(d) 6 Debris, 2 Rows 3 Column

Figure 6.38: Multi-Debris Study - Debris Impact Orientations

6.12.5 Conclusions

Based on the results from the multi-debris study the following conclusions can be made:

1. There was an insignificant difference in computational time as the number of debris being modelled increased. This is because the debris are all using the same materials, element formulations, and element sizes, which means the critical time step does not change as more debris are added.

2. At wave gauges one, two, and three, the water surface elevation was not influenced by the number of debris, as these wave gauges are upstream of the debris start location. Hence, the same conclusions made about the water surface elevations in Section 6.10.1 can be applied to these wave gauges.

3. At wave gauge four, which is located directly in front of the structure, there was no clear indication that the water surface elevation becomes more disrupted as the number of debris being simulated increased. This is because there are only a maximum of six debris being simulated, which is not enough to significantly influence the water surface elevation.

4. Typically, the numerical model resulted in a bore front that was larger than the experimental data of Stolle et al. (2019) and the Chanson (2006) solution. This is due to an overestimation of the downstream water being modelled.

5. The numerical model resulted in a bore front that is traveling at a higher velocity when compared to the Chanson (2006) solution and the experimental data of Stolle et al. (2019). This can be determined as the bore front arrival time occurs sooner at the wave gauges in the numerical model when compared to the bore fronts from the Chanson (2006) solution and the experimental data of Stolle et al. (2019).

6. The quasi-steady state water surface elevation from the numerical model converges to the Chanson (2006) solution, which typically falls within the lower bounds of the experimental data of Stolle et al. (2019).

7. The hydrodynamic force is directly related to the water surface elevation at the face of the structure. As such, there is no clear relationship between the number of debris being modelled and the hydrodynamic force. Instead, the hydrodynamic force on the structure increased as the water surface elevation at the face of the structured increased as expected.

8. The initial hydrodynamic force developed in the numerical model fit within the bounds of the experimental data of Stolle et al. (2019). However, the quasi-steady state hydrodynamic force overestimated the experimental data of Stolle et al. (2019). This is due to the numerical model resulting in a larger bore front velocity and a water surface elevation that falls in the upper bounds of the experimental data of Stolle et al. (2019), it is the combined influence of these two factors that causes the numerical model to overestimate the hydrodynamic forces.

9. The debris spreading areas outlined in Naito et al. (2014) and Nistor et al. (2017b) were modified as the current definitions start the debris spreading areas at a point, which is problematic when more than one debris is being considered. The modification of the debris spreading area starts the spreading area at a line defined by a

y-coordinate equal to the debris centroid that is furthest upstream of the structure and has a length defined by the x-coordinates of the debris centroids that are furthest away from each other. This modification to start the debris spreading area at a line rather than a point is currently being proposed for a change in ASCE 7 (2016).

10. Using the modified debris spreading areas, all except one of the debris traces fall within the area defined by Nistor et al. (2017b). All debris traces fall within the more conservative debris spreading area defined by Naito et al. (2014).

11. All debris that impacted the structure that are not associated with glancing impacts, resulted in initial debris impact force histories that are realistic when compared to the impact force histories developed from the MDOF fitting method outlined in Section 3.5.

12. The debris impact velocities not associated with glancing impacts fall within the experimental data of Stolle et al. (2019).

13. The numerical model is capable of simulating the hydrodynamics, debris transport, and debris impact events for both single and multi-debris simulations.

6.13 Conclusions and Recommendations

This section will outline the general conclusions and recommendations for future studies:

1. One of the main limitations to using the ALE formulation in LS-DYNA to model the fluid is that there is no option to define a turbulence model, which influences the debris motion (Stolle, 2019) and hence, the debris impact loads.

2. Mesh insensitivity was not reached for ALE mesh modelling the hydrodynamics, as the memory required to simulate a finer mesh was significant. An adaptive mesh algorithm would be better suited to simulate a finer mesh, however, this option was not investigated for this study but could be investigated in future studies.

3. Mesh insensitivity was not reached for the FEM mesh modelling the debris as the computational time required for simulating smaller element sizes increased significantly.

4. The numerical model typically overestimated the size of the bore front but converged to Chanson (2006) solution for the propagation of dam-break waves, both solutions fell within the lower bounds of the experimental data of Stolle et al. (2019). The overestimation of the bore front size in the numerical model is due to an overestimation of the downstream water.

5. The numerical model resulted in hydrodynamic forces due to the splash up of water at the face of the structure that fell within the bounds of the experimental data of Stolle et al. (2019). However, the quasi-steady state hydrodynamic force from the numerical model overestimated the experimental data.

6. The influence of using an elastic structure on the debris impact force was significant, however, further investigation into the contact parameters associated with the debris-structure interaction need to be investigated if an elastic structure were to be used in a future simulation.

7. The numerical model was capable of simulating multi-debris impact events that resulted in debris transport that fell within the modified bounds of Naito et al. (2014) and Nistor et al. (2017b). The modified bounds started the debris spreading area at a line rather than a point. Furthermore, the numerical model resulted in debris impact force histories that compared well to the debris impact force histories developed from the MDOF fitting method.

This chapter showed that LS-DYNA is capable of simulating dam-break wave generated debris impact events by comparing the numerical modelling results to the experimental data of Stolle et al. (2019, 2020b). Some of the limitations associated with using LS-DYNA for this type of simulation are the lack of the ability to simulate turbulence using the ALE method and the complexity of defining an adaptive mesh algorithm. Furthermore, a small time step is required to capture the debris impact event ($< 1e^{-3}s$), which means implicit time integration schemes may not suitable for this type of simulation. As such, an explicit time integration scheme is used, for which GPU acceleration is not an option in LS-DYNA. Additionally, these types of simulations require the use of a large number of computational cores and memory usage, which restricts using desktop computers for performing these types of simulations, computational-clusters are required. As LS-DYNA has the capabilities of simulating these types of debris impact events some future studies that could potentially be investigated are outlined below:

- Investigating the influence of the model scale on the hydrodynamics, debris transport, and debris impacts.

- Investigating the debris transport and impact forces for negatively-buoyant debris.

- Investigating the debris transport and impact forces for extraordinary debris such as marine vessels.

- Investigating the debris transport and impact forces for vehicle impacts. The United States Department of Transportation has several vehicle models for LS-DYNA that are freely available, which would greatly ease the model setup of this type of simulation.

Chapter 7

General Conclusions and Recommendations for Future Work

7.1 General Conclusions

The thesis presented herein examined the debris impact loads generated from extreme hydrodynamic events. The overall research project can be divided into two main sections. The first section of this research project focused on investigating how Chapter 6 of ASCE 7 (2016) defines debris impact loads and how the assumptions made about debris impacts in ASCE 7 (2016) influence structural response parameters. The second section of this research project focused on investigating the validity and practicality of numerically simulating dam-break wave generated debris impact events. Based on the results of these studies the following general conclusions can be drawn:

- Consideration should be given that many tsunamis are generated from earthquakes and as such, infrastructure may already be damaged before the tsunami reaches land.
- Following a single-degree-of-freedom (SDOF) method or Clauses 6.11.2 and 6.11.8 to develop debris impact force histories resulted in a force response of a column that overestimated both the magnitude and frequency of the experimental force response. A multiple-degree-of-freedom (MDOF) method was capable of producing debris impact force histories that resulted in a force response that fit well to the experimental data.
- Using a SDOF method to estimate the debris impact force histories from experimental data can result in debris impact force histories that do not fit the experimental data when applied back to a MDOF model. This implies that while a SDOF model subjected to the debris impact force histories may fit the general response from the experimental data, when that same debris impact force history is applied to a MDOF model, the results no longer follow the response of the experimental data. This suggests that the SDOF method may not be adequate for estimating debris impact force histories for MDOF systems.

- Within the elastic capacity of a column, using a rectangular impact shape as required in Clause 6.11.8 of ASCE 7 (2016), resulted in the largest forces and deformations developed in the column. A triangular impact shape resulted in the smallest forces and deformations developed. While, the half-sine, parabolic, and trapezoidal impact shapes resulted in forces and deformations that were bounded by the results from the triangular and rectangular impact shapes.

- Within the elastic capacity of a column, it was found that the shear forces and bending moments at support locations increased as the structural stiffness increased. While, the deformations in the column decreased as the structure stiffness increased.

- Using the dynamic amplification factor outlined in Table 6.11-1 of ASCE 7 (2016) for the column in Chapter 5 resulted in the amplified static solution always providing response parameters that are larger than the dynamic results. The amplified static results overestimated the shear reaction forces by a maximum factor of 1.71, the reaction bending moments were overestimated by a maximum factor of 1.45, and the midspan deflection was overestimated by a maximum factor of 9.01.

- The largest forces developed in the columns investigated were at the support and impact locations, which highlights the importance of understanding the debris impact location.

- Using the ALE formulation in LS-DYNA, the numerical model was shown to be capable of simulating dam-break wave generated debris impact events, using either one debris or multiple debris. The numerical model was capable of approximating the water surface elevations, hydrodynamic forces, debris transport, and debris impact forces from the experimental data of Stolle et al. (2019, 2020b). Additionally, the computational power required to run the simulation was not unreasonably larger for computational clusters, 64 cores, $256GB$ of memory, and approximately three days of computational time were required to simulate these debris impact events.

This thesis investigated how debris impact loads are defined and how the assumptions made about debris impact loads in Chapter 6 of ASCE 7 (2016) influence structural response parameters. Within the bounds of this thesis, it was shown that using the methods and assumptions outlined in Chapter 6 of ASCE 7 (2016) for debris impact loads, the corresponding structural response was conservative when compared to debris impact loads generated using alternative methods. Furthermore, this thesis showed that LS-DYNA was capable of simulating dam-break wave generated debris impact events by approximating the results from the experimental studies of Stolle et al. (2019, 2020b). Additionally, the numerical model did not require the use of an unreasonable amount of computational resources or computational time, which is promising for future studies that are investigating numerically simulating debris impact events generated from extreme hydrodynamic conditions.

7.2 Recommendations for Future Work

The studies presented throughout this thesis examined how to estimate debris impact loads generated from extreme hydrodynamic events and limitations to the studies performed that would benefit from further investigations were also presented. Below is a list of recommendations for future work that may aid in furthering the understanding of debris impact loads generated from extreme hydrodynamic events:

- Debris impact loads were approximated by taking the force response data from the experimental program of Stolle et al. (2019) and iteratively estimating the debris impact force history until the numerically modelled force response was approximately equal to the experimental force response. A single-degree-of-freedom model and multiple-degree-of-freedom model constructed of two-dimensional beam elements were investigated. A future study could extend this method to a full three-dimensional finite element model to investigate how the debris impact force histories developed by each method compare to each other. This would provide insight into how effective and accurate the single-degree-of-freedom or two-dimensional multiple-degree-of-freedom models are at estimating debris impact loads.

- The debris impact loads in Chapter 3 were estimated by using the simplifying assumption that the debris impact load can be treated as a point load instead of as a separate body in the simulation. A future study could investigate the validity of this assumption by performing a two-body impact simulation and comparing how the structural response is influenced by the impacting body. This would also provide insight into the dynamics associated with a two-body impact simulation.

- The influence of the impact shape on the response of a column was only investigated within the elastic range of a column. A future study could investigate how the response changes as nonlinearity is introduced into the model. This would provide more insight into understanding how the debris impact shape influences the response of a structure in the nonlinear range.

- The influence of the structural stiffness on how a column responds to debris impact loads was investigated within the columns elastic capacity. A future study could investigate how the nonlinear response of a column is influenced as the structural stiffness changes.

- The influence of the structural stiffness on how a column responds to debris impact loads was investigated by using a two-dimensional fiber model for a column. A future study could investigate a full three-dimensional finite element model to see if the same conclusions can be drawn. A finite element model would also allow the crack patterns and failure mechanisms to be observed, which is critical in understanding how a column responds to lateral loads.

- LS-DYNA was shown to be capable of replicating experimental results from dam-break wave generated debris impact events outlined in Stolle et al. (2019, 2020b). Future studies could investigate the following phenomena:

- Investigate the influence of a range of structural properties on the debris impact force, such as structural stiffness.
- Investigate the influence of the model scale on the hydrodynamics, debris transport, and debris impact force.
- Investigating the debris transport and impact forces for negatively-buoyant debris.
- Investigate the debris transport and impact force for extraordinary debris such as marine vessels.
- Investigate the debris transport and impact force for vehicle impacts.
- Investigate the influence of three-dimensional impact geometry on debris impact forces, as a numerical model allows for the tracking of the debris motion in three-dimensional space.
- Investigate the influence of the hydrodynamics on the debris impact force. The added mass due to the decelerated fluid around the debris impact causes an apparent increase in the mass of the debris, which is a phenomenon that has not been widely investigated.
- Investigate failure-mechanisms of structures under the combined hydrodynamic and debris loading.

References

AASHTO (2012). Bridge design specifications. Standard, American Association of State Highway and Transportation Officials.

Aghl, P. P., Naito, C. J., and Riggs, H. R. (2014). Full-scale experimental study of impact demands resulting from high mass, low velocity debris. *Journal of Structural Engineering*, 140.

Aghl, P. P., Naito, C. J., and Riggs, H. R. (2015). Estimation of demands resulting from inelastic axial impact of steel debris. *Engineering Structures*, 82.

Amsden, A. A., Ruppel, H. M., and Hirt, C. W. (1980). Sale: A simplified ale computer program for fluid flow at all speeds. Technical report, Los Alamos National Lab.

Ancheta, T., Darragh, R., Stewart, J., Seyhan, E., Silva, W., B.S.J., Wooddell, K., Graves, R., Kottke, A., Boore, D., Kishida, T., and Donahue, J. (2013). Peer nga-west2 database.

ANSYS® (2018). Ansys granta design sample materials. Version 19.1.

Aquelet, N., Souli, M., and Olovsson, L. (2006). Euler–lagrange coupling with damping effects: Application to slamming problems. *Computer Methods in Applied Mechanics and Engineering*, 195:110 – 132.

Arnason, H., Petroff, C., and Yeh, H. (2009). Tsunami bore impingement onto a vertical column. *Journal of Disaster Research*, 4:391 – 403.

ASCE 7 (2016). Minimum design loads and associated criteria for buildings and other structures. Standard, American Society of Civil Engineers.

Bathe, K.-J. (2007). Conserving energy and momentum in nonlinear dynamics: A simple implicit time integration scheme. *Computers & Structures*, 85(7-8):437 – 445.

Benson, D. J. (1992a). Computational methods in lagrangian and eulerian hydrocodes. *Computer Methods in Applied Mechanics and Engineering*, 99:235 – 394.

Benson, D. J. (1992b). Momentum advection on a staggered mesh. *Journal of Computational Physics*, 200(2):143 – 162.

Biggs, J. M. (1964). *Introduction to Structural Dynamics*. McGraw-Hill.

Bridge Software Institute (2008). Fb-multipier user's manual.

CAC (2016). *Concrete Design Handbook*. Cement Association of Canada/Association Canadienne du Ciment, 4th edition.

Chang, G. and Mander, J. (1994). Seismic energy based fatigue damage ananlysis of bridge columns: Part 1 – evaluation of seismic capacity. Technical Report NCEER-94-000, State University of New York.

Chanson, H. (2006). Tsunami surges on dry coastal plains: Application of dam break wave equations. *Coastal Engineering Journal*, 48(4):355 – 370.

Chau, K. and Bao, J. (2010). Hydrodynamic analysis of boulder transportation on phi-phi island during the 2004 indian ocean tsunami. In *The Fifth International Conference on Earthquake Engineering (5ICEE)*, pages 1693 – 1699.

Chopra, A. k. (2017). *Dynamics of Structures*. Pearson, 5th edition.

Chung, J. and Hulbert, G. M. (1993). A time integration algorithm for structural dynamics with improved numerical dissipation: The generalized-α method. *Journal of Applied Mechanics*, 60(2):371 – 375.

Consolazio, G. R., Cowan, D. R., Biggs, A., Cook, R. A., Ansley, M., and Bollmann, H. T. (2005). *Full-scale experimental measurement of barge impact loads on bridge piers*. Transportation Research Board.

Contact Modeling in LS-DYNA (2010). `https://www.dynasupport.com/tutorial/ls-dyna-users-guide/contact-modeling-in-ls-dyna`. Accessed: 2020-10-31.

Cotsovos, D. M., Stathopoulos, N. D., and Zeris, C. A. (2008). Behavior of rc beams subjected to high rates of concentrated loading. *Journal of Structural Engineering*, 134:1839 – 1851.

Cowan, D. R., Consolazio, G. R., and Davidson, M. T. (2015). Response-spectrum analysis for barge impacts on bridge structures. *Journal of Bridge Engineering*, 20.

CSA A23.3-14 (2014). Design of concrete structures. Standard, CSA Group.

Das Adhikary, S. and Li, B. (2018). Simplified analytical models to predict low-velocity impact response of rc beams. *Practice Periodical on Structural Design and Construction*, 23:1 – 10.

Derschum, C., Nistor, I., Stolle, J., and Goseberg, N. (2018). Debris impact under extreme hydrodynamic conditions part 1 : Hydrodynamics and impact geometry. *Coastal Engineering*, 141:24 – 35.

Esteban, M., Takagi, H., and Shibayama, T. (2015). *Handbook of Coastal Disaster Mitigation for Engineers and Planners*. Butterworth-Heinemann.

FEMA P646 (2012). Guidelines for design of structure for vertical evacuation from tsunamis. Standard, Federal Emergency Management Agency.

Fu-Pei, H., Wen-Cheng, S., Pu-Wen, W., and Yi-An, L. (2018). Rc column cyclic tests.

Fujikake, K., Li, B., and Soeun, S. (2009). Impact response of reinforced concrete beam and its analytical evaluation. *Journal of Structural Engineering*, 135:938 – 950.

Haehnel, R. B. and Daly, S. F. (2002). Maximum impact force of woody debris on floodplain structures. Technical report, US Army Corps of Engineers.

Haehnel, R. B. and Daly, S. F. (2004). Maximum impact force of woody debris on floodplain structures. *Journal of Hydraulic Engineering*, 130:112 – 120.

Hallquist, J. O. (2006). *LS-DYNA Theory Manual*. Livermore Software Technology Corporation.

Hilber, H. M., Hughes, T. J. R., and Taylor, R. L. (1977). Improved numerical dissipation for time integration algorithms in structural dynamics. *Earthquake engineering & structural dynamics*, 5:283 – 292.

Huang, N. E., Shen, Z., Long, S. R., Wu, M. C., Shih, H. H., Zheng, Q., Yen, N.-C., Tung, C. C., and Liu, H. H. (1998). The empirical mode decomposition and the hilbert spectrum for nonlinear and non-stationary time series analysis. *Proceedings of the Royal Society. A, Mathematical, physical, and engineering sciences*, 454:903 – 995.

Ikeno, M., Kihara, N., and Takabatake, D. (2013). Simple and practical estimation of movement possibility and collision force of debris due to tsunami. *Journal of Japan Society of Civil Engineers*, 69:861 – 865.

Ikeno, M., Takabatake, D., Kihara, N., Kaida, H., Miyagawa, Y., and Shibayama, A. (2016). Improvement of collision force formula for woody debris by airborne and hydraulic experiments. *Coastal Engineering Journal*, 58:1 – 23.

Imbeau, P. (2012). Response of reinforced concrete columns subjected to impact loading. Master's thesis, University of Ottawa.

Kent, C. D. and Park, R. (1971). Flexural members with confined concrete. *Journal of the Structural Division*, 97:1969 – 1990.

Khowitar, E., Riggs, H. R., and Kobayashi, M. H. (2014). Beam response to longitudinal impact by a pole. *Journal of Engineering Mechanics*, 140.

Khowitar, E., Riggs, H. R., and Kobayashi, M. H. (2015). Transverse impact of a horizontal beam on a vertical column. *Journal of Engineering Mechanics*, 142.

Ko, H. T.-S., Cox, D. T., Riggs, H. R., and Naito, C. J. (2015). Hydraulic experiments on impact forces from tsunami-driven debris. *Journal of Waterway, Port, Coastal, and Ocean Engineering*, 141.

Kuilanoff, G. and Drake, R. (1991). Design of doe facilities for wind-generated missiles. *Third DOE Natural Phenomena Hazards Mitigation Conference*.

LST (2020). Ls-dyna keyword user's manual. *Livermore Software Technology*. LS-DYNA®. Version R12.0.

Matsutomi, H. (2009). Method for estimating collision force of driftwood accompanying tsunami inundation flow. *Journal of Disaster Research*, 4.

McKenna, F., Scott, M. H., and Fenves, G. L. (2010). Nonlinear finite-element analysis software architecture using object composition. *Journal of Computing in Civil Engineering*, 24:95 – 107.

Mohammadian, M. (2019). Lecture notes in cvg5112 computational hydrodynamics. Faculty of Civil Engineering, University of Ottawa.

Monaghan, J. J. and Kos, A. (1999). Solitary waves on a cretan beach. *Journal of Waterway, Port, Coastal, and Ocean Engineering*, 125(3):145 – 155.

Murnaghan, F. D. (1944). The compressibility of media under extreme pressures. *Proceedings of the National Academy of Sciences*, 30(9):244 – 247.

Naito, C., Cercone, C., Riggs, H. R., and Cox, D. (2014). Procedure for site assessment of the potential for tsunami debris impact. *Journal of Waterway, Port, Coastal and Ocean Engineering*, 140:223 – 232.

Navaratnam, C. U., Tørum, A., and Arntsen, Ø. A. (2013). Preliminary analysis of wave slamming force response data from tests on a truss structure in large wave flume, hannover, germany. Technical Report BAT/MB-R1/2013, Department of Civil and Transport Engineering, Norwegian University of Science and Technology.

Newmark, N. M. (1959). A method of computation for structural dynamics. *Journal of the Engineering Mechanics Division*, 85:67 – 94.

Newville, M., Otten, R., Nelson, A., Ingargiola, A., Stensitzki, T., Allan, D., Fox, A., Carter, F., Michał, Pustakhod, D., Ram, Y., Glenn, Deil, C., Stuermer, Beelen, A., Frost, O., Zobrist, N., Mark, Pasquevich, G., Hansen, A. L. R., Spillane, T., Caldwell, S., Polloreno, A., andrewhannum, Fraine, J., deep 42-thought, Maier, B. F., Gamari, B., Persaud, A., and Almarza, A. (2020). lmfit/lmfit-py 1.0.1.

Nistor, I., Goseberg, N., and Stolle, J. (2017a). Tsunami-driven debris motion and loads: A critical review. *Frontiers in Built Environment*, 3.

Nistor, I., Goseberg, N., Stolle, J., Mikami, T., Shibayama, T., Nakamura, R., and Matsuba, S. (2017b). Experimental investigations of debris dynamics over a horizontal plane. *Journal of Waterway, Port, Coastal, and Ocean Engineering*, 143(3).

Oumeraci, H., Partenscky, H. W., Kohlhase, S., and Klammer, P. (1993). Impact loading and dynamic response of caisson breakwaters. *Coastal Engineering*, pages 1475 – 1488.

Palermo, D., Nistor, I., Al-Faesly, T., and Cornett, A. (2012). Impact of tsunami forces on structures: The university of ottawa experience. In *Proceedings of the Fifth International Tsunami Symposium, Ispra, Italy*.

Popovics, S. (1973). A numerical approach to the complete stress-strain curve of concrete. *Cement and Concrete Research*, 3(5):583 – 599.

Prandtl, L. (1926). Über die ausgebildete turbulenz (investigations on turbulent flow). In *Proceedings of the Second International Congress for Applied Mechanics*, pages 136 – 139.

Riggs, H. R., Kobayashi, M. H., Cox, D. T., Aghl, P. P., Khowitar, E., Naito, C. J., and Ko, H. T.-S. (2013). Water-driven debris impact forces on structures: Experimental and theoretical program. *ASME 2013 32nd International Conference on Ocean, Offshore and Arctic Engineering*.

Saatcioglu, M., Ghobarah, A., and Nistor, I. (2005). Effects of the december 26, 2004 sumatra earthquake and tsunami on physical infrastructure. *ISET Journal of Earthquake Technology*, 42:79 – 94.

Saatcioglu, M. and Razvi, S. R. (1992). Strength and ductility of confined concrete. *Journal of Structural Engineering*, 118:1590 – 1607.

Stolle, J. (2019). *Debris Hazard Assessment in Extreme Flooding Events*. PhD thesis, University of Ottawa.

Stolle, J., Derschum, C., Goseberg, N., Nistor, I., and Petriu, E. (2018a). Debris impact under extreme hydrodynamic conditions part 2 : Impact force responses for non-rigid debris collisions. *Coastal Engineering*, 141:107 – 118.

Stolle, J., Ghodoosipour, B., Derschum, C., Nistor, I., Petriu, E., and Goseberg, N. (2018b). Swing gate generated dam-break waves. *Journal of Hydraulic Research*, 57(5):675 – 687.

Stolle, J., Goseberg, N., Nistor, I., and Petriu, E. (2018c). Probabilistic investigation and risk assessment of debris transport in extreme hydrodynamic conditions. *Journal of Waterway, Port, Coastal and Ocean Engineering*, 144:1 – 14.

Stolle, J., Goseberg, N., Nistor, I., and Petriu, E. (2019). Debris impact forces on flexible structures in extreme hydrodynamic conditions. *Journal of Fluids and Structures*, 84:391 – 407.

Stolle, J., Krautwald, C., Robertson, I., Achiari, H., Mikami, T., Nakamura, R., Takabatake, T., Nishida, Y., Shibayama, T., Esteban, M., Nistor, I., and Goseberg, N. (2020a). Engineering lessons from the 28 september 2018 indonesian tsunami: Debris loading. *Canadian Journal of Civil Engineering*, 47(1):1 – 12.

Stolle, J., Nistor, I., Goseberg, N., and Petriu, E. (2020b). Multiple debris impact loads in extreme hydrodynamic conditions. *Journal of Waterway, Port, Coastal, and Ocean Engineering*, 146(2).

Stolle, J., Takabatake, T., Nistor, I., Mikami, T., Nishizaki, S., and Hamano, G. (2018d). Experimental investigation of debris damming loads under transient supercritical flow conditions. *Coastal Engineering*, 139:16 – 31.

Syamsidik, Benazir, Umar, M., Margaglio, G., and Fitrayansyah, A. (2019). Post-tsunami survey of the 28 september 2018 tsunami near palu bay in central sulawesi, indonesia: Impacts and challenges to coastal communities. *International Journal of Disaster Risk Reduction*, 38:110 – 132.

Tedesco, J. W., McDougal, W. G., and Ross, C. A. (1999). *Structural Dynamics: Theory and Applications*. Addison Wesley Longman.

Van Leer, B. (1977). Towards the ultimate conservative difference scheme. iv. a new approach to numerical convection. *Journal of Computational Physics*, 23(2):276 – 299.

Winslow, A. M. (1963). Equipotential zoning of two-dimensional meshes. Technical report, Lawrence Livermore National Lab.

Wood Handbook (1999). Wood as an engineering material. Handbook, USDA Forest Service.

Youcef, Y. S. and Chemrouk, M. (2012). Curvature ductility factor of rectangular sections reinforced concrete beams. *International Journal of Civil and Environmental Engineering*, 6:971 – 976.

Zhang, C., Gholipour, G., and Mousavi, A. A. (2020). State-of-the-art review on responses of rc structures subjected to lateral impact loads. *Archives of Computational Methods in Engineering*.

Zhong, Z.-H. (1993). *Finite Element Procedures for Contact-Impact Problems*. Oxford University Press.

APPENDICES

Appendix A

Example Calculations

The following sections will use all of the same assumptions outlined from the SDOF model comparison section. All other assumptions required will be clearly outlined in the respective sections.

A.1 Debris Impact

This section outlines the example calculations regarding single debris impacts with an impact velocity of $10\frac{m}{s}$.

A.1.1 Haehnel and Daly (2004)

$$k_e^{-1} = \frac{1}{k_s} + \frac{1}{k_d} \tag{A.1}$$

$$k_e^{-1} = \frac{1}{4.67 \times 10^9 \frac{N}{m}} + \frac{1}{7.80 \times 10^7 \frac{N}{m}} \tag{A.2}$$

$$\boldsymbol{k_e = 7.68 \times 10^7 \frac{N}{m}} \tag{A.3}$$

A.1.1.1 Contact Stiffness Method

$C_f = 0$ for a cylindrical log impact at a 0° angle (Haehnel and Daly, 2004).

$$F_{ni} = u_{max}\sqrt{k_e\left(m_d + C_f m_f\right)} \tag{A.4}$$

$$F_{ni} = 10\frac{m}{s}\sqrt{\left(7.68 \times 10^7 \frac{N}{m}\right)(1980kg)} \tag{A.5}$$

$$\boldsymbol{F_{ni} = 3897kN} \tag{A.6}$$

A.1.1.2 Work Energy Method

$$F_{ni} = \frac{m_d u_{max}^2}{d} \tag{A.7}$$

$$d = u_{max}\sqrt{\frac{m_d}{k_d}} \tag{A.8}$$

$$d = 10\frac{m}{s}\sqrt{\frac{1980kg}{7.80 \times 10^7 \frac{N}{m}}} \tag{A.9}$$

$$\boldsymbol{d = 0.05m} \tag{A.10}$$

$$F_{ni} = \frac{(1980kg)\left(10\frac{m}{s}\right)^2}{0.05m} \tag{A.11}$$

$$\boldsymbol{F_{ni} = 3897kN} \tag{A.12}$$

A.1.1.3 Impulse Momentum Method

$$F_{ni} = \frac{\pi}{2}\frac{m_d u_{max}^2}{t_d} \tag{A.13}$$

$$t_d = \frac{\pi}{2}\sqrt{\frac{m_d}{k_d}} \tag{A.14}$$

$$t_d = \frac{\pi}{2}\sqrt{\frac{1980kg}{7.80 \times 10^7 \frac{N}{m}}} \tag{A.15}$$

$$\boldsymbol{t_d = 0.0079s} \tag{A.16}$$

$$F_{ni} = \frac{\pi}{2}\frac{(1980kg)\left(10\frac{m}{s}\right)^2}{0.0079s} \tag{A.17}$$

$$\boldsymbol{F_{ni} = 3897kN} \tag{A.18}$$

A.1.2 Matsutomi (2009)

$$F_{ni} = 3.04\left(\frac{v_{A0}}{\sqrt{gD_w}}\right)^{1.2}\left(\frac{\sigma_{df}}{\gamma_d L_w}\right)^{0.4}\left(\gamma_d D_w^2 L_w\right) \tag{A.19}$$

$$F_{ni} = 3.04\left(\frac{10\frac{m}{s}}{\sqrt{\left(9.81\frac{m}{s}\right)(0.6m)}}\right)^{1.2}\left(\frac{9.79 \times 10^6 \frac{N}{m^2}}{\left(350\frac{kg}{m^3}\right)(20m)}\right)^{0.4}\left(\left(350\frac{kg}{m^3}\right)(0.6m)^2(20m)\right) \tag{A.20}$$

$$\boldsymbol{F_{ni} = 759kN} \tag{A.21}$$

A.1.3 Riggs et al. (2013)

$$F_{ni} = -v_0\sqrt{k_d m_d} \tag{A.22}$$

$$F_{ni} = -10\frac{m}{s}\sqrt{\left(7.80\times10^7\frac{N}{m}\right)(1980kg)} \tag{A.23}$$

$$\boldsymbol{F_{ni} = -3930kN} \text{ (Negative implies compression)} \tag{A.24}$$

A.1.4 Aghl et al. (2015)

$$k_{de} = \frac{EA}{L} \tag{A.25}$$

$$k_{de} = \frac{\left(5.52\times10^9\frac{N}{m^2}\right)(0.283m^2)}{20m} \tag{A.26}$$

$$\boldsymbol{k_{de} = 7.81\times10^7\frac{N}{m}} \tag{A.27}$$

$$k_{dp} = \frac{E_p A}{L} \tag{A.28}$$

$$k_{dp} = \frac{\left(4.45\times10^7\frac{N}{m^2}\right)(0.282m^2)}{20m} \tag{A.29}$$

$$\boldsymbol{k_{dp} = 6.30\times10^5\frac{N}{m}} \tag{A.30}$$

$$v_y = \frac{F_y}{\sqrt{m_d k_{de}}} \tag{A.31}$$

$$v_y = \frac{9.79\times10^6\frac{N}{m^2}}{\sqrt{(1980kg)\left(7.81\times10^7\frac{N}{m}\right)}} \tag{A.32}$$

$$\boldsymbol{v_y = 24.90\frac{m}{s}} \tag{A.33}$$

$$v = 10\frac{m}{s} < v_y = 24.90\frac{m}{s} \tag{A.34}$$

$$F_{ni} = \begin{cases} v\sqrt{m_d k_{de}} & v \le v_y \\ v_y\sqrt{m_d k_{de}} + (v - v_y)\sqrt{m_d k_{dp}} & v > v_y \end{cases}$$

$$F_{ni} = v\sqrt{m_d k_d e} \tag{A.35}$$

$$F_{ni} = 10\frac{m}{s}\sqrt{(1980kg)\left(7.81\times10^7\frac{N}{m}\right)} \tag{A.36}$$

$$\boldsymbol{F_{ni} = 3932kN} \tag{A.37}$$

A.1.5 Ikeno et al. (2016)

Due to the impact angle (θ_c) being 90° the reduction factor for an oblique impact angle (λ) is equal to 1.

$$\theta_c = 90° - \theta_c' \tag{A.38}$$

$$\theta_c = 90° - 0° \tag{A.39}$$

$$\boldsymbol{\theta_c = 90°} \tag{A.40}$$

$$\tilde{E} = \frac{E_d E_s}{E_s(1-\nu_d^2) + E_d(1-\nu_s^2)} \tag{A.41}$$

$$\tilde{E} = \frac{\left(5.52 \times 10^9 \frac{N}{m^2}\right)\left(2.66 \times 10^{10} \frac{N}{m^2}\right)}{\left(2.66 \times 10^{10} \frac{N}{m^2}\right)(1-0.34^2) + \left(5.52 \times 10^9 \frac{N}{m^2}\right)(1-0.15^2)} \tag{A.42}$$

$$\boldsymbol{\tilde{E} = 5.08 \times 10^9 \frac{N}{m^2}} \tag{A.43}$$

$$F_{ni} = 0.243\,(1 \times 1980kg)^{0.6}\left(10\frac{m}{s}\right)^{1.2}(0.6m)^{0.2}\left(5.08 \times 10^9 \frac{N}{m^2}\right)^{0.4}(1.0) \tag{A.44}$$

$$\boldsymbol{F_{ni} = 2520kN} \tag{A.45}$$

A.1.6 Stolle et al. (2018a)

Effective stiffness is calculated from Haehnel and Daly (2004). Scale up the k_{HD} by a factor of 40^2 as per Stolle et al. (2018a).

$$k_{HD} = \left(2.46 \times 10^7 \frac{N}{m}\right) \times 40^2 \tag{A.46}$$

$$\boldsymbol{k_{HD} = 3.94 \times 10^{10} \frac{N}{m}} \tag{A.47}$$

$$b_s = \frac{k_s}{k_{HD}} \tag{A.48}$$

$$b_s = \frac{4.67 \times 10^9 \frac{N}{m}}{3.94 \times 10^{10} \frac{N}{m}} \tag{A.49}$$

$$\boldsymbol{b_s = 0.12} \tag{A.50}$$

$$F_{ni} = u_{max}\sqrt{b_s k_e m_d} \tag{A.51}$$

$$F_{ni} = \left(10\frac{m}{s}\right)\sqrt{(0.12)\left(7.68 \times 10^7 \frac{N}{m}\right)(1980kg)} \tag{A.52}$$

$$\boldsymbol{F_{ni} = 1342kN} \tag{A.53}$$

A.1.7 ASCE 7 (2016)

The stiffness value is selected as the minimum between the structure stiffness and the debris stiffness. Therefore, the stiffness is equal to $7.80 \times 10^7 \frac{N}{m}$.

$$F_{ni} = u_{max}\sqrt{km_d} \tag{A.54}$$

$$F_{ni} = \left(10\frac{m}{s}\right)\sqrt{\left(7.80 \times 10^7 \frac{N}{m}\right)(1980kg)} \tag{A.55}$$

$$\boldsymbol{F_{ni} = 3930kN} \tag{A.56}$$

A.1.8 AASHTO (2012)

Impact duration is calculated from Haehnel and Daly (2004).

$$F_{ni} = \frac{m_d u_{max}}{t_d} \tag{A.57}$$

$$F_{ni} = \frac{(1980kg)\left(10\frac{m}{s}\right)}{0.0079s} \tag{A.58}$$

$$\boldsymbol{F_{ni} = 2506kN} \tag{A.59}$$

A.1.9 FEMA P646 (2012)

The stiffness value is selected as the debris stiffness. Therefore, the stiffness is equal to $7.80 \times 10^7 \frac{N}{m}$.

$$F_{ni} = C_f u_{max}\sqrt{m_d k_e} \tag{A.60}$$

$$F_{ni} = (2)\left(10\frac{m}{s}\right)\sqrt{\left(7.80 \times 10^7 \frac{N}{m}\right)(1980kg)} \tag{A.61}$$

$$\boldsymbol{F_{ni} = 7860kN} \tag{A.62}$$

A.1.10 Stolle et al. (2019)

Effective stiffness and impact duration are calculated from Haehnel and Daly (2004).

$$a = \frac{m_s}{m_d} \tag{A.63}$$

$$a = \frac{5606kg}{1980kg} \tag{A.64}$$

$$\boldsymbol{a = 2.83} \tag{A.65}$$

$$b = \frac{k_s}{k_d} \tag{A.66}$$

$$b = \frac{4.67 \times 10^9 \frac{N}{m}}{7.80 \times 10^7 \frac{N}{m}} \tag{A.67}$$

$$\boldsymbol{b = 59.87} \tag{A.68}$$

$$A = \frac{(a+b+1) + \sqrt{(a+b+1)^2 - 4ab}}{2a} \tag{A.69}$$

$$A = \frac{(2.83+59.87+1) + \sqrt{(2.83+59.87+1)^2 - 4\,(2.83)\,(59.87)}}{2\,(2.83)} \tag{A.70}$$

$$\boldsymbol{A = 21.53} \tag{A.71}$$

$$B = \frac{(a+b+1) - \sqrt{(a+b+1)^2 - 4ab}}{2a} \tag{A.72}$$

$$B = \frac{(2.83+59.87+1) - \sqrt{(2.83+59.87+1)^2 - 4\,(2.83)\,(59.87)}}{2\,(2.83)} \tag{A.73}$$

$$\boldsymbol{B = 0.98} \tag{A.74}$$

$$\omega_1 = \sqrt{A\frac{k_e}{m}} \tag{A.75}$$

$$\omega_1 = \sqrt{21.53\frac{7.80 \times 10^7 \frac{N}{m}}{1980kg}} \tag{A.76}$$

$$\boldsymbol{\omega_1 = 920.95Hz} \tag{A.77}$$

$$\omega_2 = \sqrt{B\frac{k_e}{m}} \tag{A.78}$$

$$\omega_2 = \sqrt{0.98\frac{7.80 \times 10^7 \frac{N}{m}}{1980kg}} \tag{A.79}$$

$$\boldsymbol{\omega_2 = 196.48Hz} \tag{A.80}$$

$$C = \frac{1-B}{A-1}\frac{1}{\left(\frac{1-B}{A-1}+1\right)\omega_1} \tag{A.81}$$

$$C = \frac{1-0.98}{21.53-1}\frac{1}{\left(\frac{1-0.98}{21.53-1}+1\right)920.95Hz} \tag{A.82}$$

$$\boldsymbol{C = 1.06 \times 10^{-6}} \tag{A.83}$$

$$D = \frac{1}{\left(\frac{1-B}{A-1}+1\right)\omega_2} \tag{A.84}$$

$$D = \frac{1}{\left(\frac{1-0.98}{21.53-1}+1\right)196.48Hz} \tag{A.85}$$

$$\boldsymbol{D = 5.08 \times 10^{-3}} \tag{A.86}$$

$$\begin{bmatrix} x_s \\ x_d \end{bmatrix} = \left(10\frac{m}{s}\right)(1.06 \times 10^{-6} \begin{bmatrix} 1 - 21.53 \\ 1 \end{bmatrix} \sin(920.95Hz \times 0.0079s) + 5.08 \times 10^{-3} \begin{bmatrix} 1 - 0.98 \\ 1 \end{bmatrix} \sin(196.48Hz \times 0.0079s)) \tag{A.87}$$

$$\begin{bmatrix} \boldsymbol{x_s} \\ \boldsymbol{x_d} \end{bmatrix} = \begin{bmatrix} \mathbf{0.0007} \\ \mathbf{0.0508} \end{bmatrix} \boldsymbol{m} \tag{A.88}$$

$$F_{ni} = max\left(k_e\left((\frac{k_s}{k_d} + 1)x_s - x_d\right)\right) \tag{A.89}$$

$$F_{ni} = max\left(\left(7.68 \times 10^7 \frac{N}{m}\right)\left(\left(\frac{4.67 \times 10^9 \frac{N}{m}}{7.80 \times 10^7 \frac{N}{m}} + 1\right)(0.0007m) - 0.0508m\right)\right) \tag{A.90}$$

$$\boldsymbol{F_{ni} = 628kN} \tag{A.91}$$

A.2 Response to Impacts

This section outlines the example calculations regarding beam and column response due to debris impacts.

A.2.1 Khowitar et al. (2014)

$$c_s = \sqrt{\frac{\kappa G}{\rho}} \tag{A.92}$$

$$c_s = \sqrt{\frac{(0.833)\left(1.16 \times 10^{10} \frac{N}{m^2}\right)}{2400 \frac{kg}{m^3}}} \tag{A.93}$$

$$\boldsymbol{c_s = 2006.93\frac{m}{s}} \tag{A.94}$$

$$c_{0p} = \sqrt{\frac{E_p}{\rho_p}} \tag{A.95}$$

$$c_{0p} = \sqrt{\frac{5.52 \times 10^9 \frac{N}{m^2}}{350 \frac{kg}{m^3}}} \tag{A.96}$$

$$\boldsymbol{c_{0p} = 3971.33\frac{m}{s}} \tag{A.97}$$

$$F_{pR} = \frac{E_p A_p}{c_{0p}} u_{max} \tag{A.98}$$

$$F_{pR} = \frac{\left(5.52 \times 10^9 \frac{N}{m^2}\right)(0.283m^2)}{3971.33 \frac{m}{s}}\left(10\frac{m}{s}\right) \tag{A.99}$$

$$\boldsymbol{F_{pR} = 3933.59kN} \tag{A.100}$$

$$F_{cR} = \frac{2\kappa GA}{c_s} u_{max} \tag{A.101}$$

$$F_{cR} = \frac{2\,(0.833)\left(1.16 \times 10^{10}\frac{N}{m^2}\right)(0.64m^2)}{2006.93\frac{m}{s}}\left(10\frac{m}{s}\right) \tag{A.102}$$

$$\boldsymbol{F_{cR} = 61653.04kN} \tag{A.103}$$

$$F_0 = \frac{F_{cR}F_{pR}}{F_{cR} + F_{pR}} \tag{A.104}$$

$$F_0 = \frac{(61653.04kN)\,(3933.59kN)}{61653.04kN + 3933.59kN} \tag{A.105}$$

$$\boldsymbol{F_0 = 3697.67kN} \tag{A.106}$$

A.2.2 Khowitar et al. (2015)

$$c_{sp} = \sqrt{\frac{\kappa_p G_p}{\rho_p}} \tag{A.107}$$

$$c_{sp} = \sqrt{\frac{(0.9)\left(1.14 \times 10^9\frac{N}{m^2}\right)}{350\frac{kg}{m^3}}} \tag{A.108}$$

$$\boldsymbol{c_{sp} = 1712.14\frac{m}{s}} \tag{A.109}$$

$$c_{sc} = \sqrt{\frac{\kappa_c G_c}{\rho_c}} \tag{A.110}$$

$$c_{sc} = \sqrt{\frac{(0.833)\left(1.16 \times 10^{10}\frac{N}{m^2}\right)}{2400\frac{kg}{m^3}}} \tag{A.111}$$

$$\boldsymbol{c_{sc} = 2006.93\frac{m}{s}} \tag{A.112}$$

$$F_{pR} = 2\rho_p c_{sp} u_{max} A_p \tag{A.113}$$

$$F_{pR} = 2\left(350\frac{kg}{m^3}\right)\left(1712.14\frac{m}{s}\right)\left(10\frac{m}{s}\right)\left(0.283m^2\right) \tag{A.114}$$

$$\boldsymbol{F_{pR} = 3391.75kN} \tag{A.115}$$

$$F_{cR} = 2\rho_c c_{sc} u_{max} A_c \tag{A.116}$$

$$F_{cR} = 2\left(2400\frac{kg}{m^3}\right)\left(2006.93\frac{m}{s}\right)\left(10\frac{m}{s}\right)\left(0.64m^2\right) \tag{A.117}$$

$$\boldsymbol{F_{cR} = 61652.89kN} \tag{A.118}$$

$$F_0 = \frac{F_{cR} F_{pR}}{F_{cR} + F_{pR}} \tag{A.119}$$

$$F_0 = \frac{(3391.75kN)\,(61652.89kN)}{3391.75kN + 61652.89kN} \tag{A.120}$$

$$\boldsymbol{F_0 = 3214.89kN} \tag{A.121}$$

A.3 Energy Method

This section outlines the procedure for calculating the force capacity of an element using the energy method specified in Clause 6.11.8 of ASCE 7 (2016).

A.3.1 Clause 6.11.8 of ASCE 7 (2016)

The following are assumptions made in order to complete the calculation:

- Coefficient of restitution, $C_e = 0.12$ (Aghl et al., 2015).
- Initial elastic stiffness of the structure is the same as calculated for the SDOF models.
- Permissible ductility ratio, $\mu = 12.5$ (Youcef and Chemrouk, 2012).
- M_e and M_m are equal to the mass of the cross section of the column element, $1536kg$.

$$F_{cap} = u_{max} \frac{1 + C_e}{(1 + \frac{M_m}{m_d})\sqrt{2\mu - 1}} \sqrt{k_e M_e} \tag{A.122}$$

$$F_{cap} = \left(10\frac{m}{s}\right) \left[\frac{1 + 0.12}{(1 + \frac{1536kg}{1980kg})\sqrt{2\,(12.5) - 1}}\right] \sqrt{\left(4.67 \times 10^9 \frac{N}{m}\right)(1536kg)} \tag{A.123}$$

$$\boldsymbol{F_{cap} = 3448kN} \tag{A.124}$$

A.4 Debris Damming

This section outlines the example calculations for debris damming loads. Also assumed:

- Width of dam, $b = 10m$.
- Inundation height, $h_e = 5m$.
- Fluid density, $\rho_f = 1025\frac{kg}{m^3}$.
- Drag coefficient, $C_d = 2.0$ (FEMA P646, 2012).
- Resistance coefficient, $C_R = 1.2$ (corresponding to a $R_{ed}F_{rd} = 1.15$, as per Stolle et al. (2018d)).
- Width of the channel, $w = 15m$.

A.4.1 ASCE 7 (2016)

$$F_{nd} = \frac{1}{2}\rho_f C_d b \left(h_e u_{flow}^2\right) \tag{A.125}$$

$$F_{nd} = \frac{1}{2}\left(1025\frac{kg}{m^3}\right)(2.0)\,(10.0m)\left((5.0m)\left(10.0\frac{m}{s}\right)^2\right) \tag{A.126}$$

$$\boldsymbol{F_{nd} = 5125kN} \tag{A.127}$$

A.4.2 Stolle et al. (2018c)

$$C_{R0} = C_R\left(1 + \frac{C_R b}{w}\right)^2 \tag{A.128}$$

$$C_{R0} = (1.2)\left(1 + \frac{(1.2)\,(10.0m)}{15.0m}\right)^2 \tag{A.129}$$

$$\boldsymbol{C_{R0} = 3.89} \tag{A.130}$$

$$F_{nd} = \frac{1}{2}\rho_f C_{R0} b \left(h_e u_{flow}^2\right) \tag{A.131}$$

$$F_{nd} = \frac{1}{2}\left(1025\frac{kg}{m^3}\right)(3.89)\,(10.0m)\left((5.0m)\left(10.0\frac{m}{s}\right)^2\right) \tag{A.132}$$

$$\boldsymbol{F_{nd} = 9968kN} \tag{A.133}$$

Appendix B

OpenSees Modelling Decisions - NCREE Structure

B.1 Nodal Mass

The mass for any particular member was estimated by taking the volume of the member and multiplying it by the density of concrete, with this total mass it was then equally lumped at each node in the x-direction for that specific member. The mass was placed in the x-direction as the loads being applied onto the structure only corresponded to the x-direction.

B.2 Geometric Transformation

Geometric transformation describes the transformation method which transforms beam element stiffness and resisting forces from the local system to the global system. Three options are available in *OpenSees*: (1) *linear transformation*, (2) *P-delta transformation*, and (3) *full corotational transformation*. The *linear transformation* does not consider large deformation effects and hence was not chosen for this analysis as large deformations are expected. The *P-delta transformation* considers large deformations by considering the second-order P-Delta effects and hence was a candidate for this analysis. The *full corotational transformation* also deals with large displacement and small strain problems and hence was also a candidate for this analysis. For this chosen analysis the *P-Delta* and *corotational transformations* were compared and there appeared to be no computational time difference or difference in response parameters. Additionally, the model was more stable when using the *corotational transformation* when compared to the *P-Delta transformation*. Hence, because there was no noticeable computational time difference and there was increased model stability using the *corotational transformation*, this geometric transformation was chosen for this analysis.

B.3 Steel Model

The steel model used in this study corresponded to the *ReinforcingSteel* model. This model constructs a material object that is specifically meant for use in reinforced concrete fiber sections. The inputs consist of the yield stress in tension, ultimate stress in tension, initial elastic tangent, tangent at initial strain hardening, strain corresponding to initial strain hardening, and the strain at peak stress, these values were taken from full scale experimental testing completed by Fu-Pei et al. (2018).

B.4 Concrete Model

The properties of the unconfined and confined concrete were calculated as per Chang and Mander (1994). The concrete model that was selected for the beams was the *Concrete02* model. This model assumes a linear tension softening branch which describes the relationship between the tensile stress and strain in the concrete. The inputs consist of the compressive strength at 28 days, concrete strain at maximum strength, concrete crushing strength, concrete strain at crushing strength, ratio between the unloading slope at the crushing strength and the initial slope, the tensile strength, and the tension softening stiffness, these values were taken from full scale experimental testing completed by Fu-Pei et al. (2018). It should be noted that the full-scale experimental testing did not provide a force-displacement history to calibrate the model data to, hence why the least complicated concrete model was selected for the beams.

The concrete model selected for the columns was the *Concrete07* model. This concrete model was compared to the *Concrete02* model using similar input parameters. The difference between the two models is that the tension branch is assumed to be linear in the *Concrete02* model whereas, in the *Concrete07* it is nonlinear. Comparing the *Concrete02* model to the *Concrete07* model showed that the *Concrete02* model did not fit the force-displacement hysteresis adequately for the columns. The *Concrete02* model typically overestimated the force in the hysteresis when compared to the physical results. Due to the simplicity in defining the *Concrete07* model and the *Concrete02* model overestimating the force-displacement hysteresis for the columns, the *Concrete07* model was chosen to model the unconfined and confined concrete of the column sections. The *Conrete07* model fit to the experimental data can be seen below in Figure B.1.

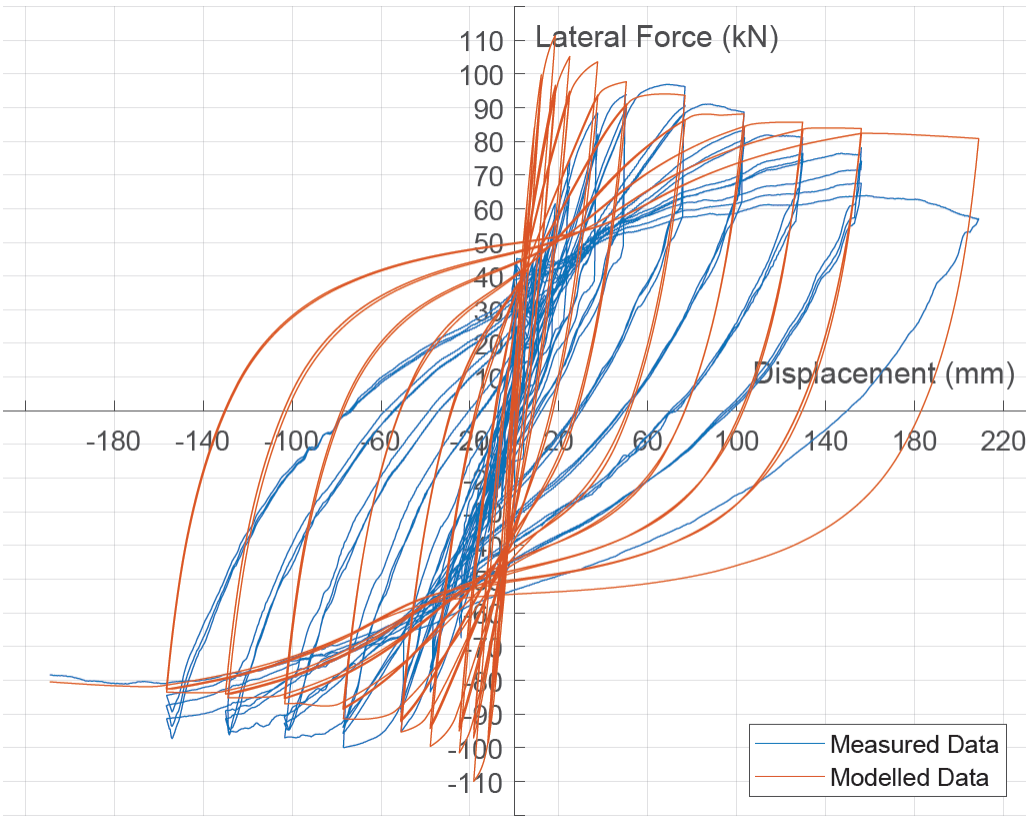


Figure B.1: Force-Displacement History Comparison

B.5 Section Model

The section model selected for analysis was the *Fiber section* model. This model was selected as it allowed for the unconfined regions and confined regions of concrete to be explicitly modelled. The fiber model was discretized into 32 patched quadrature sections in each direction for both the confined and unconfined concrete, this provides a fine mesh over the section which typically results in a more accurate model. 32 sections were chosen overusing a smaller number as no extra computational time was incurred by increasing the number of sections; this is likely due to having a very simplistic model.

B.6 Analysis Type and Damping Model

Transient analysis was chosen as the earthquake and impact load are both time dependent loads hence, it is unsuitable to use a *Static* analysis. Inherent damping was included in the model by the use of *Raleigh* damping with a damping coefficient of 3%.

B.7 System of Equations Solver

The system of equations was solved using the *BandGeneral* solver which is a direct solver for banded asymmetric matrices. This solver was compared to the *UmfPack* solver used in the dynamic analysis where it was found that the *BandGeneral* solver was more stable than the *UmfPack* solver. Additionally, the *BandGeneral* solver does not rely on the system of equations being positive definite which is beneficial for complex models with large deformations. The *BandSPD* solver is similar but more efficient than the *BandGeneral* solver however, it requires that the system of equations be positive definite and hence was not used for this analysis.

B.8 Convergence Test

The convergence test used for this analysis was selected as the *EnergyIncr* test. This type of convergence test specifies a tolerance on the dot product of the unbalanced load and displacement increment, which is typically equated to the energy unbalance in the system. This convergence test was selected as it takes into consideration both the unbalanced load and displacement increment in the system. Whereas, the other available convergence tests consider only either the unbalanced load or displacement increment. Additionally, the *EnergyIncr* test provided more model stability when compared to the alternative convergence tests.

B.9 Integrator

The integrator used for this analysis was the *Newmark* method with the constant average acceleration assumption, which is an implicit method, meaning it is unconditionally stable. The gamma and beta terms selected were 0.5 and 0.25, which means the constant average acceleration assumption is used instead of the linear acceleration assumption. The linear acceleration method is conditionally stable based on the time step and hence was not used for this analysis. An alternative integrator is the *HHT* integrator which is based off of the three parameter Hilbert-Hughes-Taylor time-stepping method which can introduce an unknown amount of numerical damping into the system. Due to the addition of an unknown amount of numerical damping being added into the system the *HHT* integrator was not used. Another integrator is the *TRBDF2* integrator, which is a composite scheme that alternates between the trapezoidal scheme and 3-point backward Euler scheme, in doing so this method conserves both energy and momentum which is not always true for the *Newmark* scheme. Even though this method conserves energy and momentum, the *Newmark* integrator was selected as this is the most commonly used method for solving dynamic analysis problems.

B.10 Solution Algorithm

The algorithm selected for this analysis was the *BFGS* algorithm which is based off of the Broyden-Fletcher-Goldfarb-Shanno method. This method was selected based off of an adaptive algorithm scheme in which the analysis runs for one type of algorithm and if it fails, the script skips to the next algorithm and performs the analysis. Initially the *KrylovNewton* algorithm was used for this analysis, however, it was quickly determined that this algorithm was not stable for this specific earthquake record. Other algorithm schemes included in the adaptive analysis were the *NewtonLineSearch* and the *Broyden* algorithms. All algorithms proved to be unstable for this earthquake record except for the *BFGS* scheme and hence, the *BFGS* algorithm was used for the analysis.

Appendix C

Numerical Solution Algorithms

C.1 Duhamel's Integral Solution Algorithm

Duhamel's integral is a function of two main components, the first being the impact loading history and the second being the impulse response of the system. The impulse response is defined as a function of the damping ratio, damped and undamped natural frequencies, time, and the elapsed time since impact as shown below:

$$h(t-\tau) = e^{-\xi\omega_n(t-\tau)} \sin \omega_d (t-\tau) \tag{C.1}$$

Substituting this definition of the impulse response into Duhamel's integral results in the following equation for the force response of a SDOF system:

$$R(t) = \frac{k}{m_s \omega_d} \int_0^t p(\tau) e^{-\xi\omega_n(t-\tau)} \sin \omega_d (t-\tau) d\tau \tag{C.2}$$

The solution to the Duhamel integral follows an iterative procedure where the integral is evaluated by using an incremental summation over time as outlined in Navaratnam et al. (2013). The response of the structure at time t can be estimated by the following equation:

$$R(t) = A(t) \sin \omega_d t - B(t) \cos \omega_d t \tag{C.3}$$

Where the parameters A and B are defined by the following integrals:

$$A(t) = \frac{k}{m_s \omega_d} \int_0^t p(\tau) \left(\frac{e^{\xi\omega_n \tau}}{e^{\xi\omega_n t}} \right) \cos \omega_d \tau d\tau \tag{C.4}$$

$$B(t) = \frac{k}{m_s \omega_d} \int_0^t p(\tau) \left(\frac{e^{\xi\omega_n \tau}}{e^{\xi\omega_n t}} \right) \sin \omega_d \tau d\tau \tag{C.5}$$

Navaratnam et al. (2013) state that the integrals A and B can be solved by an incremental summation procedure for a time, t_N, where $N = 1, 2, 3, ...$ as shown below:

$$A_{N+1} = A_N e^{-\xi\omega_n \Delta\tau} + \frac{\Delta\tau k}{m_s \omega_d} e^{\xi\omega_d \Delta\tau} p(N) \cos \omega_d t_N \tag{C.6}$$

$$B_{N+1} = B_N e^{-\xi\omega_n \Delta\tau} + \frac{\Delta\tau k}{m_s \omega_d} e^{\xi\omega_d \Delta\tau} p\,(N) \sin \omega_d t_N \tag{C.7}$$

Following these definitions, the response of the system at time t_{N+1} can be estimated by the following formula:

$$R_{N+1} = A_{N+1} \sin \omega_d t_{N+1} - B_{N+1} \cos \omega_d t_{N+1} \tag{C.8}$$

This procedure is repeated for the next time step by increasing i by 1.

C.2 Newmark's Constant Average Acceleration Solution Algorithm for Linear Systems

The solution to Newmark's constant average acceleration method for linear systems follows a time-stepping procedure as outlined in Chopra (2017). Newmark's method relies on the stiffness, mass, and damping matrices of the system. Furthermore, to start the algorithm, the time step, displacement vector, and velocity vector at the first time step must be known, along with the forcing function. If all of these parameters are known, four other initial parameters (a_1, a_2, a_3, $\hat{k}$), and the initial acceleration vector can be calculated as shown below (Chopra, 2017):

$$\{\ddot{u}_0\} = [m]^{-1} \Big[p\,(0) - [c]\,\{\dot{u}_0\} - [k]\,\{u_o\} \Big] \tag{C.9}$$

$$a_1 = \frac{1}{\beta(\Delta t)^2}\,[m] + \frac{\gamma}{\beta \Delta t}\,[c] \tag{C.10}$$

$$a_2 = \frac{1}{\beta \Delta t}\,[m] + \left(\frac{\gamma}{\beta} - 1\right)[c] \tag{C.11}$$

$$a_3 = \left(\frac{1}{2\beta} - 1\right)[m] + \Delta t \left(\frac{\gamma}{2\beta} - 1\right)[c] \tag{C.12}$$

$$\hat{k} = [k] + a_1 \tag{C.13}$$

Where γ and β are constants for Newmark's method and for the constant average acceleration method, γ is equal to 0.5 and β is equal to 0.25. With these initial parameters defined, the response of the system at time t_{i+1} can be approximated by the following formulas.

The forcing vector at time t_{i+1}:

$$\hat{p}(t_{i+1}) = p(t_{i+1}) + a_1\,\{u_i\} + a_2\,\{\dot{u}_i\} + a_3\,\{\ddot{u}_i\} \tag{C.14}$$

The displacement vector at time t_{i+1}:

$$\{u_{i+1}\} = \hat{k}^{-1}\hat{p}(t_{i+1}) \tag{C.15}$$

The velocity vector at time t_{i+1}:

$$\{\dot{u}_{i+1}\} = \frac{\gamma}{\beta\Delta t}\left(\{u_{i+1}\} - \{u_i\}\right) + \left(1 - \frac{\gamma}{\beta}\right)\{\dot{u}_i\} + \Delta t\left(1 - \frac{\gamma}{2\beta}\right)\{\ddot{u}_i\} \tag{C.16}$$

The acceleration vector at time t_{i+1}:

$$\{\ddot{u}_{i+1}\} = \frac{1}{\beta\left(\Delta t\right)^2}\left(\{u_{i+1}\} - \{u_i\}\right) - \frac{1}{\beta\Delta t}\{\dot{u}_i\} - \left(\frac{1}{2\beta} - 1\right)\{\ddot{u}_i\} \tag{C.17}$$

This procedure is repeated for the next time step by increasing i by 1.